2018

The Effect of Calcium Aluminates on the Kinetics of Coke Analogue Gasification in CO2 Gas

Apsara Saumyakumari Jayasekara

UNIVERSITY
OF WOLLONGONG
AUSTRALIA

The Effect of Calcium Aluminates on the Kinetics of Coke Analogue Gasification in CO_2 Gas

A thesis submitted in fulfilment of the

requirements for the award of the degree

Doctor of Philosophy

from

University of Wollongong

by

Apsara Saumyakumari Jayasekara

Faculty of Engineering and Information Sciences

School of Mechanical, Materials, Mechatronic and Biomedical Engineering

April 2018

Certification

I, Apsara Saumyakumari Jayasekara, declare that this thesis, submitted in partial fulfilment of the requirements for the award of Doctor of Philosophy, in the Faculty of Engineering and Information Sciences, University of Wollongong, is my own work unless otherwise referenced or acknowledged. This document has not been submitted for qualifications at any other academic institution.

APSARA SAUMYAKUMARI JAYASEKARA

April 2018

Abstract

Metallurgical coke is a key component in the blast furnace ironmaking process. It is a complex composite material containing different forms of carbonaceous materials, mineral components and a pore structure. It also has significant heterogeneity in its mineralogy (type and particle size), carbon forms and phase dispersion. This complexity and heterogeneity increases the uncertainty in any testing of the coke and makes it difficult to quantitatively evaluate specific factors that influence coke gasification in CO_2 gas.

The mineralogy metallurgical of coke is a key parameter that affects coke gasification. Further, it is also known that Ca-containing minerals increase the gasification rate. A better understanding of their effect on coke is of particular interest to coke producers and users.

In this study, the effects of Ca-containing minerals on coke analogue gasification are evaluated. The use of the coke analogue is to overcome/address uncertainty issues associated with coke complexity and heterogeneity.

The primary aims of this thesis are:

1. To establish how representative the coke analogue is of metallurgical coke.
2. To test whether the analogue has similar rate controlling kinetics to that of industrial coke.
3. To test the effects of the Ca containing minerals on coke analogue gasification in CO_2.
4. To test whether the Random Pore Model can be used to predict coke analogue gasification.

The findings relating to these aims are dealt with in turn.

How representative the coke analogue is of metallurgical coke?

How representative the coke analogue is of the metallurgical coke was established by characterising the coke analogue and a metallurgical coke with respect to their porosity, microstructure, carbon bonding (sp^2–sp^3) general gasification reactivity in

CO_2, and reaction kinetics in CO_2. The coke analogue was found to be representative of metallurgical coke, as summarised below.

- Two different but complementary techniques, optical microscopy and mercury porosimetry, were used to assess the porosity of the coke analogues and a metallurgical coke. It was found that the porosity and pore size distribution of the analogues were well controlled and more reproducible than that of metallurgical coke. The majority of the pores in the coke analogue(s) were in the 10–100 µm pore diameter range and broadly representative of the pores in metallurgical coke in the size range of <200 µm.

- Microscopy and XRD were used to characterise the mineralogy of the coke analogue and metallurgical coke. The mineral phases in the fired coke analogue were in general found to be the same as those added to the "green" unfired analogue. In general, the size, composition and morphology of the minerals in the coke analogue was less complex, homogenously dispersed, and well controlled compared to that of the metallurgical coke.

- Microscopy and Raman spectroscopy were used to characterise the carbon bonding of the coke analogue and compared to that of metallurgical coke. Optical and scanning electron microscopy (SEM) showed that the coke analogue had a uniform and well-controlled microstructure relative to that of metallurgical coke. The microstructure of the analogue was made up of graphite grains and carbonised phenolic resin, minerals and pores. Under optical microscopy, the graphite grains showed similar characteristics to those of metallurgical coke RMDC while the carbonised phenolic resin of the fired analogue was similar to IMDC in metallurgical coke.

- The Raman spectroscopy measurements carried out to assess the coke analogue carbon bonding showed the carbon bonding to be a mixture of sp^2 and sp^2–sp^3 bonding. Assessment of the analogue bonding was mainly through the $I_{(D)}/I_{(G)}$ and $I_{(V)}/I_{(G)}$ ratios. The analogue ratios were 0.16–1.55 and 0–0.41 respectively. These values overlap with the $I_{(D)}/I_{(G)}$ (1.16–1.45) and $I_{(V)}/I_{(G)}$ (0.38–0.62) ratios reported in the literature for metallurgical coke.

- TGA was used to assess the general reactivity of the coke analogue in CO_2 gas over the temperature range of 1173 – 1623 K. The reactivity trend with respect to time and the effects of temperature on the reaction kinetics of the coke analogue were similar to that of metallurgical coke. The coke analogue showed a greater reproducibility than metallurgical coke. This better reproducibility is a result of the controlled porosity, the simplified carbonaceous characteristics and homogeneous nature of the coke analogue.

Does the analogue have similar rate controlling kinetics to that of industrial coke?

- To understand the reaction kinetics, the Walker *et al.* Arrhenius approach was used. From this approach, two temperature zones corresponding to different kinetic control regimes were identified in the analogue: the chemical reaction controlled regime (Zone I) and the mixed controlled regime (Zone II). These control regimes are the same as those reported for metallurgical coke.

  The activation energy value obtained for the coke analogue (no minerals added) Zone I was 271.6 ± 0.5 kJ mol^{-1}. This activation energy value is within the range of activation energies reported for metallurgical coke in the literature and the value evaluated in this study (222-285 kJ mol^{-1}). This similar activation energy is an indication that similar reaction mechanisms are active for the coke analogue and metallurgical coke gasification.

The effects of Ca containing minerals on coke analogue gasification in CO_2 gas

The coke analogue was used to understand the effects of Ca-containing minerals on coke gasification in CO_2. These effects were assessed by adding Ca-containing minerals to the coke analogue and reacting them with CO_2. Al_2O_3, CA6, CA, C3A and lime were added to assess the Ca bearing mineral effect on coke reactivity across the $CaO – Al_2O_3$ binary system. Most of the results in this thesis are from this system. Measurement and analysis of a ternary composition in the $CaO – Al_2O_3 – SiO_2$ (CAS) system were also conducted. CAS consists of a mixture of calcium aluminosilicates anorthite, gehlenite and mullite

The microstructure and the reactivity of the coke analogues doped with minerals were assessed using microscopy and TGA. Two different kinetic approaches were used to

understand the transient behaviour of the analogue gasification, the classical initial rate/Arrhenius approach used by Walker *et al.* (Gas reactions of Carbon, 1959) and the random pore model (RPM). These approaches were considered as the Walker *et al.* (Gas reactions of Carbon, 1959) approach is commonly used to assess coke kinetics and the RPM allows consideration of the gas – carbon contact area on analogue gasification.

The effect of Ca-containing minerals on the coke analogue gasification and the applicability of RPM for the coke analogue gasification are summarised in the following points.

- The gasification rate of the coke analogues containing minerals in the CaO – Al_2O_3 binary mineral system increased with increasing Ca content in the coke analogue. The reaction rate was found to be proportional to the total amount of Ca (n_{Ca}) and the chemical activity of CaO (a_{CaO}) in the mineral. The correlation with n_{Ca} was greater than that of the a_{CaO} indicating that it was more of a mass/volume effect than a chemical effect.

- Activation energies obtained from both the Walker *et al.* (Gas reactions of Carbon, 1959) approach and the RPM were similar and both showed a dependency on the Ca content of the minerals. The activation energy decreased with increasing Ca content. Alumina had no or negligible effect on the reactivity over the temperature range examined in this thesis.

- CAS and CA6 contained similar amounts of Ca and were found to have similar reactivities and activation energies. Both alumina and quartz were found to have no or negligible effect on the reactivity over the temperature range studied in this thesis.

- The majority of the minerals added to the analogue did not change phase or particle size on firing. The primary exception was the lime doped coke analogue. In this analogue after firing, the particle size changed significantly and the lime was dispersed throughout the coke analogue carbon matrix. The particles sizes were significantly smaller than the originally added particle size range. It was proposed that the size change/dispersion was due to a reaction between the basic CaO and the acidic -OH groups in the phenolic resins.

- The mechanism of catalysis of the gasification reaction by Ca was consistent with interactions between Ca and the carbon matrix that increase the electron density of the neighbouring carbon atoms. This has the effect of both increasing the number of active carbon sites (C_f) and by increasing the e^- density of these C_f, increasing their ability to dissociate CO_2. Both of these factors can lead to an increase the rate of gasification of the coke analogue in CO_2.

Does the RPM applicable for the coke analogue gasification in CO_2?

- The coke analogue gasification results obtained from Walker *et al.* (Gas reactions of Carbon, 1959) approach were able to be replicated using RPM for almost all the coke analogues studied. The exception being the lime doped coke analogue.

- The application of RPM for the base coke analogue over the temperature range of 1173 – 1623 K showed increasing deviation from the RPM above 1273 K. This indicated a change in the rate controlling mechanism, a transition from Zone I to Zone II kinetics. This transition temperature is similar to that obtained from the Walker *et al.* (Gas reactions of Carbon, 1959) approach.

- The gasification of the lime doped coke analogue could not be replicated by the RPM. This is likely due to different mineral dispersion in the analogue. This different mineral dispersion likely leads to the mineral – carbon surface area playing a larger role in the determination of the coke gasification rate. As the RPM only accounts for gas – carbon surface area, the increased carbon-mineral contact effect is not accounted for.

It has been shown in this study that the coke analogue can be used to study metallurgical coke gasification behaviour by minimising the complexity and heterogeneity issues associated with the metallurgical coke. It can also potentially be extended to study other coke related applications. This study helps to broaden the knowledge on the effect of Ca-containing minerals on the fundamentals of coke gasification kinetics. Furthermore, in this study it has been shown that the coke analogue gasification could be explained and predicted using the RPM kinetic model.

Table of contents

List of Tables

List of figures

Nomenclature and Abbreviations

Symbol	Definition/meaning in the text
A	Surface area, m^2
a_{CaO}	Activity of CaO in calcium aluminates
Ai	Surface area of a single particle, m^2
A_T	Total surface area per of coke analogue carbonaceous, m^2
BET	Brunauer-Emmett-Teller
CA	$CaO.Al_2O_3$
CA6	$CaO.6Al_2O_3$
C3A	$3CaO.Al_2O_3$
C_f	Carbon active sites
C(O)	Chemisorbed oxygen on carbon (intermediate)
ΔC	Concentration change of gaseous reactants, $g.m^{-3}$
C_s	Carbon concentration at the surface
CAS	Calcium aluminosilicate
CRI	Coke reactivity index and
CSR	Coke strength after reaction
d	Particle diameter, μm
$d_{(002)}$	Interlayer spacing
Ea	Activation energy, $J.mol^{-1}$
FWC	Fractional weight change
ΔG°	Gibbs free energy, J mol^{-1}
$I_{(D)}$	Intensity of the D band
$I_{(G)}$	Intensity of the G band
$I_{(V)}$	Intensity of the valley between D and G bands
IMDC	Inert maceral derived component
k	Reaction rate constant, $g.s^{-1}.m^{-2}$
k_0	Pre exponential factor, s^{-1}
K_{RPM}	Random pore model rate constant
L_0	Total initial pore length per unit volume, m/m^3

La	Crystallite width
Lc	Crystallite height
n	Order of the reaction
N	Total number of particles in coke analogue carbonaceous
n_{Ca}	Number of moles of Ca
m	Mass of particles, g
P_1	Porosity value at the coke analogue centre, position '1'
P_a	Porosity value at the coke analogue annulus
P_{O_2}	Partial pressure of O_2
P_{CO_2}	Partial pressure of CO_2
P_{CO}	Partial pressure of CO
R	Gas constant, $J.K^{-1}.mol^{-1}$
R_C	Initial reaction rate, $g.g^{-1}.s^{-1}$
R_O	Mean reflectance
RMDC	Reactive maceral derived component
RPM	Random pore model
SEM	Scanning electron microscopy
t	Time, s
T	Temperature, K or °C
TEM	Transmission electron microscopy
TGA	Thermogravimetric analyzer
V_i	Volume of a single particle, m^3
V_T	Total volume of particles in coke analogue carbonaceous, m^3
W	Weight of the sample at time t, g
X	Fractional carbon conversion
X_m	Carbon conversion at maximum reaction rate
XRD	X-ray diffraction
ε_0	Initial porosity, %
θ	Bragg scattering angle of the diffraction peak
λ	Radiation wavelength of the X-ray source
φ	Structural parameter for RPM

σW_0	Error of initial weight obtained from the TGA scale that has a quantifiable uncertainty associated with the balance and buoyancy effect
σdt	Error of the resolution of the reading
σX	Error of carbon conversion
σR_C	Error of initial reaction rate

I dedicate this work to my loving Parents

Acknowledgment

The success and final outcome of this project have been shadowed by a lot of guidance and support from many individuals and I am extremely privileged to have them throughout this project. I would like to use this opportunity to express my gratitude.

First, I offer my special thanks and appreciation to my parents, husband and daughter for their patience and understanding with my busy schedule.

I would like to express my sincere gratitude and respect to my principle supervisor Professor Brian J. Monaghan for his continuous guidance, encouragement and feedback throughout this study. During this project he provided extreme support for both experimental work and thesis and papers writing. I am extremely thankful to him for his understanding, patience and kindness during my personal constrains happened during the project timeline. I am grateful for the financial support he provided during this study.

I owe a deep gratitude to my co-supervisor, Dr. Raymond J. Longbottom for his enormous support to make this project success. He was always ready to provide guidance in laboratory instrumentation, experiments and writing. He always came up with brilliant ideas and suggestions whenever I got experimental difficulties.

I would like to highlight the contribution and assistance of the following individuals towards the success of this study,

- Greg Tillman, Nick Mackie, Matthew Franklin, Tony Romeo, Dr. Mitchel Nancarrow and other UOW technical staff for training in metallography, SEM and XRD.
- Dr. Harold Rogers assisted with the polarised optical microscopy and the SEM/EDS images from the ZEISS EVO 50 SEM instrument.

I am grateful for the financial support of the University of Wollongong through the International Postgraduate Tuition Awards (IPTA) and Faculty Scholarship without which this project would not have been possible.

Chapter 1

Introduction

Coke is the fuel and the primary source of CO gas for the reduction of iron oxide in the blast furnace. It also gives the structural support to the furnace to ensure high permeability for high productivity [1]. Coke is composed of organic components, inorganic minerals and pores [2-4]. The organic components are derived from the macerals of the parent coal [5]. The mineral matter in the coke is the inorganic component. Coke mineralogy is an essential factor that in part determines coke reactivity. The mineral content of coke is typically 8-12 % by mass [2, 6, 7]. Generally, the chemical composition of inorganic matter contains elements such as O, Si, Al, Fe, Ca, S, Mg, K, Ti and Na and less commonly P, Mn, C, H, N, Ba, Sr, F and Cl [8].

Alkali metals [6, 9-12], alkaline earth metals [6, 9, 11] and transition metals such as iron and their oxides [2, 6, 9, 10, 13, 14] have been observed to have the ability to increase coke reactivity with CO_2. It is believed that alkalis and alkaline earths influence the gasification reaction by initiating it at significantly lower temperatures (750–850 °C) compared to usual gasification starting temperatures of 950 °C, thereby lowering the temperature in the blast furnace thermal reserve zone [15].

The coke quality is critical in achieving the high production rates required for profitable iron making in a blast furnace. The coke performance in the blast furnace is related to coke strength and reactivity. Typical methods of assessing coke quality are the coke reactivity index (CRI) and coke strength after reaction (CSR) [4, 16]. These tests provide a measure of the coke susceptibility to CO_2 reaction and subsequent weakening /degradation.

However, significant variations have been observed in the published CRI and CSR tests. The experimental results do not follow uniform trends, and this makes the identification and comparison of coke reaction parameters difficult. This experimental uncertainty ultimately makes the prediction of metallurgical coke performance in the blast furnace challenging. For Australian cokes, coal characteristics such as coal rank, ash composition, various components in the ash and maceral reflectograms can account for about 70% of the variations seen in the CRI and CSR tests of cokes [17].

It is difficult to determine the factors that account for the other 30% of the variation. It is believed that the heterogeneous nature of the mineralogy, carbon forms and phase dispersion are responsible for this 30% of the variation [17]. In addition to being heterogeneous, coke is also a complex composite material. It contains different forms of carbonaceous materials, mineral components and a pore structure primarily dependent on the volatile matter in the source coal and coking conditions.

As a result of the complexity and heterogeneity, it is often difficult to isolate the effects of specific components on coke behaviour and reaction kinetics when exposed to high temperatures and reactive atmospheres. This limits the progress to be made in coke studies in assessing the impact of minerals on reactivity and reaction kinetics [18, 19]. There have been a number of experimental and statistical approaches to address the effect of minerals on coke reactivity. Generally, in the statistical approach, the results correlate coke mineralogy with coke reactivity using large industrial data sets [2, 20-22]. The experimental approaches found that the effect of mineral cations present in coke on coke reactivity could be ranked as follows [16, 23]:

$K_2CO_3 > Na_2CO_3 > CaCO_3 > MgCO_3 = MgO > FeCO_3 > FeS_2 > A1_2O_3 = SiO_2$ (little or no change).

Though the results from these approaches can be used to understand key mineral effects on reactivity, they are not readily translatable to mineral combinations and do not account for the porosity effects on reactivity or the different carbonaceous types in the coke.

To overcome these problems, a coke analogue has been developed using laboratory grade materials (graphite, Bakelite, Novolac and minerals). This approach simplifies coke. In the analogue, the porosity, carbon type, mineral type, mineral particle size, and mineral dispersion are controlled or fixed. Previous studies carried out using the analogue with mineral matter added to mimic an industrial coke, have shown similar dissolution behaviour in iron to that of industrial coke [18]. Studies carried out with coke analogue doped with different minerals have shown that minerals have a significant effect on the reactivity of the coke analogue, with similar relations between specific minerals and reactivity as observed in industrial cokes [24].

While the previous studies have shown that the coke analogue is a promising tool in studying coke, the aim of this thesis is to address the following questions.

1. How representative is the coke analogue to the metallurgical coke with respect to general characteristics?

2. Does the analogue have similar rate controlling kinetics to these of industrial coke?

3. How do Ca-containing minerals affect coke reactivity and kinetics when it is in binary and ternary mineral combinations?

4. Can the Random Pore Model be used to predict coke analogue gasification?

Ca-containing minerals are of particular interest in coke/coal studies. Calcium has been shown to be particularly mobile in coal and coke [25-27] and significantly affects the coke's reactivity. In coke, calcium is present mostly as sulphides, silicates and phosphates [2]. It can also be present as carbonate and oxide forms [28]. In coke/coal studies, possibly due to its highly dispersed behaviour, Ca is considered as one of the essential elements in coke minerals that increase coke reactivity with CO_2 [16, 24, 29-33].

The coke analogue kinetics were studied using a coke analogue without added minerals, *i.e*. a base coke analogue. These base analogue results can then ultimately be used as the control experiment to compare the effect of Ca-containing minerals in the second part of the project. The minerals used in this study are minerals in the CaO – Al_2O_3 binary systems (lime, calcium aluminates (C3A, CA and CA6) and alumina) and CaO - Al_2O_3 - SiO_2 ternary system (CAS).

The objectives of the study are:

1. To evaluate coke microstructure using optical microscopy and SEM.
2. To evaluate the porosity and pore size distribution using optical microscopy followed by image analysis and mercury porosimetry.
3. To establish the kinetics of coke analogue gasification with CO_2 using TGA.

4. To evaluate the effect of Ca in binary and ternary mineral combinations on coke analogue reactivity and structure using TGA and optical microscopy and SEM.

The experimental outcomes of the thesis will be used to provide an understanding of the effect and behaviour of Ca-containing minerals in the metallurgical coke.

Chapter 2

Literature review

2.1 Blast Furnace

The iron making blast furnace is a smelting reaction chamber. It is a counter-current reactor where raw materials are added to the top of the furnace and gases are injected into the bottom (tuyeres (*Figure 2.1*)). The raw materials consist of iron-bearing materials (oxides), fluxes and coke. Hot air (O_2, N_2), pulverised coal or hydrocarbons are injected through tuyeres at the bottom of the furnace. Iron oxides, *i.e.*, hematite (Fe_2O_3) or magnetite (Fe_3O_4) can be charged as sinter, pellets, ore or some combination thereof [1, 34-39].

Key reactions in the blast furnace

A schematic of a blast furnace showing temperature profiles and key reactions is given in *Figure 2.1* [1, 38]. From this figure three distinct zones can be identified: the direct reduction, thermal reserve and pre-heat zones.

The oxygen from the hot blast, injected at the tuyere level, reacts with the coke carbon to produce CO_2 (*Equation 2.1* [40]). CO_2 is thermodynamically unstable in the presence of carbon at above ~900 °C [36] and produces CO gas (*Equation 2.2* [40]). The reaction given in *Equation 2.2* is an endothermic reaction generally known as the Boudouard reaction, gasification reaction or solution loss reaction [1, 36-38, 40, 41].

$$C_{(s)} + O_{2(g)} \rightarrow CO_{2(g)} + \text{heat} \qquad \Delta G^0 = -394100 - 0.84T \text{ J mol}^{-1} \qquad 2.1$$

$$CO_{2(g)} + C_{(s)} \rightleftharpoons 2CO_{(g)} \qquad \Delta G^0 = 165300 - 170.76 \text{ T J mol}^{-1} \qquad 2.2$$

The reaction given in *Equation 2.1* is highly exothermic and is likely to dominate at low temperatures and high oxygen partial pressures, while the reaction given in *Equation 2.2* dominates at high temperatures and low oxygen partial pressures [42, 43].

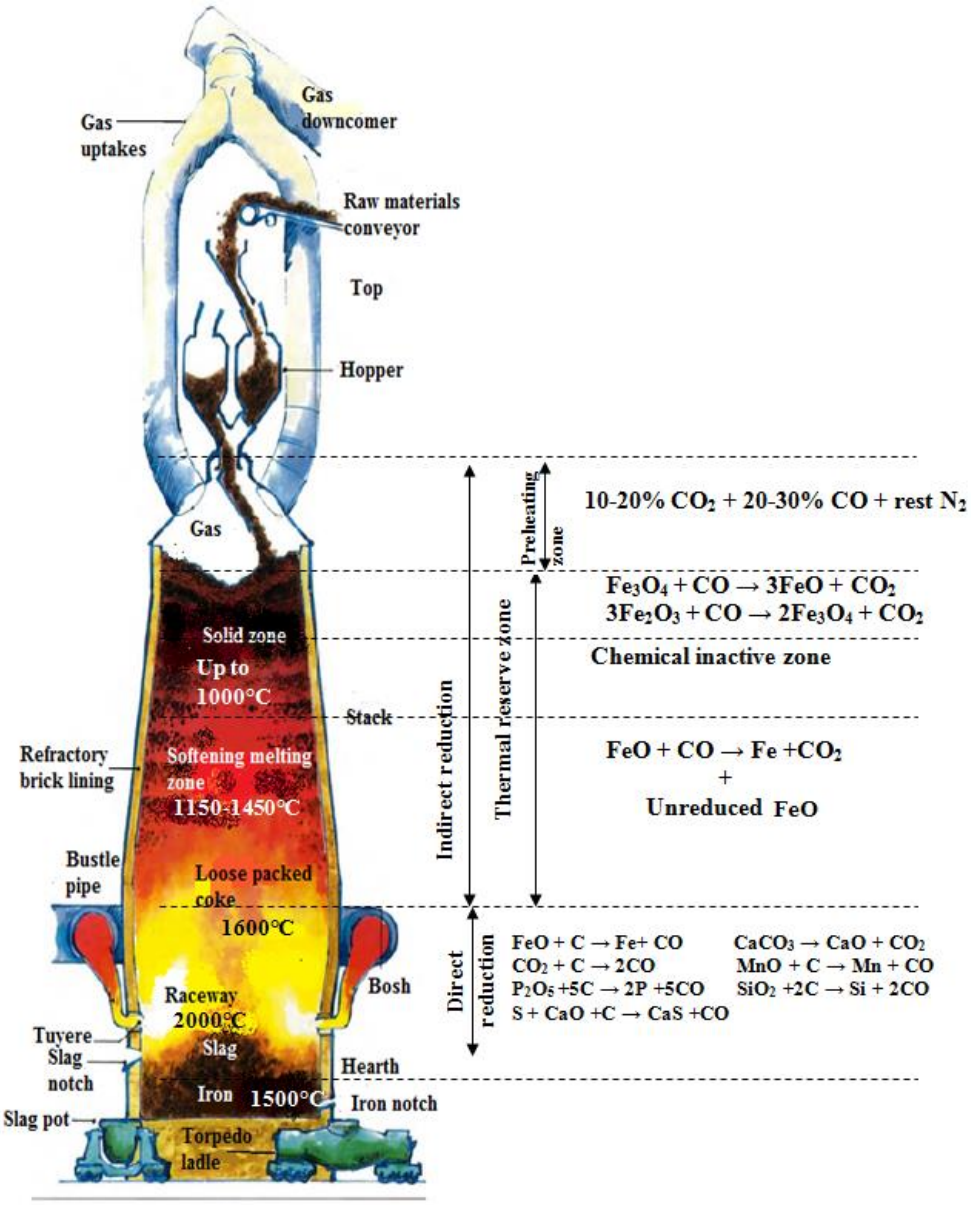

Figure 2.1: A schematic diagram of a blast furnace and reactions at each region (modified from [1, 38]).

In the indirect reduction zone (*Figure 2.1)* iron oxide reacts with $CO_{(g)}$ through exothermic reactions (*Equation 2.3 – 2.5)* [36, 40, 44].

$$FeO_{(s)} + CO_{(g)} \rightarrow Fe_{(s)} + CO_{2(g)} \qquad \Delta G^0 = -20100 + 22.14T\ J.mol^{-1} \qquad 2.3$$

$$3Fe_2O_{3(s)} + CO_{(g)} \rightarrow 2Fe_3O_{4(s)} + CO_{2(g)} \qquad \Delta G^0 = -30260 - 51.54T\ J.mol^{-1} \qquad 2.4$$

$$Fe_3O_{4(s)} + CO_{(g)} \rightarrow 3FeO_{(s)} + CO_{2(g)} \qquad \Delta G^0 = 32560 - 10.14T\ J.mol^{-1} \qquad 2.5$$

In the direct reduction zone (*Figure 2.1*), the lower part of the furnace, at temperatures higher than 1000 °C, iron oxide reacts with carbon through endothermic reactions (*Equations 2.6 – 2.7*) [36, 40, 44].

$$FeO_{(s)} + C_{(S)} \rightarrow Fe_{(s)} + CO_{(g)} \qquad \Delta G^0 = 118300 - 131.11T\ J.mol^{-1} \qquad 2.6$$

$$FeO_{(l)} + C_{(S)} \rightarrow Fe_{(l)} + CO_{(g)} \qquad \Delta G^0 = 132107 - 138.72T\ J.mol^{-1} \qquad 2.7$$

The overall reaction inside the blast furnace can be summarised as the reaction given in *Equation 2.8*, [38]:

$$Fe_2O_{3(s)} + 3CO_{(g)} \rightarrow 2Fe_{(s)} + 3CO_{2(g)} \qquad 2.8$$

2.2. Metallurgical coke

Coke is produced by heating coal in a coke oven in the absence of oxygen at a temperature between 1000 -1200 °C. The coke porosity, carbonaceous structure, and mineralogy undergo changes during the coke production. These changes also involve the release of volatile matter in gaseous forms such as CH_4, CO_2, CO, H_2S or H_2 [4, 34, 45-47].

2.2.1. Use of coke in the blast furnace

Coke is a key reagent in blast furnace iron making. Coke performance in the blast furnace is affected by its composition as well as blast furnace operational conditions. Further, coke properties change progressively as coke descends in the blast furnace. Coke has three major roles in an iron making blast furnace.

1. **Thermal**: coke is the source of fuel providing the heat required for the furnace [48].
2. **Chemical**: coke, through its reaction with oxygen from the hot blast forms CO, the primary reductant of the iron oxides [18, 38, 49-52].
3. **Physical**: coke is in part used to control the permeability of the blast furnace [38].

2.2.2. Coke components and characterisation

Metallurgical coke is a complex composite material consisting of different carbonaceous forms, minerals and pores [2-4]. In this section, these coke components and their characterisations are reviewed. The effect of these components on gasification will be discussed in Section 2.5.

Minerals in metallurgical coke

Metallurgical coke contains between 8 – 12 % by mass of mineral matter. The amount and the nature of minerals present in cokes vary and are functions of the parent coals used in the coking process [2, 6, 7]. The minerals undergo chemical, physical, and/or structural transformations during coke production [17, 20, 25, 45, 53]

Generally, coke minerals are characterised by using XRD and SEM [2, 4, 6, 20, 22, 28, 47, 54-56]. An example of SEM characterisation of coke is given in *Figure 2.2* [4].

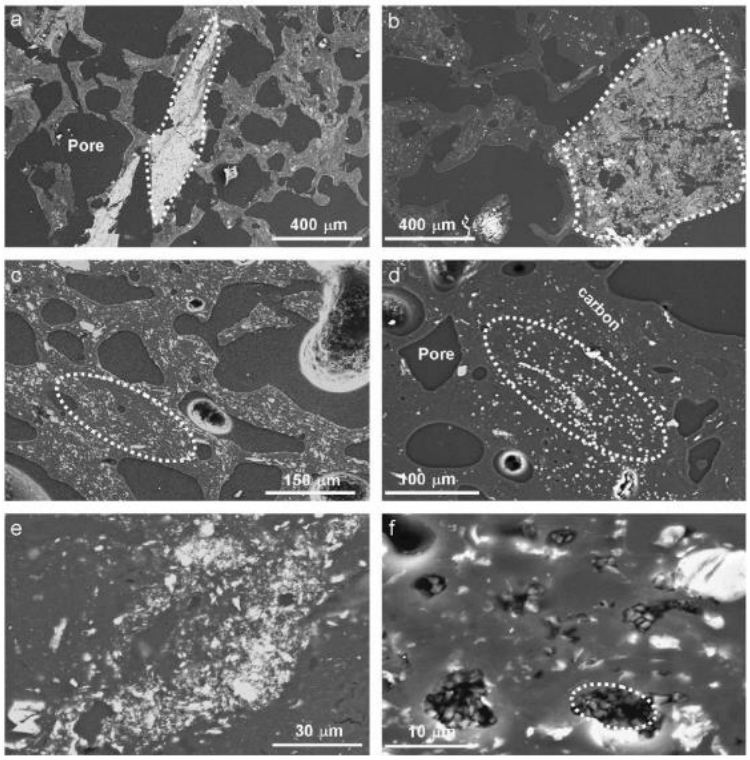

Figure 2.2: SEM images showing heterogeneous mineral size and distribution of coke [4].

The mineral regions in the figure are highlighted using dotted lines. From this figure, it can be seen that the mineral distribution and mineral size distribution are highly variable. Gupta *et al.* [56, 57] have developed a preliminary scheme to characterise coke minerals based on their particle size as;

- Fine (<50 μm)
- Coarse (50-100 μm)
- Agglomerate (>1000 μm)

They have also described the distribution patterns of minerals in coke as discrete, disseminated, or pore inclusion [56].

The chemical composition of mineral matter generally contains elements such as O, Si, Al, Fe, Ca, S, Mg, K, Ti, and Na, and less commonly P, Mn, C, H, N, Ba, Sr, F, and Cl [8]. Examples of the minerals commonly found in coke are given in *Table 2.1* [2, 4, 17, 20-22, 28, 45-47, 56].

Table 2.1: A list of minerals identified in metallurgical coke by different authors [2, 4, 17, 20-22, 28, 45-47, 56].

Minerals	**Composition**	**Minerals**	**Composition**
Akermanite	$Ca_2Mg_2Si_2O_7$	Iron	Fe
Albeit	$NaAlSi_3O_8$	Iron phosphate	$FePO_4$
Alumina	Al_2O_3	Iron silicon	Fe_3Si
Anatase	TiO_2	Jarosite Hydronian	$(K,H_3O)Fe_3(SO_4)_2(OH)_6$
Bassanite	$CaSO_4.\ 0.5H_2O$	Leucite	$KAlSi_2O_6$
Brookite	TiO_2	Magnetite	Fe_3O_4
Calcite	$CaCO_3$	Mullite	$Al_6Si_2O_{13}$
Coquimbite	$Fe_2(SO_4)_3.9H_2O$	Oldhamite	CaS
Cristobalite	SiO_2	Pyrrhotite	$Fe_{1-x}S$
Diopside	$CaMgSi_2O_6$	Quartz	SiO_2
Fayalite	Fe_2SiO_4	Rutile	TiO_2
Fluorapatite	$Ca_5(PO_4)_3F$	Spinel	$MgAl_2O_4$
Gehlenite	$Ca_2Al_2SiO_7$	Troilite	FeS
Hematite	Fe_2O_3	Wustite	FeO
Hercynite	$FeAl_2O_4$		

The minerals in coke are comprised of both crystalline and amorphous phases [2]. Gupta *et al.* [4] reported that the percentage of crystalline minerals was approximately 20-50% of the total mineral content.

Coke minerals can be grouped on the basis of their potential resistance to thermal and reactive environments as:

- Refractory: Quartz, cristobalite, mullite, and high melting point aluminosilicates.
- Semi refractory: Low melting point aluminosilicates containing high fluxing elements (K, Fe).
- Reactive: Iron and calcium phases except for oldhamite (CaS) and some silicate phases.

Coking conditions have a strong effect on the minerals observed in cokes [46]. The mineralogical composition of coke is different from its parent coal as a result of the decomposition of some minerals and mineral reactions occurring during coking. High-temperature conditions and the low p_{O_2} characteristic of coking can cause various changes in minerals and lead to the formation of new phases [46, 58].

Grigore *et al.* [2, 46] and Rodriguous *et al.* [47] examined the mineral transformations in coke by subjecting some Australian coals to coking in a laboratory furnace. An example of mineral transformation identified by Rodriguous *et al.* [47] is given in *Figure 2.3.*

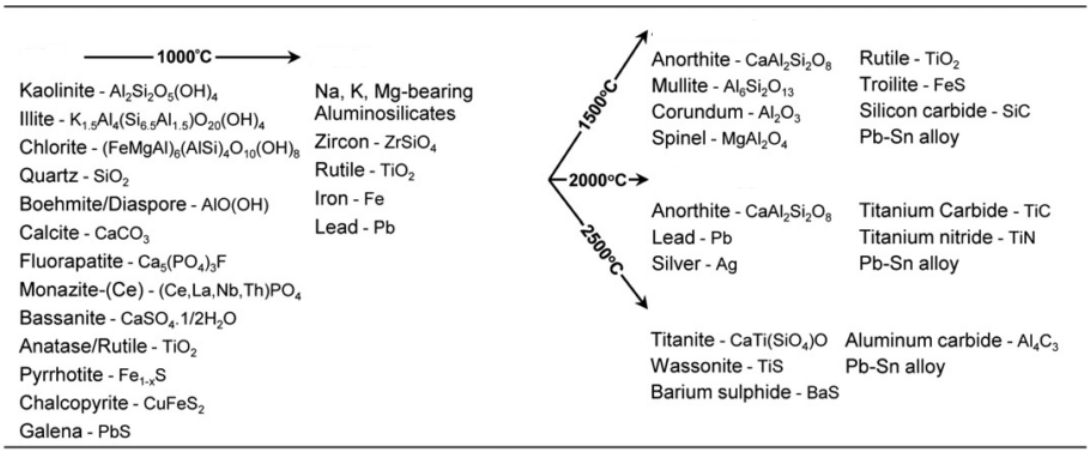

Figure 2.3: Mineral transformation observed by heat treatment of coal [47].

Minerals in coke also undergo changes during the gasification with CO_2. Grigore *et al.* [28] found that most mineral phases present in coke were changed by the gasification process to some degree. Some of the mineral phases found in the unreacted (raw) coke

were absent in reacted cokes. Some new mineral phases were formed during gasification, and the amount of some mineral phases changed significantly during coke gasification in CO_2. They further observed that the amorphous phase present in coke decreased significantly in the cokes reacted after ~75% gasification. Some of their results [28] are given in *Table 2.2*.

Table 2.2: Mineral phases identified in the low-temperature ashes (LTA) of a raw coke sample and the corresponding annealed coke and reacted coke (in CO_2) to 75% burn-off, and their relative concentrations (%, mass) [28].

Mineral phase	Chemical formula	Raw coke %	Annealed coke	75% Burn-off
			%	%
Pyrrhotite	$Fe_{1-x}S$	4.0	2.4	
Jarosite	$(K,H_3O)Fe_3(SO_4)_2(OH)_6$	4.3	3.2	
Iron	Fe	1.6	0.8	
Iron phosphate	$FePO_4$	0.3	0.2	
Oldhamite	CaS	0.6	0.1	
Diopside	$CaMgSi_2O_6$	0.3	0.4	
Anatase	TiO_2	0.2	0.1	
Quartz	SiO_2	32.7	28.7	28.3
Mullite	$Al_6Si_2O_{13}$	5.7	2.9	9.8
Spinel	$MgAl_2O_4$	0.6	1.7	4.3
Fluorapatite	$Ca_5(PO_4)_3F$	3.5	2.4	0.8
Bassanite	$CaSO_4 \times 0.5H_2O$	1.6	1.1	0.5
Akermanite	$Ca_2MgSi_2O_7$	0.3	0.5	0.9
Rutile	TiO_2	0.3	0.6	0.3
Anorthite	$(Ca,Na)(Si,Al)_4O_8$		0.5	2.4
Fayalite	$(Fe,Mg)_2SiO_4$		0.9	1.4
Hercynite	$FeAl_2O_4$		0.4	6.2
Magnetite	Fe_3O_4		0.3	1.7
Magnesioferrite	$MgFe_3O_4$		0.3	0.4
Hematite	Fe_2O_3			0.3
Rankinite	$Ca_3Si_2O_7$			1.4
Calcium ferrite	$Ca_4Fe_9O_{17}$			0.6
Calcite	$CaCO_3$			0.2
Leucite	$KAlSi_2O_6$			0.3
Cristobalite	SiO_2			0.9
Amorphous		44.0	52.4	39.3

The mineralogy of metallurgical coke is a broad area of study, and it is not practical to cover all the possible minerals and mineral effects in one thesis. Therefore in this thesis, only specific minerals containing Ca are considered. Ca, an alkaline earth

element, was chosen because Ca in coke minerals has been found to increase the coke reactivity [16, 24, 29-33].

Ca-containing minerals have been studied more in coal studies than in coke studies. One of the main differences in the mineralogy between low-rank coals (lignite and sub-bituminous) and high-rank coals (bituminous) is based on the Ca-containing mineral content. In high-rank coals, the Ca content is low (< 5% of ash), and all the Ca is in the calcite ($CaCO_3$) form [59, 60]. In lignite, Ca content is high (CaO 10 – 30 % of ash) and dispersed throughout the coal macerals as salts of carboxylic acids [59-61]. A similar dispersive occurrence has also been seen in severely weathered bituminous coals [60]. The presence of Ca in the form of carboxylic acids has been confirmed by EXAFS (extended X-ray absorption fine structure) spectroscopy [59, 60] and XANES (X-Ray absorption near-edge spectroscopy) [60]. Huggins *et al.* [60] have recorded X-ray spectra of coals (lignites, fresh bituminous and weathered bituminous) and some Ca-containing reference materials (lime, calcite and calcium acetate) (*Figure 2.4* and *2.5*). These spectra show that in bituminous coals, Ca is present in an acetate form.

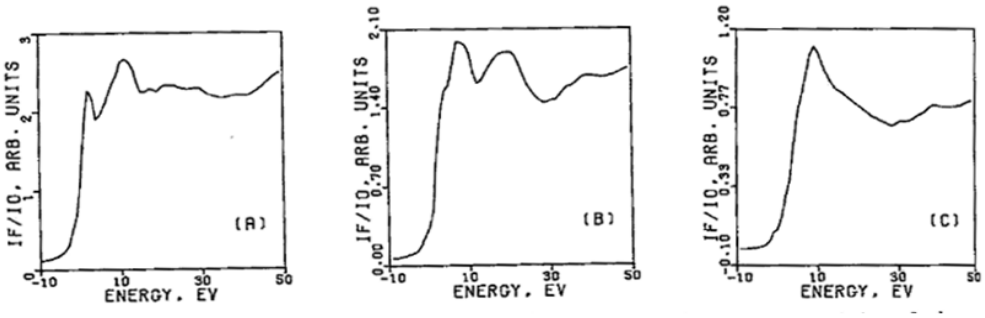

Figure 2.4 XANES of Ca standards: (A) lime (B) calcite (C) calcium acetate

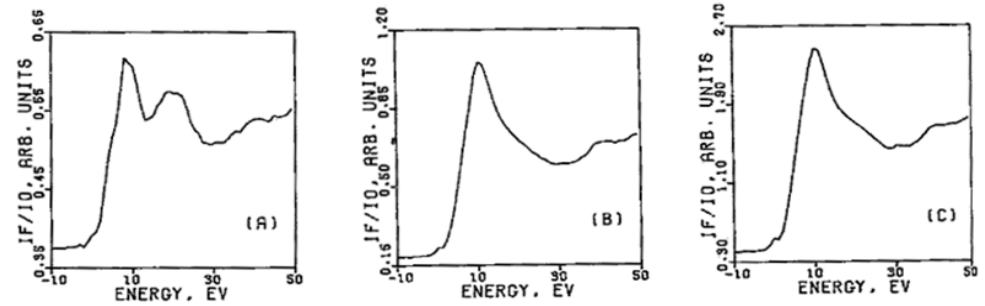

Figure 2.5: XANES of coals: (A) fresh bituminous (B) lignite (C) weathered bituminous.

In coke, Ca is present mostly as sulphide, silicates, aluminosilicates and phosphates. Ca is also presents in carbonate and oxide forms (see *Table 2.1* and *Figure 2.3*) [2, 28, 47].

Metallurgical coke porosity and pore distribution

The pore structure of metallurgical coke is related to its parent coal as well as to the coking process. The pores are the voids left after the release of volatile matter during coking [26]. The development of pores is affected by the amount of reactive macerals in the coal, the rank of the parent coal, fluidity and the coking process conditions [62]. Large pores are formed due to the fissures formed from internal stress in cokes and the release of volatile matter during carbonisation [26].

From a microscopic perspective, Turkdogan *et al*. [63] observed that pores in coke have different morphologies such as circular, elliptical, rectangular, triangular and slit-like. In addition to the different pore morphologies, metallurgical coke has a wide pore size distribution, with the size ranging from 1 nm to several µm [63]. Based on the size of the pores in metallurgical coke, they are classified into three groups [34, 64].

1. Coarse pores (pore diameter > 10 µm)
2. Macropores (pore diameter 0.05 µm – 10 µm)
3. Micropores (pore diameter < 0.002 µm)

The coke pore size distribution varies from coke lump to lump and also for different positions in the coking oven, see *Figure 2.6* [34]. In *Figure 2.6*, metallurgical cokes are numbered such that 1 and 2 represent different cokes, and a, b and c represent different positions in the coking oven. The total porosity of coke is in the range of 35 - 70 % [34, 49, 65-70].

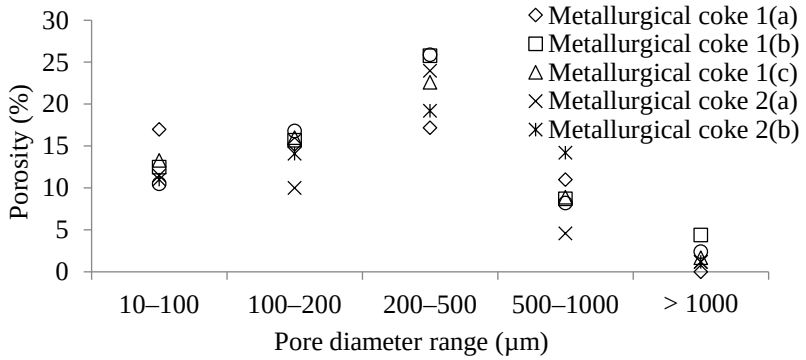

Figure 2.6: A plot of coke pore size distribution, coke sample 1 (a, b and c) are from the same batch, and 2 (a, b and c) are from a different batch. a, b and c represent different positions in the coke oven (after [34]).

There are a number of different methods for measuring/characterising coke porosity as listed below [71].

1. Mercury porosimetry.
2. Optical microscopy followed by image analysis.
3. Volumetric method.
4. X-ray computed tomography scan (micro-CT scan).

The most widely used methods for porosity measurement are optical microscopy/image analysis [34, 49, 63, 68-70, 72, 73] and mercury porosimetry [63, 64, 66] techniques. Image analysis is carried out using micrographs, usually obtained with optical microscopy, and image analysis software such as Image J. This method can characterise porosity, pore size distribution and pore shapes [49, 63, 69].

Mercury porosimetry provides information about pore volume distribution. It can be used to characterise smaller pores (0.0035 µm equivalent pore diameter) that are not measurable using optical microscopy and image analysis [63, 66].

In the volumetric method, the porosity is measured by water displacement to obtain apparent and real density [71].

Among the current techniques used to characterise coke porosity, Micro-CT scanning allows the detailed study of 3D pore morphology and can measure the pore diameter range from 20 – 800 µm [74, 75]. For example, Jenkins *et al.* [74] evaluated the 3D pore structure of different coke samples using micro-CT scanning.

Metallurgical coke carbonaceous matter

The carbonaceous forms of coke are derived from the macerals present in the precursor coal. The structural and textural properties of these carbonaceous forms depend on the rank of the parent coal [5, 38, 49]. The coke carbonaceous forms can be categorised into inert macerals derived components (IMDC), and reactive macerals derived components (RMDC) based on their precursor coal macerals (*Figure 2.7*) [5, 38, 49]. IMDC is derived from coal macerals that do not fuse during the carbonisation process of coke formation (inertinites) and from fused vitrinite from low-rank coals. RMDC is derived from the macerals that have fused during the carbonisation process (liptinite and vitrinite).

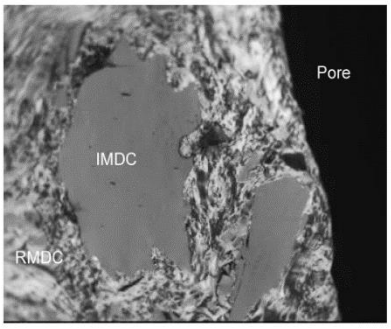

Figure 2.7: The structure of coke [49].

The coke carbonaceous structure can be characterised using techniques such as optical microscopy, SEM, TEM, XRD and Raman spectroscopy [5, 17, 37, 39, 54, 55, 62, 67, 76-80].

Optical /SEM microscopy

Optical/ SEM microscopy is primarily used to study the coke microstructure. From optical microscopy, the coke carbonaceous forms are classified as anisotropic (RMDC) or isotropic (IMDC) [5].

Coke formed from low-rank coal has more isotropic carbonaceous forms. As the rank increases the anisotropic carbonaceous form replaces isotropic carbonaceous forms in the coke [2]. Cokes made from high-rank coals have smaller amounts of isotropic and fine mosaic carbonaceous forms (*Figure 2.8*). The anisotropic carbonaceous forms are further classified as fine, medium and coarse mosaic units and flow types based on the size, shape and form of the textural units (*Figure 2.8*).

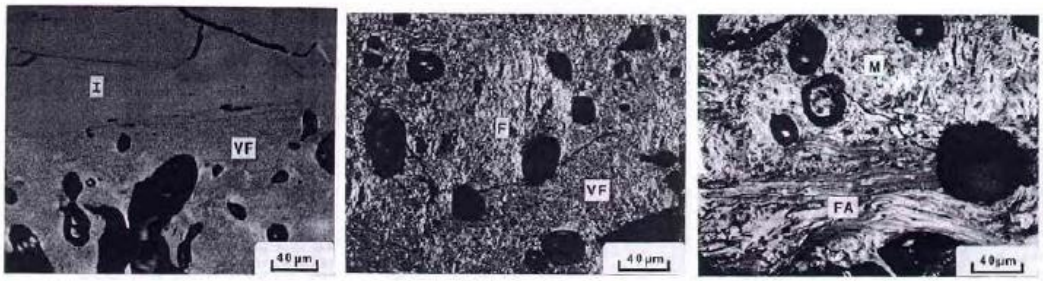

Figure 2.8: Micrographs of coke carbonaceous forms where:
***I**: Isotropic* ***VF**: Very fine mosaic* ***F**: Fine mosaic* ***M**: Medium mosaic*
***FA**: Flow-like anisotropic [38].*

SEM can be used to study the carbon structure and mineral component at a higher resolution than the optical microscopy can allow.

TEM

TEM studies enable the observation of coke carbonaceous forms at very small scales. It shows that coke carbonaceous forms consist of polyaromatic basic structural units (BSU) and they are ordered in stacked planes of the aromatic layers called molecular orientation domains (MOD) or local molecular orientations (LMO) [62, 81]. *Figure 2.9* is a schematic representation of MOD inside where BSUs are misoriented or locally oriented in parallel.

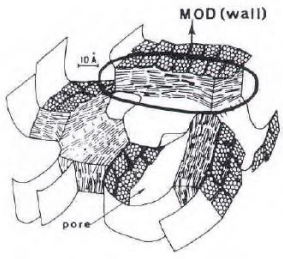

Figure 2.9: A schematic representation of MOD [38, 82].

XRD

The XRD technique is primarily used to study the structural order in coke [2, 4, 20, 39, 54, 69, 77, 78, 80, 83]. A typical XRD pattern of coke is given in *Figure 2.10.*

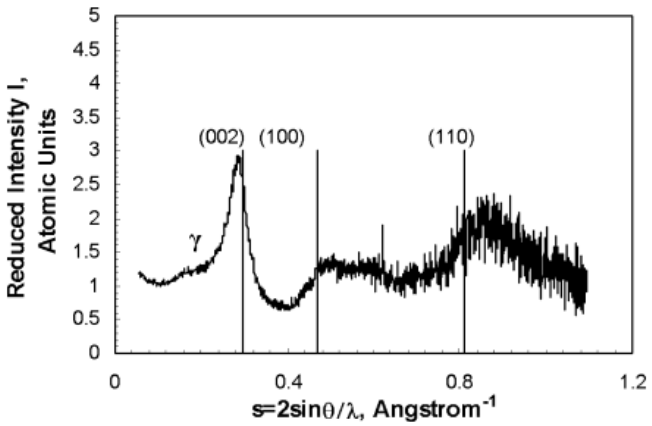

Figure 2.10: XRD patterns of a metallurgical coke [78].

Generally, an XRD pattern of coke contains diffuse peaks corresponding to the (002), (100) and (110) reflections [78, 84] of graphite.

The (002) peak represents the average stacking height of the aromatic planes of the carbon crystallite. The peaks corresponding to (100) and (110) represent the hexagonal ring structure [78, 84].

XRD can be used to calculate coke structural parameters such as crystallite height (L_c), crystallite width (L_a) and the interlayer spacing (d_{002}). Reported values of L_c, L_a and d_{002} are given in *Table 2.3*. The L_c value is used to assess the structural order of a metallurgical coke (*Equation 2.9*) [85] where higher crystallite height indicates increasing structural order.

$$L_c = \frac{K\lambda}{B\cos\theta} \qquad 2.9$$

where:

L_c = crystallite height
K = constant which depends on the reflection plane
λ = wavelength of the incident radiation
B = width of the peak at half maximum intensity
θ = peak position.

Table 2.3: Reported values L_a, L_c and d of metallurgical coke

	L_c(nm)	L_a(nm)	d_{002}(nm)
Dong *et al.* [80]	4.66–9.27	9.09–13.26	0.34–0.35
Gupta *et al.* [83]	1.81–4.61	-	-
Kawakami *et al.* [78]	1.00–15.00	1.80–4.00	0.34–0.35
Smedowski *et al.* [39]	1.20–2.60	-	0.35–0.36
Xing *et al.* [69]	1.80–1.70	-	0.34–0.35
French *et al.* [20]	1.61–1.66	3.33–3.74	-
Grigore *et al.* [86]	1.39–1.72	3.53–3.96	-

(-) No data

Raman spectroscopy

Raman spectroscopy is generally used to study the structural order of metallurgical coke, and carbon bonding, *i.e.* ordered sp^2 and disordered sp^2-sp^3 bonding in coke. A typical Raman spectrum for a carbonaceous material is given in *Figure 2.11*.

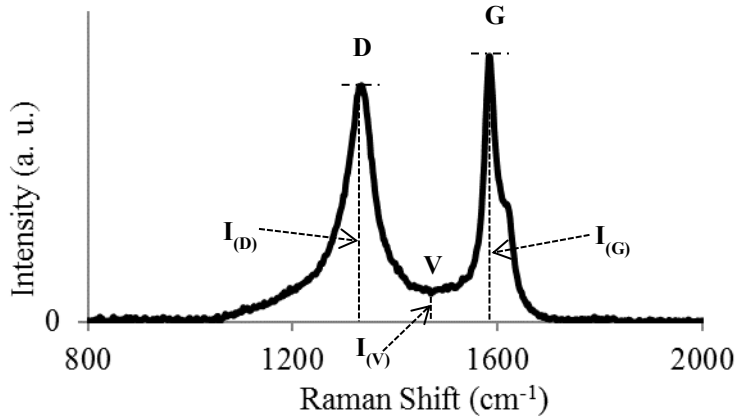

Figure 2.11: A typical Raman spectrum of a carbonaceous material.

In *Figure 2.11*, D and G are the bands at 1330 and 1580 cm^{-1} respectively. The D band is associated with the sp^2 bonding with structural defects while the G band is associated with the sp^2 bonding without any defect. The V valley represents less ordered carbonaceous bonding such as sp^3 like defects in sp^2 bonding. $I_{(D)}$, $I_{(G)}$ and $I_{(V)}$ are the band intensities of D and G bands and the valley between the D and G bands respectively. The intensity ratios of $I_{(D)}/I_{(G)}$ *vs* $I_{(V)}/I_{(G)}$ are used to assess the degree of defects in carbon bonding [78, 87]. A typical plot and values of $I_{(D)}/I_{(G)}$ *vs* $I_{(V)}/I_{(G)}$ for coke are given in *Figure 2.12 [88]* and *Table 2.4* respectively.

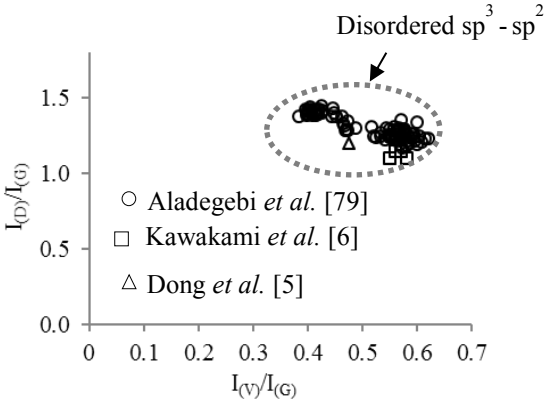

Figure 2.12: A plot of $I_{(D)}/I_{(G)}$ vs $I_{(V)}/I_{(G)}$ for metallurgical cokes[88].

Table 2.4: Raman peak intensity ratios for coke analogue and metallurgical cokes [88].

Material	$I_{(D)}/I_{(G)}$	$I_{(V)}/I_{(G)}$
Metallurgical coke [88]	1.1-1.5	0.4-0.6
Metallurgical coke [87]	0.1-1.7	0-0.6
Metallurgical coke [77]	1.3-1.4	0.1-0.6

2.3. Kinetics of the coke gasification

In this section, general gasification reactions are reviewed followed by gas – porous solid reactions. Then the mechanism and reaction rate measurements of coke are reviewed in detail. Finally, gasification kinetic models which explain and predict gasification of porous solids such as coke are discussed.

2.3.1. Gasification reactions in general

Any gas-solid reaction can be represented as one of the following [89, 90].

Gas + Solid → Gas/liquid product
→ Gas/Solid products
→ Gas/liquid and solid products

When the gas contacts the solid during the reaction, the solid particles remain relatively unchanged in size when they;

- contain large amounts of impurities, which remain as non-flaking ash or,
- form firm product material due to the reaction (*Figure 2.13*)

Solid particles shrink in size during the reaction when;

- flaking ash or flaking product is formed or,
- the reactant solid is pure (*Figure 2.13*) [89, 90].

In a reaction between carbon dioxide and carbonaceous materials (e.g. coal briquettes, wood, coke, etc.) with low ash, the size of the solid shrinks [89, 90].

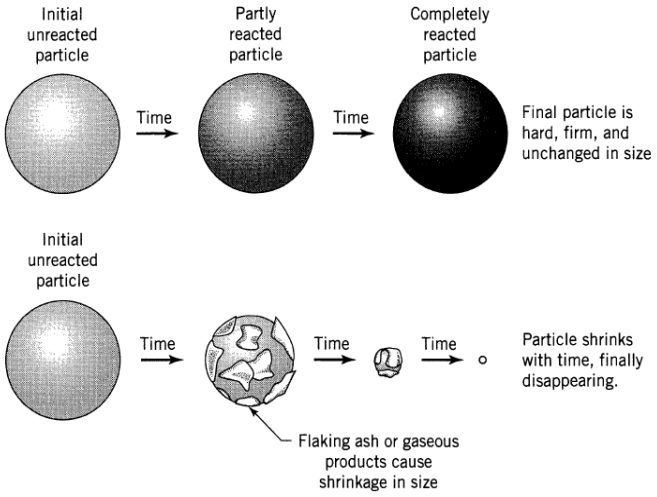

Figure 2.13: Different forms of gas-solid reactions [89].

2.3.2. Gas – porous solid reaction

Gasification of porous solids such as coke involves several steps [66, 89-91]:

1. Mass transport of the reactants to the reaction interface across the gas film surrounding the particle.
2. Mass transport of the products from the reaction interface across the gas film surrounding the particle.
3. Diffusion of reactants and products through the pores.
4. Chemical reactions occur at the reaction site, either:
    a. by adsorption of the gaseous reactants to the solid surface, or
    b. by desorption of product(s) from the solid surface.

In addition to these reaction steps, coke gasification is also associated with convective or conductive heat transfer as the Boudouard reaction is endothermic [64, 90].

Mechanism of coke – CO_2 reaction

The reaction mechanism of a coke – CO_2 reaction is based on the ability of coke carbon to dissociate an oxygen atom from a carbon dioxide molecule and retain it on a specific site by chemical bonding [38]. These sites are known as active carbon sites. Unit areas of coke surfaces may not have an equal susceptibility to the reaction even under standardised gasification conditions, and the reaction occurs principally at active sites

[92]. Active carbon sites are formed by surface irregularities which have the ability to chemisorb a gas phase through electron transfer. These are [91];

- carbon edges
- dislocations
- inorganic impurities
- oxygen and/or hydrogen functional.

For many researchers [66, 93-98] the following mechanism is the most widely accepted for a coke – CO_2 reaction:

$$C_f + CO_{2(g)} \underset{j_2}{\overset{j_1}{\rightleftarrows}} C(O) + CO_{(g)} \qquad 2.10$$

$$C(O) \overset{j_3}{\rightarrow} CO_{(g)} + C_f \qquad 2.11$$

where:

C_f = active carbon site

$C(O)$ = chemisorbed oxygen on carbon (intermediate)

$j_1, j_2 \; and \; j_3$ = rate constants.

In the first step, CO_2 dissociates into CO forming an oxidised surface complex C(O). This step is known as an oxygen exchange reaction [99, 100] which has been proven by isotopic tracer methods [100]. The surface oxygen complex has a broad range of chemical functionality (e.g. lactone, carboxyl, quinone, ketene etc.). In the second step, the surface complex produces another CO molecule leaving a free active C site for further reaction. The second step is considered as the rate controlling step [94, 100]. Both the forward and backward reactions of the reaction given in *Equation 2.10* are very rapid, and therefore there is an equilibrium between CO and CO_2 in the system [66, 93].

The presence of CO can inhibit the overall reaction. The presence of CO may promote the reverse reaction given in 2.10 causing a decrease in the concentration of the C(O) complex, thereby inhibiting the reaction shown in *Equation 2.11* [91, 101, 102].

Langmuir – Hinshelwood kinetics for coke gasification in CO_2

Generally, the Langmuir-Hinshelwood Equation (*Equation 2.12*) is used to describe the effects of both CO_2 and CO for the reaction rate [66, 91, 93, 103] in the absence of diffusion and mass transfer effects.

$$R_C = \frac{K_1 P_{co_2}}{1+K_2 P_{CO} + K_3 P_{co_2}} \quad 2.12$$

where $K_1 \equiv j_1 \Sigma_C$ 2.13

$$K_2 \equiv \frac{j_2}{j_3} \quad 2.14$$

$$K_3 \equiv \frac{j_1}{j_3} \quad 2.15$$

Σ_c = total available active carbon sites

R_C = reaction rate.

This model considered adsorption/desorption theories and was developed based on three assumptions [104]:

1. The surface is homogeneous.
2. No interactions occur among adsorbed species.
3. Surface migration is either non-existent or very rapid, such that only adsorption and desorption can be rate controlling.

Equation 2.12 can be rearranged as follows for plotting.

$$\frac{1}{R_C} = \left(\frac{1+K_2 P_{CO}}{K_1}\right)\frac{1}{P_{co_2}} + \frac{K_3}{K_1} \quad 2.16$$

By plotting $1/R_C$ against $1/P_{CO_2}$ at different P_{CO}/P_{CO_2}, K_1, K_2 and K_3 can be obtained [66]. The K values are specific to the particular coke investigated. The reaction rate, R_C, is usually obtained using the weight loss of the sample during the reaction. Aderibigbe *et al.* [66] observed an increase in K_1 and a decrease in K_2 and K_3 with increasing temperature. By plotting ln $K_{(1 \text{ or } 2 \text{ or } 3)}$ against 1/T, the activation energies for all the elemental steps can be obtained.

Reaction rate measurements

The rate of coke gasification reaction can be determined using the following Equation [38, 104, 105]:

$$R_C = -\frac{1}{W_O}\frac{dW}{dt} \quad 2.17$$

where R_C = rate of the reaction (g g^{-1} s^{-1})
W_0 = initial mass of the sample (g)
dW = weight change of the sample (g)
t = time (s).

The rate can also be related to fractional carbon conversion during the reaction, X [38, 104, 105]:

$$X = \frac{W_0 - W}{W_0} \quad 2.18$$

where W = mass of the dry ash/mineral free sample at time t (g).

Consequently [38, 104, 105],

$$R_C = \frac{1}{(1-X)}\frac{dX}{dt} \quad 2.19$$

Effect of temperature on reaction rate

The temperature dependency of the rate constant takes the Arrhenius form as [38, 97, 104]:

$$k = k_o e^{-\frac{E_a}{RT}} \quad 2.20$$

which can be linearised (see *Equation 2.21*),

$$\ln k = -\frac{E_a}{R}\frac{1}{T} + \ln k_o \quad 2.21$$

where k_o = pre-exponential factor [$(g\ cm^{-3})^{-m}\ s^{-1}$]; m= order of the reaction
E_a = activation energy (kJ mol^{-1})
R = universal gas constant (J mol^{-1} K^{-1})
T = absolute temperature (K).

In general, a plot of ln k against 1/T is used to study the effect of temperature on rate constants [106, 107]. Though the Arrhenius Equation is usually written for the rate constant rather than the reaction rate, several researchers [2, 38, 91, 104] have used it directly as an expression for the rate as given in *Equation 2.22* to determine the temperature dependency on the reaction rate:

$$R_C = k_o e^{-\frac{E_a}{RT}} \qquad 2.22$$

To distinguish *Equation 2.22* from the standard Arrhenius form in *Equation 2.20,* it is referred to as the **Walker *et al.* approach** [91] in this thesis. Using the Walker *et al.* approach [91], three temperature zones can be identified which correspond to different rate controlling mechanism(s) (*Figure 2.14*). The change of reactant gas concentration at each zone is also shown using *Figure 2.14* where δ is the thickness of the surrounding gas film and C_g is the gas concentration.

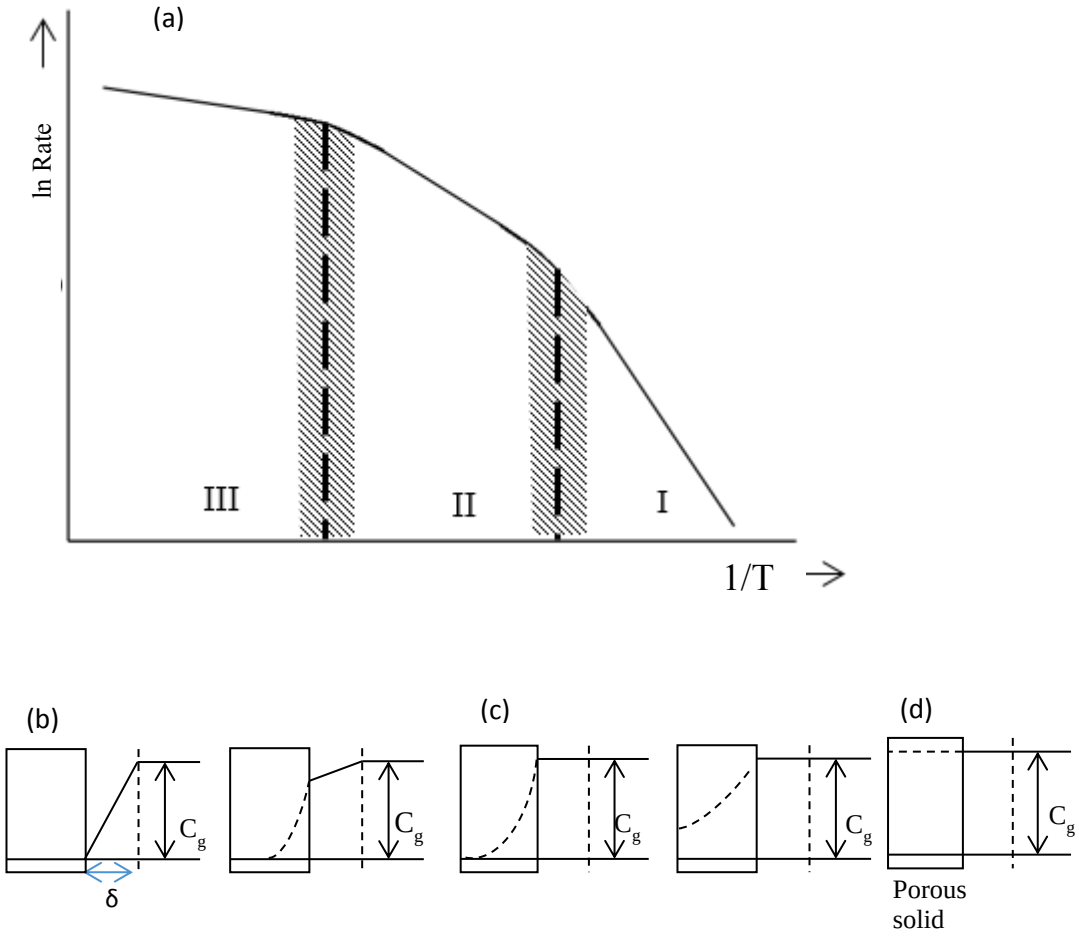

Figure 2.14: Ideal representation of three zones of gas- carbon reaction and the concentration profile diagram at each zone [90, 91].

Zone I

In Zone I (*Figure 2.14 a*), the low-temperature zone, the rate is controlled by the chemical reaction at the coke−gas interface [38, 90, 91]. At low temperatures the chemical reaction between the carbon and carbon dioxide within the particle is slower than the diffusion of the reactant gas from the surface to the reactant site. The probability of the gaseous reactant diffusing deeper in the solid is high, and therefore the concentration of the gaseous reactant is uniform throughout the solid and it is the same as for the bulk gas stream (*Figure 2.14(d)*) [90]. Therefore, the reaction takes place evenly throughout the solid. Even if the pore size increases inside the solid, the overall size of the solid will remain approximately unchanged [90].

Zone II

In Zone II, the intermediate temperature zone, the rate is controlled by a combination of chemical reaction at the coke gas interface and pore diffusion [38, 97]. When the temperature increases, the diffusion of the reactant and the product(s) are influenced by the molecular diffusion (collision between gas molecules inside the furnace) or Knudsen diffusion (collision of gas molecules with pore walls). The increase in the rate of diffusion is not as great as the increase in the rate of the chemical reaction with the temperature. Therefore the probability of the gaseous reactant diffusing deeper into the solid is lower [90]. As such, the reaction occurs close to the external surface of the coke. Diffusion within the pores and the chemical reaction influence the rate of the reaction under these conditions. In this region, the external dimensions of the solid may be reduced and/or the porosity of the external surface may increase, keeping the centre of the solid unchanged until the final stage of the reaction [90].

Zone III

In Zone III, the high-temperature zone, the rate is controlled by gas mass transfer to the external coke surface [38, 91, 108]. Therefore, the concentration of the gaseous reactant at the external surface is close to zero [90]. In this region, the reaction takes place at the external surface, and therefore the interior of the solid is unaffected until it is exposed to gaseous reactant by the gasification [90].

The intermediate zones a and b shown in *Figure 2.14(a)* represent the transitions between Zone I and II and Zone II and III respectively. The transition temperatures between each zone are determined by the gas flow rate, gas type, pressure, particle size, porosity and the concentration of active sites [38, 63, 66, 104, 109].

2.3.3. Gasification kinetics models

Gasification kinetic models can be used to explain and to predict the rate of coke – CO_2 gasification reactions. There are several different single – step chemical reaction models in the relevant literature to describe the kinetics of coke – CO_2 gasification. These are mostly only applicable if the reaction takes place in the Zone I, chemically controlled region. The shrinking core model [89, 110], integrated model [111],

volumetric model [111], modified volumetric model [112] and random pore models (RPM) [113, 114] (*Equation 2.23*) are some of the widely used models in coke gasification kinetic studies. However, the RPM is the only model that considers the pore development during the gasification and this is the model which this thesis discusses in more detail.

Random pore model (RPM)

This model has been developed in terms of the pore size distribution of a reacting solid *i.e*. this model considers the effect of the contact surface area on the reactivity. It considers two competing structural changes that affect the gasification rates during the reaction. These are [113, 114],

- The growth of accessible pores during the initial stage of the reaction.
- The overlapping of neighboring pores that decrease the available surface area for the reaction.

By incorporating these two structural changes, the RPM is able to predict a maximum in the reaction rate observed in coke gasification [113, 115]. Other gasification kinetic models: Shrinking core, integrated and volumetric models, were not able to predict this reaction rate maximum

In the absence of any gas diffusion control *i.e*. for the chemical reaction control zone, the reaction rate is expressed as *Equation 2.23* [113, 116-118]:

$$\left(\frac{dX}{dt}\right) = \frac{R_C A_0(1-X)\sqrt{1-\varphi \ln(1-X)}}{(1-\varepsilon_0)} = K_{RPM}(1-X)\sqrt{[1-\varphi \ln(1-X)]} \qquad 2.23$$

$$\varphi = \frac{4\pi L_0(1-\varepsilon_0)}{A_0^2} \qquad 2.24$$

where
R_C = reaction rate
K_{RPM} = RPM reaction rate constant
A_0 = initial surface area
ε_0 = initial porosity
φ = structural parameter
L_0 = total initial pore length per unit volume.

It can be seen from the equation 2.24 that φ is a measure of the initial pore structure in terms of initial porosity, initial pore length per unit volume and initial surface area per unit volume. φ is normally determined using BET and image analysis. This approach can bring problems with accuracy due to structural complexities such as non-uniform pore size distributions. To overcome this problem, Bhatia *et al.* [113] developed another approach based on the *Equation 2.25* to determine φ,

$$\varphi = 2(1 - \varphi \ln(1 - X_m) = \frac{2}{(1+2ln(1-X_m)} \quad 2.25$$

where X_m is the carbon conversion at the reaction rate maximum. X_m is obtained from plots of R_C vs X. *Equation 2.25* can be used when the reaction rate maximum is observed in the carbon conversion range $0 \leq X < 0.393$ [113].

An alternative approach was also used by researchers [119] using carbon conversion and reduced time (*Equation 2.26*), where *t* and t_x are the time required for carbon conversions *X* and X_x respectively where *x* values are user definable. Malekshahian *et al.* [119] used $t/t_{0.5}$ while Everson *et al.* used $t/t_{0.9}$. The use of $t/t_{0.9}$ is believed to eliminate the possible uncertainty due to the asymptotic results near the end of the reaction.

$$\frac{t}{t_x} = \frac{\sqrt{1-\varphi \ln(1-X)}-1}{\sqrt{1-\varphi \ln(1-X_x)}-1} \quad 2.26$$

2.4. Coke reactivity testing

There are many coke reactivity tests, some of which are listed below [120].

- NSC reactivity test
- ECE test
- ECE-INCAR test
- NCB
- Gost 10089-73
- IRSID-CERCHAR
- Okstad and Hoy

Among these, the NSC reactivity test is the most widely used method for evaluating coke quality and reactivity in the iron and steel industry, so this test is discussed in further detail.

NSC reactivity test

The NSC reactivity test is actually two tests and was introduced by the Nippon Steel Corporation (NSC) [4, 16], to measure the quality of coke in the blast furnace. The tests are the coke reactivity index (CRI) and the coke strength after reaction (CSR).

To establish the CRI, the coke sample is allowed to react with CO_2 at 1100 °C for 2 hours. The mass loss due to the reaction, as expressed in *Equation 2.27*, is known as the CRI [121]: .

$$CRI = \frac{(m_1 - m_2)}{m_1} \times 100 \qquad 2.27$$

where m_1 = initial sample mass (g)

m_2 = final mass (g).

To establish the CSR, the reacted sample is then placed in an I-shaped tumble drum and it is rotated 600 times at a speed of 20 RPM. The proportion of material greater than 10 mm left at post tumbling is used to obtain the CSR via *Equation 2.28*:

$$CSR = \frac{m_3}{m_2} \times 100 \qquad 2.28$$

where m_2 = final mass from CRI testing (g)

m_3 = mass retained >10.0 mm.

Figure 2.15 shows the relationship between CRI and CSR for a series of more than 60 cokes produced from coals of different rank, geographical origin and complex blends [120].

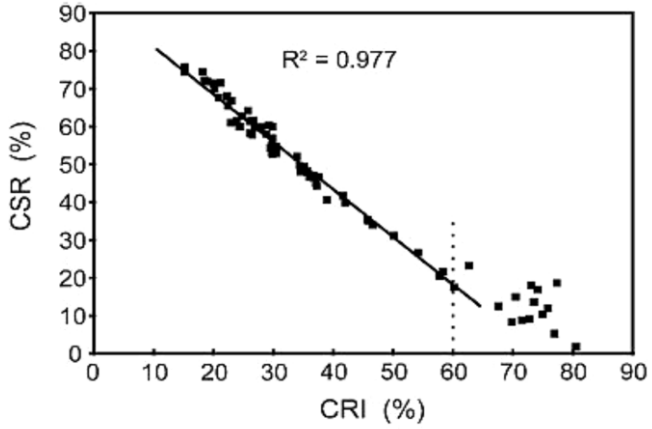

Figure 2.15: A plot to show the relationship between CRI and CSR indices [120].

These tests provide a measure of the susceptibility of coke to attacks from CO_2 and an indication of coke strength following the weakening effect of gasification. However, it does not simulate the real blast furnace conditions. Inside the blast furnace there is a complex gas mixture, rather than only pure CO_2, and a temperature range of (1000 - 2000 °C) [16].

The most common laboratory method used to study the coke reactivity is the thermogravimetric analysis (TGA). This method can be used to study the coke reactivity under varying reaction conditions such as temperature, gas composition and particle size [19, 24, 65, 66]. The weight changes of the coke samples during the reaction with CO_2 are measured and expressed as a plot of fractional weight change (FWC, *Equation 2.29*) with time [65]. *Figure 2.16* [65] is a plot of FWC vs time for different coke samples studied using the TGA at 1100 °C with CO_2.

$$X = \frac{W - W_0}{W_0} = -FWC \qquad 2.29$$

where W = the weight at time t

W_0 = the initial weight.

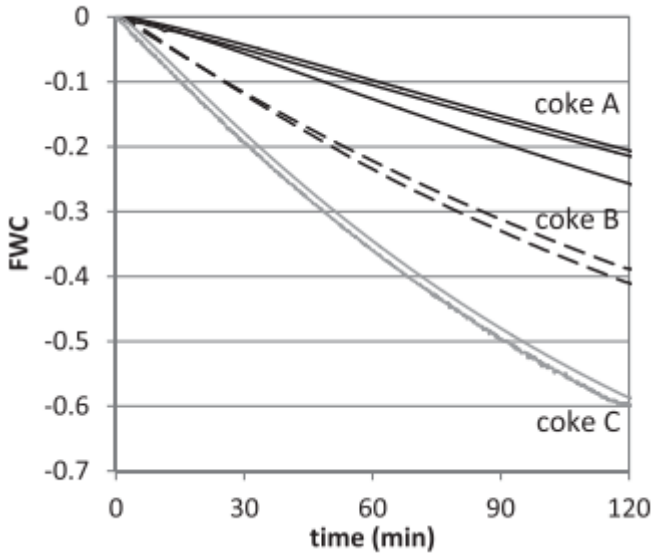

Figure 2.16: A plot of FWC vs time for three different coke samples for the reaction with CO_2 at 1100 °C [65].

2.5. Factors affecting coke reactivity

The factors that determine coke gasification kinetics are very important to coke researchers. The main factors that determine the coke gasification are coke mineral matter, porosity carbonaceous forms, particle size, temperature, and pressure (gas composition) [15, 38, 122, 123].

2.5.1. Effect of coke minerals on coke gasification in CO_2

Minerals that increase/ catalyse the gasification rate

Alkali metals [6, 9-12, 16, 76, 124], alkaline earth metals [6, 9, 11, 16, 76] and transition metals and their oxides [2, 6, 10, 13, 14] are identified as minerals that increase the rate of coke gasification.

Alkalis are known to influence the gasification reaction and initiate it at significantly lower temperatures (750–850 °C) compared to the usual gasification starting temperatures of ~950 °C [54].

The increasing gasification by different minerals follows different mechanisms, as discussed below. Generally, the catalytic mechanisms increase the amount of carbon active sites (C_f) (*Equations 2.10* and *2.11*) in the coke, leading to an increase in the reaction rate.

$$C_f + CO_{2(g)} \underset{j_2}{\overset{j_1}{\rightleftarrows}} C(O) + CO_{(g)}$$

$$C(O) \xrightarrow{j_3} CO_{(g)} + C_f$$

It should be noted that more than one of the mechanisms discussed below may be applicable for an individual mineral.

1. Catalysis by dissolution of coke carbon into metals

Catalysis by dissolution of coke carbon into metals may be applied when the gasification is increased by a metal such as Fe [11, 125-127]. When carbon dissolves into Fe, C – C bonds at the C – Fe interface are weakened. These weakened C – C bonds are considered to be active sites (C_f) which increase the carbon gasification.

An illustration of the mechanism of the carbon dissolution into a metal is given in *Figure 2.17.*

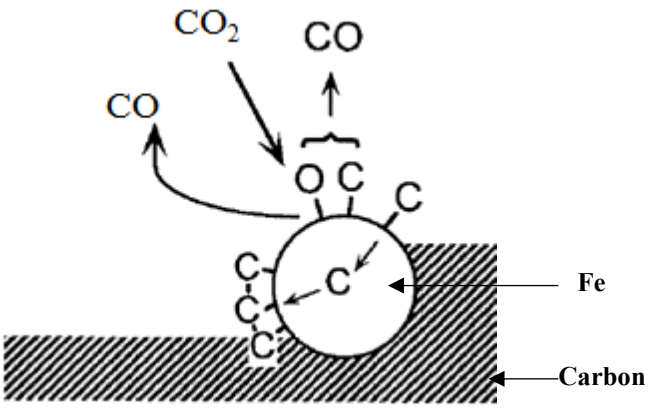

Figure 2.17: An illustration of the carbon dissolution into a metal mechanism using Fe as an example [11].

2. Catalysis by dissociation of CO_2 on mineral / metal surfaces

Catalysis by dissociation of CO_2 on mineral / metal surfaces is applicable for metal and / or metal oxide containing systems (Fe, CaO) [11, 37, 98, 125, 126, 128, 129]. In this mechanism, CO_2 gas is dissociated on the mineral / metal surfaces to form CO and a complex of adsorbed oxygen on the metal / mineral (M(O)s). Then the oxygen adsorbed can either;

i) react with C_f at the mineral / metal – carbon interface, or
ii) "spill over" from the mineral / metal surface to find a C_f.

This mechanism is represented in *Equations 2.30 – 2.35*.

$$M_{(s)} + CO_{2(g)} \rightarrow M(O)_{(s)} + CO_{(g)} \quad 2.30$$

$$M(O)_{(s)} + C_{(s)} \rightarrow M_{(s)} + C(O)_{(s)} \quad 2.31$$

$$C(O)_{(s)} \rightarrow CO_{(g)} \quad 2.32$$

$$MO_{(s)} + CO_{2(g)} \leftrightarrow MO.O_{(s)} + CO_{(g)} \quad 2.33$$

$$MO.O_{(s)} + C_{(s)} \leftrightarrow MO_{(s)} + C(O)_{(s)} \quad 2.34$$

$$C(O)_{(s)} \leftrightarrow CO_{(g)} \quad 2.35$$

where M represents a metal, MO a metallic oxide, M(O), and MO.O is chemisorbed oxygen on a metal / mineral surface.

An illustration of the CO_2 dissociation onto metallic Fe, as an example, is given in *Figure 2.18.*

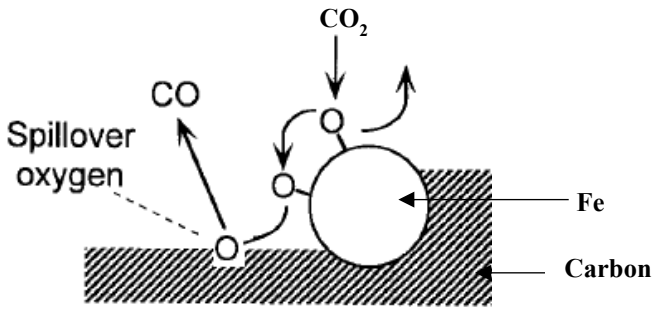

Figure 2.18: An illustration of the CO_2 dissociation mechanism onto metallic Fe [11].

3. Catalysis by formation of carbonates

Catalysis by the formation of carbonates mechanism is suggested for mineral oxides (eg. CaO, K_2O) [129-132]. In this case, the mineral carbonate acts as a medium for the transport of CO_2 to the carbon surface.

$$MO_{(s)} + CO_{2(g)} \leftrightarrow MCO_{3(s)} \quad 2.36$$

$$MCO_{3(s)} + C_{(s)} \leftrightarrow MO_{(s)} + 2CO_{(g)} \quad 2.37$$

4. Catalysis by electron transfer from carbon to mineral or metal

Catalysis by electron transfer from carbon to a mineral or metal is applied by transition metals that have the ability to accept electrons to influence the π electron distribution in the carbonaceous material's aromatic layers [38, 133]. *Figure 2.19* shows two types of distribution of π electrons that can occur at a carbon active site (Cf in *Equation 2.10 and 2.11*). Transition metals can interact with the π electron distribution in the carbon structure to induce the distribution shown in *Figure 2.19(b)*, which requires less energy to break the C – C bond and release a CO molecule.

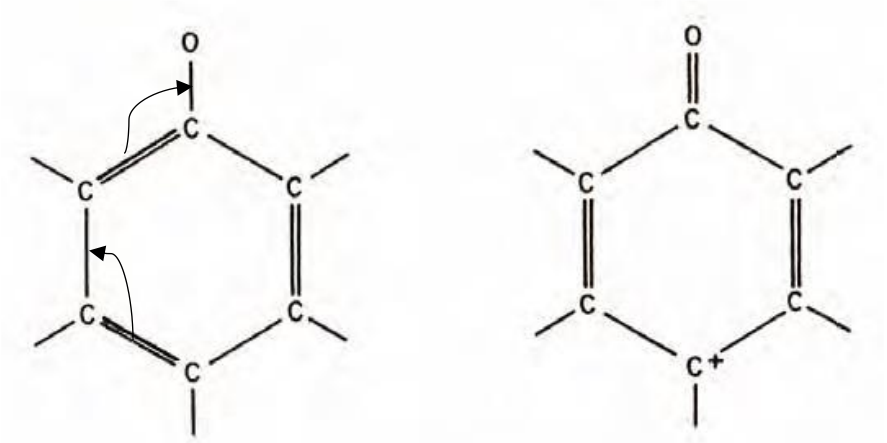

(a) (b)

Figure 2.19: An illustration showing the distribution of π electrons in the aromatic ring (a) under no influence by catalysts (b) under the influence of catalysts [133].

5. Catalysis by increasing electron density of the neighbouring carbons

Catalysis by increasing the electron density of the neighbouring carbons is suggested for the catalysis of carbon gasification in the presence of a Ca-containing species. Density functional theory (DFT) has been used to evaluate the interaction between Ca and carbonaceous materials and how that interaction can affect the neighbouring C atoms where the reaction with oxygen coming from CO_2 dissociation could take place [134]. This has been carried out by considering several possible interactions between CaO and graphene layers. *Figure 2.20* is an illustration of an example of a mechanism which is the most thermodynamically favourable [134]. The most favourable mechanism takes place when the carbonaceous material has a zigzag edge (*Figure 2.20 (a)*). ΔH values have been calculated using a Gaussian 09 package and have shown that there is an exothermic interaction occurring between C and Ca (*Figure 2.20 (b)*). Due to this interaction the electron density in the C close to the interaction site increases (*Figure 2.20 (b)*). The authors [134] suggested that this would make the edge carbon more reactive and suitable for bonding with oxygen coming from CO_2 dissociation to form the semiquinone structure in *Figure 2.20 (c)*. The authors carried out modelling followed by thermodynamic calculations of the CO removal from the catalysed semiquinone (*Figure 2.20 (c)*). They have compared the energies need to remove CO from un-catalysed and catalysed semiquinone complexes and found that the removal of CO is thermodynamically more favourable after the catalysis by Ca/CaO [134].

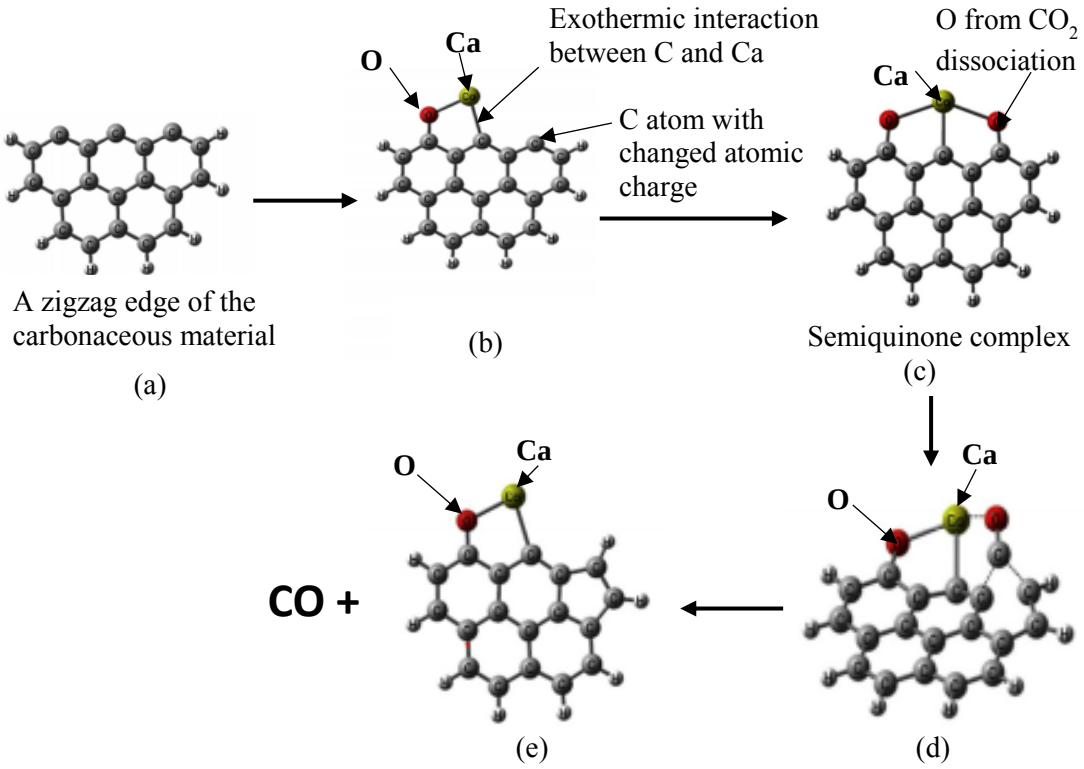

Figure 2.20: An illustration of a possible mechanism for carbonaceous material catalysis by CaO (modified from [134]).

6. Formation of intercalates in-between the crystal structure of graphite

The formation of intercalates between the crystal structure of graphite is suggested for the systems containing K and Na [54, 55, 80]. These minerals can form intercalates in the crystal structure of graphite. The formation of intercalates can cause an expansion of the coke carbon lattice (to form cracks), increase stress, modify the coke surface area, decrease coke strength and weaken coke structure. These can create carbon active sites (Cf in *Equation 2.10* and *2.11*) and thereby increase the reaction rate.

Minerals that decrease the gasification rate

Some minerals are found to decrease the gasification rate. Most of such minerals cover the pores and pore walls and thereby reduce the available surface area for the gasification [16, 53, 63, 70, 104]. For example, at high temperature, aluminosilicates in coke can form a thin layer of molten oxide on the coke surface, and cover the pore structure to act as a barrier to gas penetration and reduce the contact of gas with the carbon [63].

Some oxides of coke mineral matter such as SiO_2 are reduced by carbon inside the coke lump, usually at high temperatures, and therefore reduce the amount of available carbon for the gasification [16].

Minerals that have no effect on the gasification rate

There are some minerals that have no effect on the gasification rate. Gill *et al.* [16] and Monaghan *et al.* [135] conducted experiments to study the effect of minerals by adding minerals to very low ash coals. They observed that Al_2O_3 had no effect on the reactivity under the experimental conditions studied.

2.5.2 Effect of coke pore structure on gasification in CO_2

Coke porosity can partially influence coke reactivity [90, 123, 136]. The general relationship between coke porosity and reaction rate can be expressed as *Equation 2.38:*

$$\text{reaction rate} \propto \text{specific surface area} \propto \text{porosity} \qquad 2.38$$

Patrick *et al.* [68] studied the gasification of three metallurgical cokes in CO_2 with different initial porosities at 1000 °C. They found that the gasification rate of the coke samples was directly proportional to the initial porosity (*Figure 2.21*).

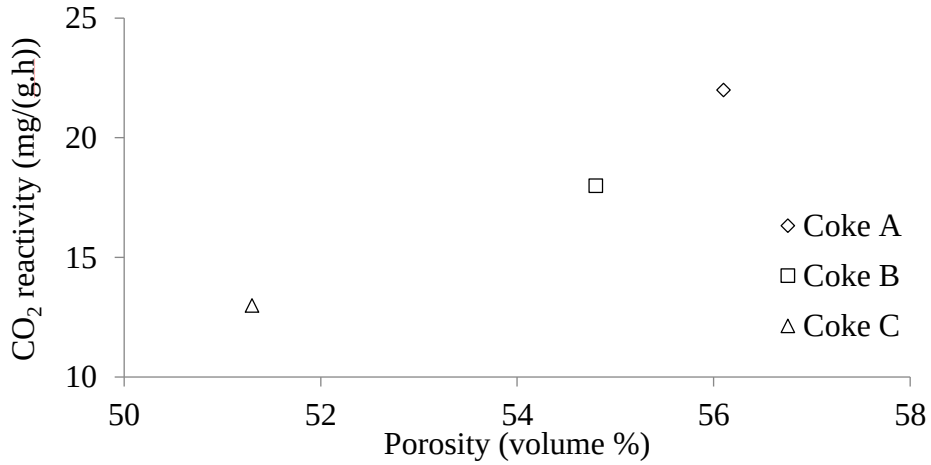

Figure 2.21: A plot of metallurgical coke – CO2 reactivity against initial porosity (modified from [68]).

Szekely and Aderibigbe [64, 66] studied the evolution of coke pore structure with the coke gasification in CO_2 at 1000 °C. They observed that the enlargement of pores occurred primarily near the surface, while the core of the specimen remained unreacted under their reaction conditions. They observed increasing total porosity with increasing gasification (*Figure 2.22*).

Pore size is an important parameter in determining the effect of total porosity on gasification [105, 137-139]. *Figure 2.22* indicates that the major contribution to the increase in the total porosity is from the enlarging of larger pores (pores with >35 μm diameter).

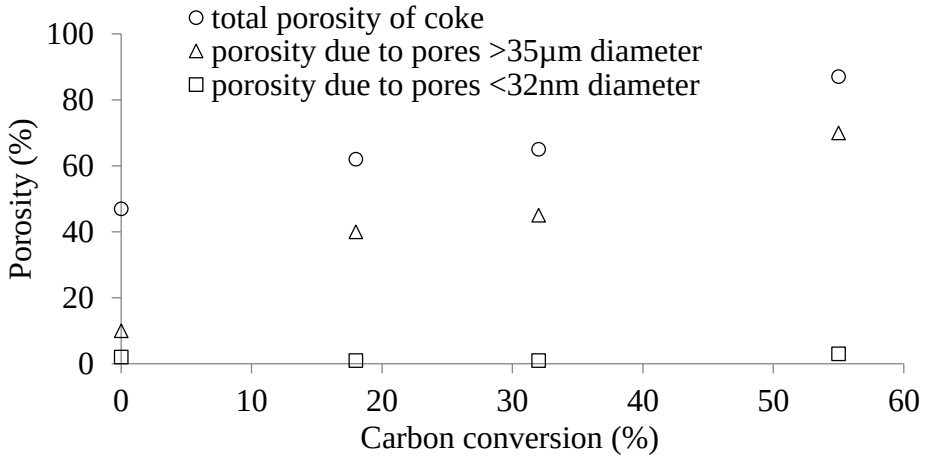

Figure 2.22: Plot of porosity of coke against percentage carbon conversion (modified from [66]).

2.5.3 Effect of coke carbonaceous forms on gasification in CO_2

The coke reactivity in CO_2 is also related to the coke carbonaceous forms. Both RMDC and IMDC react with CO_2 at different rates. Generally, IMDC is more reactive than RMDC. See *Figure 2.23* which shows the loss of more IMDC than RMDC after the reaction with CO_2 at 1100 °C [17]. This difference in the reactivities is in part due to the higher structural order of RMDC compared to that of IMDC [17, 20, 57, 62, 67, 79, 86, 140, 141].

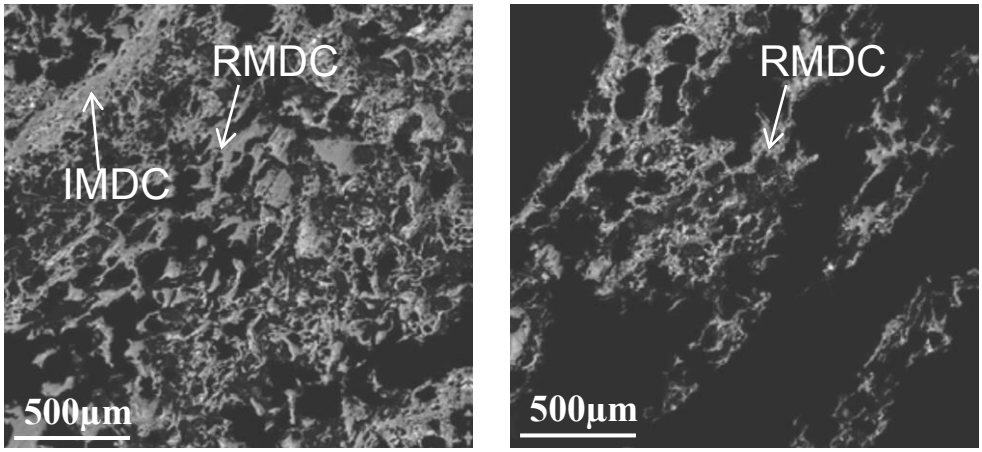

(a) (b)

Figure 2.23: The RMDC and IMDC of a metallurgical coke sample before and after the reaction with CO_2 at 1100 °C[17].

2.5.4 Effect of coke particle size on coke gasification in CO_2

Coke particle size has an effect on the gasification rate [122, 142-144]. A decrease in the coke particle size increases the surface area available for the gasification [122, 142] and increases the reaction rate. An example of the increasing gasification in CO_2 with decreasing particle size at 750 °C is given in *Figure 2.24*.

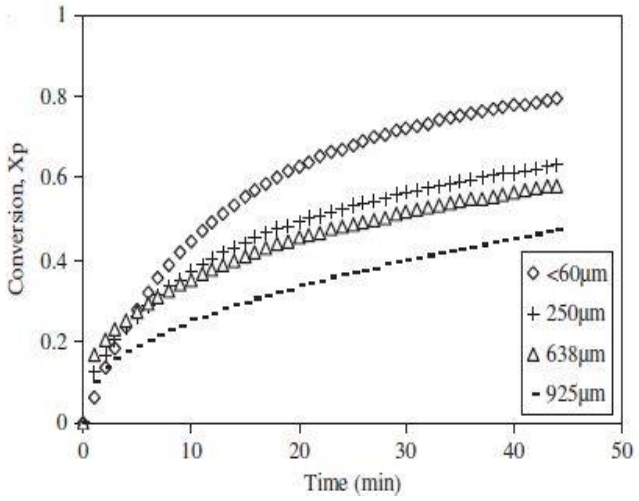

Figure 2.24: The effect of particle size on coke gasification in CO_2 at 750 °C [122].

2.5.5 Effect of temperature on gasification in CO_2

The gasification rate of coke increases with increasing temperature regardless of the reactant gas used [116, 122, 123, 145-147]. The effect of temperature on the gasification reaction is best explained using the Arrhenius equation, discussed in detail in Section 2.3.2.

2.5.6 Effect of gas composition on coke gasification in CO_2

The gas composition, partial pressure of reactants, affects the gasification rate in CO_2. Generally the gasification rate increases with increasing P_{CO_2} and decreases with increasing P_{CO} [103, 119, 144, 148, 149]. The effect of both CO_2 and CO pressures on coke gasification is expressed in the Langmuir - Hinshelwood rate Equation (*Equation 2.12*).

2.6 Coke analogue

Coke strength and resistance to degradation at high temperatures are used to predict coke quality and performance (discussed in Section 2.4). Progress in coke studies to assess the impact of minerals on reactivity has often been limited by the inherent complexity of coke, the heterogeneity in coke structure and the spacial distribution of coke minerals [18, 19]. A coke analogue has been developed for using at the laboratory scale to address the complexity and heterogeneity issues. It is made from a number of different carbon or carbon-containing materials and minerals to replicate the behaviour of industrial coke. Components used to produce the coke analogue are shown in *Table 2.5*. These mixtures are then pressed, cured and fired at elevated temperatures under an inert atmosphere [18].

Table 2.5: Components used to produce coke analogue [19].

Material	Purity	Size	Addition	Primary function(s)
Graphite powder 1	99.99+%	<45 μm	28 % of dry base	Carbon source
Graphite powder 2	99.99+%	<150 μm	28 % of dry base	Carbon source
Phenolic resin (Bakelite)	N/A	+100 μm -250 μm	44 % of dry base	Porosity control
Liquid 45% Novolac resin in propylene glycol	N/A		Ration of 0.52 liquid/ dry mix	Binder Porosity control
Hexamethylenetetramine (HTMA)	N/A		3 mass % of liquid resin	Curing agent

Use of the coke analogue has several advantages [19]:

- It can be doped with minerals required for the study.
- Porosity and mineral dispersion can be controlled.
- The control over carbon forms, pores and minerals helps to minimise the heterogeneity issues in coke at the lab scale.
- It can be formed into different shapes.
- It can be used to study coke mineral reactivity at high temperatures.

The coke analogue was found to have a well-controlled porosity and pore size distribution. The observed porosity in coke analogue was in a narrow range of 29 % ± 2.3 % while that in a single metallurgical coke was 30 % ± 5.2 % [88].

The dissolution behaviour of coke analogue in liquid iron, with mineral matter added to mimic industrial coke, was studied and the results were compared with both graphite and industrial coke [18]. The results obtained (*Figure 2.25*) suggested that the coke analogue behaves more like metallurgical cokes than graphite. Hence it could be seen to be replicating the dissolution behaviour of industrial coke in iron to some extent.

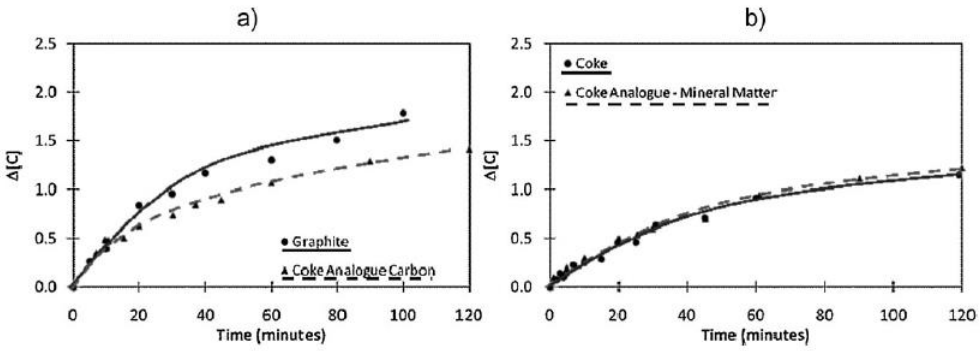

Figure 2.25: The dissolution behaviour of the coke analogue in iron at 1450 ^{O}C. (a) compared with graphite (b) compared with industrial coke [18].

The analogue has been used mainly to study the effect of minerals on coke analogue reactivity with CO_2. The effect of minerals was studied using single minerals (e.g. hematite, magnetite, lime, troilite, gypsum, pyrite, feldspar, quartz, and kaolinite) and binary / ternary combinations of minerals (e.g. alumina – quartz – iron oxides) and coke ash added to the analogue [19, 24, 65, 88, 150]. Reid *et al.* [24] studied the effect of different single minerals on coke analogue reactivity. In their study, they added minerals in a constant concentration of 0.1 mol cations of minerals per 100 g of the base coke analogue. The reactivity test with CO_2 has been carried out using the TGA technique at 1100 °C, similar to the NSC-CRI reactivity testing. They have distinguished the effect of selected single minerals on the coke analogue reactivity (*Figure 2.26*). The results have been compared with a base coke analogue that has no added minerals, for a clear understanding of the effect of the minerals. It was found that the relative effect on the rate of reaction as expressed in the weight change of the sample over 2 hours was,

hematite > lime > magnetite > troilite > gypsum > pyrite > base analogue (no mineral) > Na Feldspar > K feldspar > quartz > kaolinite

Note that the mineral names represent what was added to the green analogue and may not represent the mineral state during the reaction.

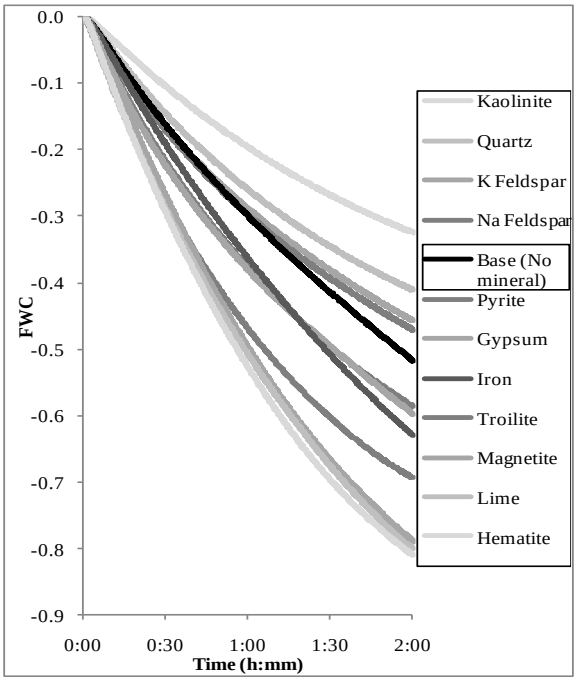

Figure 2.26: Changes in fractional weight loss with time for single mineral containing coke analogue in CO_2 gas at 1100 ^{O}C [24].

Binary and ternary mineral combinations of iron-bearing minerals and quartz were studied by Longbottom *et al.* [150] and Reid *et al.* [24]. The coke analogues were prepared to obtain a total mineral cation concentration of 0.1 mols per 100 g of base coke analogue. The reactivity with CO_2 was tested at 1100 °C. They observed decreasing reactivity with increasing quartz and decreasing Fe bearing mineral concentration. The reactivity trends in both binary and ternary systems were similar, suggesting the possibility of using a coke analogue to predict the effect of mineralogy on the metallurgical coke reactivity.

The coke analogue was also used to study the effect of the mineral matter of coke on reactivity and its replication in a coke analogue [65]. In this study, the authors have replicated three metallurgical cokes by adding the metallurgical coke ash of -38 μm at 10 mass %. The reactivity tests for all metallurgical cokes and coke analogues studied under similar reaction conditions showed that the coke analogue can replicate the metallurgical coke reactivity. In the coke analogues, the difference between porosities and carbon structure was minimised so that the effect of mineralogy on the reactivity was highlighted.

From Raman spectroscopy studies it was observed that the analogue has sp^2-sp^3

bonding [88, 151]. A plot of $I_{(D)}/I_{(G)}$ *vs* $I_{(V)}/I_{(G)}$ for base coke analogue is given in *Figure 2.27*. The $I_{(D)}/I_{(G)}$ observed for base coke analogue is 0.2 – 1.5 and $I_{(V)}/I_{(G)}$ is 0 – 0.4.

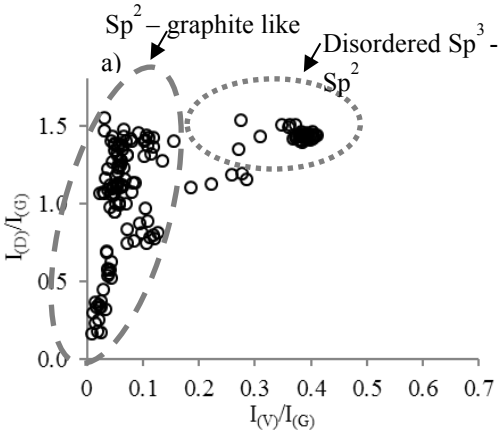

Figure 2.27: A plot of $I_{(D)}/I_{(G)}$ vs $I_{(V)}/I_{(G)}$ for base coke analogue [88].

Figure 2.27 shows that the coke analogue has a broader range of possible carbon bonding types than has the metallurgical coke, but the carbon bonding types in the analogue are reproducible [88].

2.7 Key issues in the literature that need to be considered

- Metallurgical coke is a complex material that is made up of different forms of carbonaceous matter, mineral components and pore morphologies and pore size distribution. Coke often displays significant heterogeneity in any matric used to characterise its carbonaceous forms, mineralogy, phase dispersion, morphology and porosity.

- Coke performance in the blast furnace is affected by the coke's carbonaceous forms, mineralogy and pore structure. As a result of the coke complexity and heterogeneity, it is difficult to isolate the effects of specific components on coke behaviour and on reaction kinetics when exposed to high temperatures and reactive atmospheres. This limits the progress in coke studies in assessing the impact of minerals on reactivity and reaction kinetics.

- The minerals in metallurgical cokes are known to either increase or decrease

coke reactivity with CO_2. Minerals can increase metallurgical coke reactivity by producing more active carbon sites (C_f). Minerals can also decrease coke reactivity by hindering pore walls, pore surfaces and carbon surfaces.

- The literature review on coke studies shows the importance of having a laboratory material (the coke analogue) that is representative of metallurgical coke but with controlled carbonaceous matter, mineralogy, mineral size and dispersion, porosity and pore size distribution, in order to access the effect of individual coke components. This thesis presents validation of the use of the coke analogue to study the effect of mineralogy on metallurgical coke gasification.

- The mineralogy of metallurgical coke is a broad area, and it is not practical to cover all possible minerals and mineral effects in one thesis. Therefore in this thesis, only specific minerals containing Ca are considered. Ca, an alkaline earth element, was chosen because it has been found to increase the coke reactivity.

Chapter 3

Experimental

Experiments were carried out to investigate the kinetics of the coke analogue reactivity with CO_2 and the effect of minerals on this reactivity. A thermogravimetric analysis (TGA) system was used to carry out the reactivity experiments in the temperature range of 1173 – 1623 K.

A coke analogue without any mineral, referred to as the base coke analogue throughout this thesis, was studied as a control experiment. This base coke analogue was doped with selected minerals containing Ca to assess their effects on reactivity. The minerals containing Ca used in this study were CaO – Al_2O_3 binary (lime, calcium aluminates (C3A, CA and CA6) and alumina) and a CaO-Al_2O_3-SiO_2 ternary (CAS) composition. Quartz (SiO_2) doped coke analogue was also studied to understand the coke analogue ternary mineral system. The CAS was studied in an attempt to understand the effect of crystallinity on the reaction kinetics.

For further evaluation of coke analogue performance, selected characterisation such as optical microscopy, SEM, and TGA measurements were also carried out on a metallurgical coke for comparison.

3.1.Coke analogue reactivity measured using a TGA

A schematic of the TGA set-up used in the CO_2 gasification reactivity test is given in *Figure 3.1*. A coke analogue sample of ~8g and 18 mm diameter and 30 mm height was weighed and then placed in the furnace hot zone on an alumina pedestal (*Figure 3.2*) suspended from a balance. The pedestal configuration represents a compromise between maximising gas contact with the sample ensuring only weight loss from the solid phase is measured and not “bits” dropping off the sample.

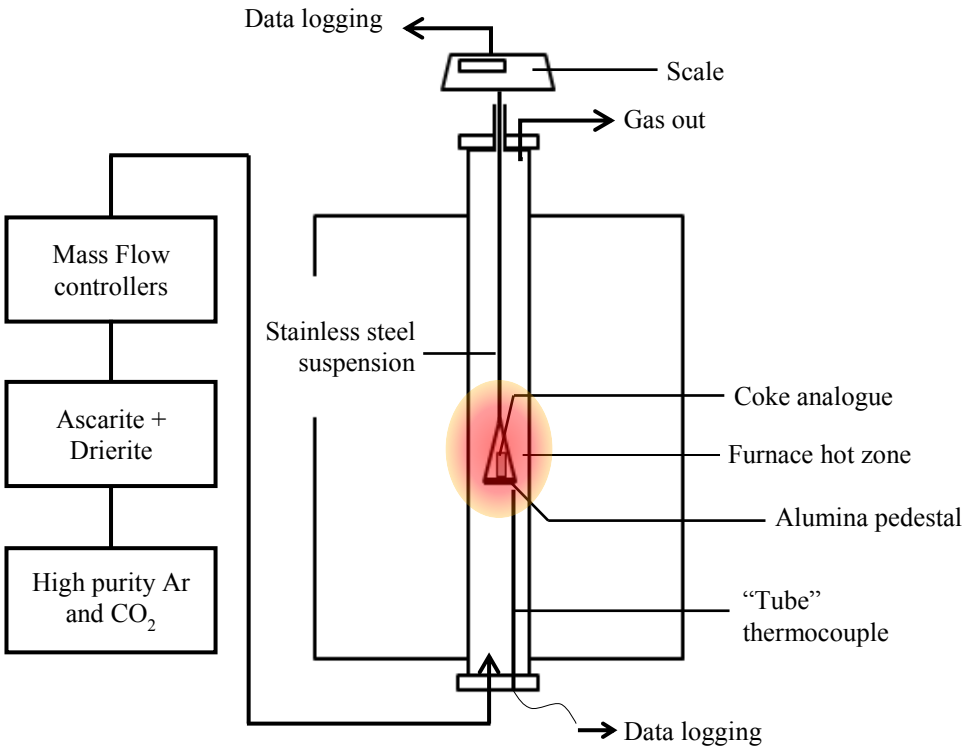

Figure 3.1: A schematic of the TGA set-up used for the reactivity test.

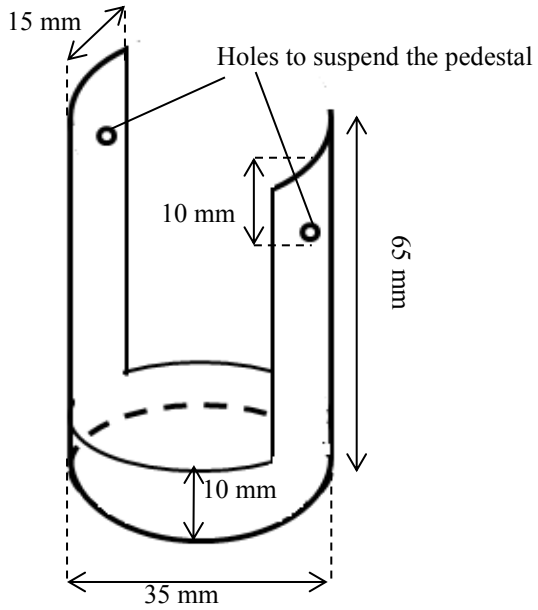

Figure 3.2: A schematic of the alumina pedestal used for TGA reactivity tests.

The system was heated at 10 K / min to the desired temperature under Ar at a flow rate of 1 L / min. The gas was switched from Ar to CO_2 once the experimental temperature was reached. The experiments were carried out in ~100 % CO_2 atmosphere to provide comparable reaction conditions to that of industrial CRI test [121]. A gas phase equilibrium approach based on *Equation 3.1* was used to evaluate the thermal stability of CO_2 gas during the test (see Appendix I for full detail). Note this is only considering the possibility of thermal decomposition of the gas, not a reaction with the coke analogue or coke. This was carried out to determine whether the gas composition changed during the test or could be assumed to be constant.

$$CO_{2(g)} \rightarrow CO_{(g)} + \frac{1}{2}O_{2(g)} \qquad 3.1$$

It was found that the reaction gas can be assumed to be constant as the amount of CO and O_2 are negligibly small.

The standard gas flow rate used for CO_2 gas was 4.5 L / min. This flow rate was set to avoid the reaction rate dependency on the gas flow rate. How this flow rate was established is discussed in detail in section 3.1.1.

The gases used were high purity (99.99%) and scrubbed by passing through drierite and ascarite prior to entering the furnace. The Ar was further cleaned by passing it through Cu turnings heated to 573 K.

The experimental temperatures examined were in the range of 1173−1623 K. The TGA was calibrated with respect to temperature prior to carrying out the experiments. The calibration process is detailed in section 3.1.2. The reaction in CO_2 gas was generally run for 2 hours, after which the gas was switched to Ar and the sample cooled down. The weight change during the reaction was logged, and the fractional weight change (FWC) was calculated based on the initial weight (W_0) and the weight at time t, (W) using *Equation 3.2*.

$$\mathrm{FWC} = \frac{\mathrm{W} - \mathrm{W_0}}{\mathrm{W_0}} \qquad 3.2$$

The reaction rate (R_C) was calculated using *Equation 2.18* and *2.19*.

$$X = \frac{W_0 - W}{W_0} = -FWC$$

$$R_C = \frac{1}{(1-X)} \frac{dX}{dt}$$

Prior to implementing the main experimental program the repeatability of the coke analogue reactivity test was evaluated at 1373 K using three coke analogue samples from three different batches (see section 3.1.3).

Using a standard approach for establishing activation energies for the reaction, the Walker *et al.* approach [91] was used to plot ln R_C against 1/T (*Equation 2.22*).

$$R_C = k_o e^{-\frac{E_a}{RT}}$$

For the comparison of the coke analogue with metallurgical coke, the reactivity of a metallurgical coke was measured over the temperature range 1173 – 1623 K.

3.1.1. Determination of the gas flow rate

Generally, the experiments were performed under conditions such that the reaction rate of the gasification reaction was independent of the gas flow rate. Under these conditions, the gas boundary layer control kinetics was eliminated. To establish the conditions for which the reaction rate was independent of gas flow rate, a series of experiments were carried out at different CO_2 flow rates (1− 5 L / min) at 1623 K (the maximum temperature of the experiment series). R_C at each flow rate was calculated and *Figure 3.3* shows the plot of R_C against flow rate. Above the flow rate of 4 L/min the reaction rate is independent of the CO_2 flow rate. Based on these data a flow rate of 4.5 L/min was used in the TGA experiments.

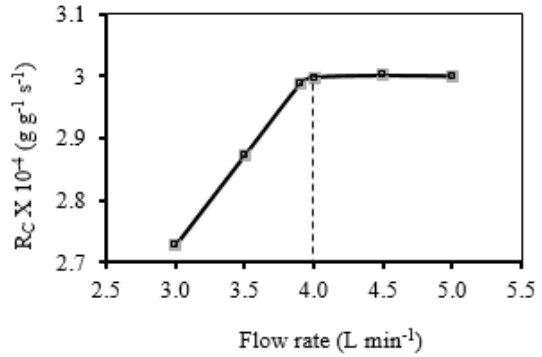

Figure 3.3: A plot of coke analogue R_C vs CO_2 flow rate at 1623 K.

3.1.2. Calibration of the TGA furnace

Establishing the hot zone

The reactivity tests were carried out in a TGA. The position and the length of the stable hot zone were determined by establishing a thermal profile using a type R thermocouple. The furnace set point was set at 1273 K and allowed to stabilise. A thermocouple was inserted into the middle of the tube equidistant from the furnace wall in 10 mm increments. At each point, the thermocouple was allowed to thermally stabilise for 10 min and the temperature was recorded. The resulting thermal profile of the TGA furnace is shown in *Figure 3.4*.

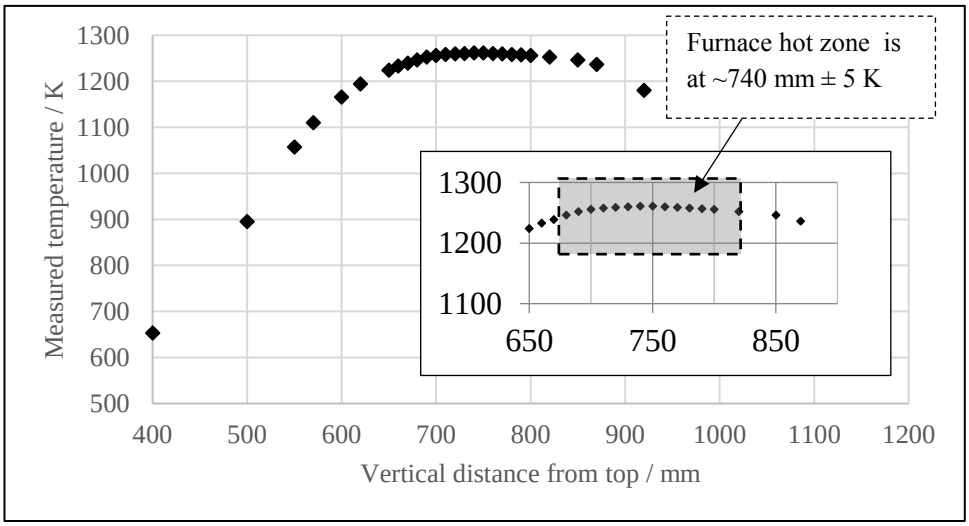

Figure 3.4: The thermal profile of the TGA furnace used for reactivity tests.

Furnace temperature calibration

The experimental temperature of the furnace was calibrated against the furnace set point temperature using a type R thermocouple. To provide similar thermal conditions to that of gasification experiments the thermocouple was inserted into a coke analogue sample (see *Figure 3.5*). Ar gas was passed in 1 L/min flow rate during the calibration. The thermocouple and the analogue were then placed in the hot zone of the furnace. The furnace temperature was increased stepwise to cover the experimental temperature range used in this study. At each temperature, the system was allowed to thermally stabilise for 30 minutes before recording the temperature. A plot of the furnace set temperature against the measured temperature is given in *Figure 3.6*. This calibration process is carried out every six months or when there has been a furnace element or furnace tube failure.

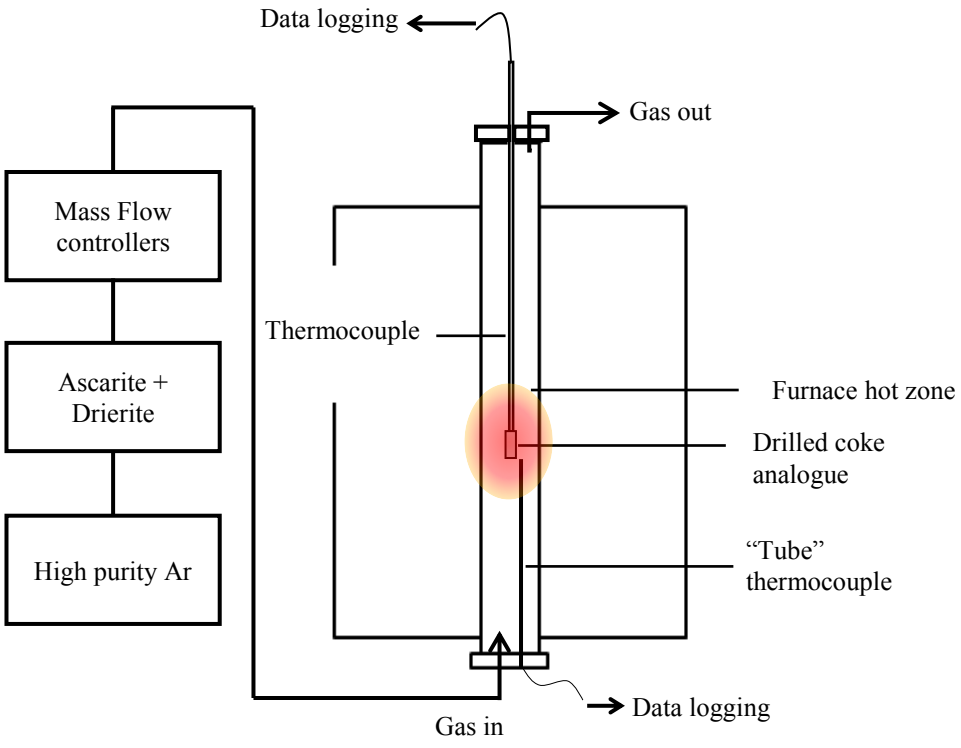

Figure 3.5: A schematic of the furnace calibration set-up.

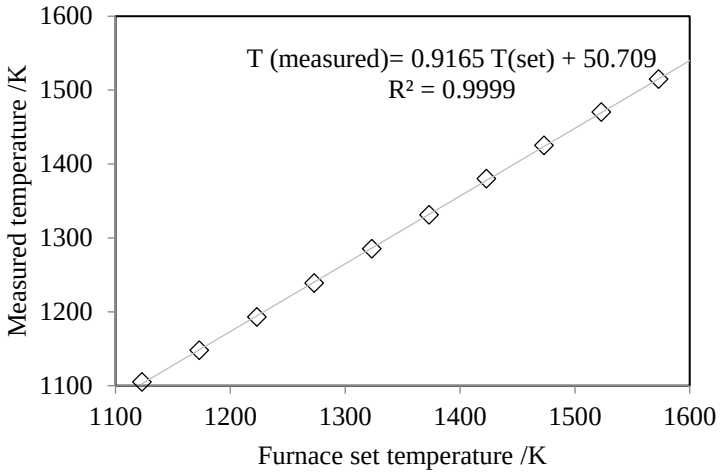

Figure 3.6: A plot of furnace set temperature against the measured temperature.

3.1.3. Repeatability of the coke analogue reactivity test

The repeatability of the coke reactivity test was evaluated at 1373 K using three coke analogue samples from three different batches (*Figure 3.7*). 1373 K is the temperature used in the industrial CRI test and represents an intermediate temperature used in this experimental program. The average FWC was 0.520 and the FWC of coke analogue 2 (the experiment with the highest variation) was 0.525. The difference of the average FWC and FWC with the greatest variation was only 0.005. This small difference demonstrates the good repeatability when using a coke analogue in gasification experiments.

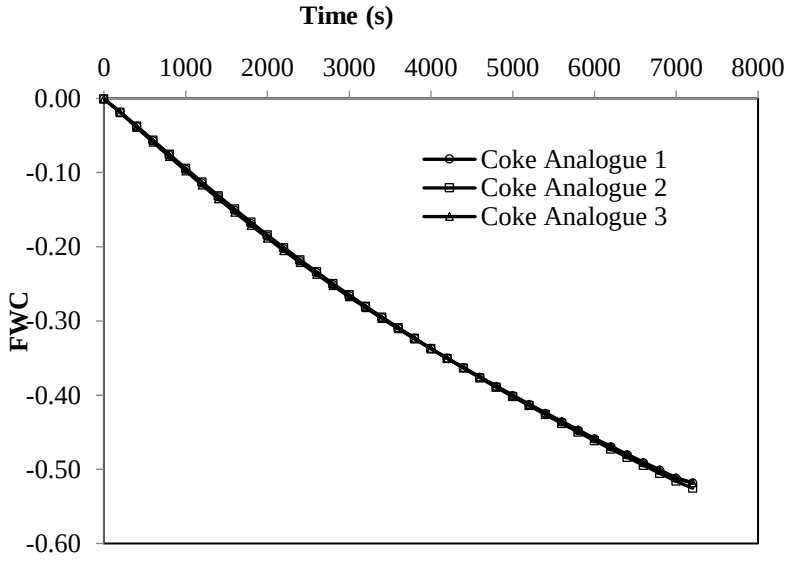

Figure 3.7: FWC against time for three coke analogues at 1373 K with CO_2 (2L/min)

3.1.4. Estimation of error/ uncertainty associated with the coke analogue reactivity tests

The errors associated with reaction rates calculated from *Equation 2.17, 2.18* and *2.19* were estimated based on the error propagation method.

The equations used for error calculation are given in *Equation 3.3 – 3.5*. The definitions of the symbols and how they were obtained are given in *Table 3.1*.

The error associated with the carbon conversion (σX) was estimated using *Equation 3.3.*

$$\sigma X = \left[X^2 \left(\left(\frac{\sigma \Delta W^2}{(\Delta W)^2} \right) + \frac{\sigma {W_0}^2}{W_0^2} \right) \right]^{1/2} \quad 3.3$$

The error of the reaction rate (σR_C) was estimated using *Equation 3.4.*

$$\sigma R_C = \left[R_C^2 \left(\frac{\sigma dX^2}{dX^2} + \frac{\sigma dt^2}{dt^2} + \frac{\sigma X^2}{X^2} \right) \right]^{1/2} \quad 3.4$$

Equation 3.5 was used to estimate the error of the ln R_C ($\sigma \ln R_C$).

$$\sigma \ln R_C = \frac{\sigma R_C}{R_C} \quad 3.5$$

Table 3.1: The symbols and determination of the symbol values

Symbol	Definition	Determination method
σW_0	Error of the initial weight	The resolution of the balance used to measure W_0 is 0.001 g
$\sigma \Delta W$	Error of the weight change	This error is associated with the buoyancy effect. It has been determined by measuring the weight change of a non-reactive piece of alumina of a similar weight as the coke analogue samples exposed to a step-wise heating cycle similar to that of the coke analogue.
σdX	Error of the carbon conversion change, dX	The average σX values for the range dX
σdt	The error of the time difference	The resolution of the clock in TGA software is 1s

Errors associated with the X and R_C are ≤ 5 % and ln R_C it is < 0.5 % for all the coke analogues studied at all the temperatures. Derivation of error equations and full tables of estimated error values for coke analogue reaction rates are given in Appendix II. It is noted that the error values are higher at lower temperatures where X, the carbon conversions, are lower.

3.2.Preparation of the coke analogue

The coke analogue was prepared using carbonaceous materials (laboratory grade graphite, Novolac, Bakelite and hexamethylenetetramine (HTMA)) and minerals. The carbonaceous materials, Novolac and Bakelite and their relative amounts were settled upon in unpublished research by other researchers at the UOW. Details of purity of materials used in the preparation of the analogues are given in *Table 3.2*. The "dry" ingredients, graphite, Bakelite, minerals and HTMA were mixed in an inversion mixer for 1 hour.

Table 3.2: The purity, size and supplier used in the preparation of the coke analogue.

Material	**Purity (%)**	**Size**	**Addition**	**Supplier**
Graphite Powder 1	99.99+	< 45µm	28% of dry base	Sigma Aldrich
Graphite Powder 2	99.99+	< 150µm	28% of dry base	Sigma Aldrich
Bakelite	N/A	+100µm -250µm	44% of dry base	LECO Metallurgical supplies
Liquid 45% Novolac Resin in propylene glycol (1:1 ratio)	N/A		Ratio of 0.52 liquid / dry mix	Shingawa Thermal Ceramics
hexamethylenetetramine (HTMA)	N/A		3mass% of liquid resin	Shingawa Thermal Ceramics
Non carbonaceous materials / minerals	N/A	+38 µm - 53 µm	0.1 mol cations per 100 g of base coke analogue	See *Table 3.2*
The dry base consists of graphite and Bakelite powder. The dry mix does not count the non-carbonaceous materials added. Carbonaceous material (dry base + resin) weight is ~140g Bakelite contained ~4 % by mass mineral matter as impurities (aluminum-silicon-calcium oxide) (see Appendix III for details)				

The amount of minerals added was calculated in order to get 0.1 mol cations per 100

g of base coke analogue. The particle size of the minerals was chosen to be 38 µm to 53 µm. Minerals were ground and sieved to get +38 – 53 µm sized particles. Details of the minerals used are given in *Table 3.3*. The preparation of alumina is different from this general procedure and is given in *Table 3.3*.

Table 3.3: Details of the oxide materials used in the coke analogue preparation

Mineral		**Purity (%)**	**As-received size**	**Supplier / Source**
Quartz, (SiO_2)		99.9+	1 – 5 mm grains	Creswick Quartz
Alumina, (Al_2O_3)[a]		99.9+	<10 µm	Sigma Aldrich
Calcium carbonate ($CaCO_3$) calcined to form lime (CaO)		99.9+	>10 µm	Sigma Aldrich
Calcium aluminates[b]	CA, ($CaO.Al_2O_3$)	NA	NA	Synthesised in the laboratory using materials supplied by Sigma Aldrich
	CA6, ($CaO.6Al_2O_3$)	NA	NA	
	C3A, ($3CaO.Al_2O_3$)	NA	NA	
Crystalline CAS[c]		NA	NA	Synthesised in the laboratory using materials supplied by Sigma Aldrich
Non-crystalline CAS[d]		NA	NA	

[a]Alumina discs were prepared by pressing and sintering at 1973 K for 8 hours. These disks were then ground and sieved to get particles with the size range +38 - 53 µm
[b] Details of the production method are given in 3.2.2.
[c, d] CAS = calcium aluminosilicate
Contains a mixture of Anorthite, Gehlenite and Mullite. Details of the production method are given in 3.2.3.
All the mineral were analysed using XRD prior to addition to the coke analogue. XRD patterns for each mineral are given in Appendix IV.

The powder mixture (graphite, Bakelite, HTMA and minerals) was added to the Novolac resin and mixed thoroughly by hand. It was kneaded for approximately 30 minutes and divided into ~14 g lots. Each lot was then pressed into cylinders of 18mm diameter and ~30 mm height using a steel die and a Buehler specimen mount press.

These cylinders were then cured in an oven overnight at 443 K. The analogue was then fired in a high temperature vertical tube furnace in a two stage process under Ar. In stage 1 the analogue was fired at 1273 K for 60 minutes (*Figure 3.8*). In stage 2 the analogue was fired at 1473 K for 60 minutes (*Figure 3.9*).

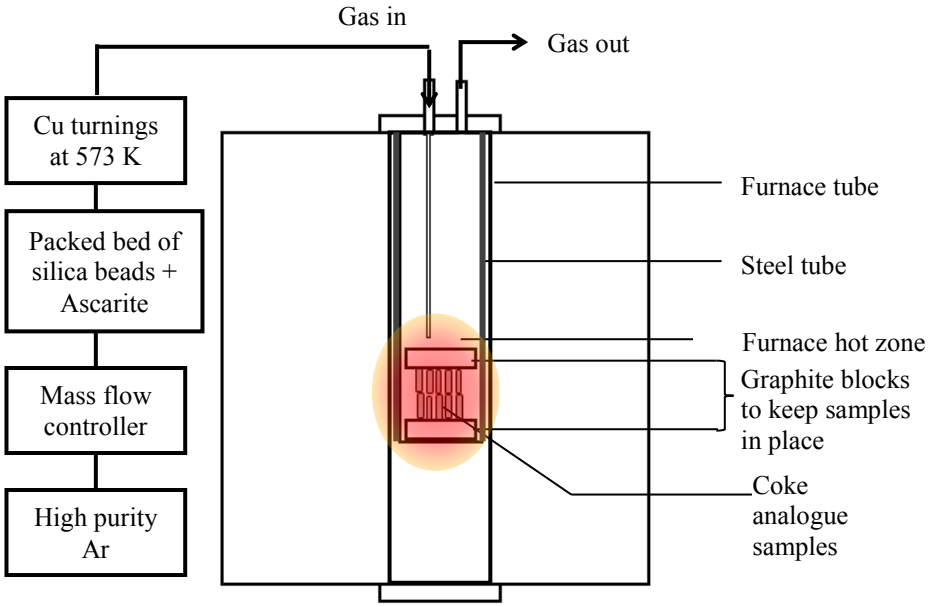

Figure 3.8:A schematic diagram of the set up for the 1st stage firing.

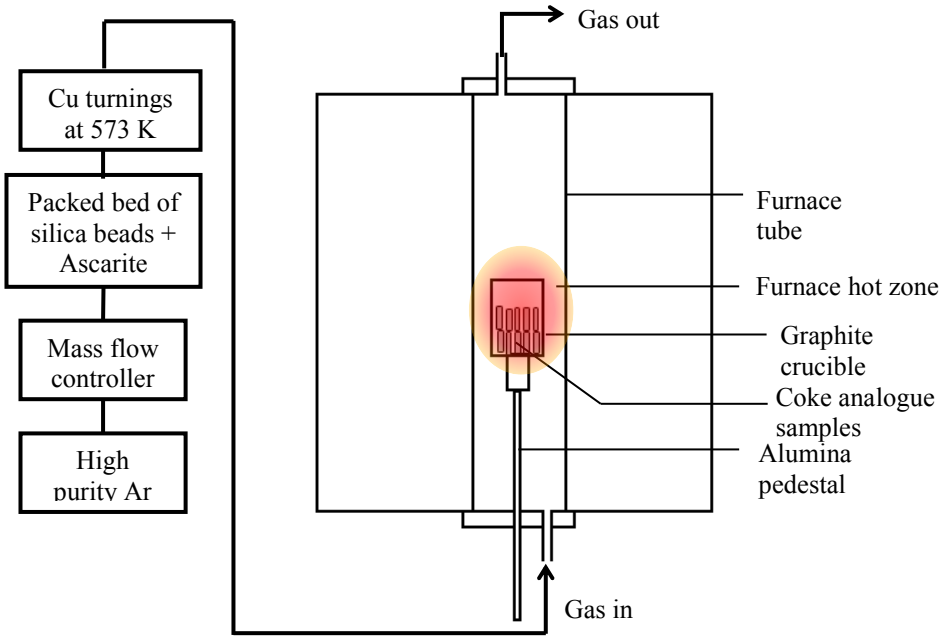

Figure 3.9: A schematic diagram of the furnace set up for the 2nd stage firing

The heating profiles for stage 1 and 2 firing are given in *Figure 3.10*. Details of the procedure for the calibration of the high temperature vertical tube furnace are given in 3.2.1.

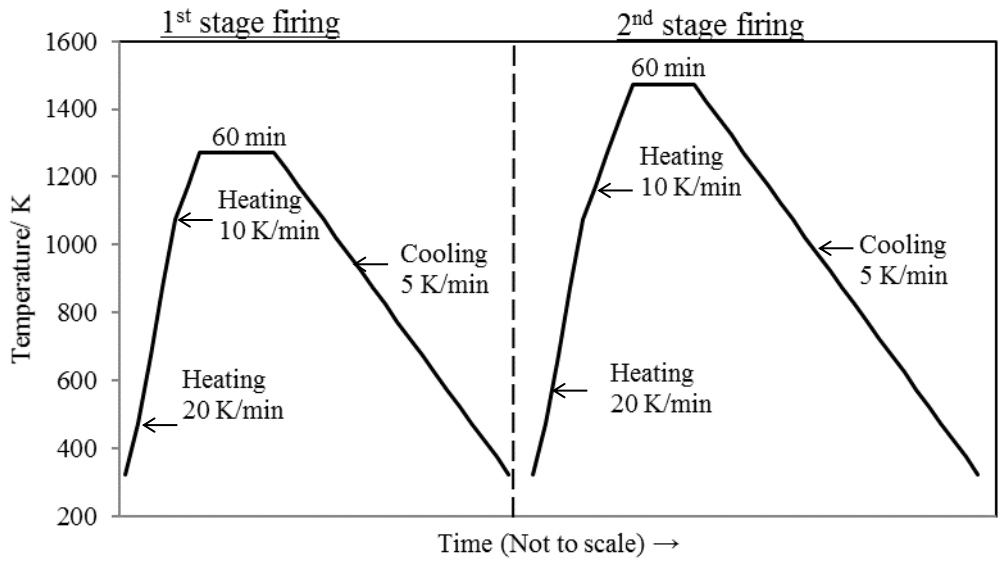

Figure 3.10: The heating profiles used in the 1st and 2nd stage firing.

3.2.1. Calibration of the high temperature vertical tube furnace used in the coke analogue firing

Establishing the hot zone

The coke analogue was fired in a high temperature vertical tube furnace. Before firing, the furnace was calibrated with respect to temperature. The position and the length of the stable hot zone were determined by establishing a thermal profile using a type R thermocouple. The furnace set point was set at 1823 K and allowed to stabilise. The thermocouple was inserted gradually into the middle of the tube equidistant from the wall of the furnace in 10 mm increments. After 10 minutes thermal stabilization at each increment the temperature was recorded and the thermocouple was inserted further into the furnace.

The thermal profile for the furnace is shown in *Figure 3.11*.

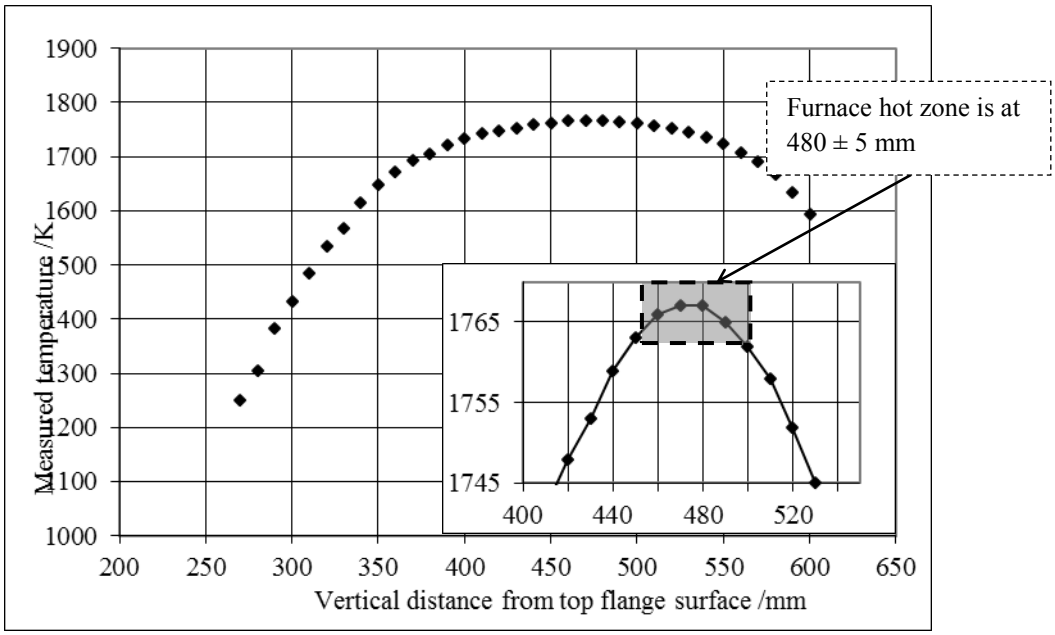

Figure 3.11: The thermal profile for the high temperature vertical tube furnace used for the coke analogue firing.

Furnace temperature calibration

The experimental temperature of the furnace was calibrated against the set point temperature using a type R thermocouple attached to a drilled coke analogue sample. The analogue sample was used to ensure the thermal response of the material being fired was at least in part accounted in for the calibration. A stainless steel tube and a graphite crucible were used for 1st and 2nd stage firings respectively (see *Figure 3.12* and *3.13*). Ar gas flow rate was set to be 1 L/ min during the calibration. The furnace temperature was increased stepwise covering the coke analogue experimental temperature range. At each temperature, the furnace was allowed to thermally stabilise for 30 minutes then the temperature was recorded.

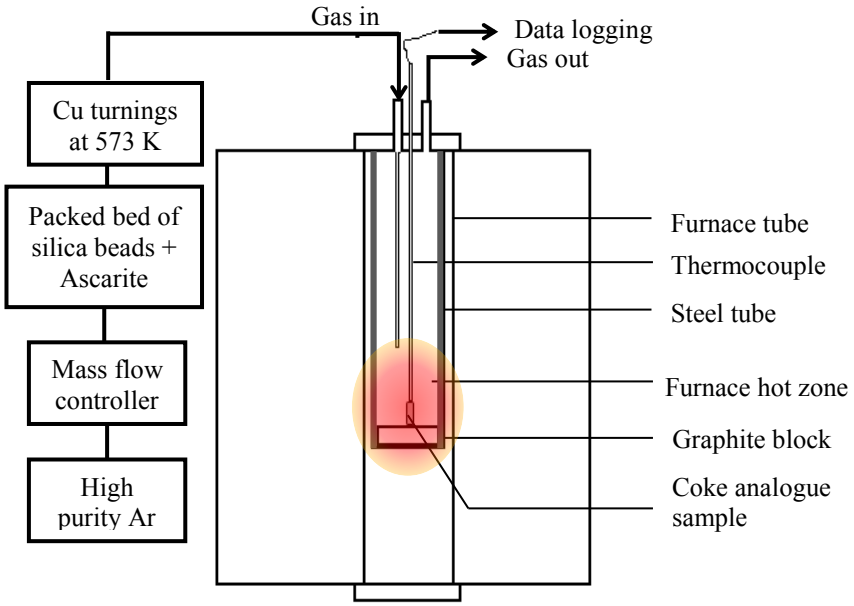

Figure 3.12: A schematic diagram of the calibration set up for first stage firing of the high temperature vertical tube furnace.

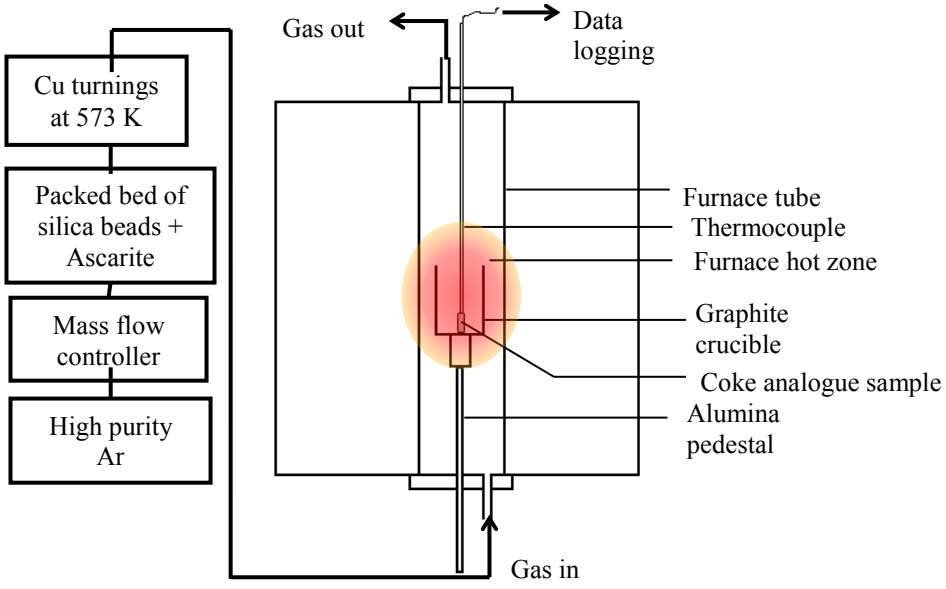

Figure 3.13: A schematic diagram of the calibration set up for second stage firing of the high temperature vertical tube furnace.

A typical plot of the furnace set temperature against the measured temperature is shown in *Figure 3.14*.

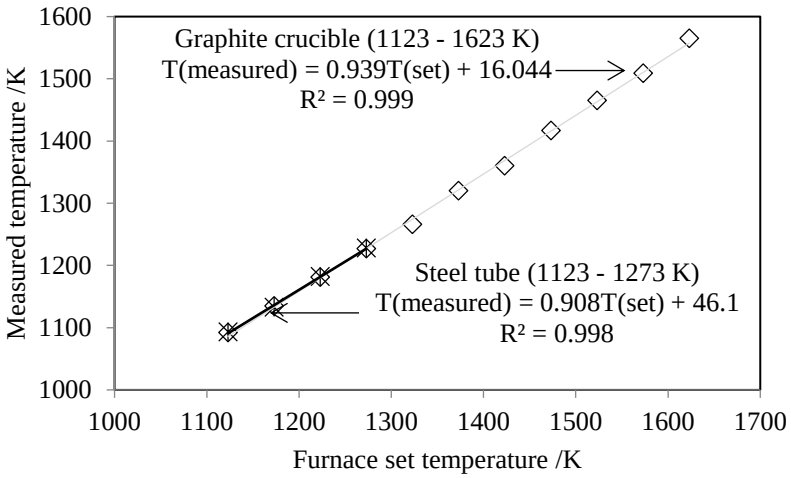

Figure 3.14: A plot of furnace set temperature against measured temperature.

3.2.2. Preparation of calcium aluminates

Three calcium aluminates (CA, CA6 and C3A) were prepared. These compositions were selected to account for changes in the calcium chemistry across the Al_2O_3 – CaO binary phase diagram (*Figure 3.15*).

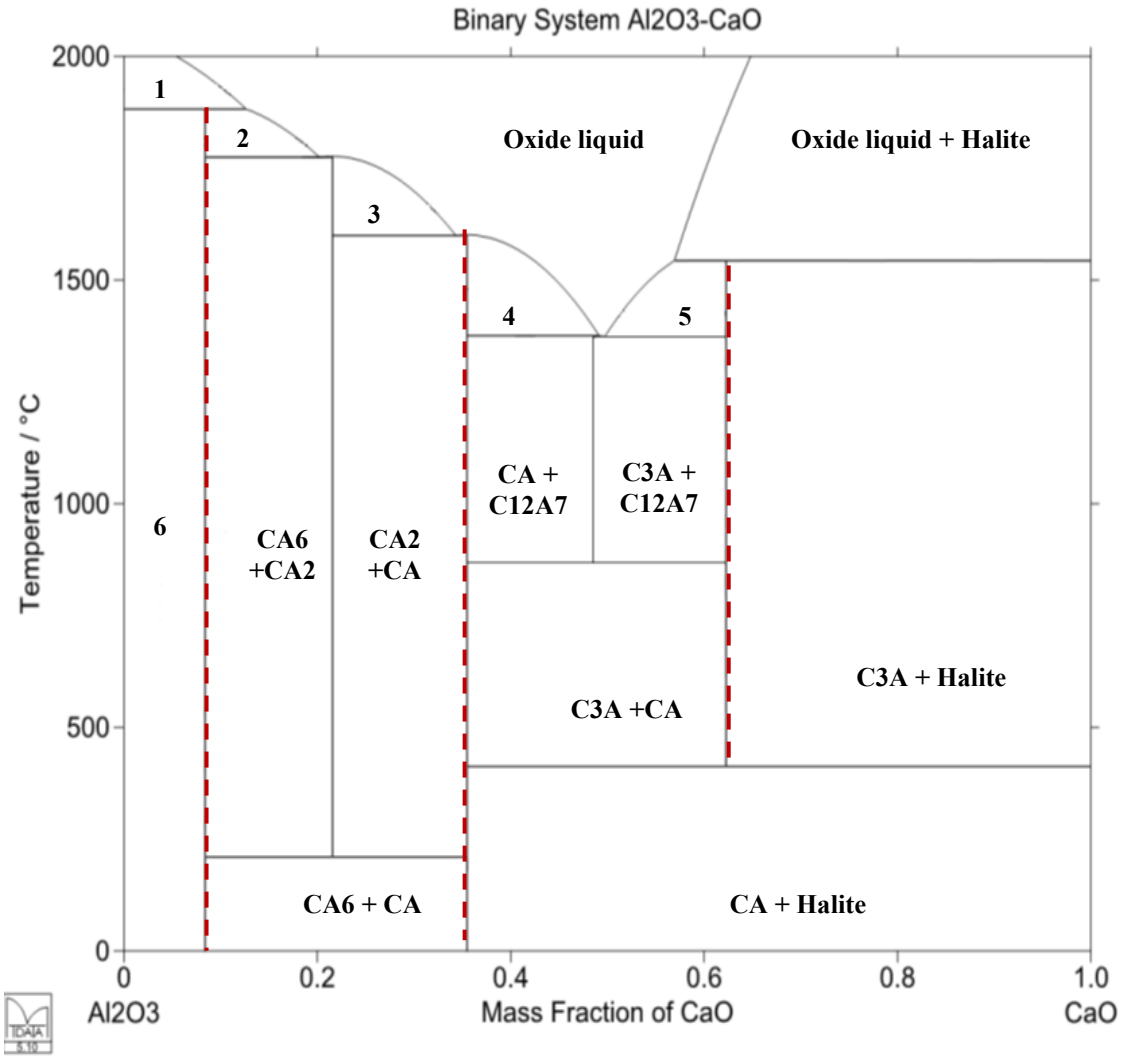

1 – Oxide liquid + Corundum

2 – CA6 + Oxide liquid

3 – CA2 + Oxide liquid

4 – CA + Oxide liquid

5 – C3A + Oxide liquid

6 – CA6 + Corundum

Figure 3.15: The phase diagram for the binary system Al_2O_3 – CaO from MTDATA [152] where the dashed lines represent a single phase calcium aluminate.

Calcium aluminates were prepared from high purity laboratory grade Al_2O_3 and $CaCO_3$ powders (See *Table 3.3*). These powders were mixed in appropriate proportions and fired as pellets to produce calcium aluminate. $CaCO_3$ was used instead of CaO to overcome the problem of CaO moisture absorption, allowing accurate weighing of the material.

The powders were first mixed with 500 ml of deionised water to make a slurry. The slurry was then filtered using a 75 mm Büchner funnel and a Filtech 2850 – 70 filter paper equivalent to Whatman #6 (pore size 3 μm). The filter cake was then oven dried at 373 K for 24 hours.

Deionised water (2 mass %) was added as a binder to the dried filter cake prior to pressing into pellets. Approximately 8 g of the mixture was pressed into a 25 mm diameter steel die under a 9.5 tonne load. The pellets were then fired in a muffle furnace at temperatures as listed below in *Table 3.4*.

Table 3.4: Firing temperatures and solidus temperatures for each calcium aluminate [152]

Calcium aluminate type	Firing temperature / K	Solidus temperature / K
CA6	1898	2049
CA	1623	1648
C3A	1623	1646

These temperatures are below the solidus temperature of the individual phases. XRD measurements of the post fired materials were made to confirm the phases. These are given in Appendix III. Solidus temperatures were established from the MTDATA thermodynamic software package [152].

3.2.3. Preparation of CAS

A CAS was prepared from Al_2O_3, $CaCO_3$ and SiO_2 powders (See *Table 3.3*). The composition (Al_2O_3 40%, CaO 10 % and SiO_2 50 %) was chosen to prepare a CAS in both crystalline and non-crystalline forms in an attempt to study the effect of mineral crystallinity on coke analogue gasification.

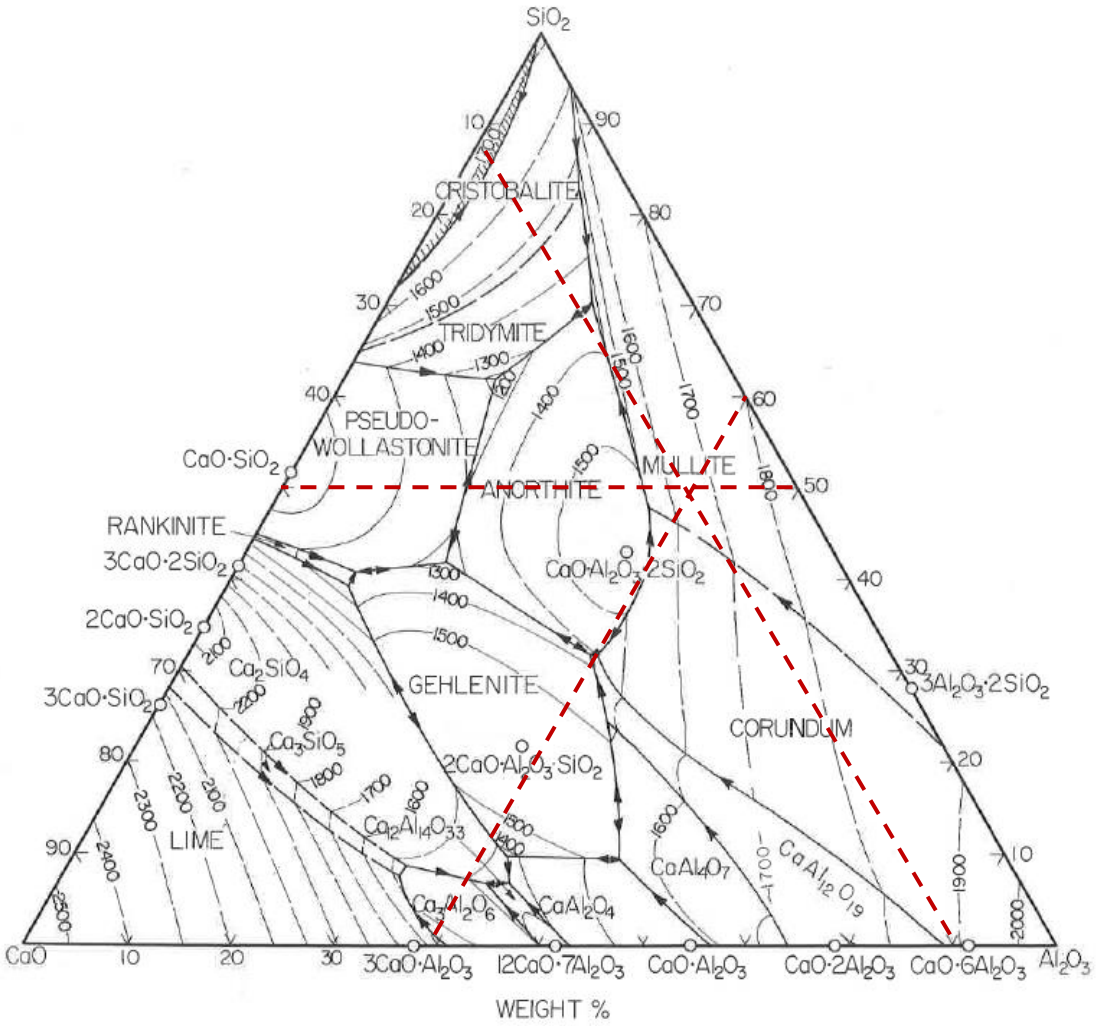

Figure 3.16: Phase diagram of CaO-Al_2O_3-SiO_2 system [153]

Preparation of non-crystalline CAS

The mixture was placed in a platinum crucible and melted in a muffle furnace heated to 2023 K for 20 minutes. The platinum crucible was removed from the furnace and the liquid oxide was quenched by pouring on to an iron slab. The quenched sample was then ground and sieved to get particles of +38 – 53 μm for coke analogue preparation. The XRD pattern of this material confirmed the sample was not in a crystalline form and is given in Appendix III (*Figure III.8*).

Preparation of crystalline CAS

Distilled water (2 % mass) was added to the ground non-crystalline CAS and then pressed into discs using the same procedure as for calcium aluminates. These discs were sintered in a muffle furnace at 1773 K for 8 hours. XRD analysis was carried out to confirm the sample is in a crystalline form (See Appendix III *Figure III.9*). The MAUD program [154] was used for the quantitative analysis of the CASs mixture (see *Table 3.5*). MAUD is a general diffraction/reflective analysis program based on the Rietveld method.

Table 3.5: Quantitative analysis of the CAS mixture

Compound	Mass %
Mullite ($Al_6Si_2O_{13}$)	31.4
Anorthite ($CaAl_2Si_2O_8$)	63.5
Gehlenite ($Ca_2Al_2SiO_7$)	5.1

3.3.Characterisation of coke analogue

The morphology of the carbon types, porosity and minerals in the coke analogue samples were characterized. Further, where appropriate, MTDATA [152] and FactSage [155] thermodynamic software have also been used to assess the mineral phase stability and reactivity in the experimental programme.

3.3.1. Coke analogue porosity

This section describes coke analogue porosity characterization using two different but complementary techniques, optical imaging and mercury porosimetry.

3.3.1.1.Optical imaging/ porosity

A Leica DMR optical microscope equipped with a green filter and a Leica DFC295 digital camera was used to acquire optical micrographs. Leica Application Suite V4.0.0 software was used to capture the optical micrographs. The resulting micrographs were used in the calculation of the porosity.

Preparation of impregnated coke analogue samples

A fired coke analogue sample was sectioned using a Struers Accutom-50 precision cutting machine using the wheel speed of 3000 rpm and the feed speed of 0.10 mm/sec. The analogue was sectioned to 5 mm depth pieces to produce six cuts per one cylindrical sample, as shown in *Figure 3.17*.

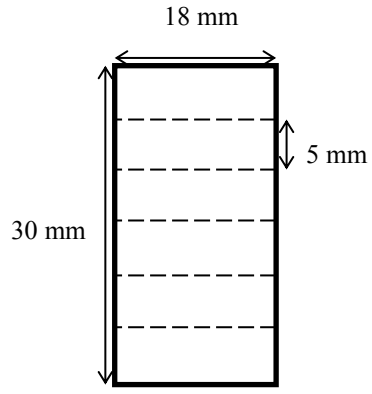

Figure 3.17: Schematic showing the position at which the coke analogue was cut

The analogue pieces were placed in standard Struers cold moulds of 30 mm diameter by 20 mm height. Thereafter, the epoxy resin produced by mixing Struers EpoFix Resin with EpoFix Hardener in a weight ratio of 25: 3 was poured into the mould. The analogues were then vacuum impregnated. These impregnated samples were left for 24 hours to harden prior to polishing.

Grinding and polishing of impregnated coke analogue samples

An automated Struers Tegrapol-21 grinder/polisher was used to obtain polished coke analogue surfaces.

A two-stage grinding step and four stage polishing step were followed. Details of each step were given in *Table 3.6*. The lubricants used were chosen based on the water

sensitivity of the coke analogue samples. Lime, calcium aluminates and CAS added coke analogues were treated as water sensitive.

The surfaces of the coke analogue samples were washed after each grinding and polishing step using deionized water (for non-water sensitive samples) or ethanol (for water sensitive samples).

Table 3.6: Details of the grinding and polishing steps used in the preparation of the analogues.

Step	Surface	Force	Time	Lubricant	
				Non-water sensitive samples	Water sensitive samples
Grinding	#500 silicon carbide paper	10 N	1 min 30 sec	Deionized water	Glycerol
	#1200 silicon carbide paper		45 sec		
Polishing	9 µm diamond paste on Struers Largo polishing pad	20 N	4 min	Struers DP-Lubricant green[a]	Struers DP-Lubricant yellow[b]
	3 µm diamond paste on Struers Dac polishing pad		4 min		
	1 µm diamond paste on Struers Dur polishing pad		5 min		
	0.25 µm diamond paste on Struers Dur polishing pad		5 min		

[a] Water based lubricant. Cooling and lubricating liquid for fine grinding and diamond polishing of most materials [156].
[b] Ethylene glycol based lubricant. Lubricating liquid for final diamond polishing of softer water-sensitive materials [156].

Porosity measurements using Image J

Using the Leica optical microscope coke micrographs were obtained at 50x magnification. The images for porosity measurement were prepared by imaging the surface of the sample with high intensity green filtered light. This method only

detected light from the highly reflective polished coke analogue material. Images were taken from 12 field to give a scale of 1 pixel to 1.0157 microns. These images were stitched together and cropped to give an area of ~4mm x 4mm of the analogue as represented by one square in *Figure 3.18*. Five positions of the coke analogue were observed to use for optical porosity calculations (the detailed calculation is given later in the section). The images were analysed using an ImageJ analysis software version 1.48 [157]. The software threshold was adjusted in order to change the colour of the pores into red and then the area of those red parts was calculated by the software (*Figure 3.19a* and *b*). Pores within the diameter range of 10 – 500 µm were considered for the calculation. Values with diameter <10µm were considered unreliable and not reported. Areas with diameter >500 µm are considered fissures rather than porosity.

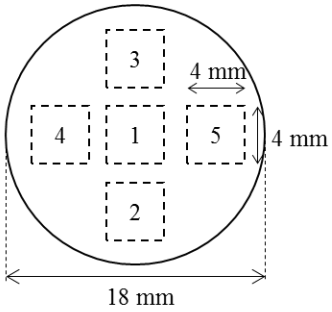

Figure 3.18: Five positions in the coke analogue assessed for porosity measurements.

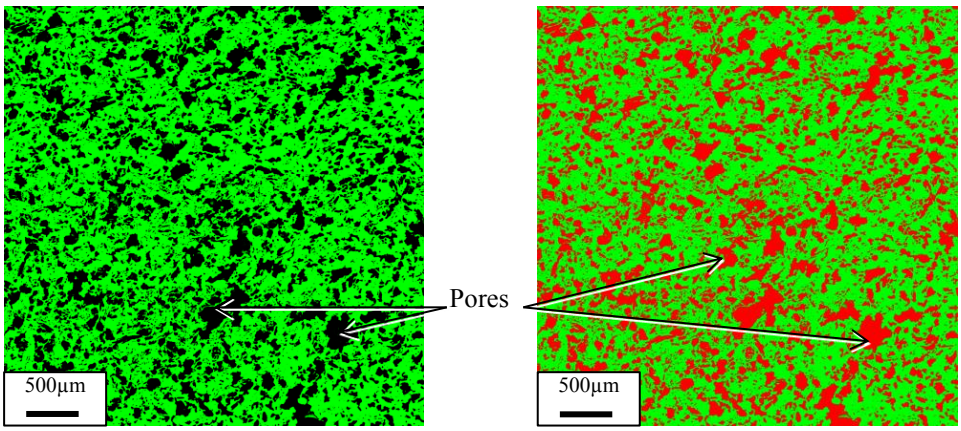

Figure 3.19: (a) optical microscopic image of the coke analogue cross section under green light (b) optical microscopic image of the coke analogue cross section after setting the colour threshold

Optical porosity calculation

Generally, the porosity at the center of the coke analogue (P_1) is slightly higher than the porosity at the annulus of the coke analogue (P_a). To account for this the total porosity of the coke analogue is expressed as *Equation 3.6.*

$$P_T = \left(\frac{\text{Area of the centre of coke analogue}}{\text{Total area}} \times P_1\right) + \left(\frac{\text{Area of the annulus of coke analoge}}{\text{Total area}} \times P_a\right) \quad 3.6$$

Total area of the coke analogue surface $= \pi r^2$

r = 9 mm

Area of the position 1 $= L^2$

L = 4 mm

Area of the annulus $= (\pi r^2 - L^2)$

Then,

$$P_T = 0.063P_1 + 0.937\,P_a \quad 3.7$$

P_a is the porosity of either of 2, 3, 4 or 5 positions. The porosities of each annulus position were measured and found to be similar with < 1 % difference in the measured value.

Repeatability of coke analogue optical porosity

The repeatability of coke analogue optical porosity was assessed using the base coke analogue samples. *Figure 3.20* shows the pore size distribution of those samples. The total porosity values (pores in the range of 10 – 500 µm) of each coke analogue samples were tabulated in *Table 3.7*. These porosity values represent different batches and different operators making the measurements. In general, there is a good agreement over the porosity range.

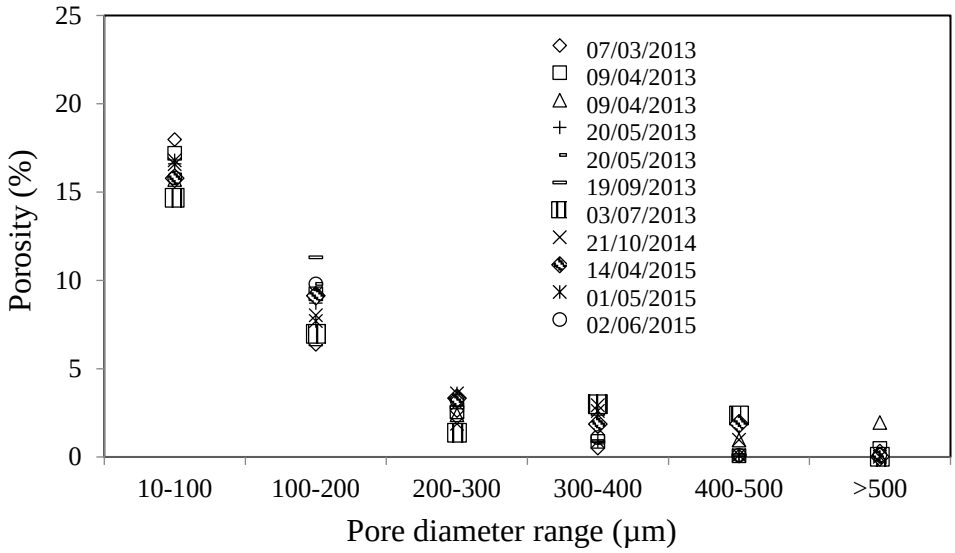

Figure 3.20: Pore size distribution of 11 different base coke analogue samples

Table 3.7: Total porosity of base coke analogue sample

Date produced	Total porosity (%)
07/03/2013	27.5
09/04/2013	29.9
09/04/2013	28.5
20/05/2013	29.7
20/05/2013	29.8
19/09/2013	30.8
03/07/2014	28.3
21/10/2014	30.3
14/04/2015	31.9
01/05/2015	30.8
02/06/2015	30.0

Figure 3.20 shows the majority of the coke analogue pores are in the diameter range of 10 – 100 µm. The base coke analogue has a total optical porosity of 29.8 ± 1.2 %.

The porosity and pore size distribution were maintained in a narrow range for all the mineral added coke analogues used in this study to minimise the effect of porosity on the coke analogue reactivity.

Porosity correction for minerals

Some minerals are non-reflecting and can be wrongly identified as pores in optical microscopy (see *Figure 3.21*). The porosity has to be corrected for such minerals. From the minerals studied in this work, only the quartz doped coke analogue suffered from this.

To correct for this, backscattered SEM images were taken from the same area used for the porosity calculation by optical microscopy. The mineral area fraction identified from the SEM image was subtracted from the total porosity value obtained from optical microscopy.

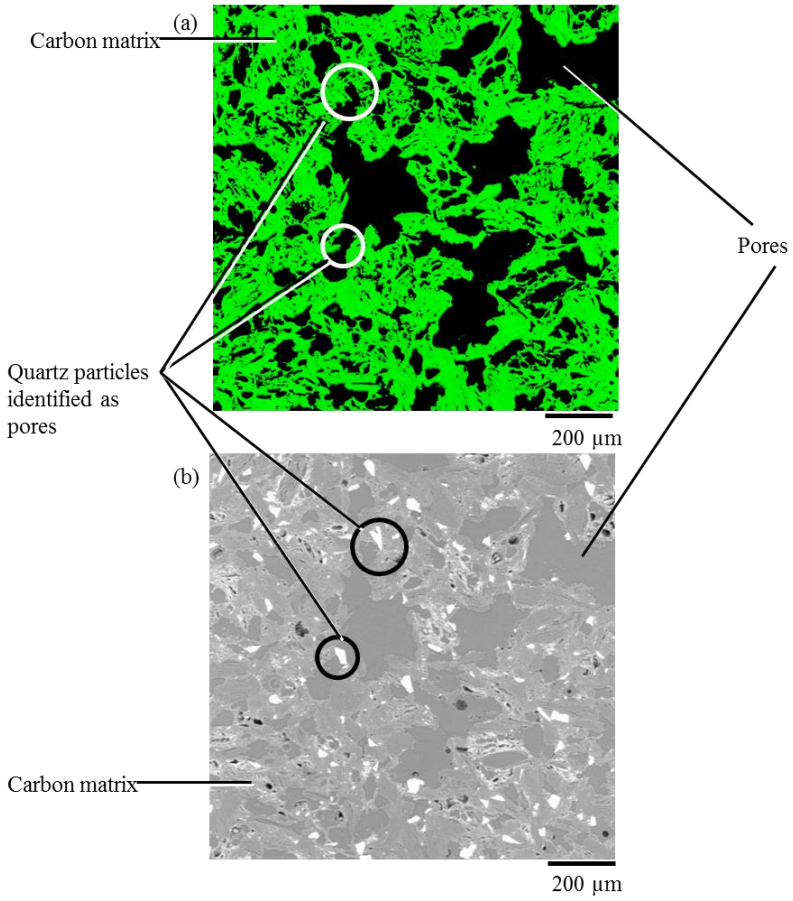

Figure 3.21: Images of quartz added coke analogue (a) optical microscopy image (b) backscattered SEM image

3.3.1.2.Mercury porosimetry

Mercury porosimetry measurements for two fired base coke analogue samples were carried out at Particles and Surface Science Pty Limited, Gosford, New South Wales Australia laboratory using a Micrometrics Autopore 9600 Mercury Porosimeter.

Mercury porosimetry is based on the intrusion of a non-wetting liquid (like Hg) under pressure. The relationship between the pressure and the pore diameter is given by Washburn equation [158] (*Equation 3.8*),

$$P = \frac{-4\gamma \cos\theta}{d} \qquad 3.8$$

where P is the pressure, γ is the surface tension of the liquid, θ is the contact angle of the liquid and d is the pore diameter. This method can measure the pores with diameter 0.003 – 250 μm.

Given in *Table 3.8* are the Hg porosimetry values obtained for a base coke analogue sample.

Table 3.8: Hg porosity values of a base coke analogue sample

Batch No	Date measured	Hg porosity / %
BN09042013 – S9	09/04/2013	41.9
BN09042013 – S4	09/04/2013	41.1

3.3.2. BET surface area

There was an attempt to use BET technique to study the gas – solid contact area in this study, however this proved to be difficult due to the degassing issues associated with carbonaceous materials. It was therefore, discontinued. See Appendix V for the details of the degassing issues associated with the coke analogue.

3.3.3. Electro-optical (SEM) characterisation

SEM-EDS analysis was carried out using a JEOL JSM 6490 LV SEM linked to a JEOL EX-54165JMU Energy Dispersive X-ray analyser. Samples prepared as detailed in sections 3.3.1.1 and were carbon coated using an SPI module carbon coater. This analysis was carried out to establish the mineralogy of the coke analogue samples and to observe the mineral shape and size after adding to the coke analogue.

3.3.4. Post reactivity analysis

XRD analysis

Mineral added coke analogue samples after the reaction with CO_2 gas at 1623 K were analysed using a GBC MMA X-Ray diffraction unit. Copper Kα radiation was used as the X-ray source at 35 kV potential and 28.4 mA electron beam current. Samples were scanned for the range of 10° - 80° 2θ at the step size 0.02 ° and 1°/min scanning speed.

Quantitative XRD was conducted using MAUD software. The quantification was based on Rietveld refinement of the patterns using the crystallographic open database. The sigma values <2% represent good refinements.

Electro-optical (SEM) analysis

SEM-EDS analyses were carried out on post reacted coke analogue samples using a JEOL JSM 6490 LV SEM linked to a JEOL EX-54165JMU Energy Dispersive X-ray analyzer. Coke analogue samples after the reaction at 1273 K were analysed. The samples were mounted in epoxy resin, ground, polished and carbon coated for the observation through SEM as per sections 3.3.1.1. Samples at > 1273 K were not selected for SEM analysis due to the lower strength of the samples after the reaction.

3.4.Metallurgical coke used in this study for comparison

The metallurgical coke used in this study was obtained from BlueScope Australia. The metallurgical coke mineral content was 11.60–11.80 mass %. This includes 0.40–0.45 mass % of sulphur. A detailed chemical composition of the mineral matter as measured by XRF after ashing of the coke at 1088 K is given in *Table 3.9*.

Table 3.9: The chemical composition of the mineral matter in the metallurgical coke [27].

Mineral Matter	SiO_2	Al_2O_3	Fe_2O_3	CaO	P_2O_5	MgO	K_2O	TiO_2	Na_2O	Mn_3O_4
Mass (%)	54.80	32.30	4.90	2.90	1.42	1.00	0.51	1.40	0.38	0.05

The metallurgical coke mineral matter was quantified by the SIROQUANT method and the details are given in *Table 3.10* [159]. The coke was found to contain 47.9 % amorphous mineral content. Minerals such as aluminosilicates can decompose during the carbonisation process and produce amorphous phase [38].

Table 3.10: A list of minerals present in the metallurgical coke mineral matter [27].

Mineral matter observed		Mass %
Mineral name	Formula	
Anatase	TiO_2	0.1
Anorthite	$(Ca,Na)(Si,Al)_4O_8$	0.2
Bassanite	$CaSO_4x_{0.5}H_2O$	0.8
Calcite	$CaCO_3$	0.3
Cristobalite	SiO_2	3.6
Fluorapatite	$Ca_5(PO_4)_3F$	1.8
Gehlenite	$Ca_2Al_2SiO_7$	0.1
Iron	Fe	0.4
Jarosite	$(K,H_3O)Fe_3(SO_4)_2(OH)_6$	0.3
Maghemite	γ-Fe_2O_3	0.4
Magnetite	Fe_3O_4	0.6
Martensite	$C_{0.055}Fe_{1.945}$	0.1
Mullite	$Al_6Si_2O_{13}$	29.7
Pyrrhotite	FeS	0.2
Quartz	SiO_2	13.5
Total mineral matter (mass%) = 11.6 - 11.8 Amorphous mineral (mass%) = 47.9		

The mean reflectance, R_o, of the metallurgical coke is 1.13 and the CRI value of the coke is 19.4% [65].

Chapter 4

Results

In this chapter the results of the experimental work are presented as follows:

This chapter is chiefly focused on the coke analogue but where applicable metallurgical coke data are also presented.

4.1.Coke analogue and metallurgical coke reactivity

The reactivity of coke analogues in CO_2 gas are presented for the base coke analogue, minerals added coke analogues and metallurgical coke. The coke analogues containing different minerals are named based on the minerals added to the green coke analogue. The minerals used in this study are minerals of CaO – Al_2O_3 binary (lime, calcium aluminates (C3A, CA and CA6) and alumina) and CaO-Al_2O_3-SiO_2 ternary (CAS), and quartz (SiO_2) (for comparison).

The focus of the reactivity experiments, in general, was to establish the suitability of the coke analogues to study the coke gasification kinetics in CO_2 and to evaluate the effect of selected minerals on the gasification kinetics. The results are presented as FWC vs time plots (*Figure 4.1 – 4.9*). These plots were used to calculate the gasification reaction rate.

CAS was added in both crystalline and non-crystalline form. The focus of this experiment was originally to establish the effect of mineral crystallinity on coke analogue gasification. However, this was unsuccessful due to the crystallization of CAS during the

coke analogue firing. Therefore, from this point onwards the mineral added is considered only as CAS. Two sets of data for CAS (CAS 1 and CAS 2) are presented.

Figure 4.1 is the FWC vs time plot for the base coke analogue and *Figure 4.2 – 4.9* are the FWC vs time plots for the coke analogues doped with minerals. All the plots have the similar relationship between FWC and time. The FWC became more negative with increasing temperatures for all the coke analogues. Increasing negativity of FWC shows increasing reactivity. By a careful observation, it can be seen that the coke analogues containing Ca in the added minerals have higher reactivity compared to the base coke analogue. These plots were used to calculate the gasification reaction rate in CO_2. The flattening of the curves at higher temperatures is due to the consumption of all the carbon.

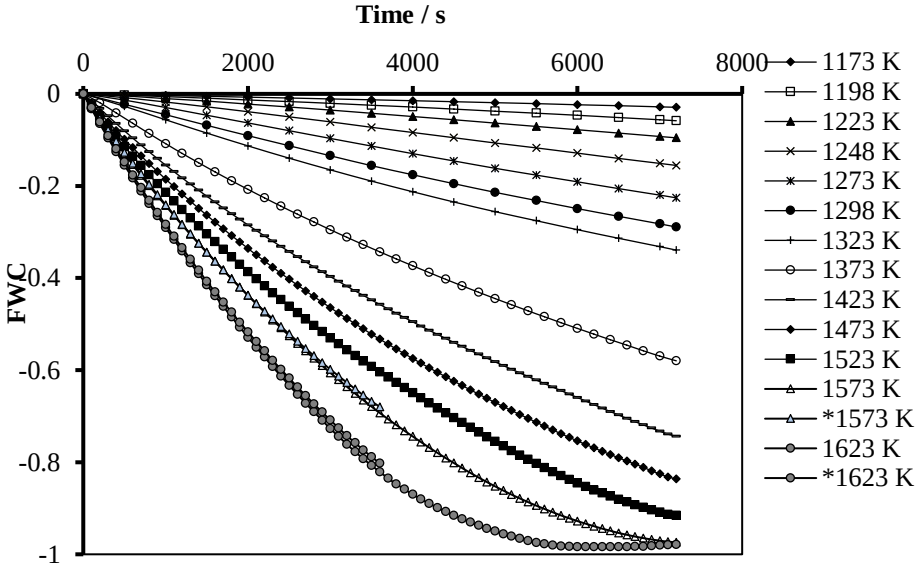

*Figure 4.1: The FWC vs time plots of base coke analogue reaction with CO_2 (4.5 L/min) over the temperature range of 1173 K- 1623K.*Experiments arrested after 1 hour.*

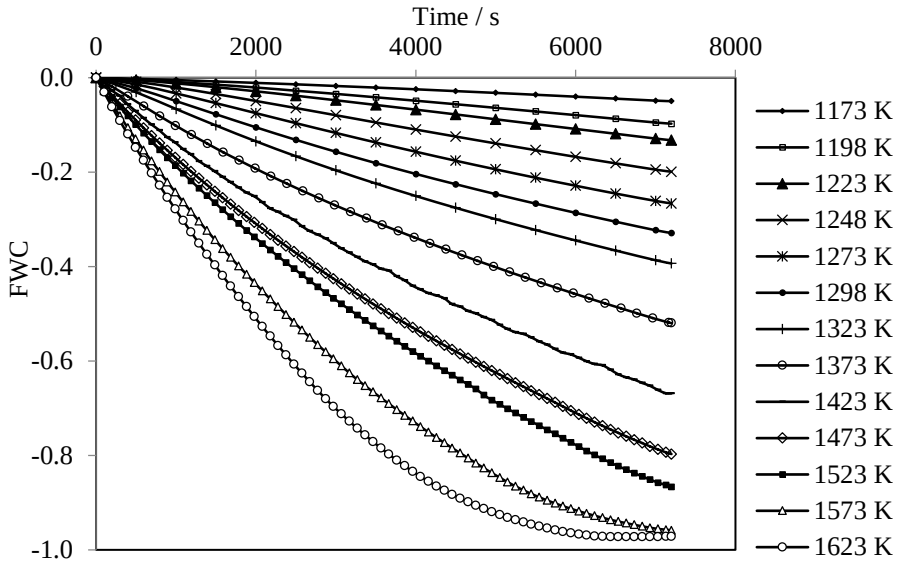

Figure 4.2: The FWC vs time plots of alumina doped coke analogue reaction with CO_2 (4.5 L/min) over the temperature range of 1173 K- 1623K.

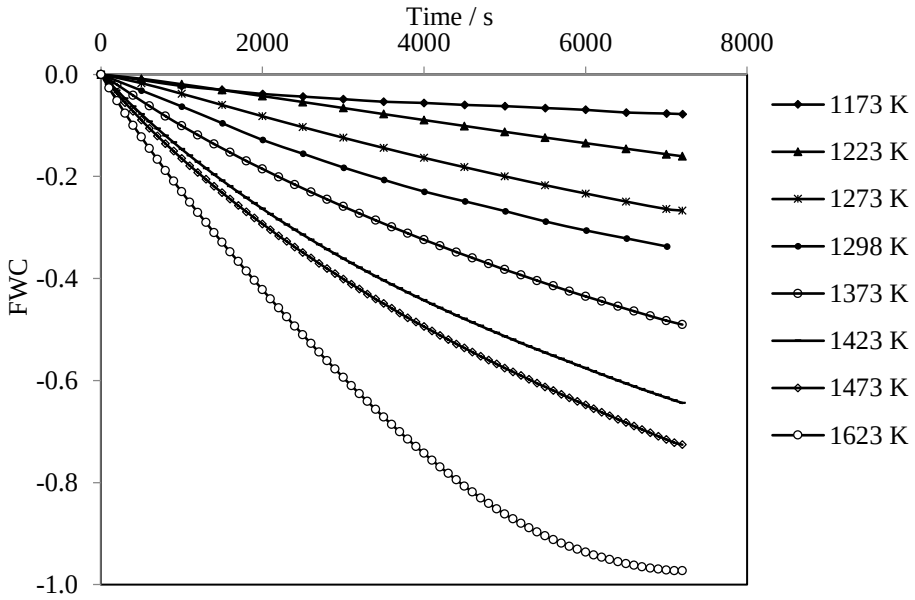

Figure 4.3: The FWC vs time plots of CA6 doped coke analogue reaction with CO_2 (4.5 L/min) over the temperature range of 1173 K- 1623K.

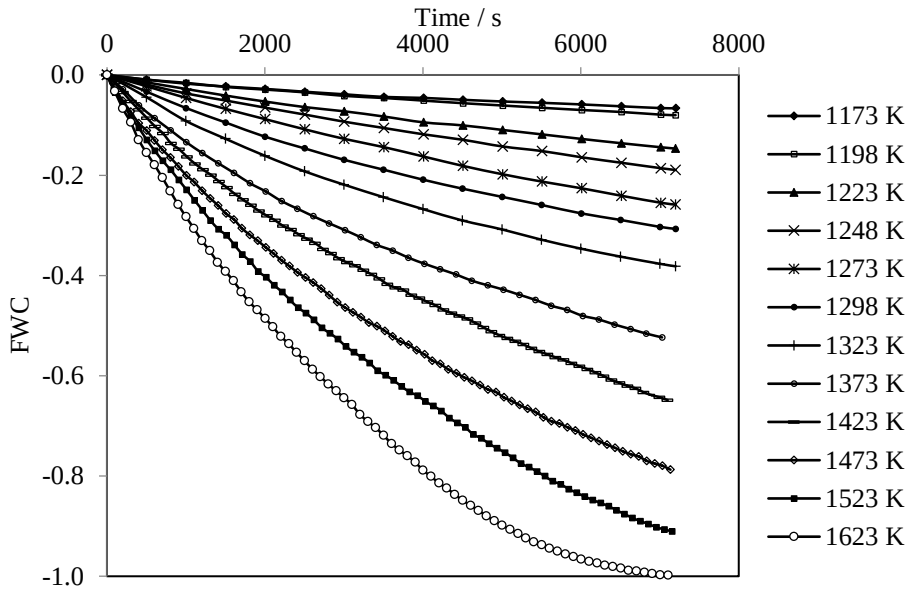

Figure 4.4: The FWC vs time plots of CA doped coke analogue reaction with CO_2 (4.5 L/min) over the temperature range of 1173 K- 1623K.

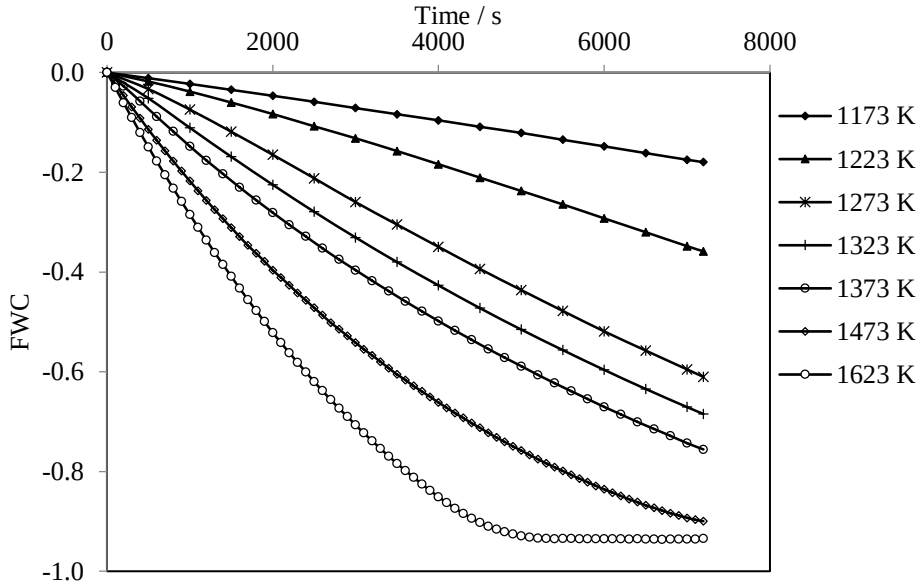

Figure 4.5: The FWC vs time plots of C3A doped coke analogue reaction with CO_2 (4.5 L/min) over the temperature range of 1173 K- 1623K.

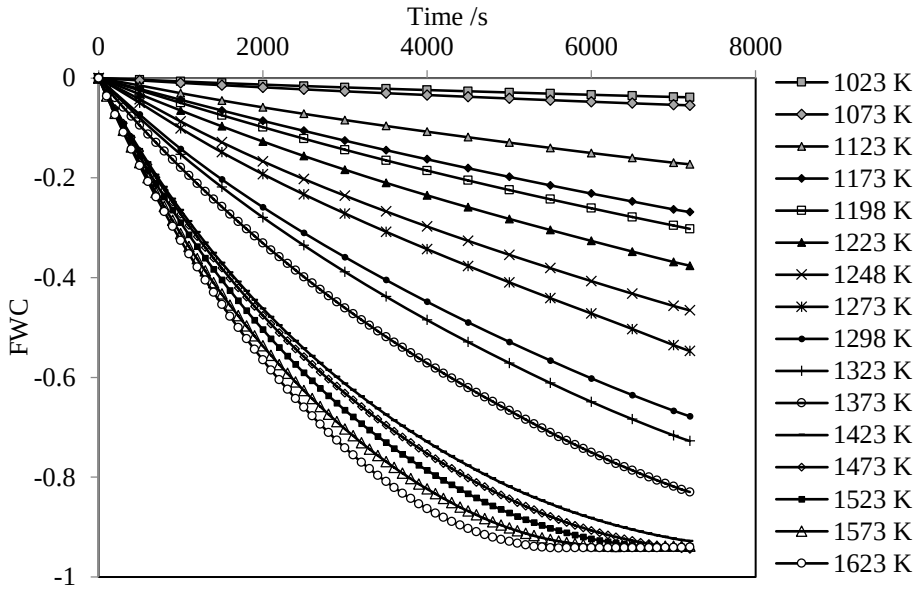

Figure 4.6: The FWC vs time plots of lime doped coke analogue reaction with CO_2 (4.5 L/min) over the temperature range of 1023 K- 1623K.

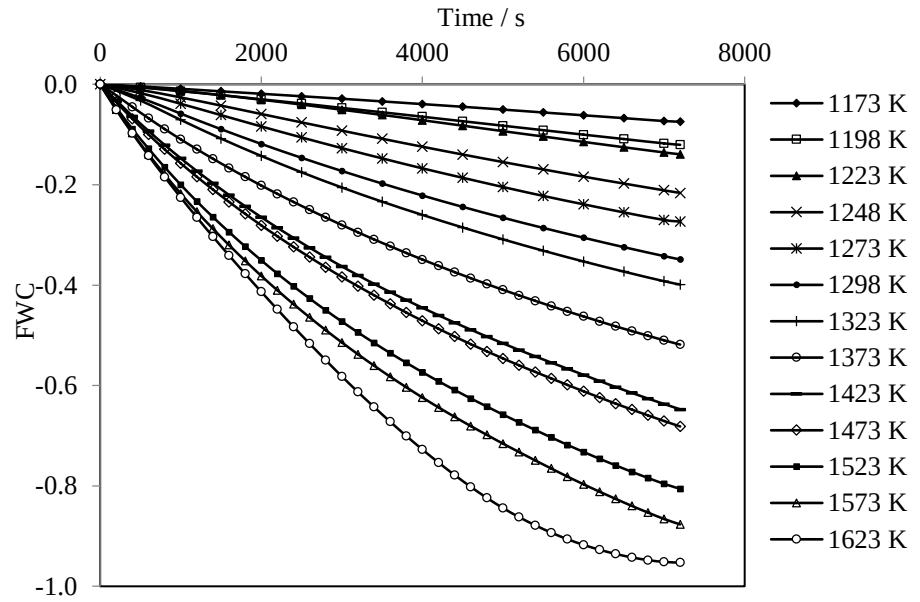

Figure 4.7: The FWC vs time plots of CAS 1 doped coke analogue reaction with CO_2 (4.5 L/min) over the temperature range of 1173 K- 1623K.

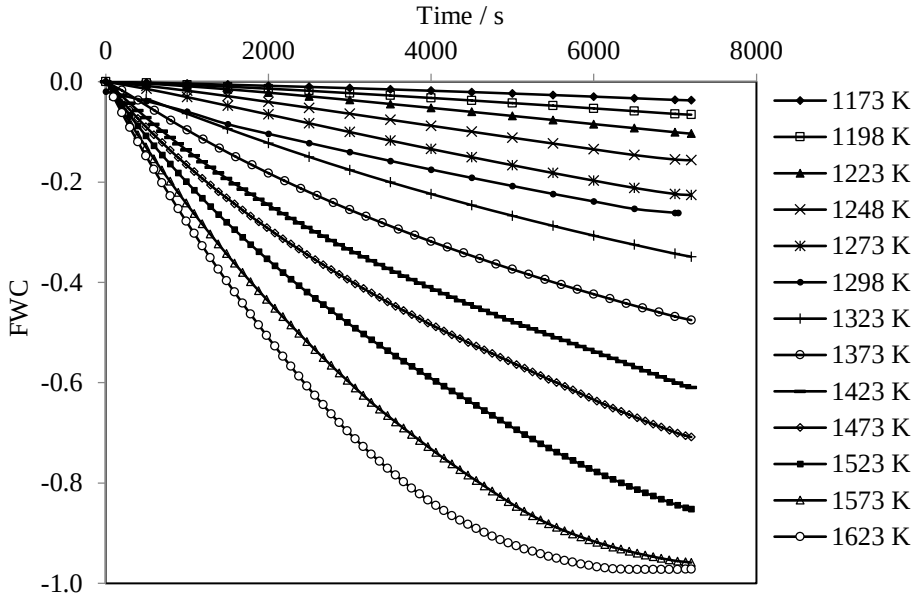

Figure 4.8: The FWC vs time plots of CAS 2 doped coke analogue reaction with CO_2 (4.5 L/min) over the temperature range of 1173 K- 1623K.

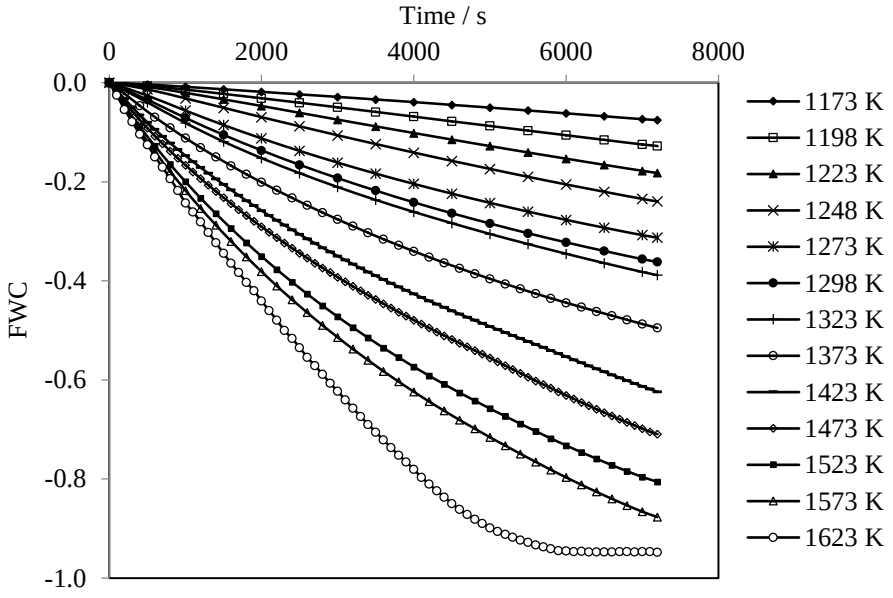

Figure 4.9: The FWC vs time plots of quartz doped coke analogue reaction with CO_2 (4.5 L/min) over the temperature range of 1173 K- 1623K.

Figure 4.10 is the FWC vs time plot for a metallurgical coke. It can be seen the metallurgical coke has the similar relationship as the coke analogues *i.e*. increasing the negativity of FWC with increasing temperature. The reactivity of the selected metallurgical coke in this study is lower than the coke analogues.

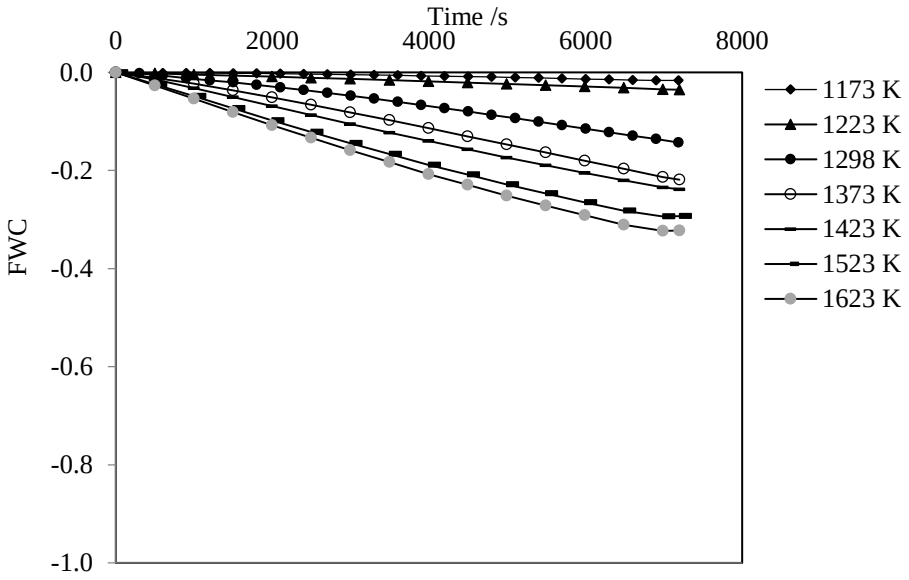

Figure 4.10: The FWC vs time plots of a metallurgical coke reaction with CO_2 (4.5 L/min) over the temperature range of 1173 K- 1623K.

Base coke analogue reactivity until complete carbon conversion at 1248 and 1273 K

Two temperatures (1248 K and 1273 K) were selected from the lower temperature region of the examined temperature range in this study to explore the reactivity and the sample behaviour up to the 0.4 carbon conversion (X = 0.4). These results are used to calculate the structural parameter to study the effect of surface area on the reactivity by using the RPM (*Equations 2.23 and 2.24).* At lower temperatures, it took very long time to reach X = 0.4 (> 4 hours). Given in *Figure 4.11* is the FWC vs time plot for 1248 and 1273 K until X = 0.4 carbon conversion.

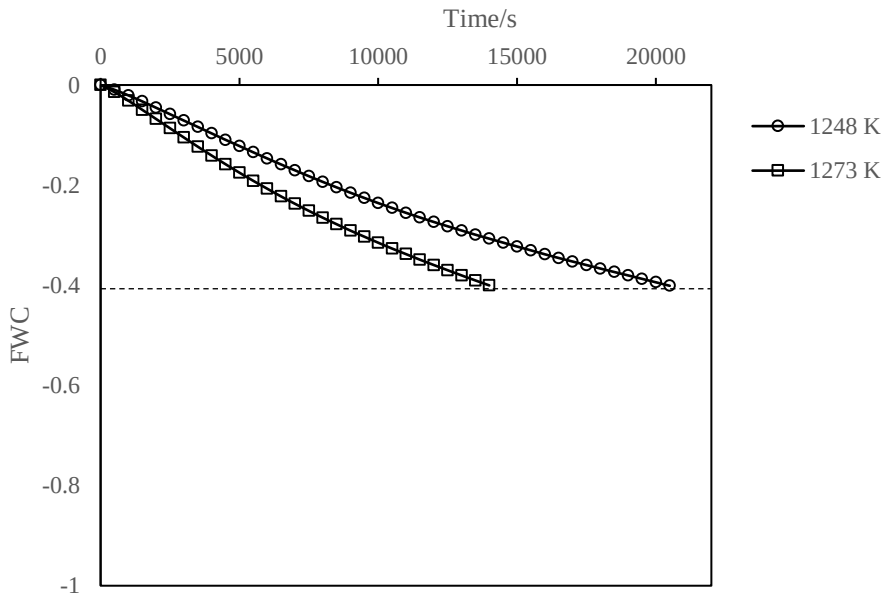

Figure 4.11: The FWC vs time plots of base coke analogue until complete carbon conversion at 1248 and 1273 K.

4.2.Characterisation of coke analogue and metallurgical coke

The coke analogues were characterised with respect to pre and post-gasification reaction.

4.2.1. Optical porosity

The porosity and pore size distribution of all the coke analogues and metallurgical coke were measured.

The porosity and pore size distribution were maintained in a narrow range for all the mineral doped coke analogues to minimise the effect of porosity for the coke analogue

reactivity. The optical porosity values and pore size distribution for each coke analogue samples are given in *Table 4.1* and *Figure 4.12*. The total porosity (P_T) is defined by *Equation 3.7*. The porosity values for P1 and Pa of all coke analogue at each size range are given in Appendix VI.

$$P_T = 0.063\, P_1 + 0.937\, P_a$$

Table 4.1: Total optical porosity values of coke analogue samples

Coke analogue	P_T / %
Base coke analogue	29.8
Alumina doped coke analogue	29.3
CA6 doped coke analogue	30.0
CA doped coke analogue	30.3
C3A doped coke analogue	31.0
Lime doped coke analogue	33.3
CAS doped coke analogue	30.3*
Quartz doped coke analogue	28.9

** Average of two CAS containing coke analogues*

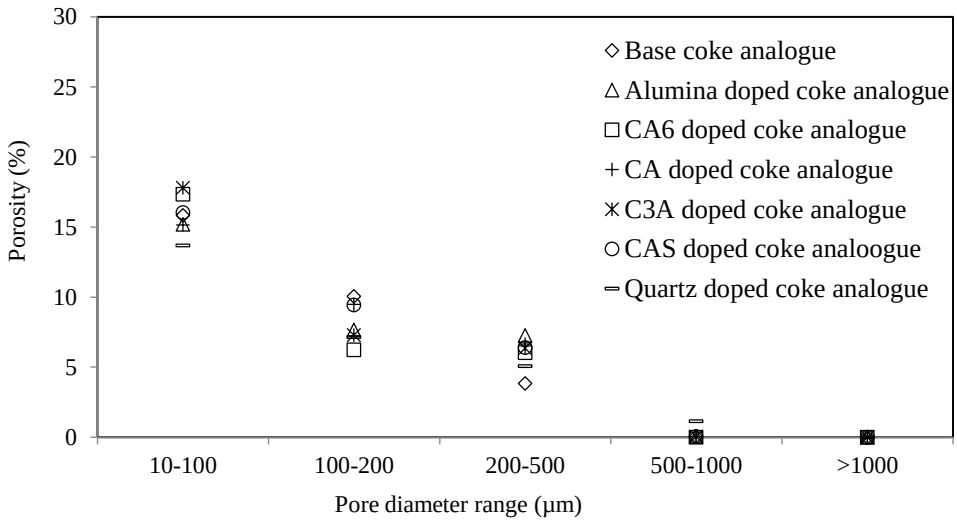

Figure 4.12: Pore size distribution of each coke analogue sample (Note: Average porosity values of P1 and Pa are presented)

The optical porosity values of three samples from the metallurgical coke were measured as 24.7%, 30.9% and 37.5%. The pore size distribution of the three metallurgical coke samples is given in *Figure 4.13*.

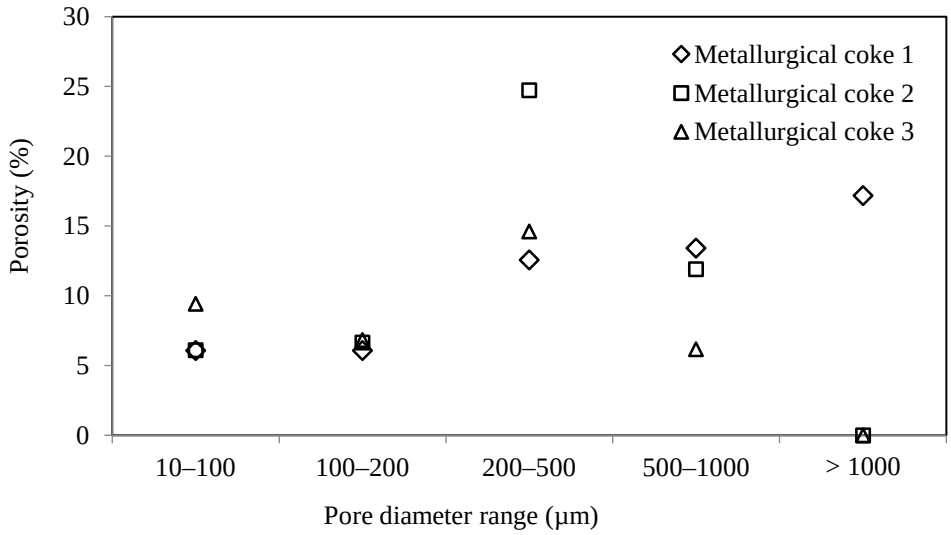

Figure 4.13: Pore size distribution of a metallurgical coke measured using the optical microscopy used for the coke analogue.

4.2.2. Polarised optical microscopy

Polarised optical microscopy of the fired base coke analogue

Polarised optical microscopy observations were carried out for base coke analogue for the elucidation of the characteristic features that are not observable in non-polarised optical microscopy. Given in *Figure 4.14* are the plane polarised and crossed polarised optical micrographs of the base coke analogue. The micrographs show the coke analogue components *i.e*. graphite grains and carbonised phenolic resins. Under both plane and cross polarised lights polarised light, the graphite grains were sensitive to reflection *i.e.* anisotropic. The areas assumed as carbonised phenolic resin are not sensitive to polarised lights *i.e.* isotropic.

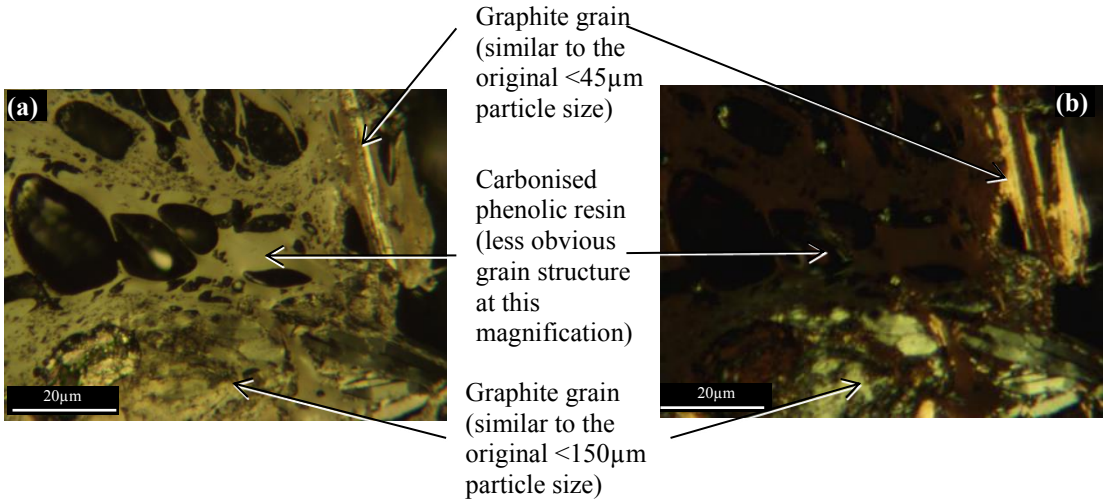

Figure 4.14: The polarised optical micrographs of the fired base coke analogue. (a) Plane polarised and (b) crossed polarised.

4.2.3. Post gasification reaction appearance

The post gasification reaction appearance of the coke analogues was noted and are given in *Table 4.2*. The deformation of the samples increases with increasing temperature. This observation is valid with all the coke analogues. The deformation trend of alumina doped and quartz doped coke analogues is similar to the base coke analogue. Deformation of lime doped coke analogue starts at a lower temperature compared to the other coke analogues. Other Ca containing minerals doped coke analogues have increasing deformation with temperature with increasing Ca content.

Table 4.2: Post gasification reaction appearance of coke analogue samples for the temperature range of 1173 – 1623 K (all experiments are for 2 hours unless stated otherwise, Shadowed areas represents no experiments)

Coke analogue	Temperature /K																			
	1023	1073	1123	1173	1198	1223	1248	1248 X= 0.3	1248 X= 0.5	1273	1273 X= 0.3	1273 X= 0.5	1298	1323	1373	1423	1473	1523	1573	1623
Base coke analogue				+	+	+	+	+	Δ	+	+	Δ	○	□	□	□	x	x	—	—
Alumina doped coke analogue				+	+	+	+			+			○	□	□	□	x	x	#	#
CA6 doped coke analogue				+		+				○			○		x	x	x			#
CA doped coke analogue				+	+	+	+			○			○	x	x	x	x	#	#	#
C3A doped coke analogue				+		○				○				x	x		#			#
Lime doped coke analogue	+	+	+	+	○	○	x			x			x	x	x	x	#	#	#	#
CAS doped coke analogue				+	+	+	+			○			○	○	x	x	x	x	#	#
Quartz doped coke analogue				+	+	+	+			+			○	□	□	□	x	x	#	#

+ Maintained the original cylindrical shape

○ Maintained the original cylindrical shape with powdery surface

□ Maintained the original cylindrical shape but slightly deformed

x Deformed cylindrical shape, powdered

Δ Maintained the original cylindrical shape, easily broken when handled, no strong core left

— No solid remained

Small amount of powder remained

4.2.4. SEM/EDS characterisation

In this section, SEM/EDS analyses carried out for the coke analogue samples and metallurgical coke before the reaction and after the reaction at 1273 K are presented.

SEM backscattered images at X100 magnification were obtained for the coke analogue samples before the gasification reaction in CO_2 to characterise the distribution of mineral particles in the coke analogues. Images at X500 and X1000 magnifications are used to observe the coke analogue components and mineral particles. Two images were taken from the same location and optimised by changing contrast/brightness conditions to get clear views of the carbon structures and mineral particles respectively. The centre and the annulus of the samples were analysed separately to identify any changes in the carbon microstructure* and minerals depending on the position. The SEM backscattered images/maps for the centre of the samples are given in this section along with the EDS point analysis where < 1 mass % is indicated as "trace". SEM backscattered images from the annulus and EDS point analysis are presented in Appendix VII.

For all minerals other than lime, mineral particles of similar size to the original addition (+38 – 53 µm) were observed to be evenly distributed through the fired coke analogue. Lime particles (see *Figures 4.35* to *4.38*) were much smaller than the original addition and distributed throughout the carbon microstructure.

Similar to the coke analogue samples before the reaction, coke analogue samples after the gasification with CO_2 at 1273 K for 2 hours were characterised. SEM backscattered images were obtained at X100, X500 and X1000. Samples at > 1273 K were not analysed by SEM due to their poor physical integrity after the reaction. The focus was to identify any changes to the mineral distribution, coke analogue carbon microstructure and mineral particles due to the reaction.

* In the metallurgical coke literature researchers often use the terms microtexture and microstructure when dealing with coke characterisation. In this thesis, it is the term microstructure that is being used for coke structure observed under microscopy.

4.2.4.1.Base coke analogue

Before the gasification reaction

SEM backscattered image in *Figure 4.15* shows a representative area from the centre of a cross-section of the base coke analogue at X500 magnification. Three main components were identified as pores, graphitic carbon and carbon from phenolic resins.

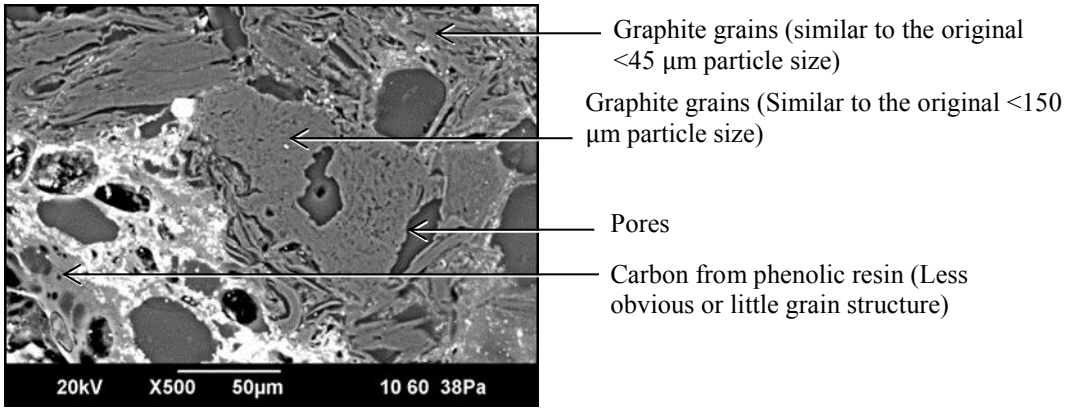

Figure 4.15: An SEM backscattered image of a representative area of the base coke analogue before the gasification reaction at X500 magnification.

The carbonaceous component is made up of two distinct forms of carbon: graphite and amorphous carbon from phenolic resins. The graphitic carbon is observed as grains with two different particle sizes. The amorphous phase derived from phenolic resin acts as a carbon matrix. The carbon matrix contains Al-Si-Ca phases as impurities. The presence of these elements represents a baseline impurity in the samples of (~1.1 mass %) in total (See Appendix III for impurity analysis). The carbonaceous component observed from SEM is similar in all the coke analogues studied in this thesis.

The SEM backscattered images and EDS maps (*Figures 4.16*) show the even distribution of these components throughout the coke analogue.

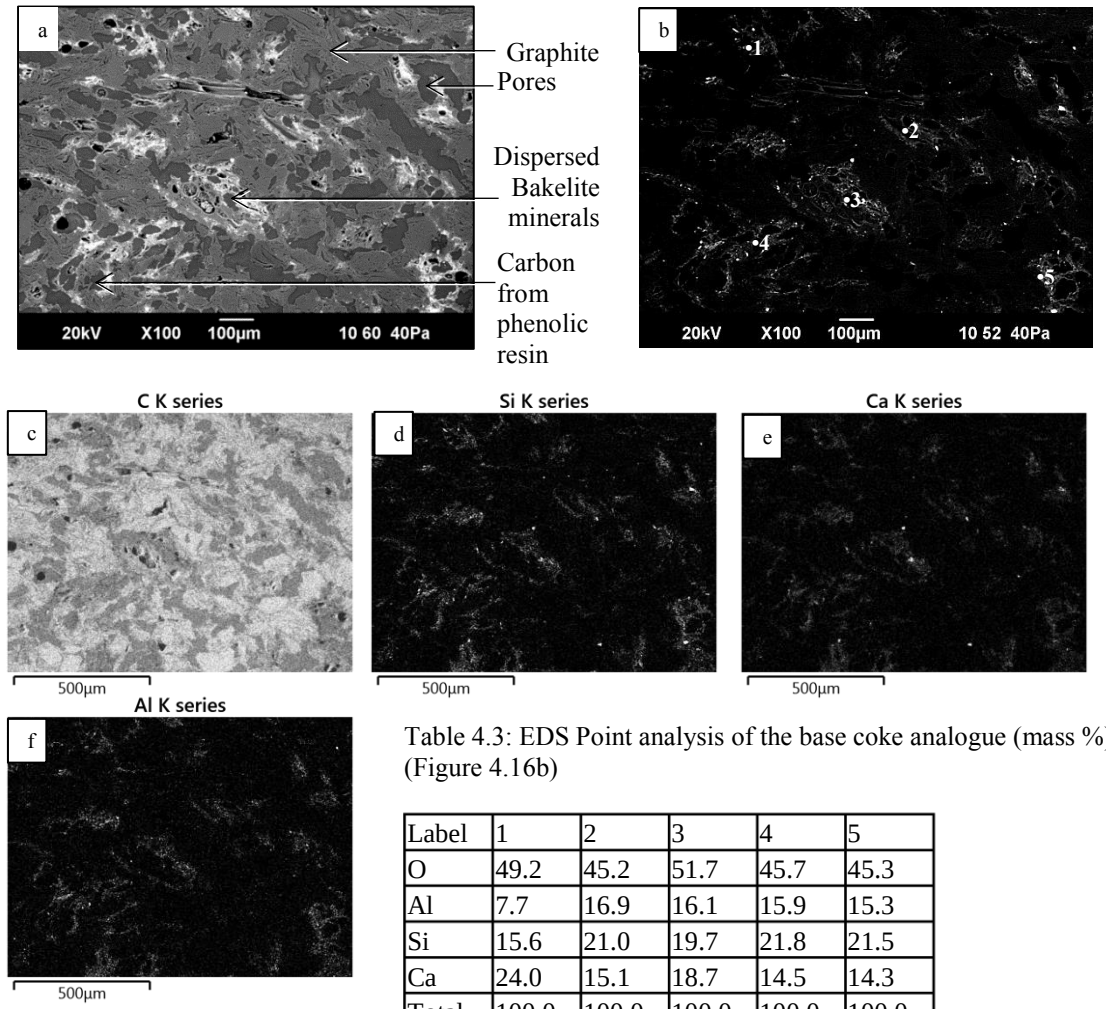

Table 4.3: EDS Point analysis of the base coke analogue (mass %) (Figure 4.16b)

Label	1	2	3	4	5
O	49.2	45.2	51.7	45.7	45.3
Al	7.7	16.9	16.1	15.9	15.3
Si	15.6	21.0	19.7	21.8	21.5
Ca	24.0	15.1	18.7	14.5	14.3
Total	100.0	100.0	100.0	100.0	100.0

Figure 4.16: SEM backscattered images and EDS maps of the base coke analogue before the gasification reaction at X100 magnification. (a) SEM backscattered image optimised for carbon microstructure (b) SEM backscattered image optimised for mineral component (c - f) EDS maps.

After the gasification reaction

The three main components, pores, graphitic carbon and carbon from phenolic resin were identified in the coke analogue after the gasification reaction with CO_2 at 1273 K for 2 hours.

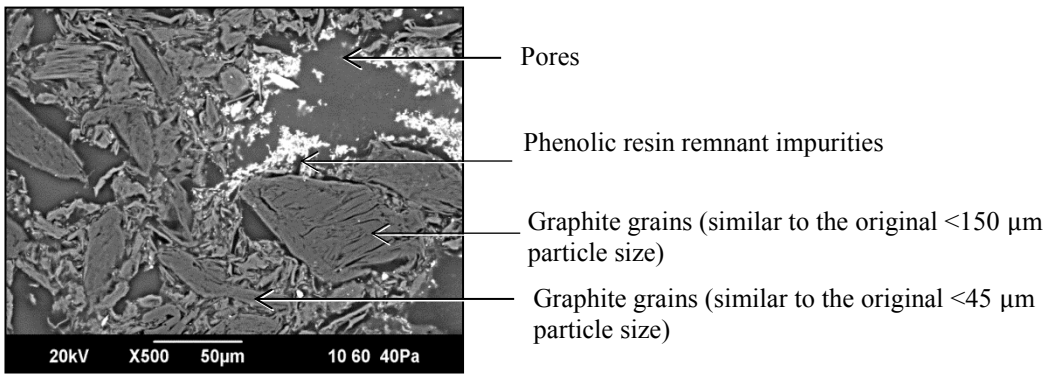

Figure 4.17: An SEM backscattered image of a representative area of the base coke analogue after the gasification reaction at 1273 K for 2 hours at X500 magnification.

The SEM backscattered images and EDS maps (*Figures 4.18*) show the even distribution of these components throughout the coke analogue.

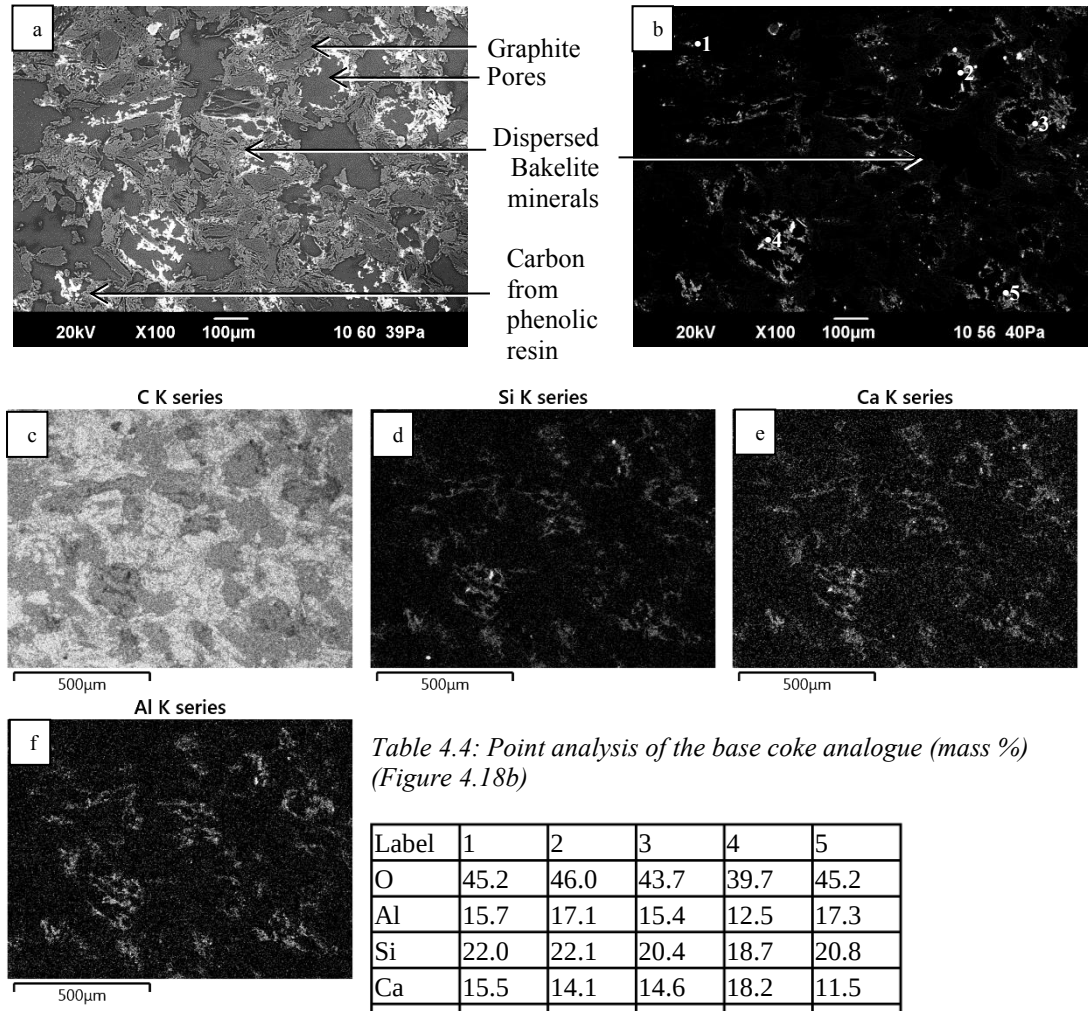

Table 4.4: Point analysis of the base coke analogue (mass %) (Figure 4.18b)

Label	1	2	3	4	5
O	45.2	46.0	43.7	39.7	45.2
Al	15.7	17.1	15.4	12.5	17.3
Si	22.0	22.1	20.4	18.7	20.8
Ca	15.5	14.1	14.6	18.2	11.5
Total	100.0	100.0	100.0	100.0	100.0

Figure 4.18: SEM backscattered images and EDS maps of the base coke analogue after the gasification reaction at 1273 K at X100 magnification. (a) SEM backscattered image optimised for carbon microstructure (b) SEM backscattered image optimised for mineral component (c – f) EDS maps.

4.2.4.2.Minerals doped coke analogues

Table 4.5 summarises the mineral distribution and mineral particle size in the coke analogues before and after the gasification reaction. Summarised results of the metallurgical coke are also included for comparison. The SEM backscattered images at X100, X500 and X1000 for all the coke analogues are presented from *Figure 4.19* to *4.50* and metallurgical coke from *Figure 4.51* to *4.54* along with the EDS maps and EDS point analysis. The mineral particles show even distribution and similar size to the original addition except for lime doped coke analogue.

Table 4.5: Summary of the SEM/EDS analysis of minerals doped coke analogues.

Added mineral to the coke analogue		Figure number	Mineral distribution	Mineral particle size	Comments
Alumina	Pre-reaction	4.19, 4.20	Even	38 – 53 µm	Alumina particles were not dense as they were prepared by sintering <10 µm alumina particles. It was observed these particles have a similar appearance and size in the coke analogue to that before addition to the coke analogue (see section 4.4 for an image of alumina particles before adding to the coke analogue).
	Post-reaction	4.21, 4.22	Even	38 – 53 µm	
CA6	Pre-reaction	4.23, 4.24	Even	38 – 53 µm	Mineral particles are angular and similar size to the original addition for both before and after the gasification reaction
	Post-reaction	4.25, 4.26	Even	38 – 53 µm	
CA	Pre-reaction	4.27, 4.28	Even	38 – 53 µm	Mineral particles are angular and similar size to the original addition for both before and after the gasification reaction
	Post-reaction	4.29, 4.30	Even	38 – 53 µm	
CA3	Pre-reaction	4.31, 4.32	Even	38 – 53 µm	Mineral particles are angular and similar size to the original addition for both before and after the gasification reaction
	Post-reaction	4.33, 4.34	Even	38 – 53 µm	
Lime	Pre-reaction	4.35, 4.36	Even	< 38 µm	Though dispersed throughout the analogue, the lime particles are significantly smaller than the original size addition of 38 – 53 µm.
	Post-reaction	4.37, 4.38	Even	< 38 µm	
CAS 1	Pre-reaction	4.39, 4.40	Even	38 – 53 µm	Mineral particles are angular and similar size to the original addition for both before and after the gasification reaction
	Post-reaction	4.41, 4.42	Even	38 – 53 µm	
CAS 2	Pre-reaction	4.43, 4.44	Even	38 – 53 µm	
	Post-reaction	4.45, 4.46	Even	38 – 53 µm	
Quartz doped coke analogue	Pre-reaction	4.47, 4.48	Even	38 – 53 µm	Mineral particles are angular and similar size to the original addition for both before and after the gasification reaction
	Post-reaction	4.49, 4.50	Even	38 – 53 µm	
Metallurgical coke	Pre-reaction	4.51,4.52	Uneven	NA	The mineral and carbon structure has high variability in size and distribution
	Post-reaction	4.53, 4.54	Uneven	NA	

Alumina doped coke analogue

Before the gasification reaction

Figure 4.19 shows a representative area of a cross-section of alumina doped coke analogue before the gasification reaction.

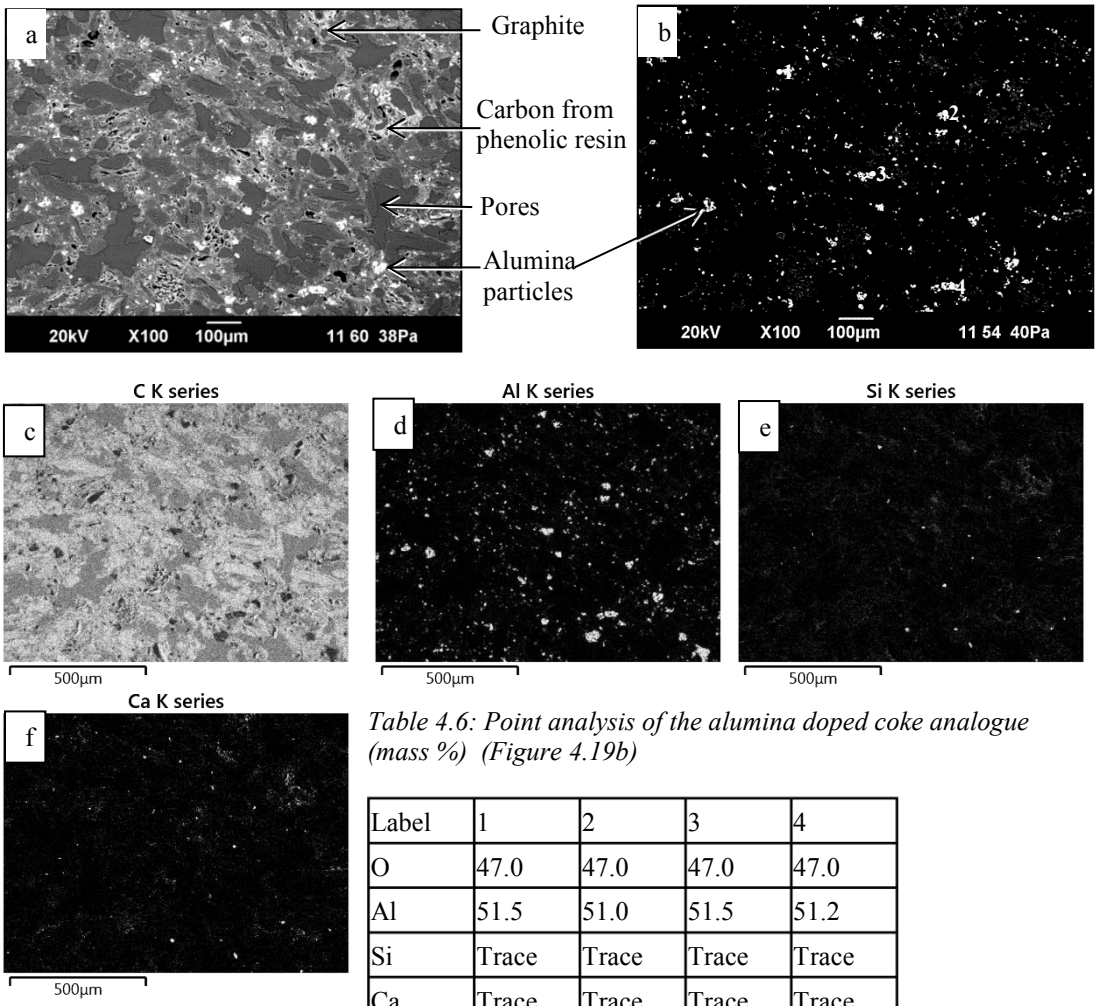

Table 4.6: Point analysis of the alumina doped coke analogue (mass %) (Figure 4.19b)

Label	1	2	3	4
O	47.0	47.0	47.0	47.0
Al	51.5	51.0	51.5	51.2
Si	Trace	Trace	Trace	Trace
Ca	Trace	Trace	Trace	Trace
Fe				
Total	100.0	100.0	100.0	100.0

Figure 4.19: SEM backscattered images and EDS maps of the alumina doped coke analogue before the gasification reaction at X100 magnification. (a) SEM backscattered image optimised for carbon microstructure (b) SEM backscattered image optimised for mineral component (c – f) EDS maps.

Figure 4.20 shows the SEM backscattered image of a selected area from *Figure 4.19 a* at X500 and X1000 magnifications for better views of the carbon structure around the mineral particle and the mineral particle.

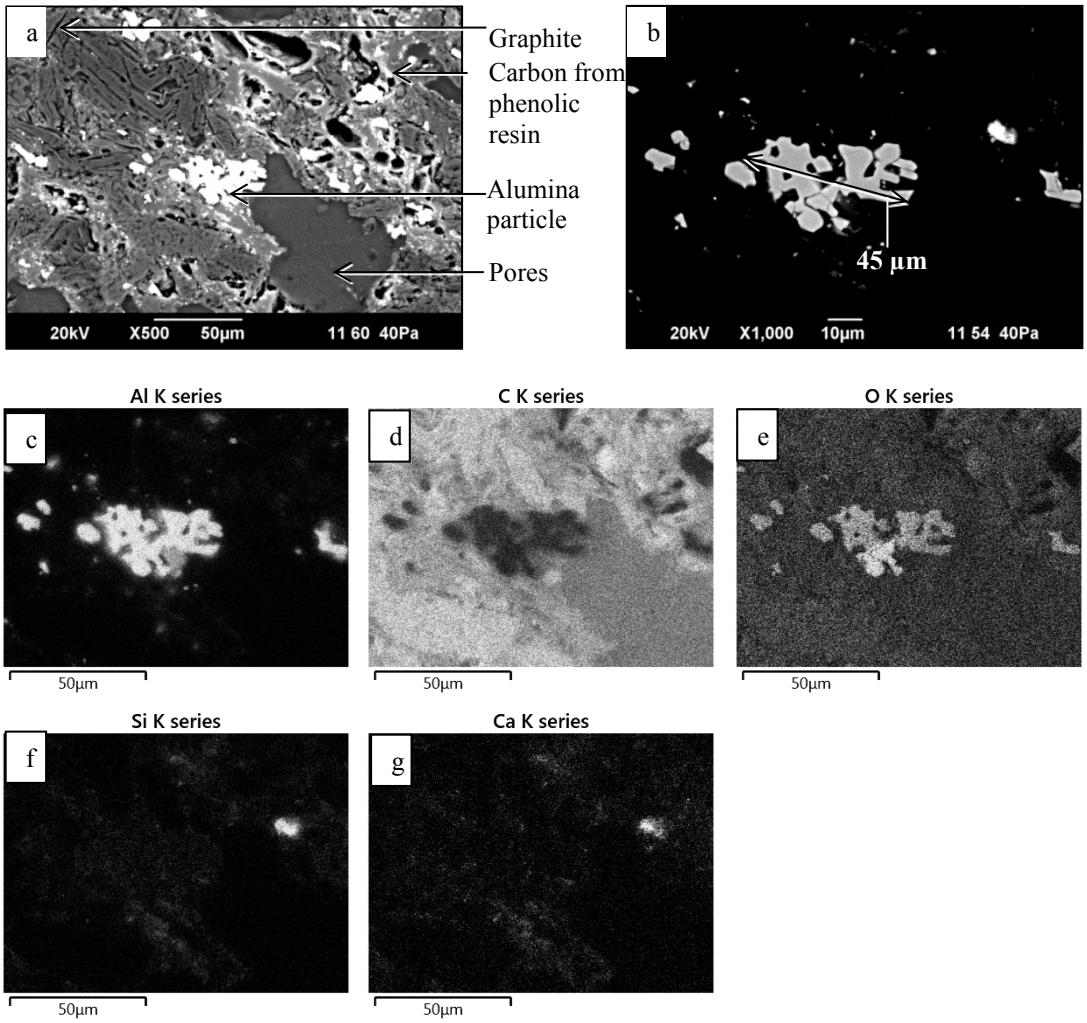

Figure 4.20: SEM backscattered images and EDS maps of the alumina doped coke analogue before the gasification reaction. (a) SEM backscattered image optimised for carbon microstructure at X500 magnification (b) SEM backscattered image optimised for the mineral component at X1000 (c – g) EDS maps.

After the gasification reaction

The same set of images was taken for the alumina doped coke analogue after reaction at 1273 K for 2 hours.

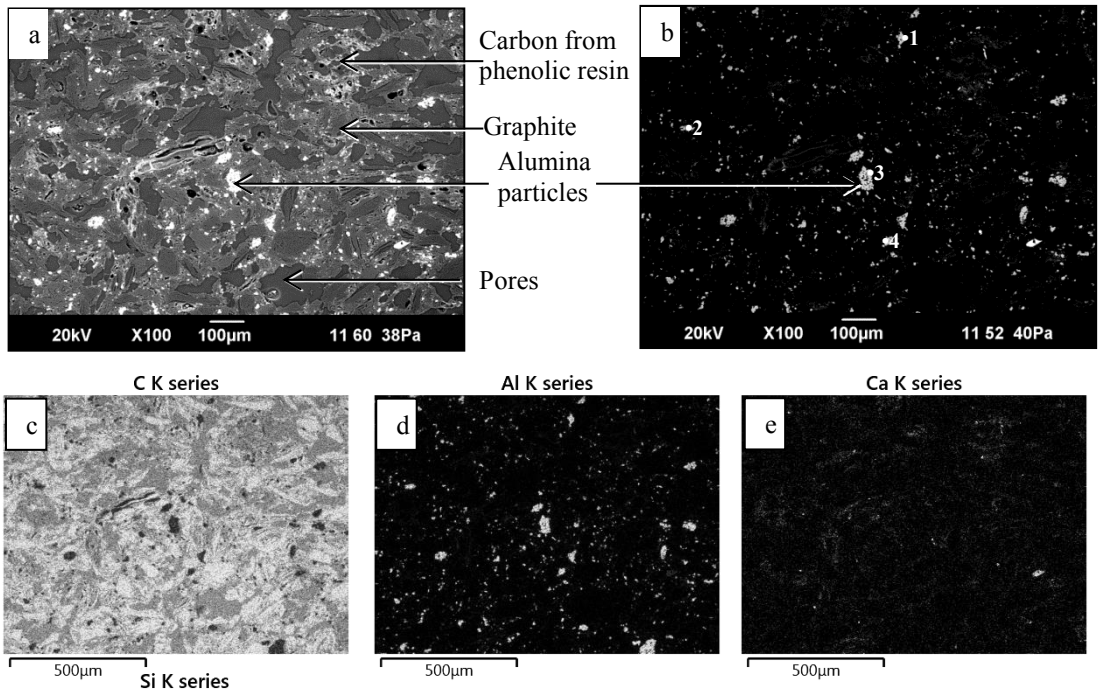

Table 4.7: Point analysis of the alumina doped coke analogue (mass %) (Figure 4.21b)

Label	1	2	3	4
O	47.4	47.2	47.4	47.4
Al	50.4	50.4	50.2	50.5
Si	Trace	Trace	Trace	Trace
Ca		Trace		
Fe				
Total	100.0	100.0	100.0	100.0

Figure 4.21: SEM backscattered images and EDS maps of the alumina doped coke analogue after the gasification reaction at 1273 K at X100 magnification. (a) SEM backscattered image optimised for carbon microstructure (b) SEM backscattered image optimised for mineral component (c – f) EDS maps.

The carbon structure and an alumina particle are presented from SEM backscattered images in *Figures 4.22* along with the EDS maps.

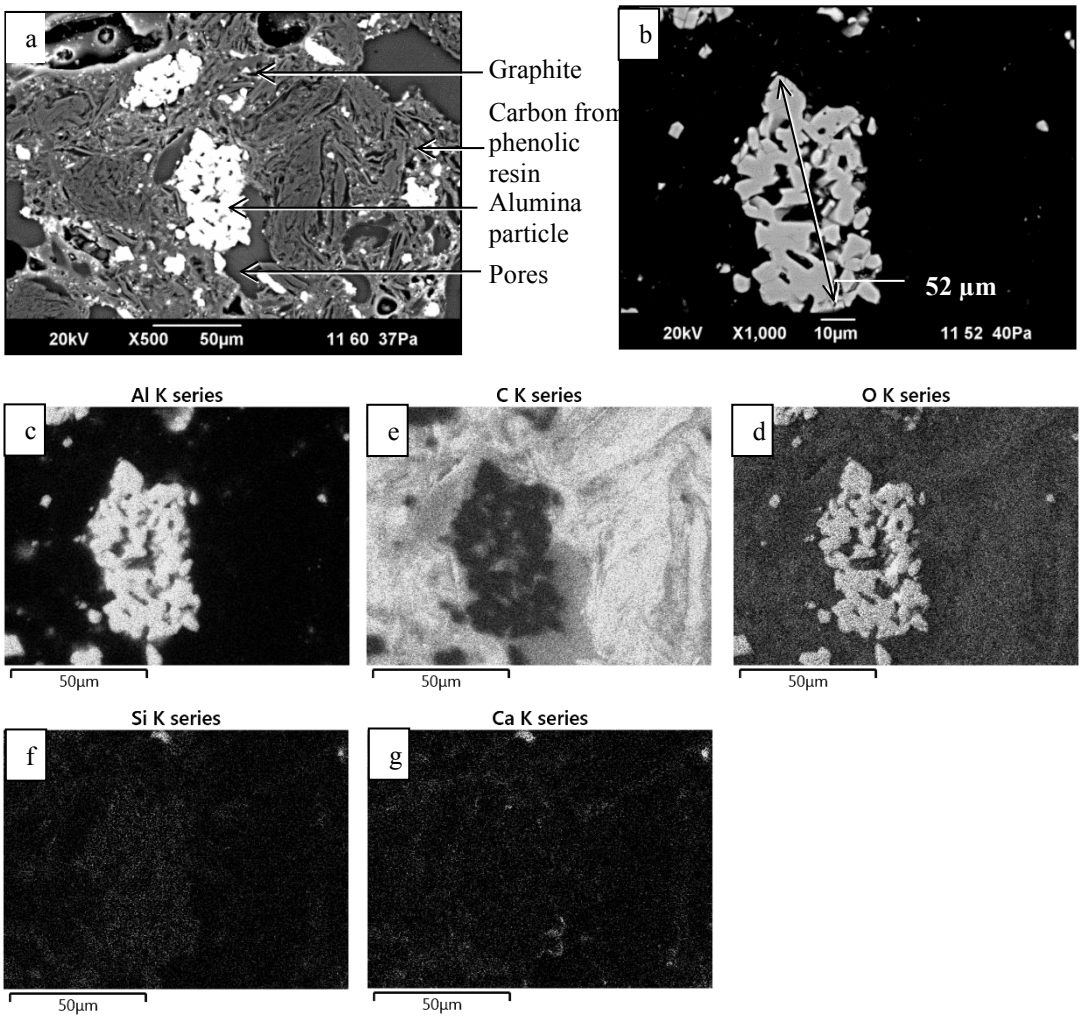

Figure 4.22: SEM backscattered images and EDS maps of the alumina doped coke analogue after the gasification reaction at 1273 K. (a) SEM backscattered image optimised for carbon microstructure at X500 magnification (b) SEM backscattered image optimised for the mineral component at X1000 (c – g) EDS maps.

CA6 doped coke analogue

Before the gasification reaction

Figure 4.23 shows a representative area of a cross-section of CA6 doped coke analogue before the gasification reaction.

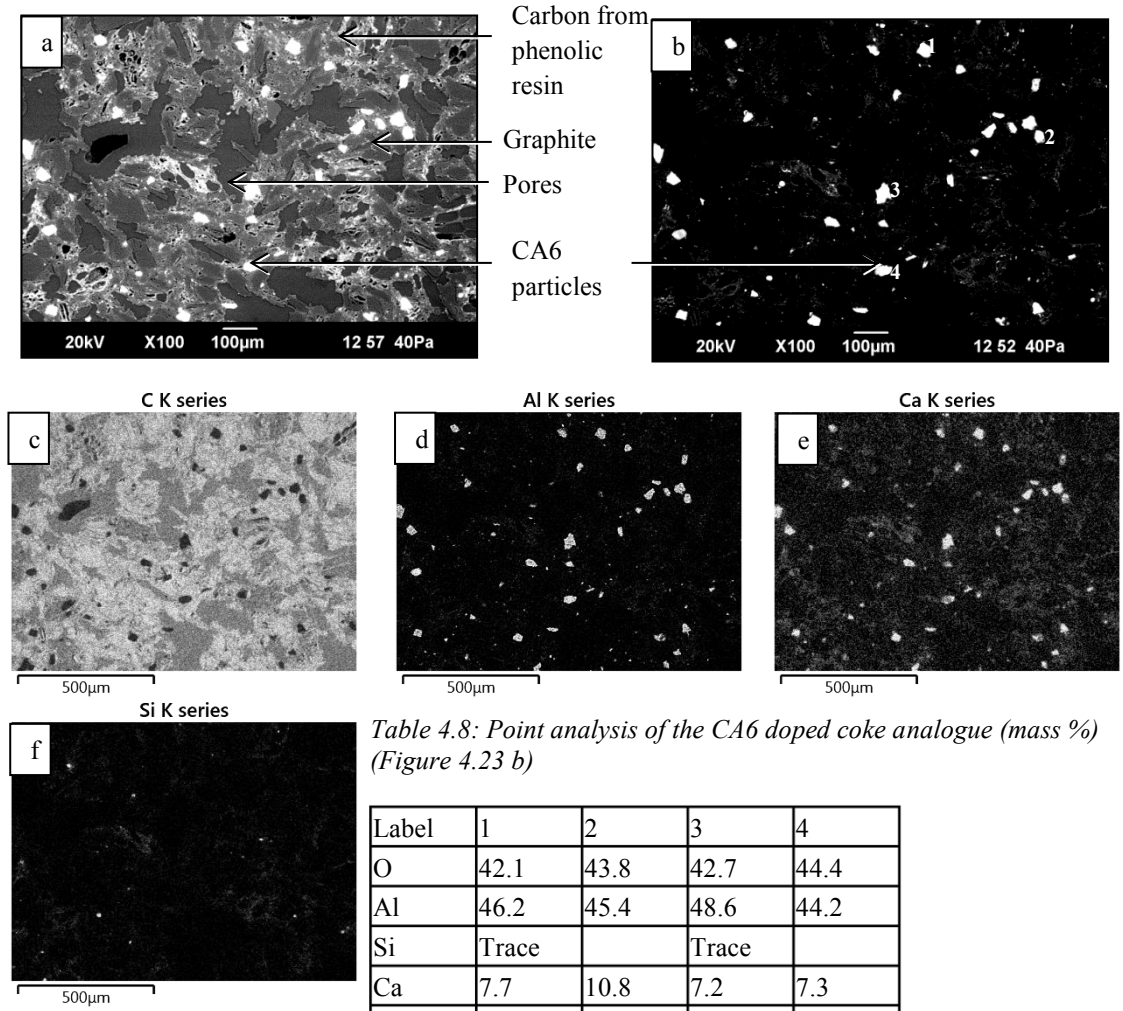

Table 4.8: Point analysis of the CA6 doped coke analogue (mass %) (Figure 4.23 b)

Label	1	2	3	4
O	42.1	43.8	42.7	44.4
Al	46.2	45.4	48.6	44.2
Si	Trace		Trace	
Ca	7.7	10.8	7.2	7.3
Fe				
Total	100.0	100.0	100.0	100.0

Figure 4.23: SEM backscattered images and EDS maps of the CA6 doped coke analogue before the gasification reaction at X100 magnification. (a) SEM backscattered image optimised for carbon microstructure (b) SEM backscattered image optimised for mineral component (c – f) EDS maps.

Figure 4.24 shows the SEM backscattered image and EDS maps of CA6 doped coke analogue at X500 and X1000 magnifications to show clear views of the carbon structure around the mineral particle and the CA6 particle.

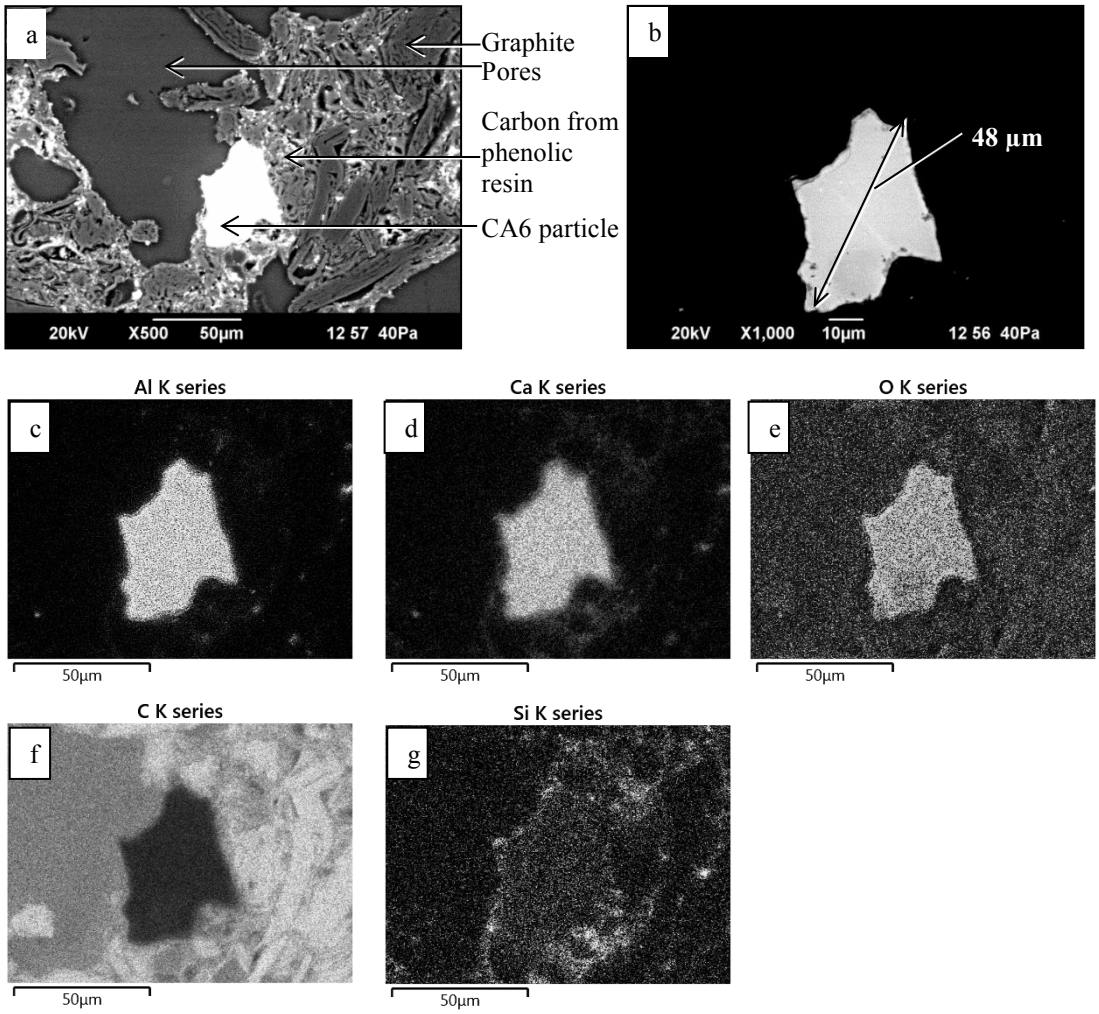

Figure 4.24: SEM backscattered images and EDS maps of the CA6 doped coke analogue before the gasification reaction. (a) SEM backscattered image optimised for carbon microstructure at X500 magnification (b) SEM backscattered image optimised for the mineral component at X1000 (c – g) EDS maps.

After the gasification reaction

Figure 4.25 shows SEM backscattered images and EDS maps of a representative area of a cross-section of CA6 doped coke analogue after the gasification reaction at 1273 K for 2 hours.

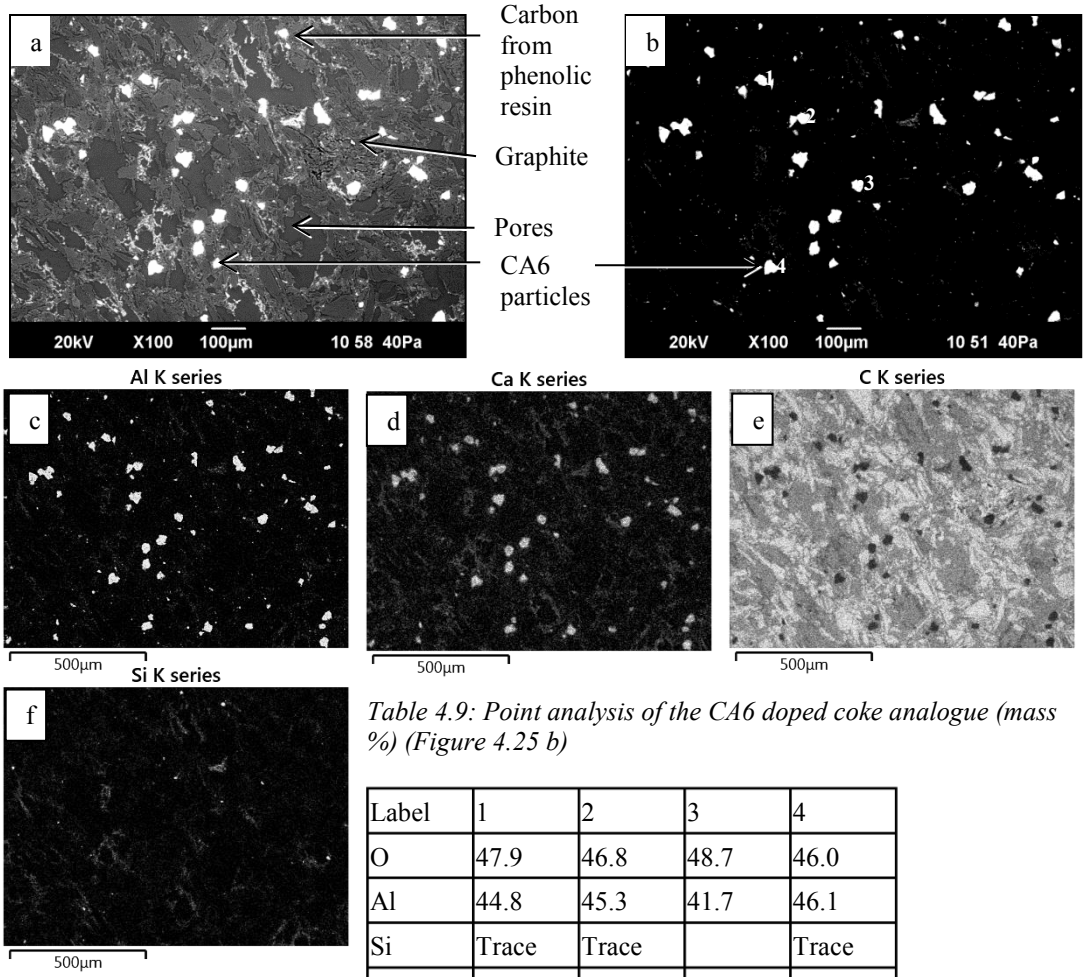

Table 4.9: Point analysis of the CA6 doped coke analogue (mass %) (Figure 4.25 b)

Label	1	2	3	4
O	47.9	46.8	48.7	46.0
Al	44.8	45.3	41.7	46.1
Si	Trace	Trace		Trace
Ca	5.2	7.0	8.9	6.9
Fe				
Total	100.0	100.0	100.0	100.0

Figure 4.25: SEM backscattered images and EDS maps of the CA6 doped coke analogue after the gasification reaction at 1273 K at X100 magnification. (a) SEM backscattered image optimised for carbon microstructure (b) SEM backscattered image optimised for mineral component (c – f) EDS maps.

The carbon structure and a CA6 particle are clearly presented from SEM backscattered images and EDS maps in *Figure 4.26.*

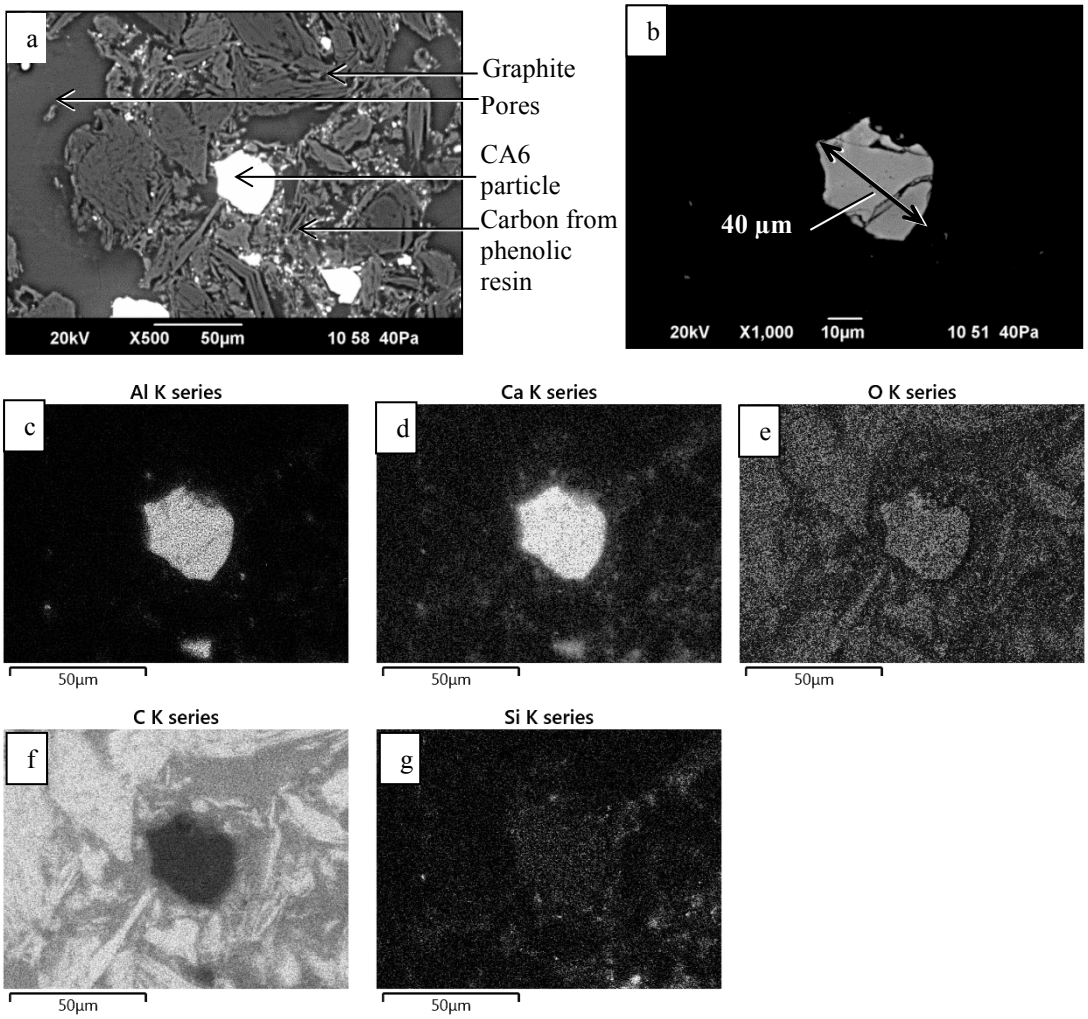

Figure 4.26: SEM backscattered images and EDS maps of the CA6 doped coke analogue after the gasification reaction at 1273 K. (a) SEM backscattered image optimised for carbon microstructure at X500 magnification (b) SEM backscattered image optimised for the mineral component at X1000 (c – g) EDS maps.

CA doped coke analogue

Before the gasification reaction

Figure 4.27 shows SEM backscattered images and EDS maps of a representative area of a cross-section of CA doped coke analogue before the gasification reaction.

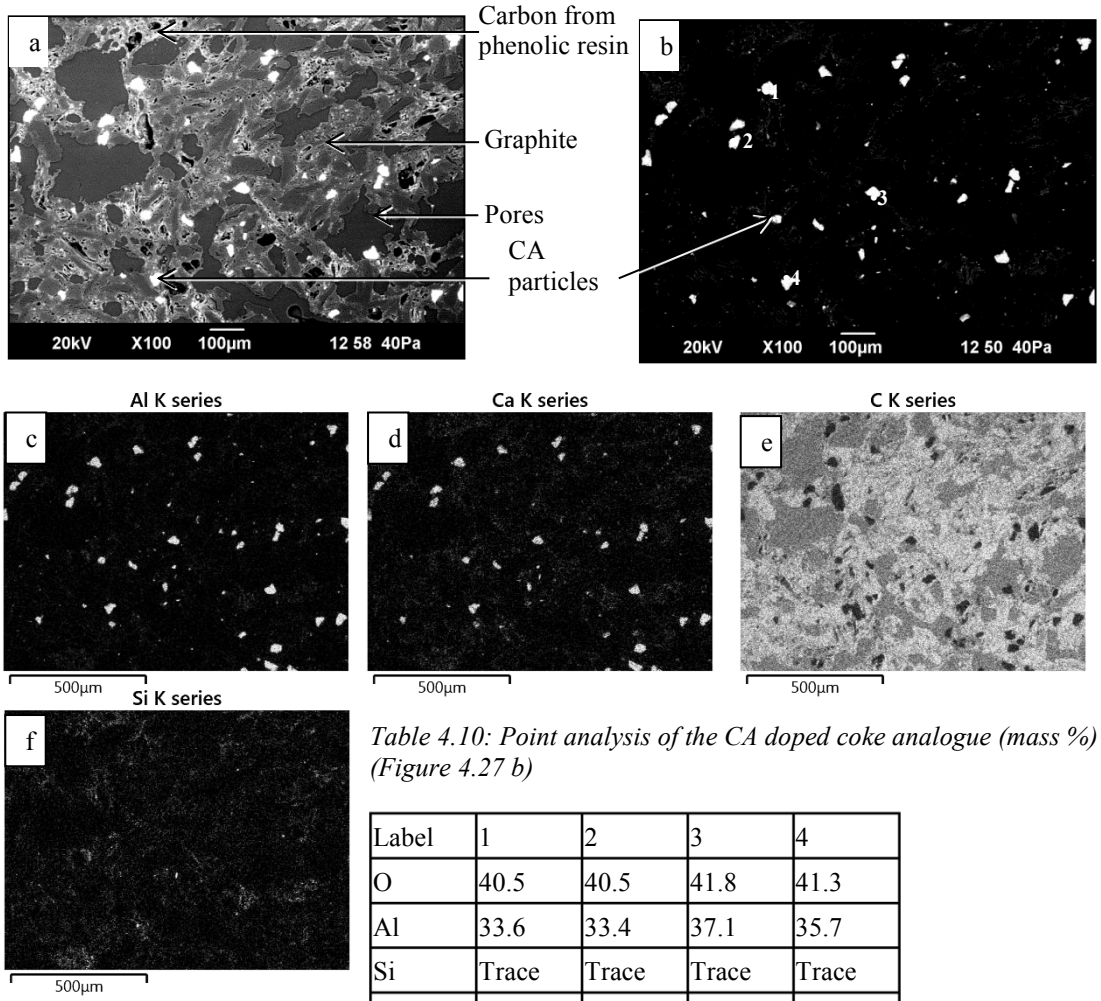

Table 4.10: Point analysis of the CA doped coke analogue (mass %) (Figure 4.27 b)

Label	1	2	3	4
O	40.5	40.5	41.8	41.3
Al	33.6	33.4	37.1	35.7
Si	Trace	Trace	Trace	Trace
Ca	25.4	25.2	20.4	22.3
Fe				
Total	100.0	100.0	100.0	100.0

Figure 4.27: SEM backscattered images and EDS maps of the CA doped coke analogue before the gasification reaction at X100 magnification. (a) SEM backscattered image optimised for carbon microstructure (b) SEM backscattered image optimised for mineral component (c – f) EDS maps.

Figure 4.28 shows the SEM backscattered images and EDS maps of a selected area of CA doped coke analogue at X500 and X1000 magnifications for better views of the carbon structure around the mineral particle and the mineral particle.

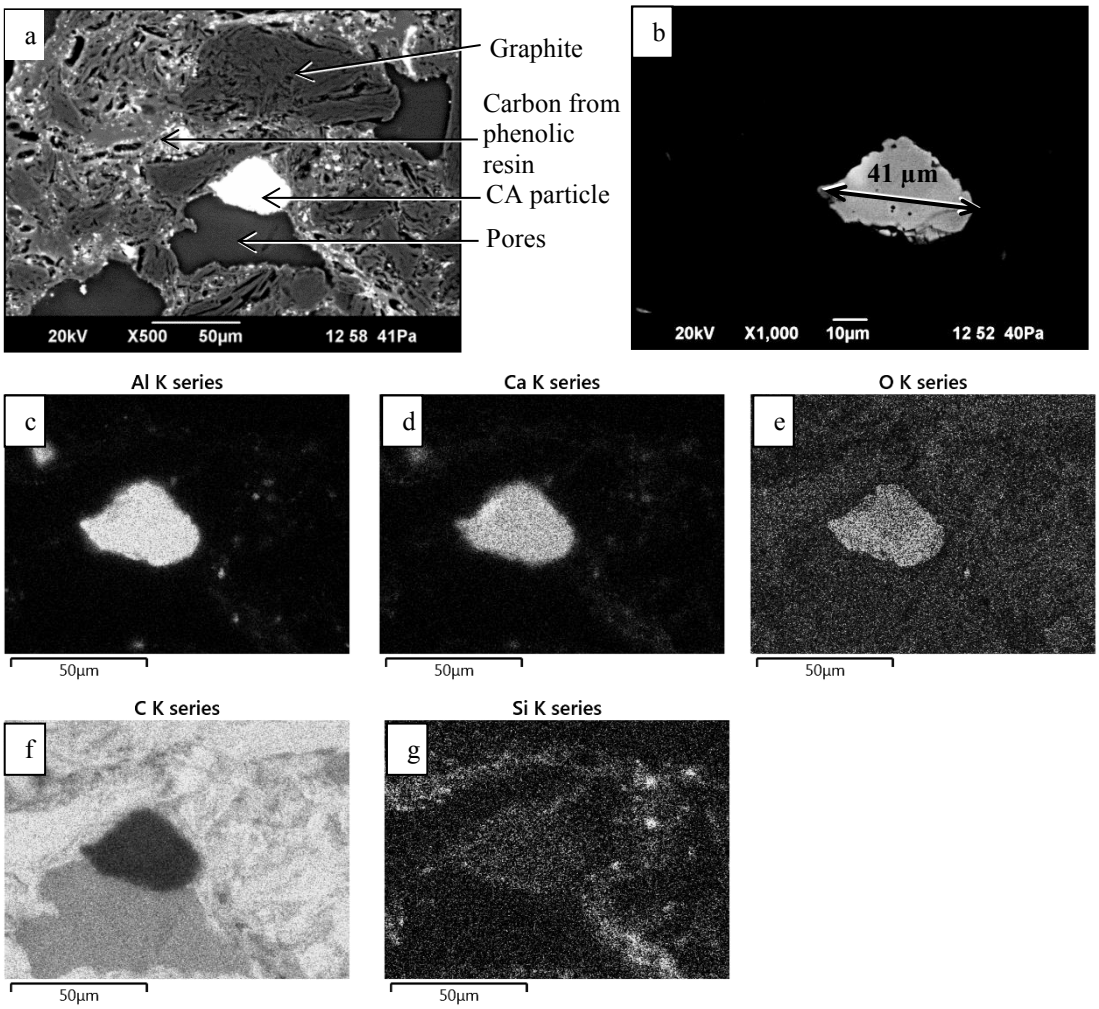

Figure 4.28: SEM backscattered images and EDS maps of the CA doped coke analogue before the gasification reaction. (a) SEM backscattered image optimised for carbon microstructure at X500 magnification (b) SEM backscattered image optimised for the mineral component at X1000 (c – g) EDS maps.

After the gasification reaction

Figure 4.29 shows SEM backscattered images and EDS maps of a representative area of a cross-section of CA doped coke analogue after the gasification reaction at 1273 K for 2 hours.

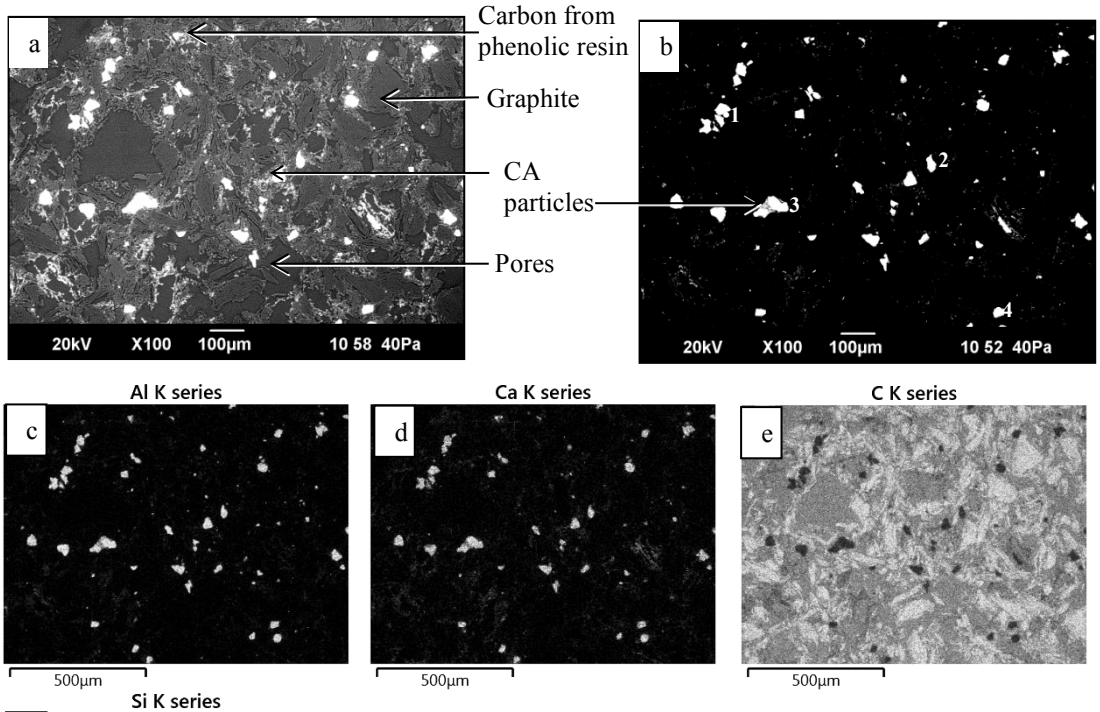

Table 4.11: Point analysis of the CA doped coke analogue (mass %) (Figure 4.29 b)

Label	1	2	3	4
O	39.9	40.2	40.1	39.8
Al	31.9	32.5	33.0	31.6
Si	Trace	Trace	Trace	Trace
Ca	27.4	26.5	25.2	27.8
Fe				
Total	100.0	100.0	100.0	100.0

Figure 4.29: SEM backscattered images and EDS maps of the CA doped coke analogue after the gasification reaction at 1273 K at X100 magnification. (a) SEM backscattered image optimised for carbon microstructure (b) SEM backscattered image optimised for mineral component (c – f) EDS maps.

The carbon structure and a CA particle are clearly presented from SEM backscattered images and EDS maps in *Figures 4.30*.

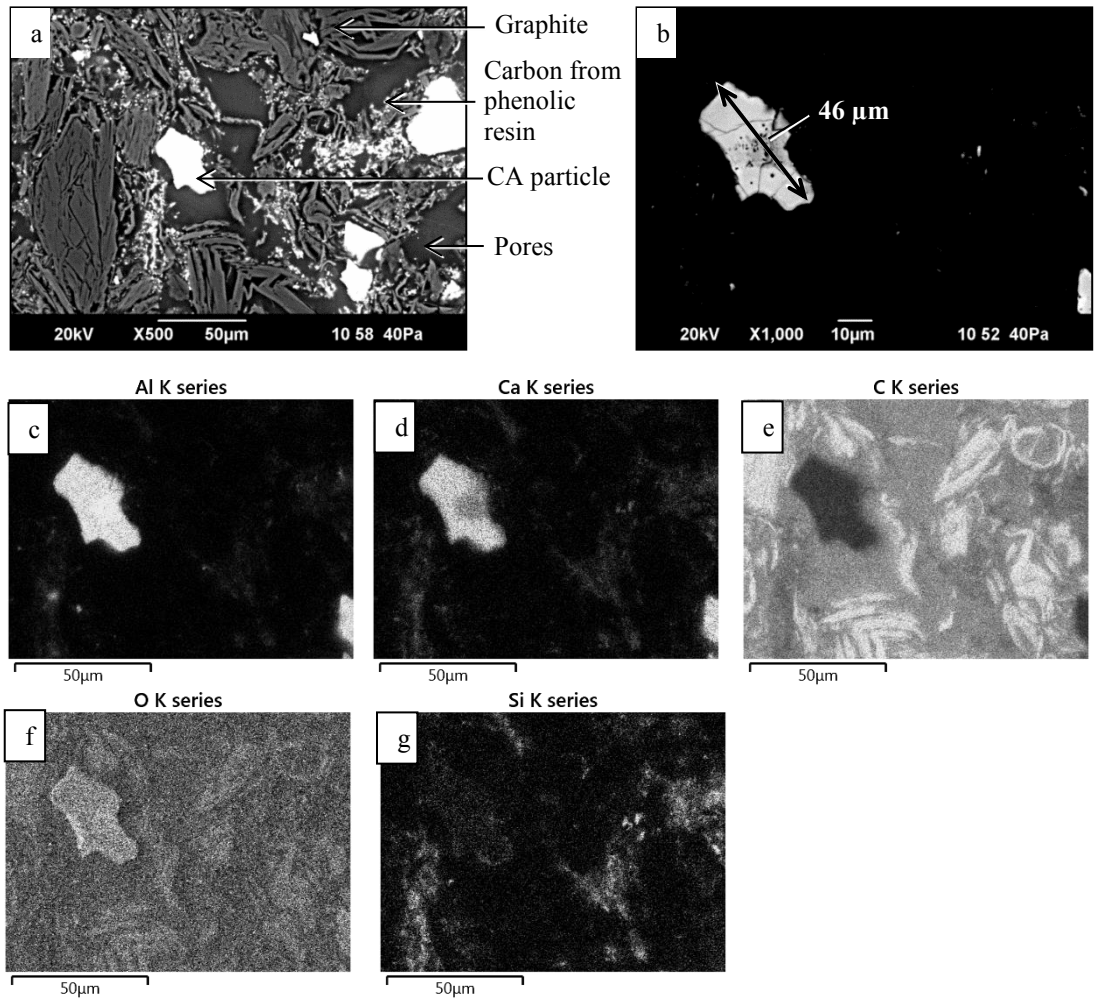

Figure 4.30: SEM backscattered images and EDS maps of the CA doped coke analogue after the gasification reaction at 1273 K. (a) SEM backscattered image optimised for carbon microstructure at X500 magnification (b) SEM backscattered image optimised for the mineral component at X1000 (c – g) EDS maps.

C3A doped coke analogue

Before the gasification reaction

Figure 4.23 shows SEM backscattered images and EDS maps of a representative area of a cross-section of C3A doped coke analogue before the gasification reaction.

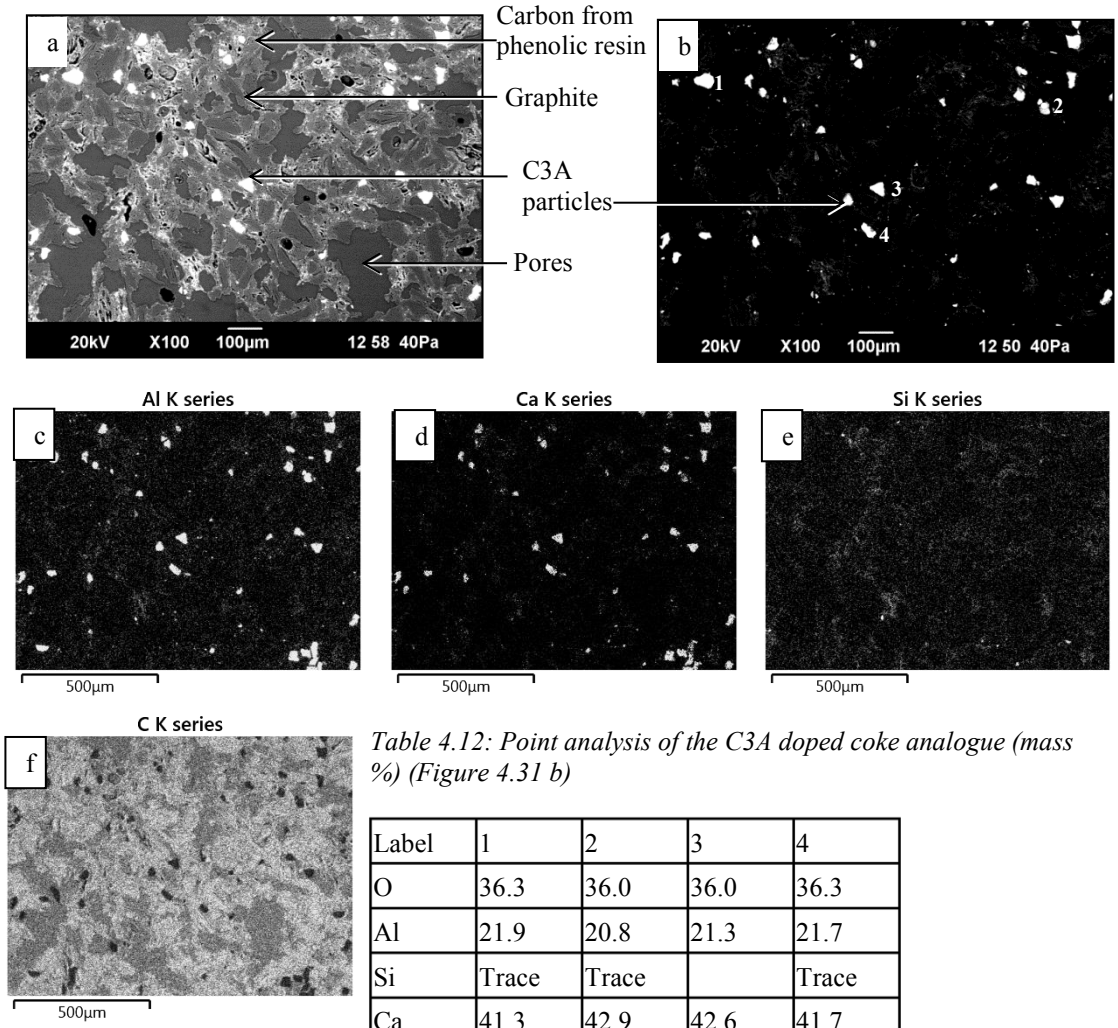

Table 4.12: Point analysis of the C3A doped coke analogue (mass %) (Figure 4.31 b)

Label	1	2	3	4
O	36.3	36.0	36.0	36.3
Al	21.9	20.8	21.3	21.7
Si	Trace	Trace		Trace
Ca	41.3	42.9	42.6	41.7
Fe				
Total	100.0	100.0	100.0	100.0

Figure 4.31: SEM backscattered images and EDS maps of the C3A doped coke analogue before the gasification reaction at X100 magnification. (a) SEM backscattered image optimised for carbon microstructure (b) SEM backscattered image optimised for mineral component (c – f) EDS maps.

Figure 4.32 shows the SEM backscattered images and EDS maps of a selected area of C3A doped coke analogue at X500 and X1000 magnifications.

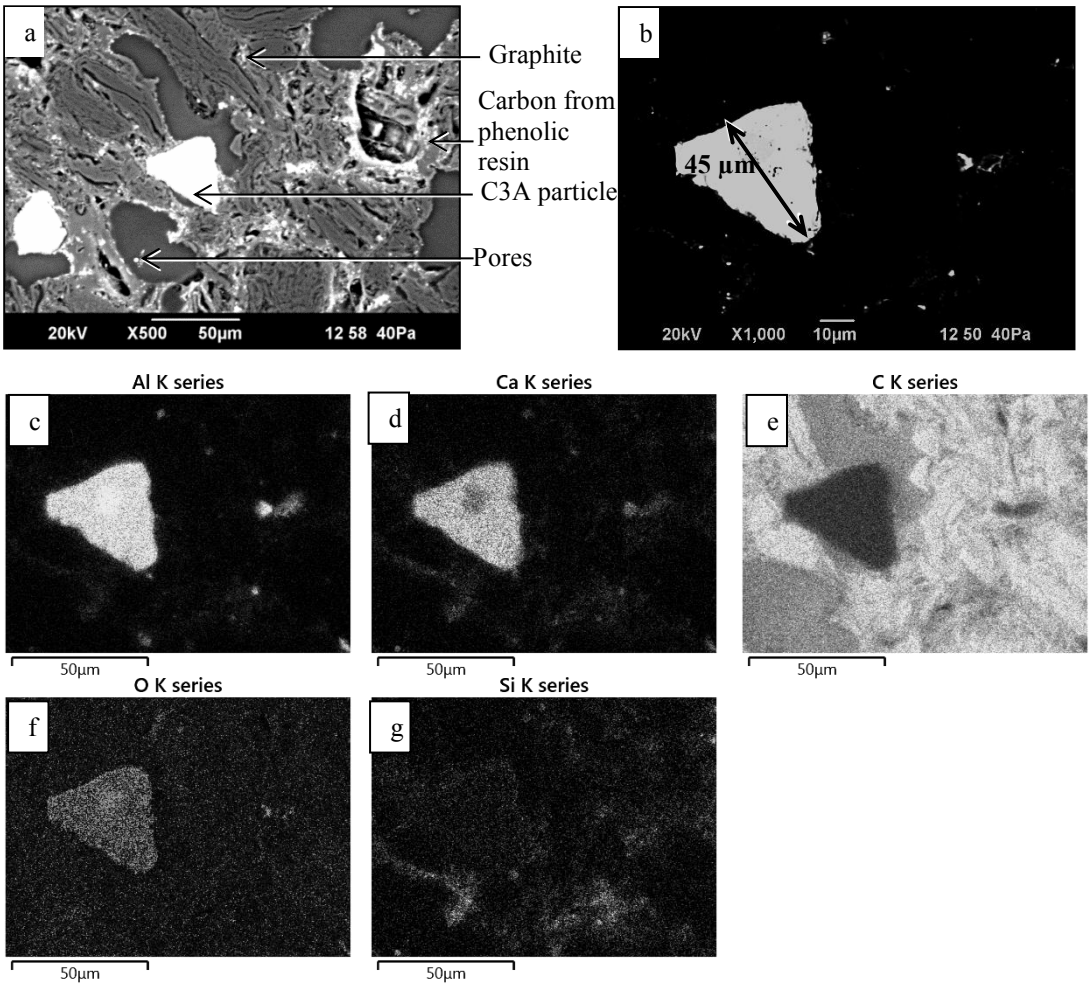

Figure 4.32: SEM backscattered images and EDS maps of the C3A doped coke analogue before the gasification reaction. (a) SEM backscattered image optimised for carbon microstructure at X500 magnification (b) SEM backscattered image optimised for the mineral component at X1000 (c – g) EDS maps.

After the gasification reaction

Figure 4.33 shows SEM backscattered images and EDS maps of a representative area of a cross-section of C3A doped coke analogue after the gasification reaction at 1273 K for 2 hours.

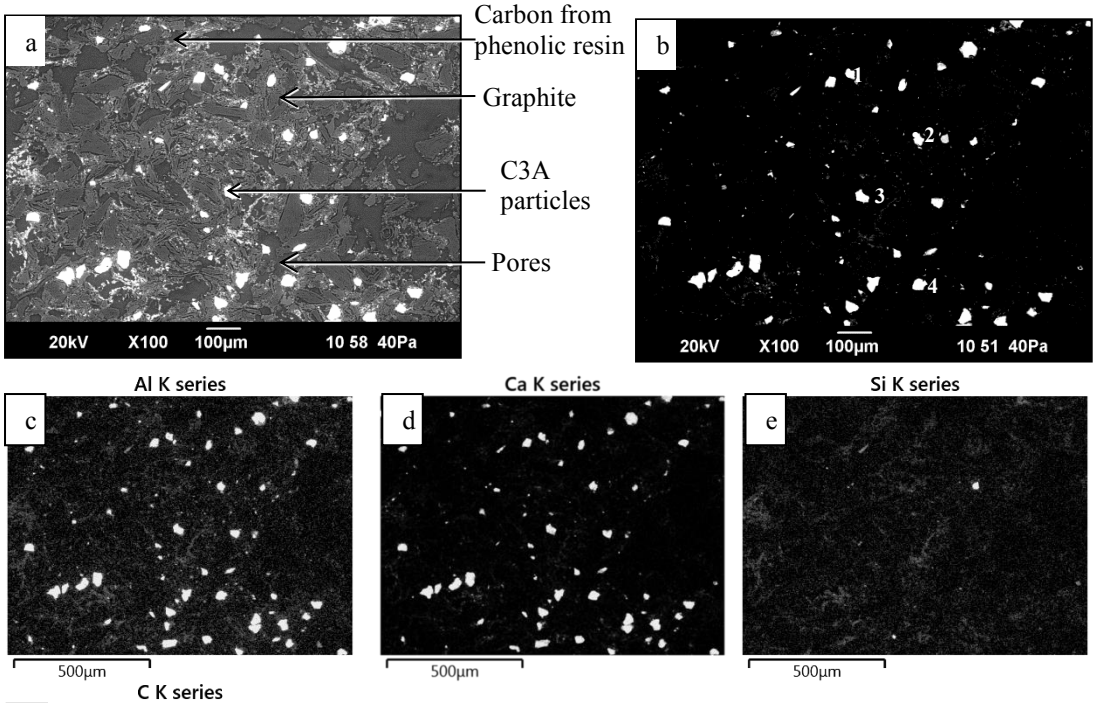

Table 4.13: Point analysis of the C3A doped coke analogue (mass %) (Figure 4.33 b)

Label	1	2	3	4
O	35.3	35.4	36.6	35.3
Al	22.4	21.1	22.5	22.2
Si	Trace	Trace		Trace
Ca	42.2	42.6	40.7	42.4
Fe				
Total	100.0	100.0	100.0	100.0

Figure 4.33: SEM backscattered images and EDS maps of the C3A doped coke analogue after the gasification reaction at 1273 K at X100 magnification. (a) SEM backscattered image optimised for carbon microstructure (b) SEM backscattered image optimised for mineral component (c – f) EDS maps.

The carbon structure and a C3A particle are clearly presented from SEM backscattered images and EDS maps in *Figures 4.34*.

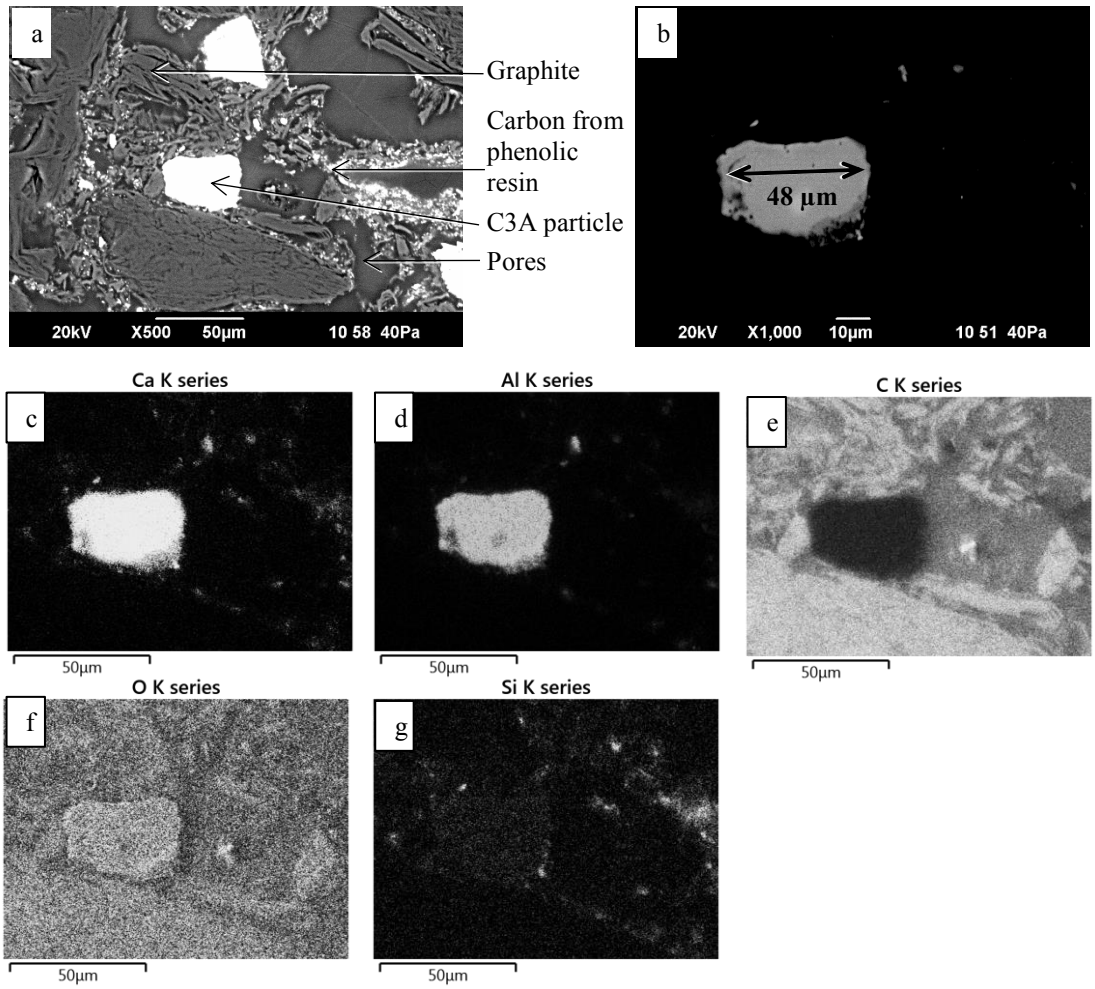

Figure 4.34: SEM backscattered images and EDS maps of the C3A doped coke analogue after the gasification reaction at 1273 K. (a) SEM backscattered image optimised for carbon microstructure at X500 magnification (b) SEM backscattered image optimised for the mineral component at X1000 (c – g) EDS maps.

Lime doped coke analogue

Before the gasification reaction

Lime in the coke analogue shows a significantly different behavior than other minerals studied in mineral distribution and mineral particle size. *Figure 4.35* shows SEM backscattered images and EDS maps of the lime doped coke analogue. The dispersion behavior required further analysis, this is detailed in section 4.3.

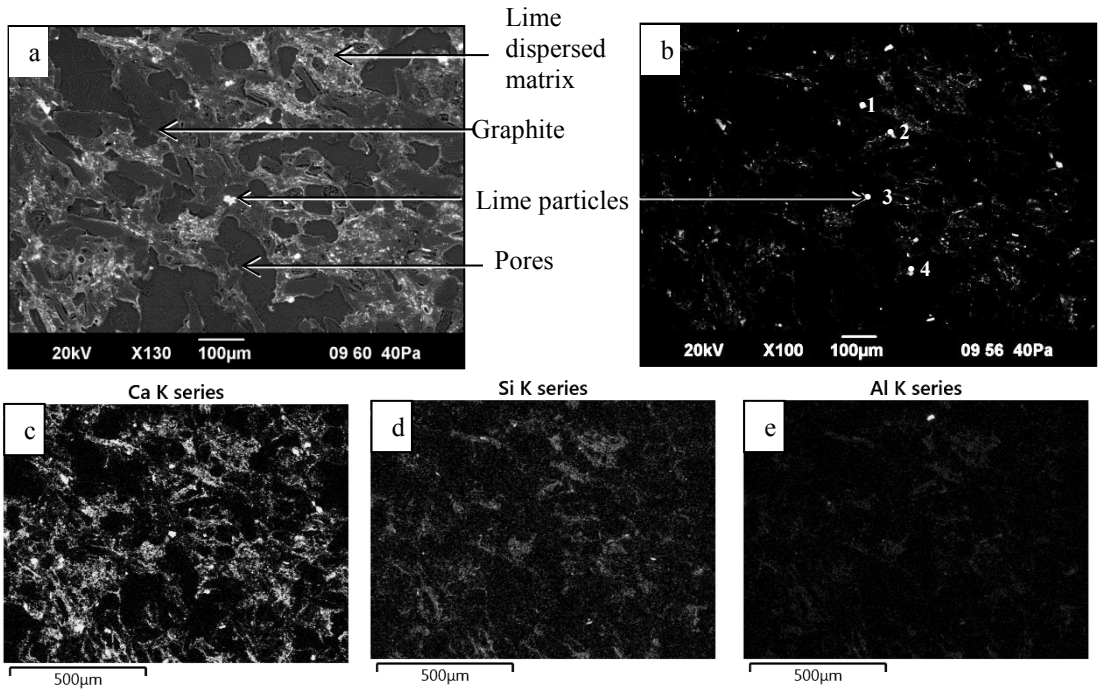

Table 4.14: Point analysis of the lime doped coke analogue (mass %) (Figure 4.35 b)

Label	1	2	3	4
O	29.3	30.0	28.2	29.1
Al	2.6	3.2	3.5	1.4
Si	1.7	2.9	1.7	2.6
Ca	63.5	60.3	64.2	63.7
Fe				
Total	100.0	100.0	100.0	100.0

Figure 4.35: SEM backscattered images and EDS maps of the lime doped coke analogue before the gasification reaction at X100 magnification. (a) SEM backscattered image optimised for carbon microstructure (b) SEM backscattered image optimised for mineral component (c – f) EDS maps.

Figures 4.36 shows SEM backscattered images and EDS maps at X500 and X100 magnifications for a clear view of the carbon and mineral structures.

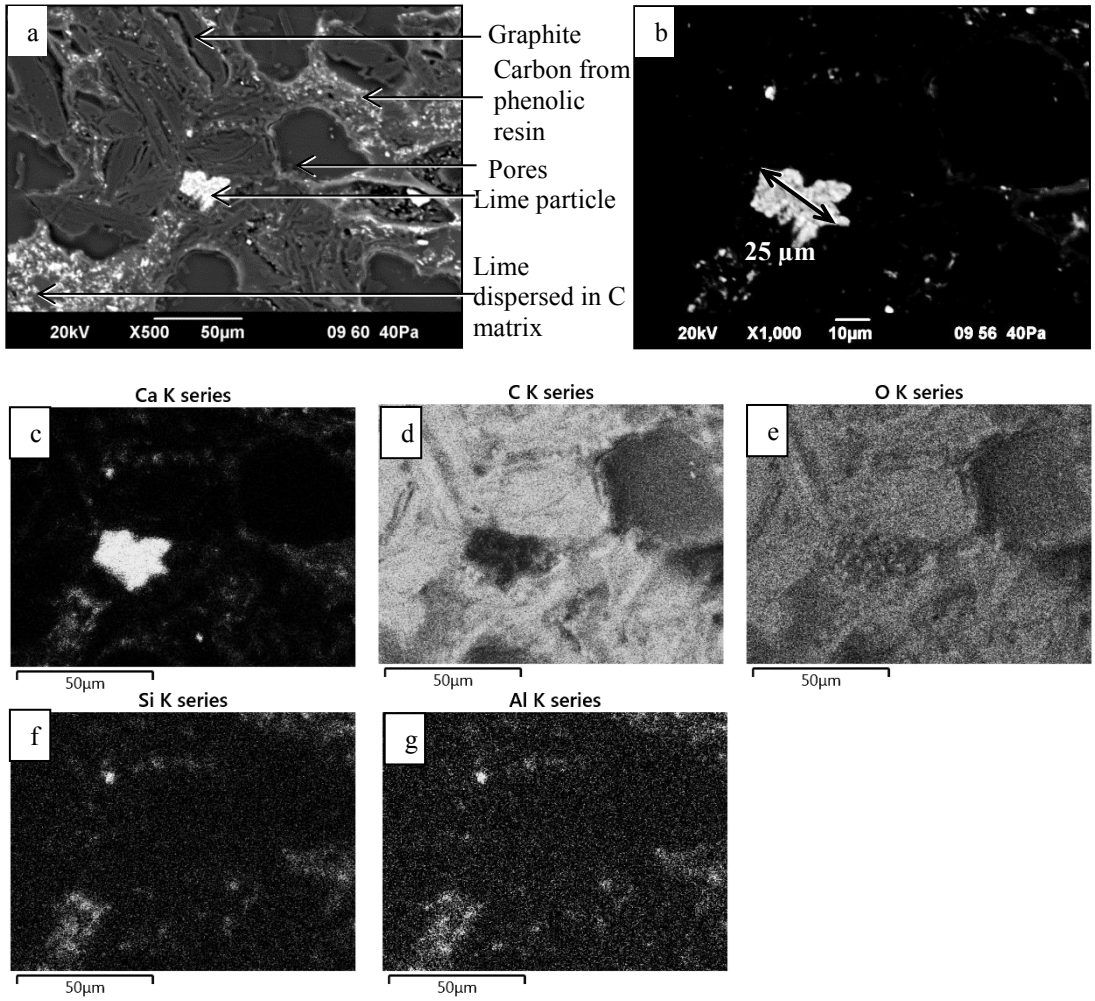

Figure 4.36: SEM backscattered images and EDS maps of the lime doped coke analogue before the gasification reaction. (a) SEM backscattered image optimised for carbon microstructure at X500 magnification (b) SEM backscattered image optimised for the mineral component at X1000 (c – g) EDS maps.

After the gasification reaction

Figure 4.37 shows SEM backscattered images and EDS maps of a representative area of a cross-section of lime doped coke analogue after the gasification reaction at 1273 K for 2 hours.

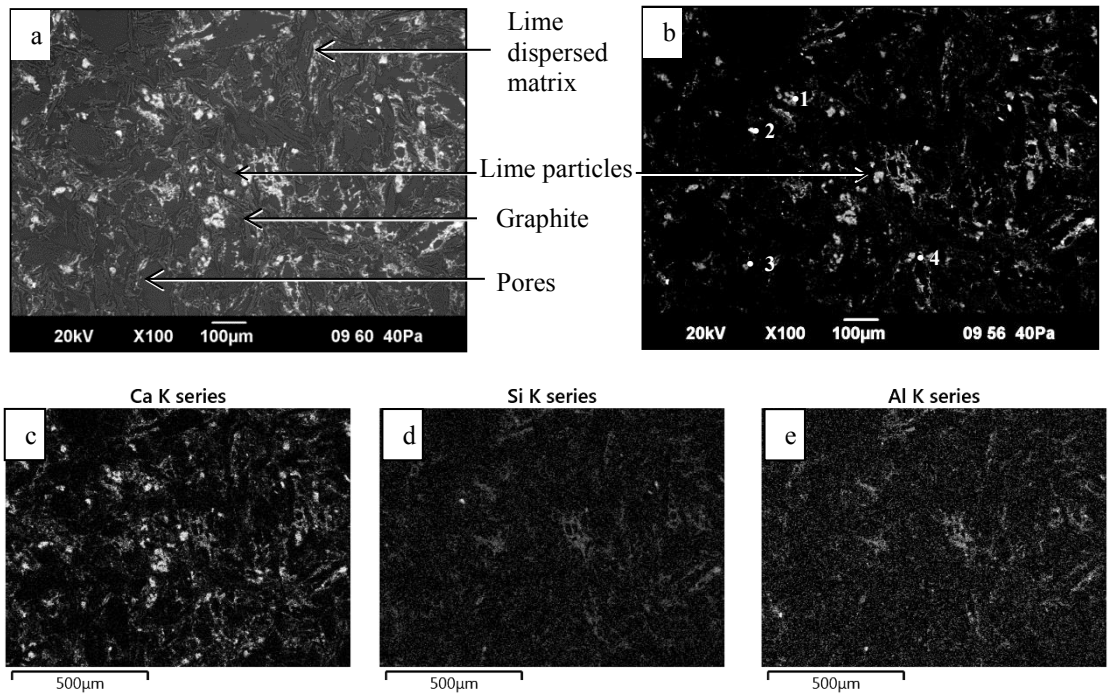

Table 4.15: Point analysis of the lime doped coke analogue (mass %) (Figure 4.37 b)

Label	1	2	3	4
O	30.0	30.4	29.8	31.2
Al	1.9	2.5	3.0	2.2
Si	1.9	3.7	3.1	2.9
Ca	62.1	61.0	61.6	61.8
Fe				
Total	100.0	100.0	100.0	100.0

Figure 4.37: SEM backscattered images and EDS maps of the lime doped coke analogue after the gasification reaction at 1273 K at X100 magnification. (a) SEM backscattered image optimised for carbon microstructure (b) SEM backscattered image optimised for mineral component (c – f) EDS maps.

The carbon structure and a lime (particle) are clearly presented from SEM backscattered images and EDS maps in *Figures 4.38*.

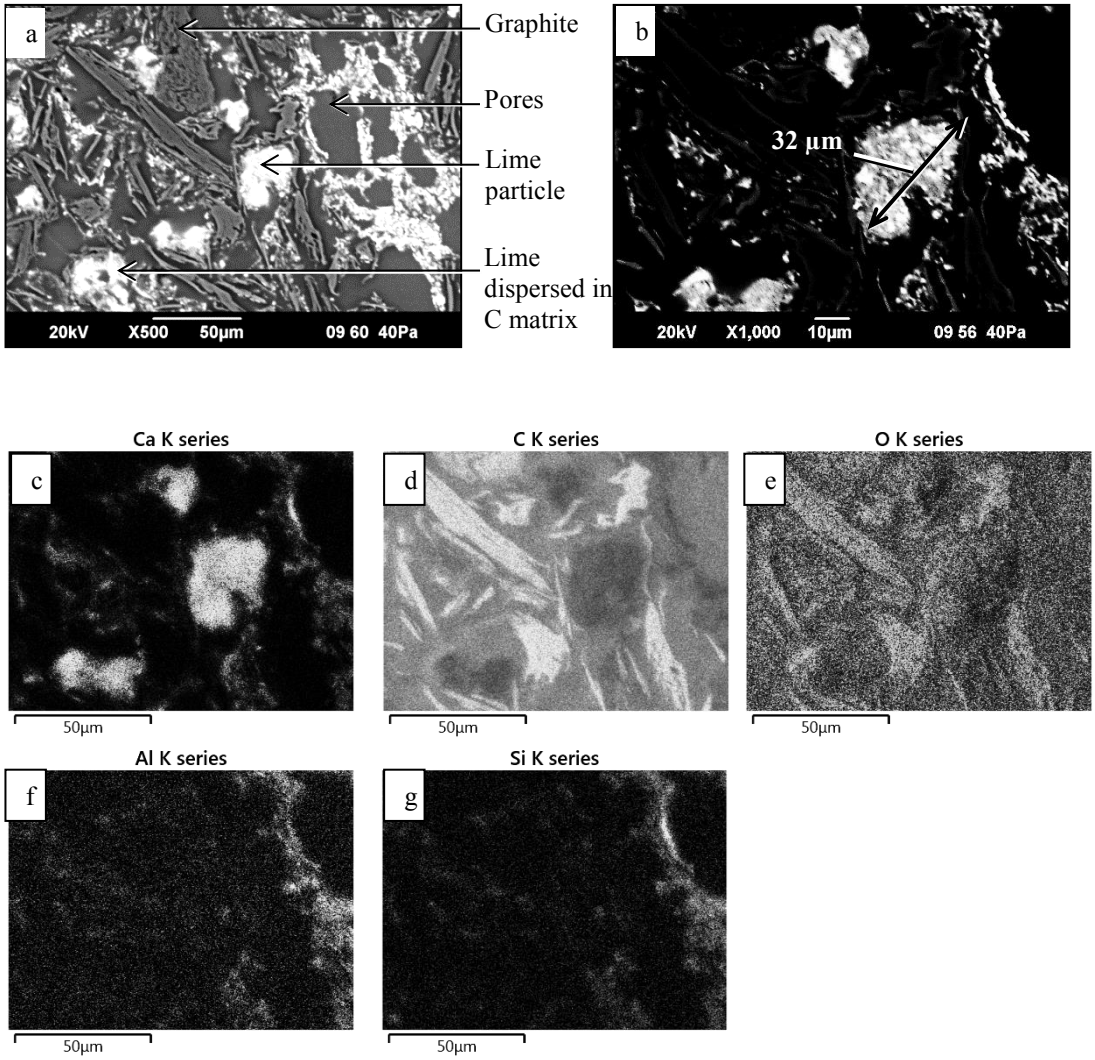

Figure 4.38: SEM backscattered images and EDS maps of the lime doped coke analogue after the gasification reaction at 1273 K. (a) SEM backscattered image optimised for carbon microstructure at X500 magnification (b) SEM backscattered image optimised for the mineral component at X1000 (c – g) EDS maps.

CAS 1 doped coke analogue

Before the gasification reaction

Figure 4.39 shows SEM backscattered images and EDS maps of the CAS 1 doped coke analogue before the gasification reaction.

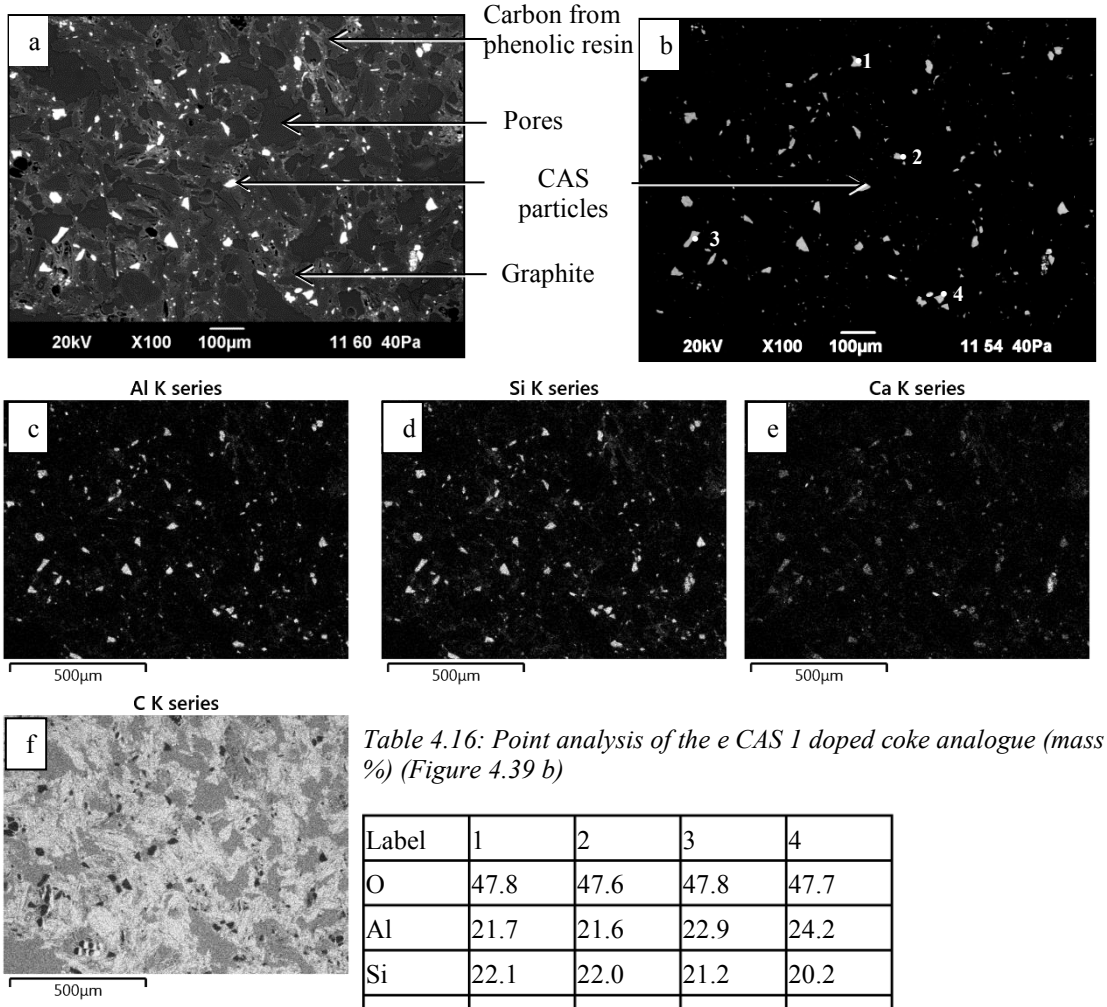

Table 4.16: Point analysis of the e CAS 1 doped coke analogue (mass %) (Figure 4.39 b)

Label	1	2	3	4
O	47.8	47.6	47.8	47.7
Al	21.7	21.6	22.9	24.2
Si	22.1	22.0	21.2	20.2
Ca	8.4	8.8	8.1	7.9
Fe				
Total	100.0	100.0	100.0	100.0

Figure 4.39: SEM backscattered images and EDS maps of the CAS 1 doped coke analogue before the gasification reaction at X100 magnification. (a) SEM backscattered image optimised for carbon microstructure (b) SEM backscattered image optimised for mineral component (c – f) EDS maps.

Figures 4.40 shows SEM backscattered images and EDS maps at X500 and X1000 magnifications for a clear view of the carbon and mineral structures.

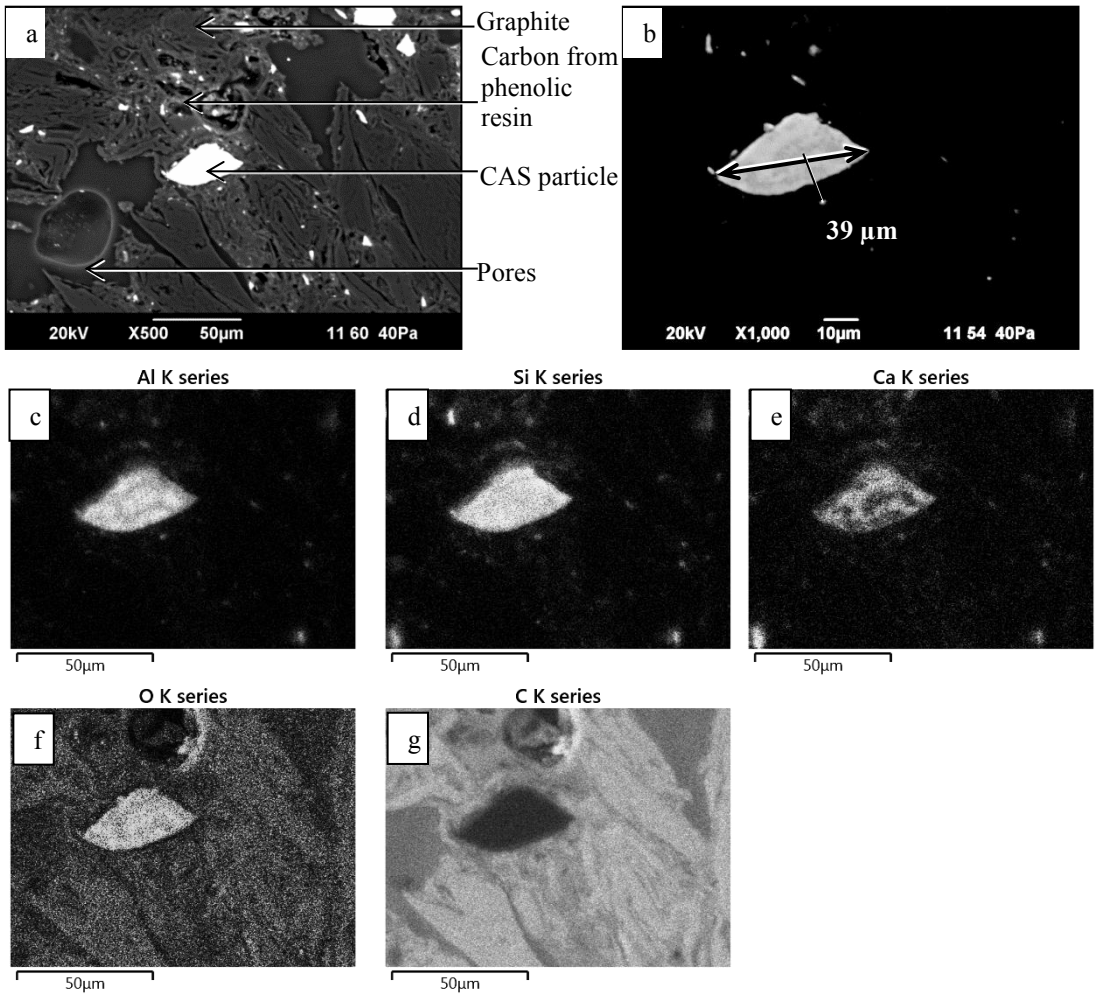

Figure 4.40: SEM backscattered images and EDS maps of the CAS 1 doped coke analogue before the gasification reaction. (a) SEM backscattered image optimised for carbon microstructure at X500 magnification (b) SEM backscattered image optimised for the mineral component at X1000 (c – g) EDS maps.

After the gasification reaction

Figure 4.41 shows SEM backscattered images and EDS maps of a cross-section of CAS 1 doped coke analogue after the gasification reaction at 1273 K for 2 hours.

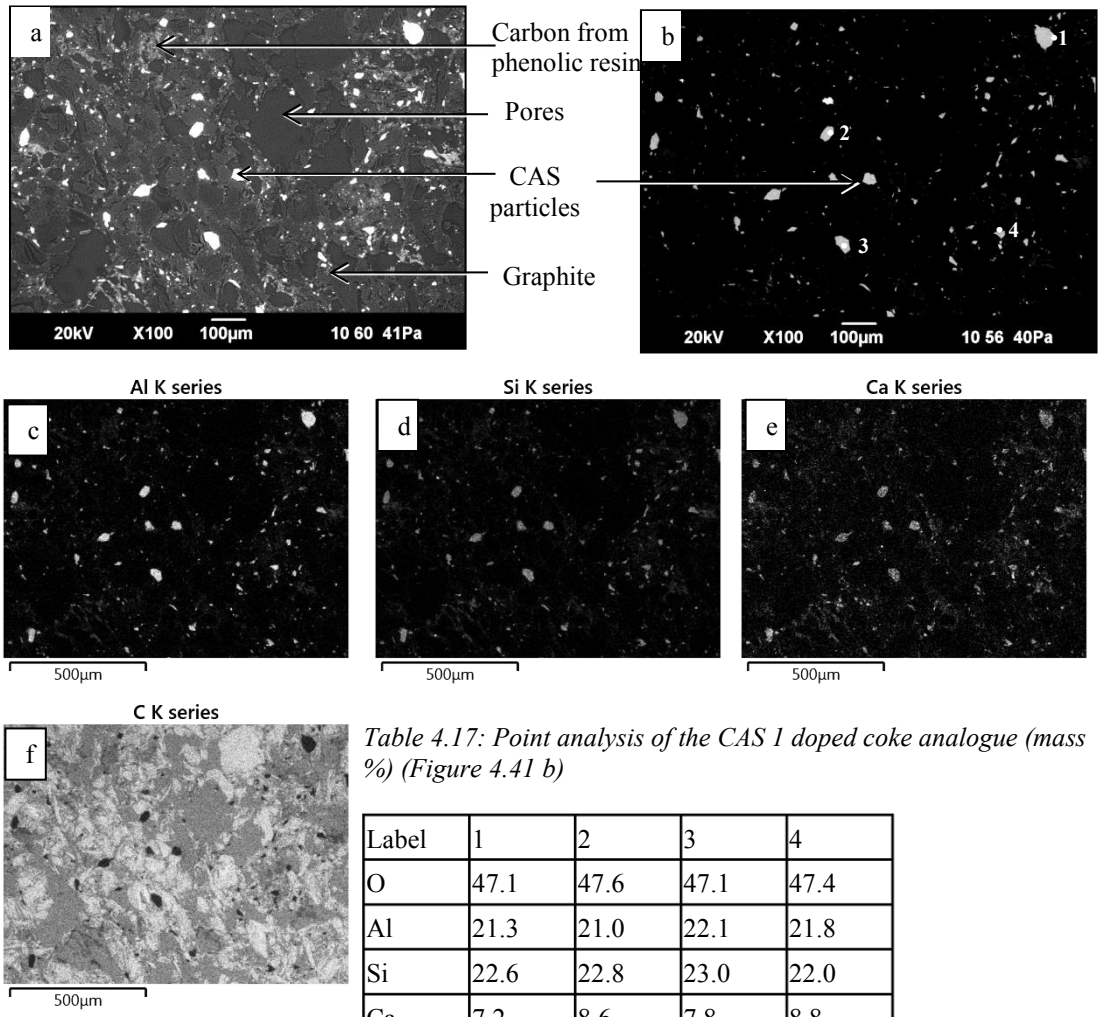

Table 4.17: Point analysis of the CAS 1 doped coke analogue (mass %) (Figure 4.41 b)

Label	1	2	3	4
O	47.1	47.6	47.1	47.4
Al	21.3	21.0	22.1	21.8
Si	22.6	22.8	23.0	22.0
Ca	7.2	8.6	7.8	8.8
Fe				
Total	100.0	100.0	100.0	100.0

Figure 4.41: SEM backscattered images and EDS maps of the CAS 1 doped coke analogue after the gasification reaction at 1273 K at X100 magnification. (a) SEM backscattered image optimised for carbon microstructure (b) SEM backscattered image optimised for mineral component (c – f) EDS maps.

Figure 4.42 shows SEM backscattered images and EDS maps of a representative area of a cross-section of CAS 1 doped coke analogue after the gasification at 1273 K for 2 hours.

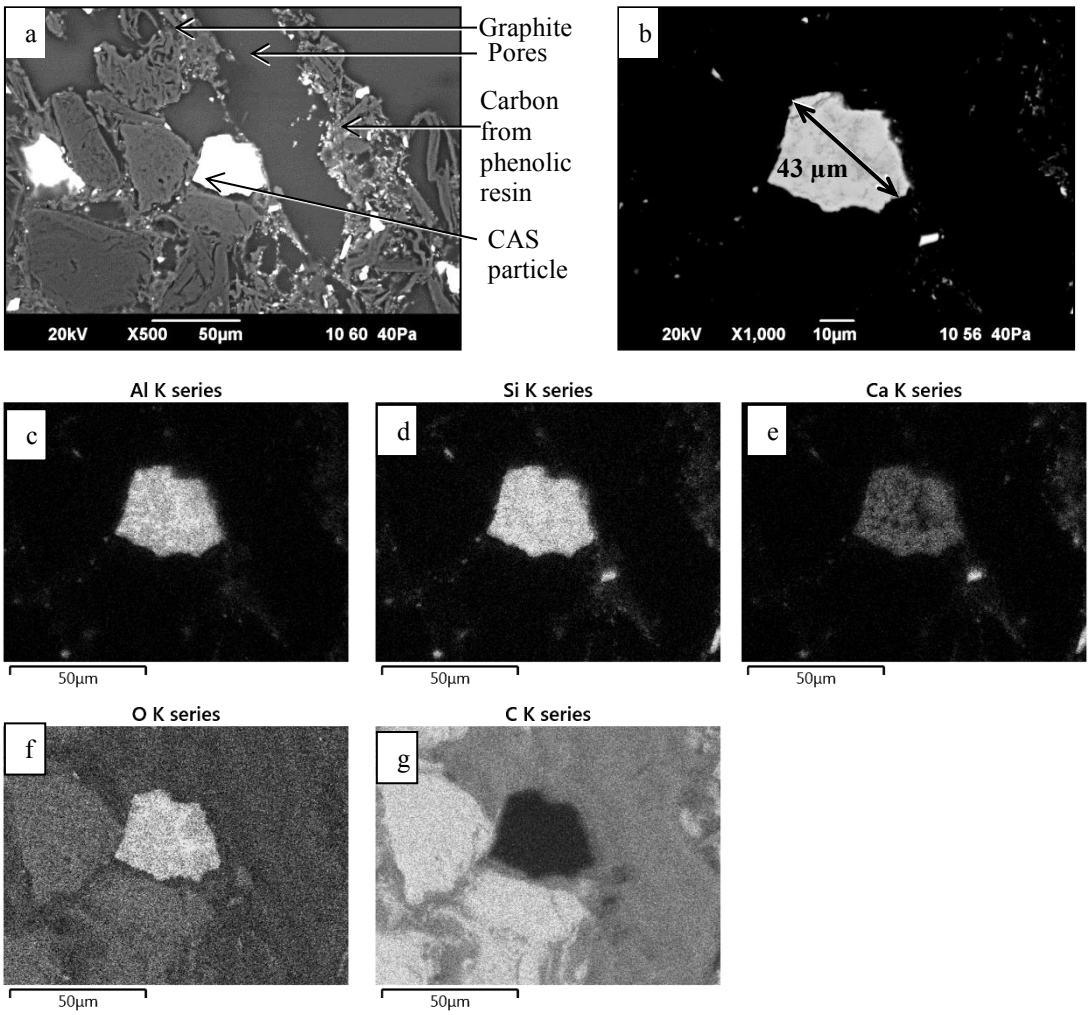

Figure 4.42: SEM backscattered images and EDS maps of the CAS 1 doped coke analogue after the gasification reaction at 1273 K. (a) SEM backscattered image optimised for carbon microstructure at X500 magnification (b) SEM backscattered image optimised for the mineral component at X1000 (c – g) EDS maps.

CAS 2 doped coke analogue

Before the gasification reaction

Figure 4.43 shows SEM backscattered images and EDS maps of a representative area of a cross-section of CAS 2 doped coke analogue before the gasification reaction.

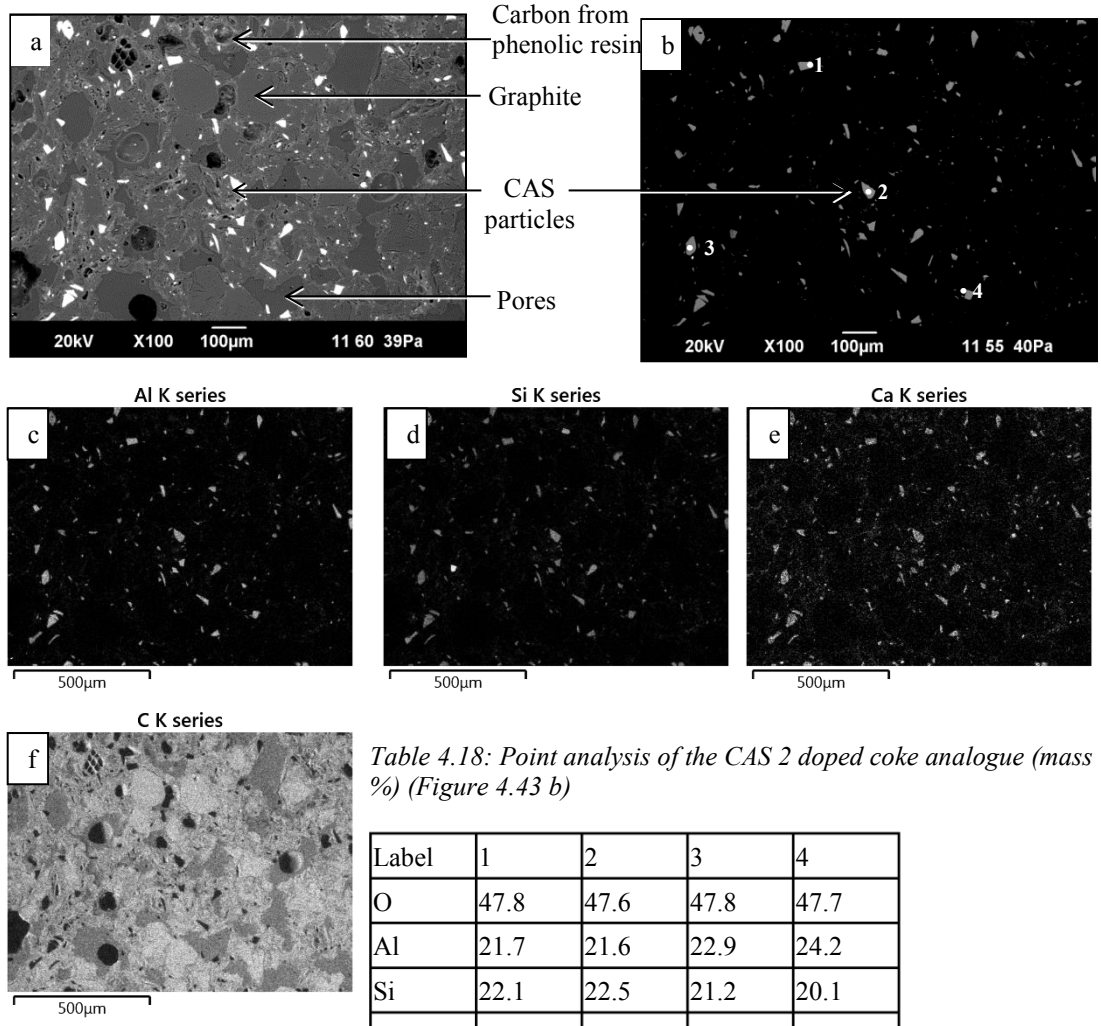

Table 4.18: Point analysis of the CAS 2 doped coke analogue (mass %) (Figure 4.43 b)

Label	1	2	3	4
O	47.8	47.6	47.8	47.7
Al	21.7	21.6	22.9	24.2
Si	22.1	22.5	21.2	20.1
Ca	8.4	8.3	8.1	8.0
Fe				
Total	100.0	100.0	100.0	100.0

Figure 4.43: SEM backscattered images and EDS maps of the CAS 2 doped coke analogue before the gasification reaction at X100 magnification. (a) SEM backscattered image optimised for carbon microstructure (b) SEM backscattered image optimised for mineral component (c – f) EDS maps.

Figures 4.44 shows SEM backscattered images and EDS maps at X500 and X1000 magnifications for a clear view of the carbon and mineral structures.

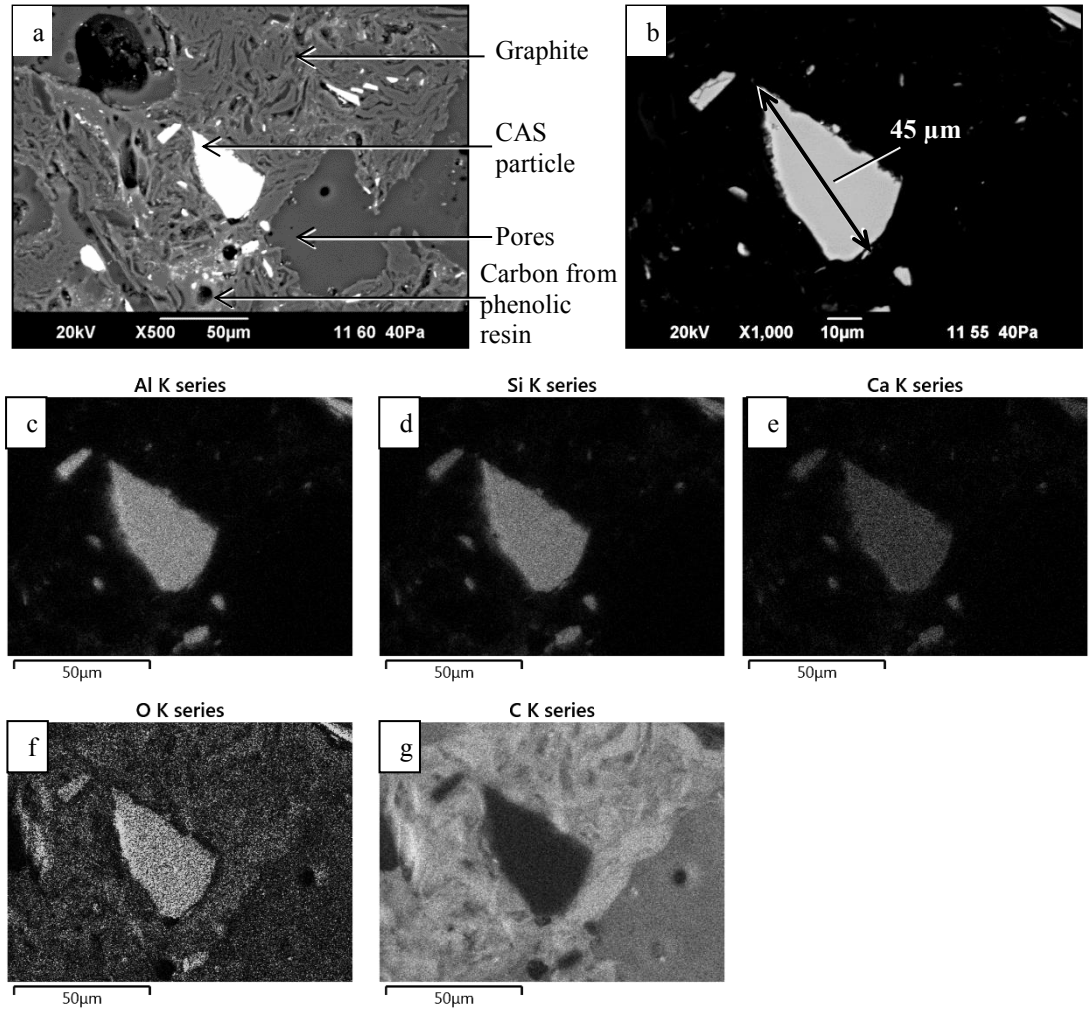

Figure 4.44: SEM backscattered images and EDS maps of the CAS 2 doped coke analogue before the gasification reaction. (a) SEM backscattered image optimised for carbon microstructure at X500 magnification (b) SEM backscattered image optimised for the mineral component at X1000 (c – g) EDS maps.

After the gasification reaction

Figure 4.45 shows SEM backscattered images and EDS maps of a cross-section of CAS 2 doped coke analogue after the gasification reaction at 1273 K for 2 hours.

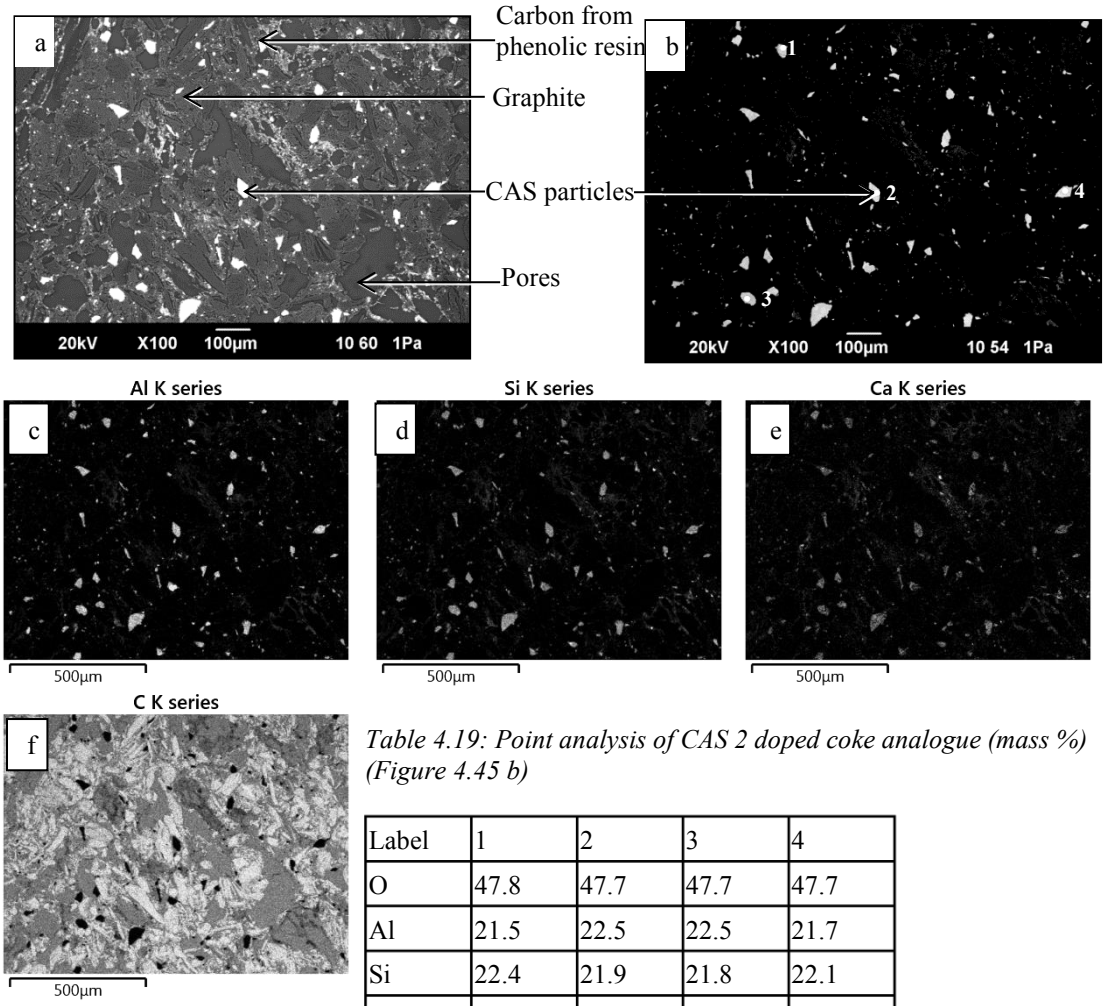

Table 4.19: Point analysis of CAS 2 doped coke analogue (mass %) (Figure 4.45 b)

Label	1	2	3	4
O	47.8	47.7	47.7	47.7
Al	21.5	22.5	22.5	21.7
Si	22.4	21.9	21.8	22.1
Ca	8.3	7.9	8.0	8.5
Fe				
Total	100.0	100.0	100.0	100.0

Figure 4.45: SEM backscattered images and EDS maps of CAS 2 doped coke analogue after the gasification reaction at 1273 K at X100 magnification. (a) SEM backscattered image optimised for carbon microstructure (b) SEM backscattered image optimised for mineral component (c – f) EDS maps.

*Figure 4.46*shows SEM backscattered images and EDS maps of a representative area of a cross-section of CAS 2 doped coke analogue after the gasification at 1273 K for 2 hours.

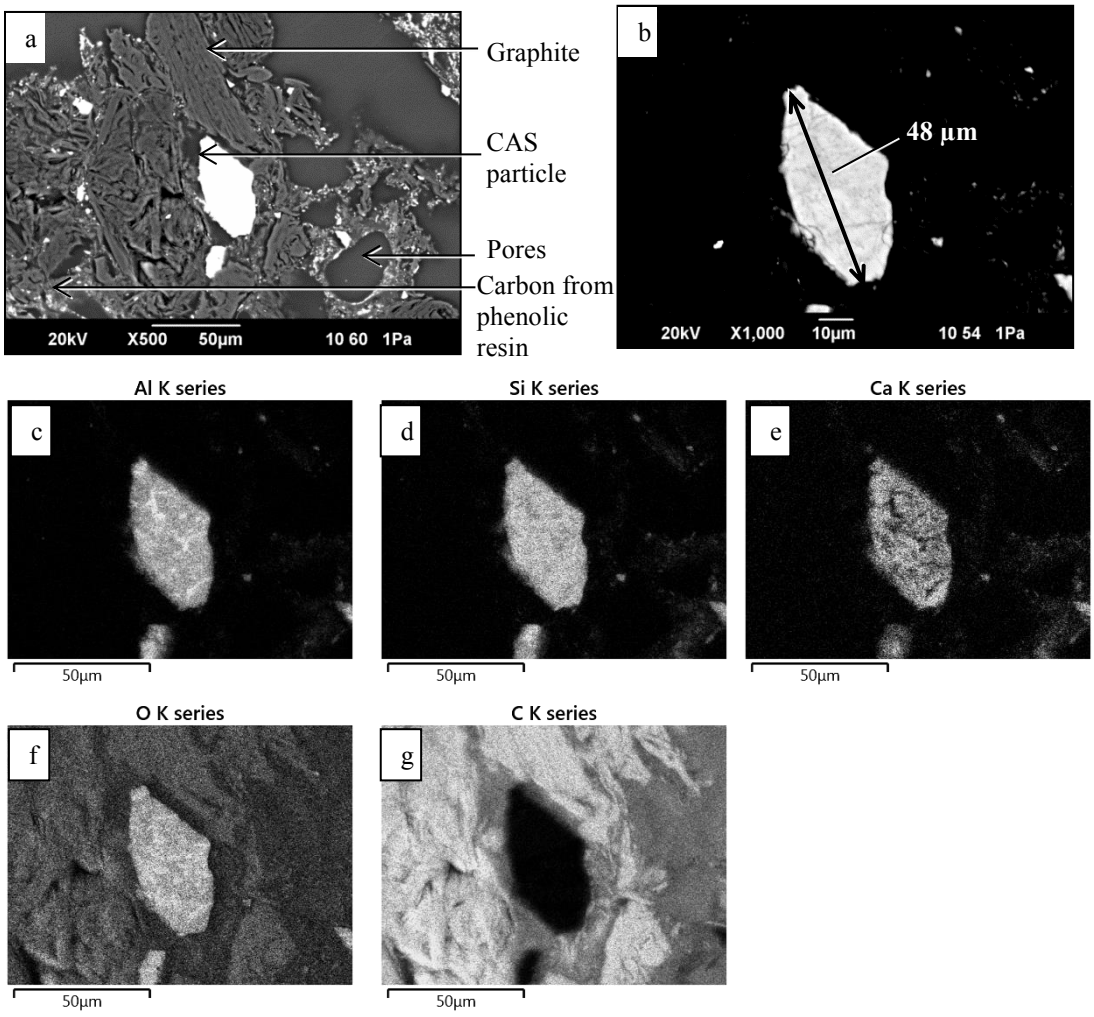

Figure 4.46: SEM backscattered images and EDS maps of CAS 2 doped coke analogue after the gasification reaction at 1273 K. (a) SEM backscattered image optimised for carbon microstructure at X500 magnification (b) SEM backscattered image optimised for the mineral component at X1000 (c – g) EDS maps.

Quartz doped coke analogue

Before the gasification reaction

Figure 4.47 shows SEM backscattered images and EDS maps of the quartz doped coke analogue before the gasification reaction.

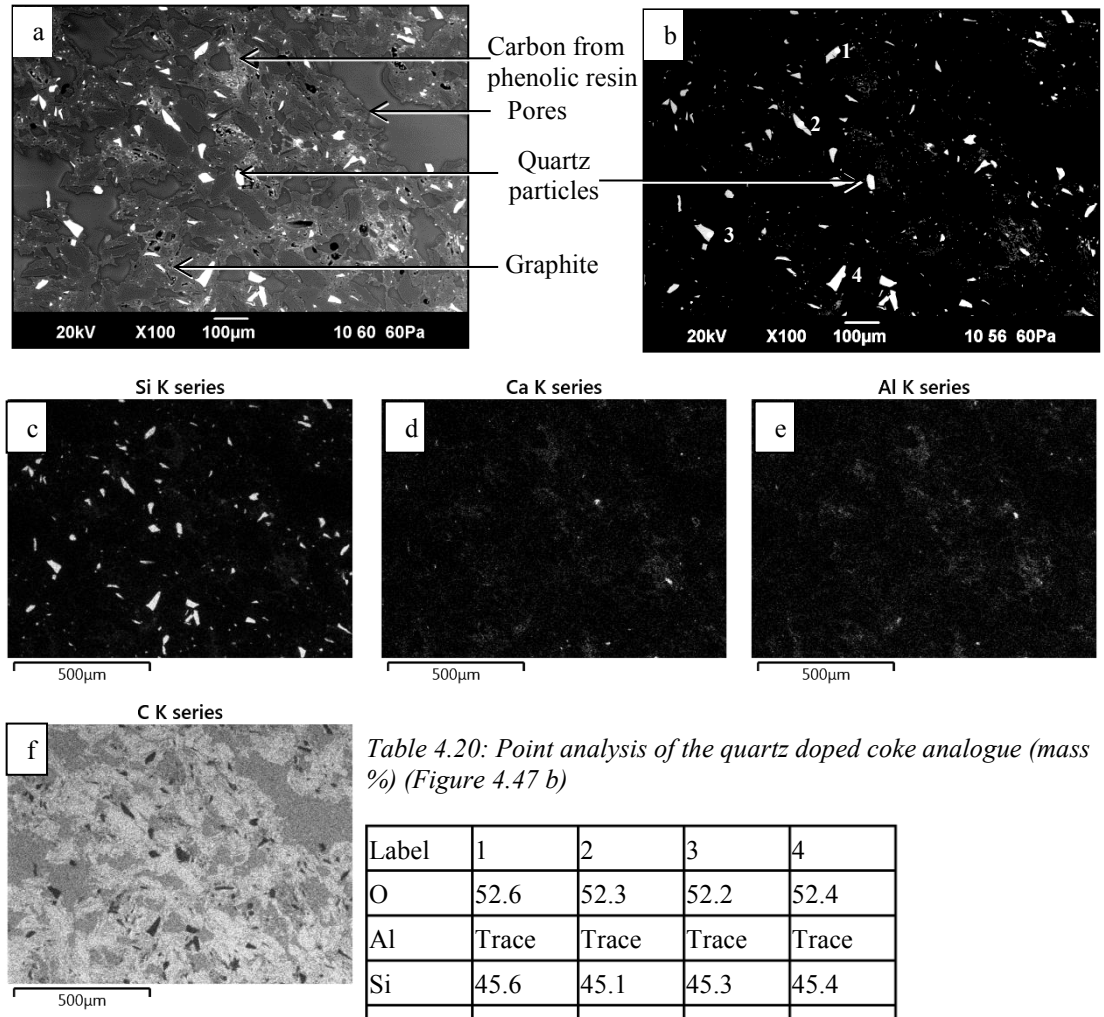

Table 4.20: Point analysis of the quartz doped coke analogue (mass %) (Figure 4.47 b)

Label	1	2	3	4
O	52.6	52.3	52.2	52.4
Al	Trace	Trace	Trace	Trace
Si	45.6	45.1	45.3	45.4
Ca		Trace	Trace	Trace
Fe				
Total	100.0	100.0	100.0	100.0

Figure 4.47: SEM backscattered images (X100) and EDS maps of the quartz doped coke analogue before the gasification reaction at X100 magnification. (a) SEM backscattered image optimised for carbon microstructure (b) SEM backscattered image optimised for mineral component (c – f) EDS maps.

Figures 4.48 shows SEM backscattered images and EDS maps at X500 and X1000 magnifications for a clear view of the carbon and mineral structures.

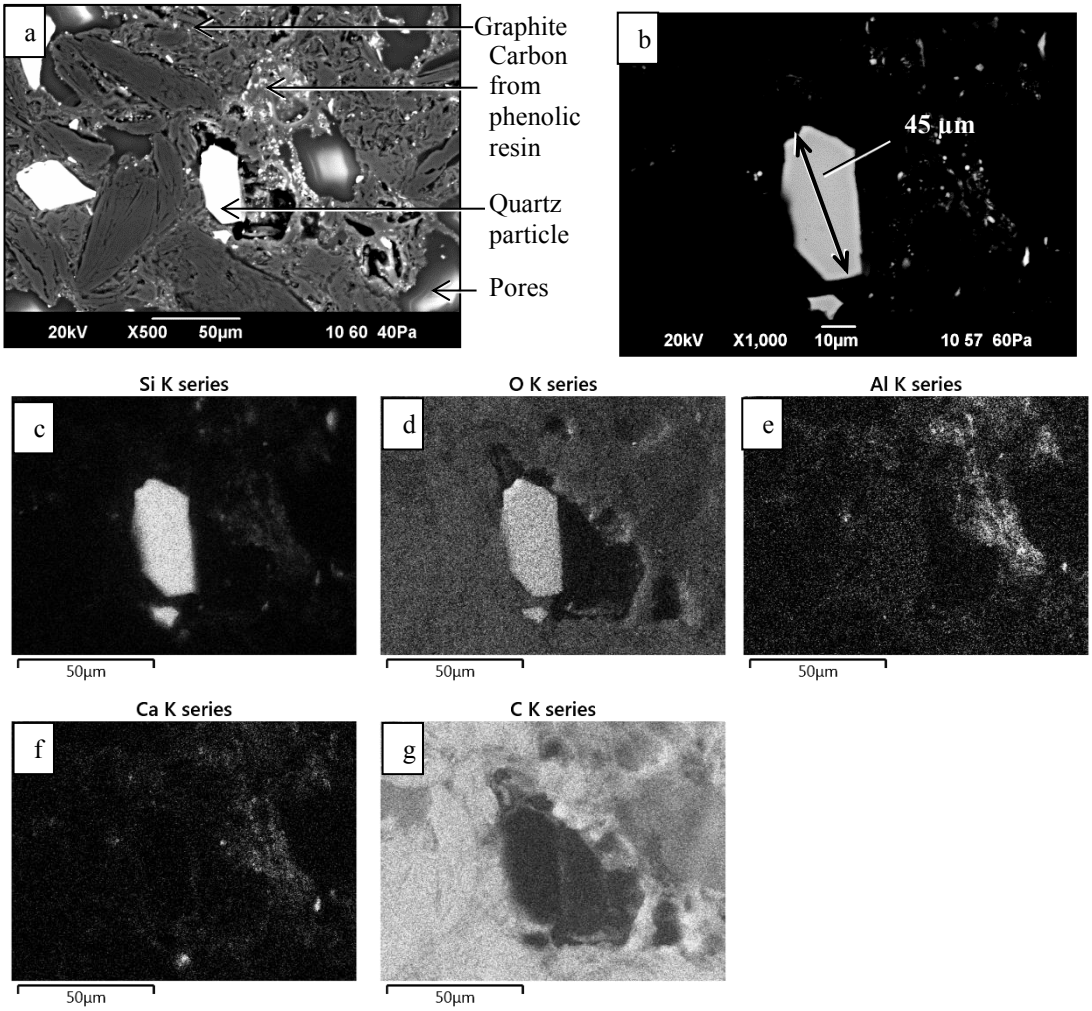

Figure 4.48: SEM backscattered images (X500 and X1000) and EDS maps of quartz doped coke analogue before the gasification reaction (a) SEM backscattered image optimised for carbon microstructure at X500 magnification (b) SEM backscattered image optimised for the mineral component at X1000 (c – g) EDS maps.

After the gasification reaction

Figure 4.49 shows SEM backscattered images and EDS maps of a cross-section of quartz doped coke analogue after the gasification reaction at 1273 K for 2 hours.

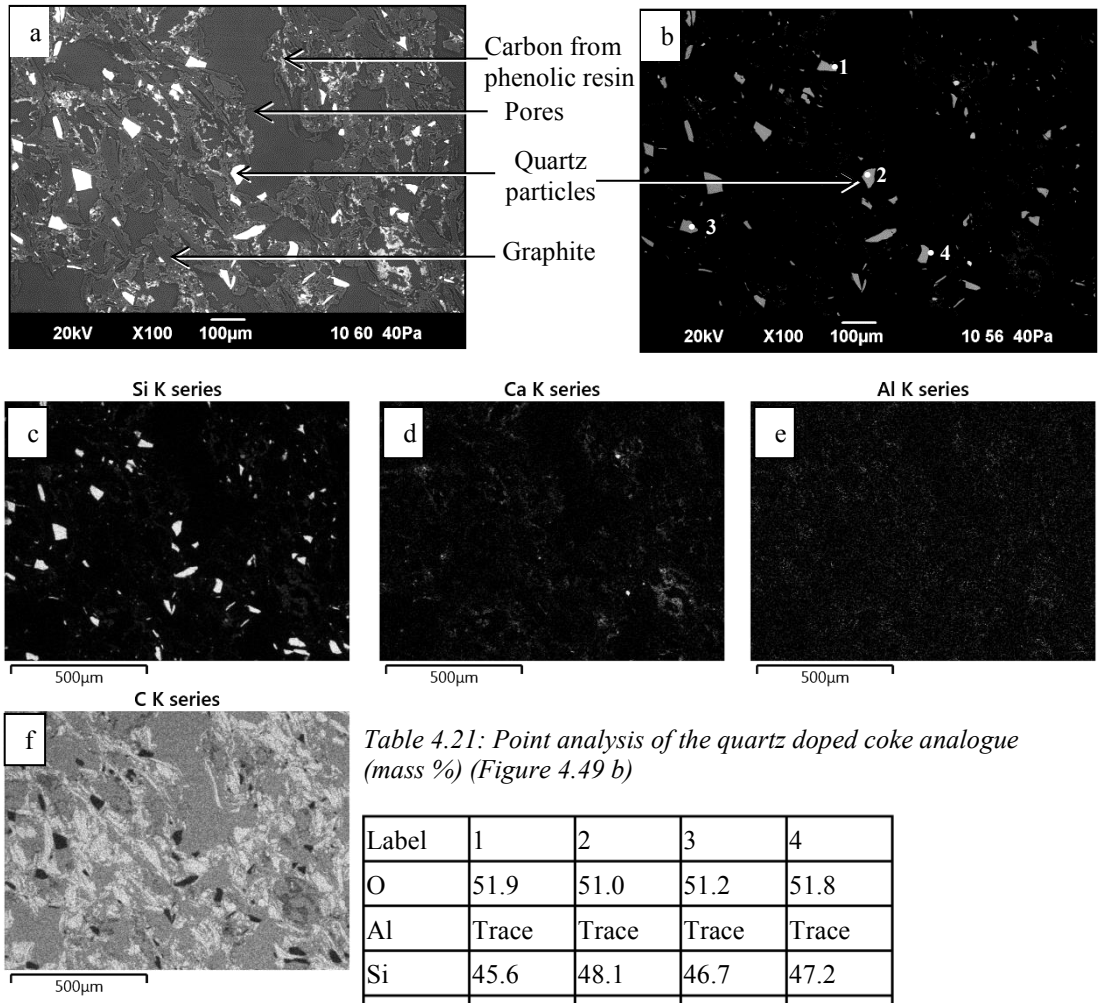

Table 4.21: Point analysis of the quartz doped coke analogue (mass %) (Figure 4.49 b)

Label	1	2	3	4
O	51.9	51.0	51.2	51.8
Al	Trace	Trace	Trace	Trace
Si	45.6	48.1	46.7	47.2
Ca	Trace		Trace	Trace
Fe				
Total	100.0	100.0	100.0	100.0

Figure 4.49: SEM backscattered images (X100) and EDS maps of the quartz doped coke analogue after the gasification reaction at 1273 K (a) SEM backscattered image optimised for carbon microstructure (b) SEM backscattered image optimised for mineral component (c – f) EDS maps.

Figure 4.50 shows SEM backscattered images and EDS maps of a representative area of a cross-section of CAS doped coke analogue after the gasification at 1273 K for 2 hours.

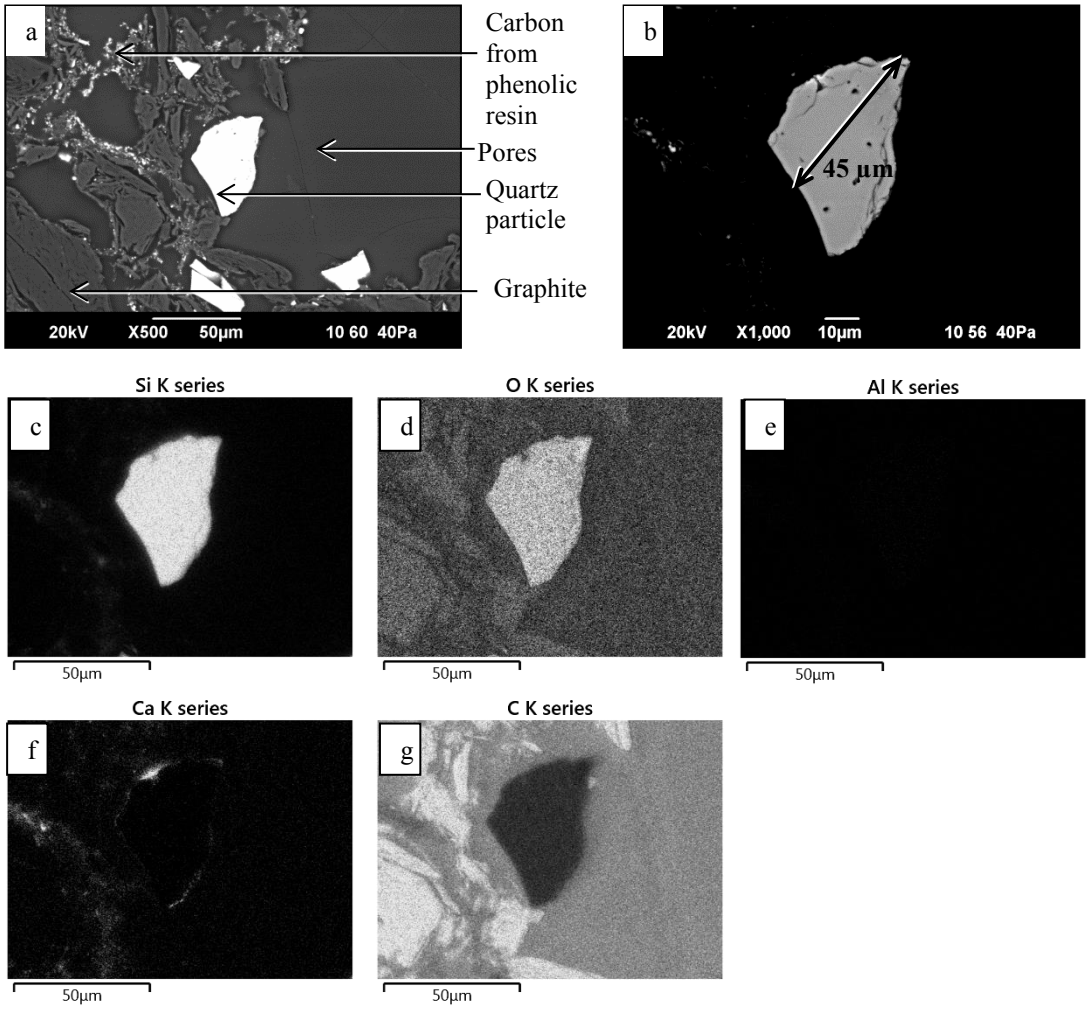

Figure 4.50: SEM backscattered images (X500 and X1000) and EDS maps of quartz doped coke analogue after the gasification reaction at 1273 K (a) SEM backscattered image optimised for carbon microstructure at X500 magnification (b) SEM backscattered image optimised for the mineral component at X1000 (c – g) EDS maps.

4.2.4.3.Metallurgical coke

Before the gasification reaction

Figure 4.51 shows SEM backscattered images and EDS maps of the metallurgical coke before the gasification reaction.

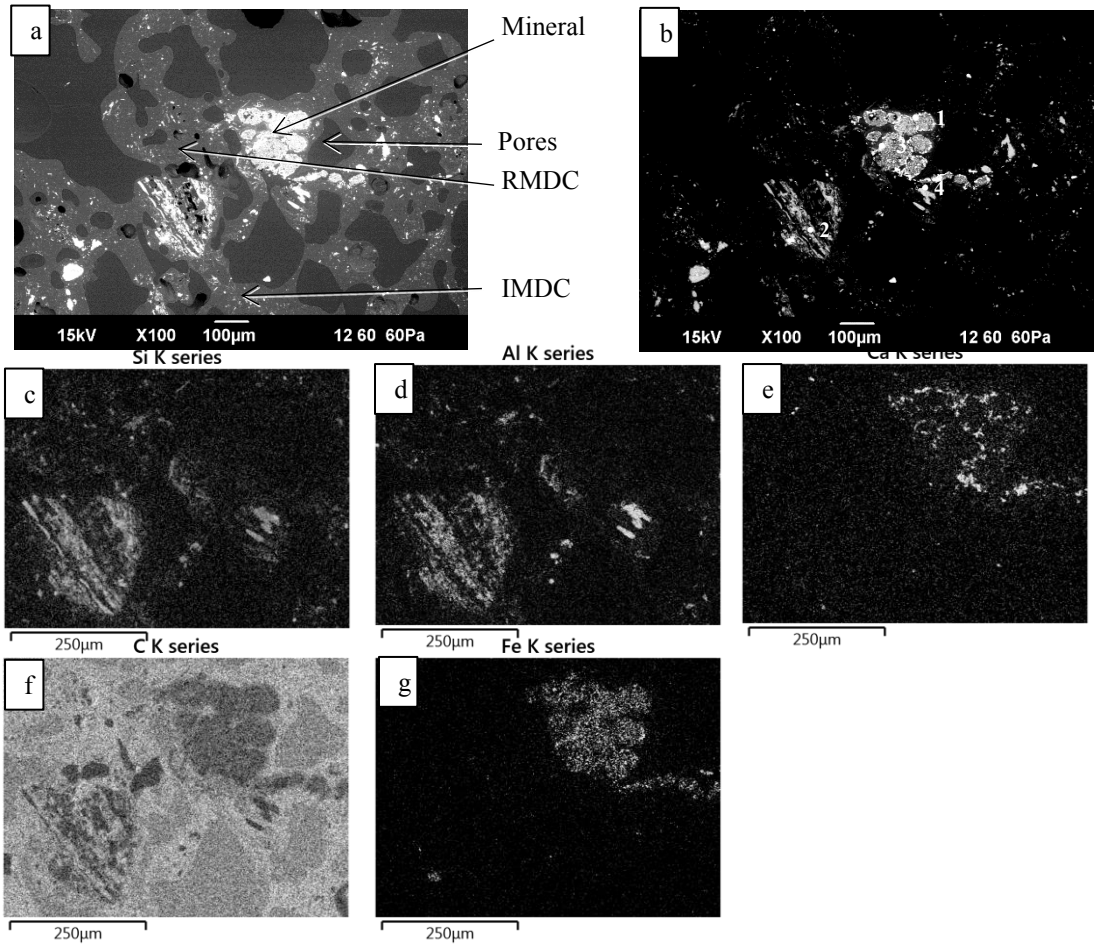

Table 4.22: Point analysis of metallurgical coke (mass %) (Figure 4.51 b)

Label	1	2	3	4
O	41.6	49.5	29.7	51.8
Al	1.2	23.1	Trace	Trace
Si	1.4	24.4	46.7	2.4
Ca	36.7	Trace	Trace	17.4
Fe	18.3			48.2
Total	100.0	100.0	100.0	100.0

Figure 4.51: SEM backscattered images (X100) and EDS maps of the metallurgical coke before the gasification reaction at X100 magnification. (a) SEM backscattered image optimised for carbon microstructure (b) SEM backscattered image optimised for mineral component (c – g) EDS maps.

Figures 4.52 shows SEM backscattered images and EDS maps at X500 and X1000 magnifications for a clear view of the carbon and mineral structures.

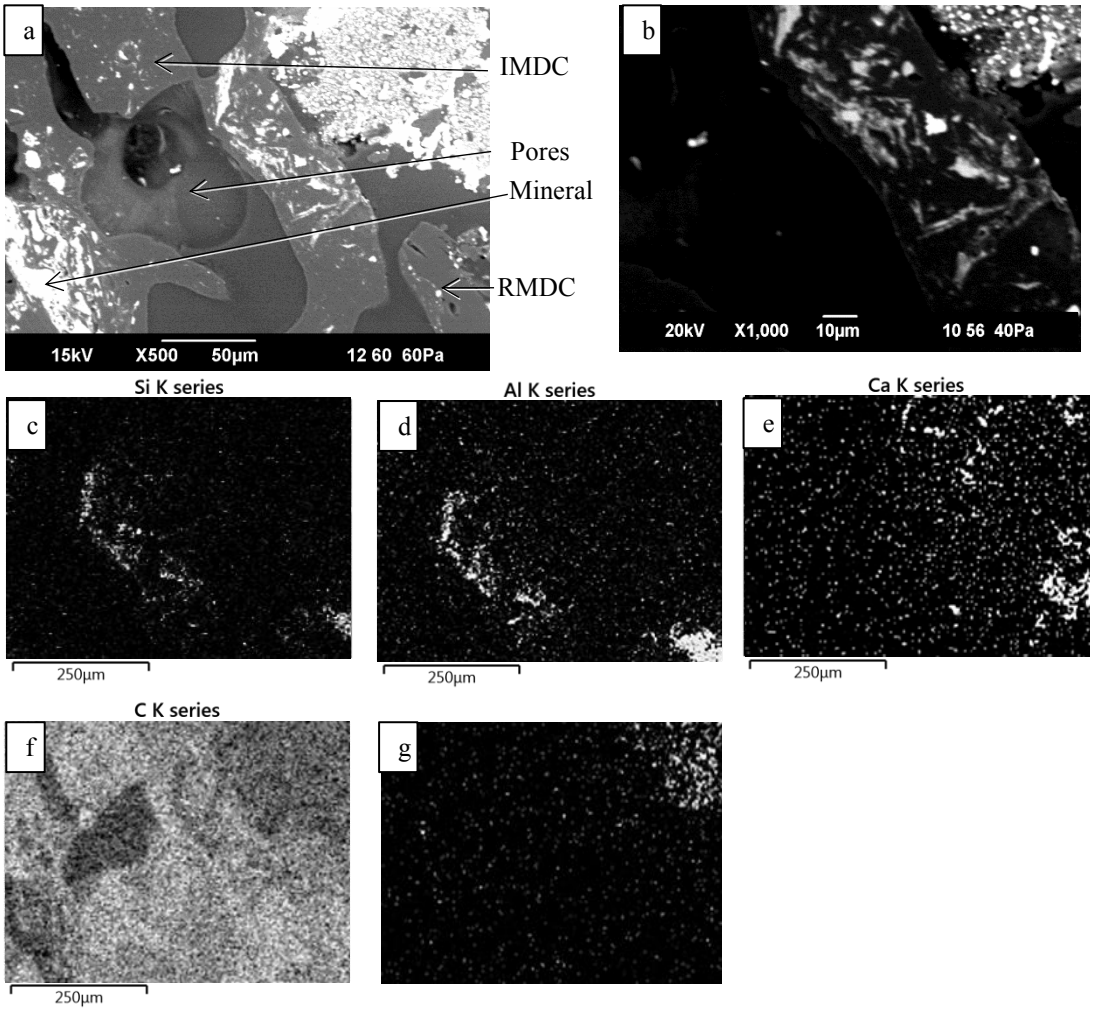

Figure 4.52: SEM backscattered images (X500 and X1000) and EDS maps of the metallurgical coke before the gasification reaction (a) SEM backscattered image optimised for carbon microstructure at X500 magnification (b) SEM backscattered image optimised for the mineral component at X1000 (c – g) EDS maps.

After the gasification reaction

Figure 4.53 shows SEM backscattered images and EDS maps of a cross-section of the metallurgical coke after the gasification reaction at 1273 K for 2 hours.

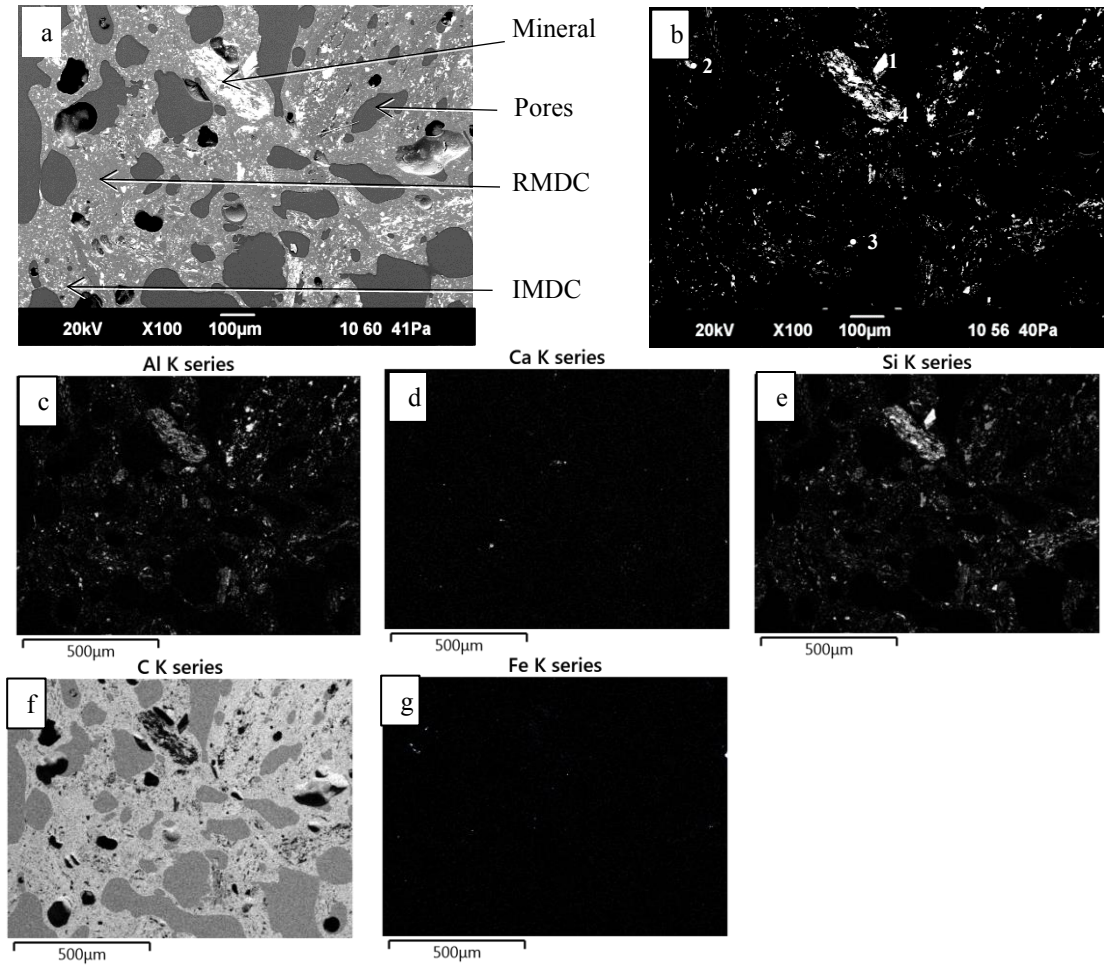

Table 4.23: Point analysis of the metallurgical coke (Figure 4.53 b)

Label	1	2	3	4
O	51.9	26.8	47.1	51.7
Al	3.1	6.8	12.1	21.5
Si	42.6	Trace	23.0	21.0
K		Trace		Trace
Ca	1.4	1.8	17.8	5.8
Fe	Trace	61.6		
Total	100.0	100.0	100.0	100.0

Figure 4.53: SEM backscattered images (X100) and EDS maps of the metallurgical coke after the gasification reaction at 1273 K (a) SEM backscattered image optimised for carbon microstructure (b) SEM backscattered image optimised for mineral component (c – g) EDS maps.

Figure 4.54 shows SEM backscattered images and EDS maps of a representative area of a cross-section of metallurgical coke after the gasification at 1273 K for 2 hours.

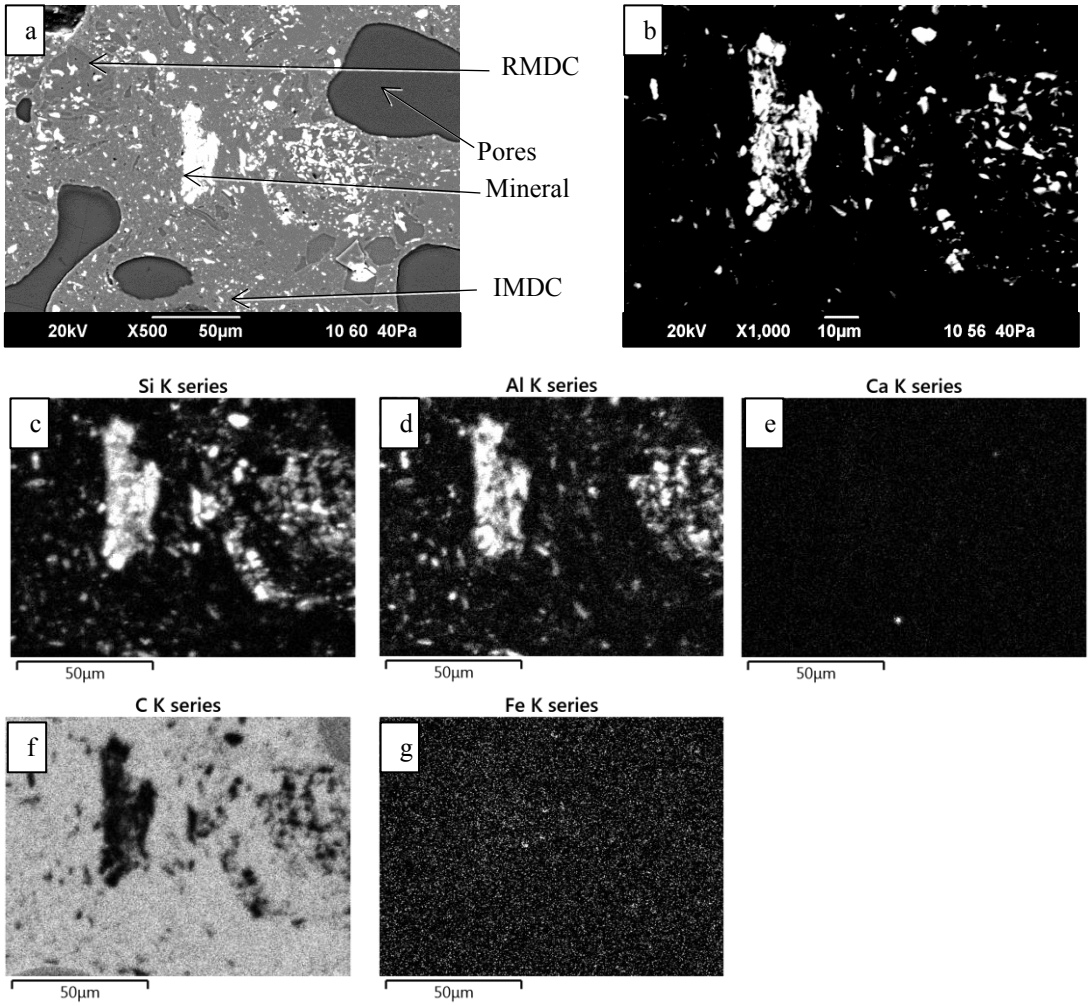

Figure 4.54: SEM backscattered images (X500 and X1000) and EDS maps of the metallurgical coke after the gasification reaction at 1273 K (a) SEM backscattered image optimised for carbon microstructure at X500 magnification (b) SEM backscattered image optimised for the mineral component at X1000 (c – g) EDS maps.

4.2.5. XRD characterisation

The analogues were subjected to XRD analysis both before the reaction and after the reaction at 1623 K. For analogues containing minerals, to ensure good resolution of the mineral phases, the XRD was performed at 30° to 80°. This removed the high-intensity carbon graphite peak. In some patterns, the graphite peaks are trimmed for clear observation of mineral peaks. The objective is to identify any change of the minerals before and after the gasification reaction. The minerals status before and after the reaction were similar except for in lime doped, non- crystalline CAS doped and quartz dopes coke analogues (See *Figures 4.60, 4.61 and 4.63).* (Peaks with low intensity were observed that are from the impurities present in Bakelite (See Appendix III for the Bakelite impurity analysis)).

Base coke analogue

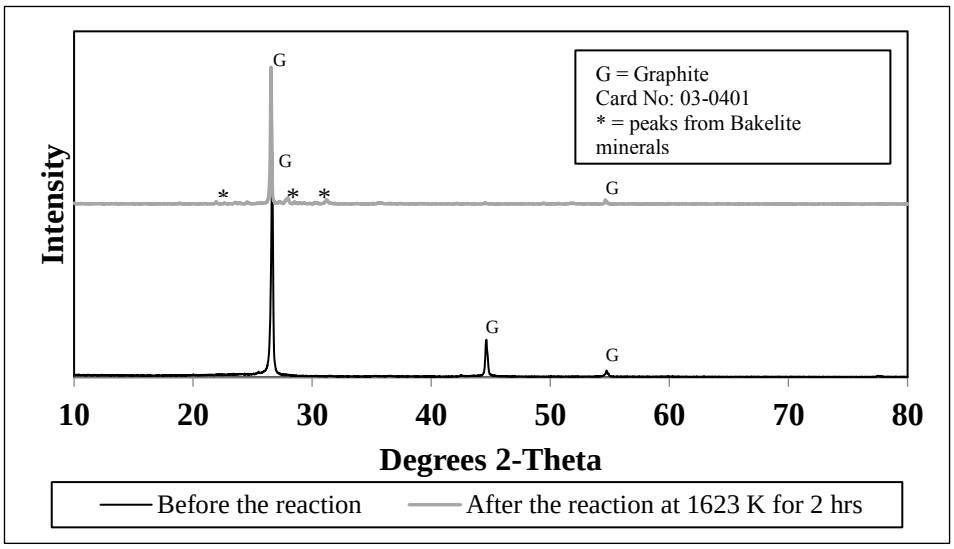

Figure 4.55: XRD patterns of the base coke analogue before and after the gasification reaction.

It can be seen from the Figure 4.55, the graphite peak at ~ 45° of the sample before the reaction has disappeared after the reaction. This may indicate preferential gasification/reaction on certain graphite planes.

Alumina doped coke analogue

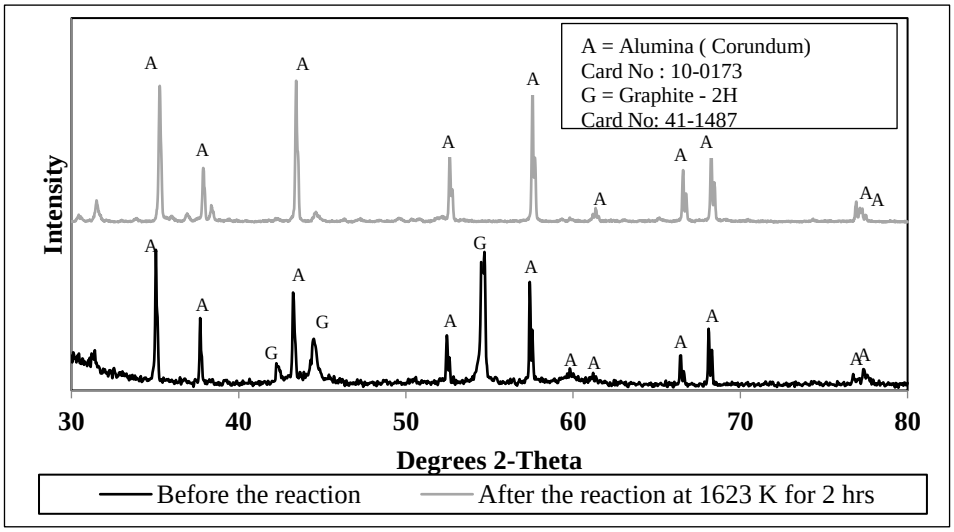

Figure 4.56: XRD patterns of the alumina doped coke analogue before and after the gasification reaction.

Calcium aluminates

XRD patterns of the calcium aluminates doped coke analogues are shown in *Figure 4.57 – 4.59*. It can be seen that the calcium aluminates originally added to the coke analogue component mixture, are observed in fired analogue.

CA6 doped coke analogue

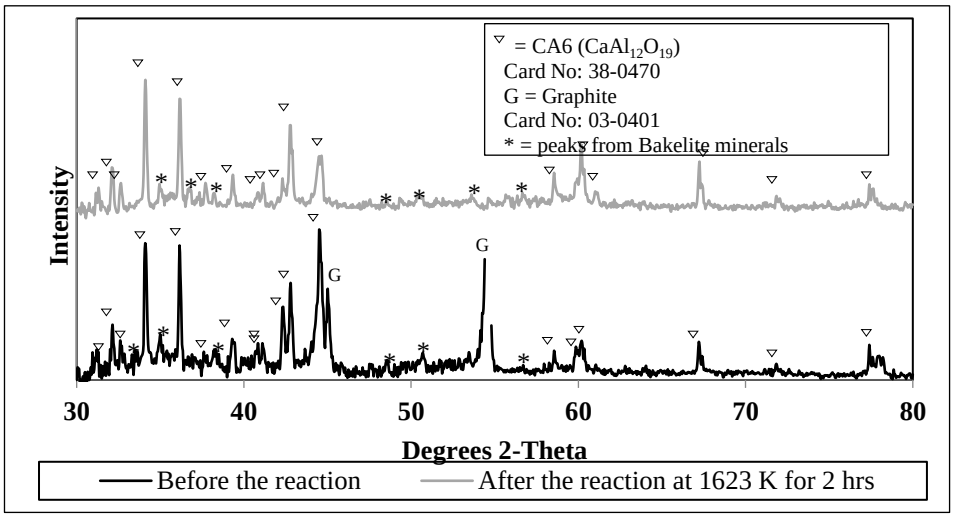

Figure 4.57: XRD patterns of the CA6 doped coke analogue before and after the gasification reaction.

CA doped coke analogue

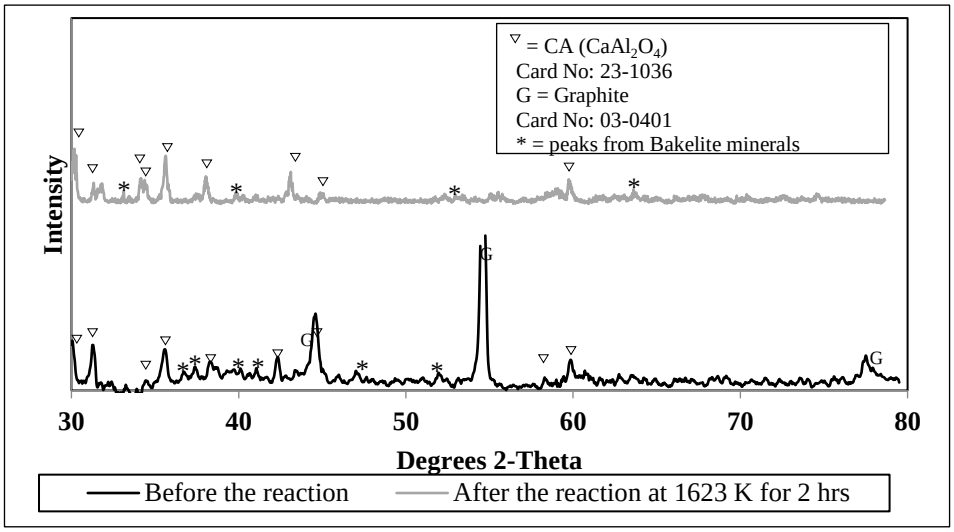

Figure 4.58: XRD patterns of the CA doped coke analogue before and after the gasification reaction.

C3A doped coke analogue

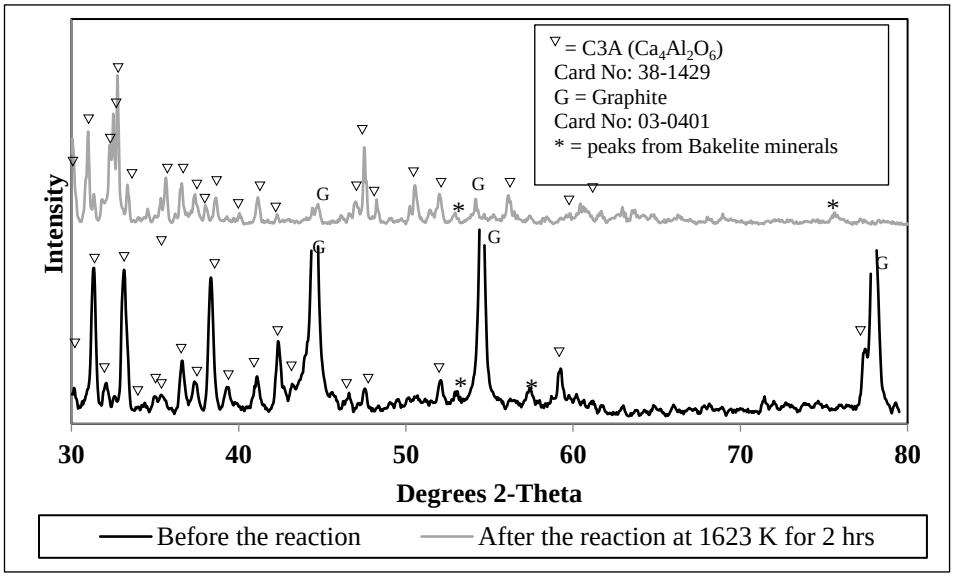

Figure 4.59: XRD patterns of the C3A doped coke analogue before and after the gasification reaction.

Lime doped coke analogue

Lime doped coke analogue was observed to contain a small amount of calcium silicate and C3A in addition to lime. The mineral components were qualitatively analysed using MAUD software and are given in *Table 4.24*. The sigma value < 2 indicates a good fitting of the experimental XRD pattern with the standard. The appearance of these additional minerals indicates a reaction of lime with the base mineral impurities during the preparation of the coke analogue. The reaction is detailed in section 4.3.

Table 4.24: Quantitative analysis of the lime doped coke analogue before and after the gasification reaction at 1623 K for 2 hours.

	Before the reaction		After the reaction	
	Quantity / %	Sigma	Quantity / %	Sigma
Lime	83.6	1.45	80.9	1.83
C3A	14.5		16.1	
Calcium silicate	1.9		3.0	

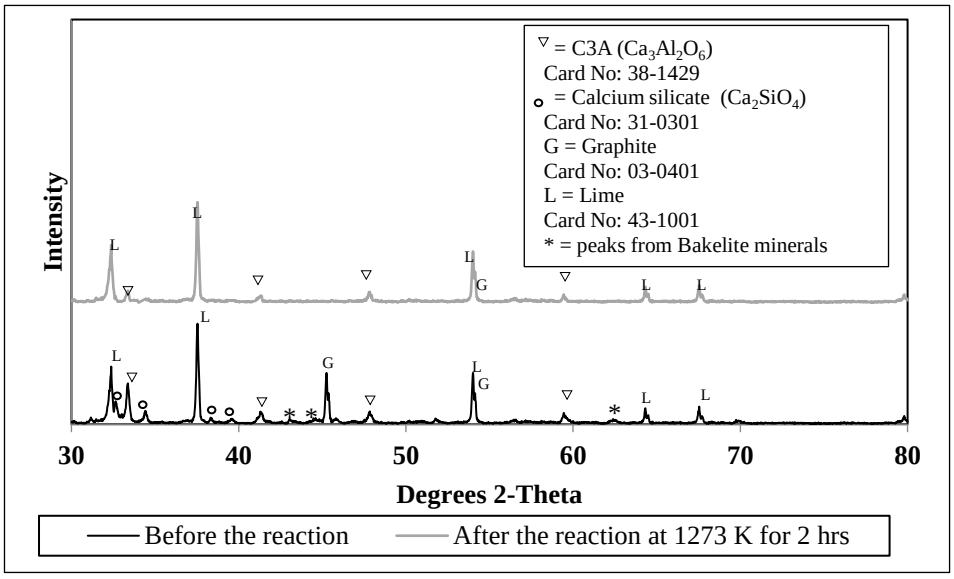

Figure 4.60: XRD patterns of the lime doped coke analogue before and after the gasification reaction.

CAS 1 doped coke analogue

Figure 4.61 and *4.62* show the XRD patterns of the fired coke analogue samples and the sample after the reaction. CAS 1 was originally crystalline CAS and CAS 2 was originally non-crystalline CAS, however, after firing both coke analogues contained the same crystallinity.

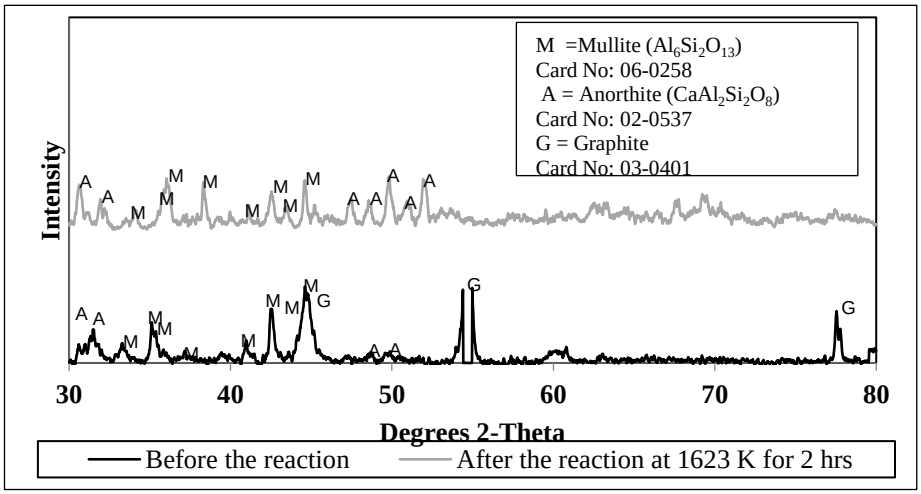

Figure 4.61: XRD patterns of the CAS 1 doped coke analogue before and after the gasification reaction.

CAS 2 doped coke analogue

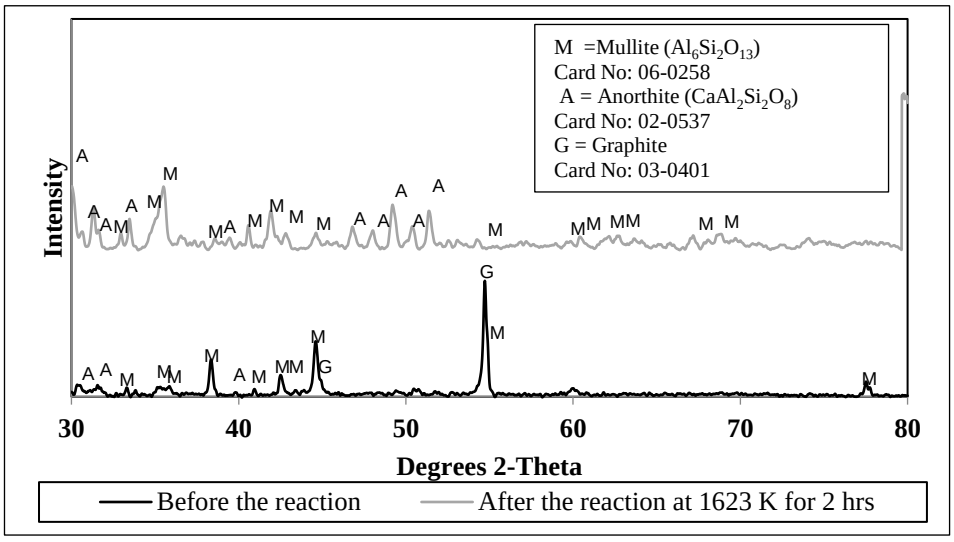

Figure 4.62: XRD patterns of the CAS 2 doped coke analogue before and after the gasification reaction.

Quartz doped coke analogue

Figure 4.63 shows the XRD patterns of the quartz doped coke analogue before and after the gasification reaction. The patterns show the formation of cristobalite (a high-temperature polymorph of SiO_2) during the reaction probably due to the temperature (1623 K) used for the reaction.

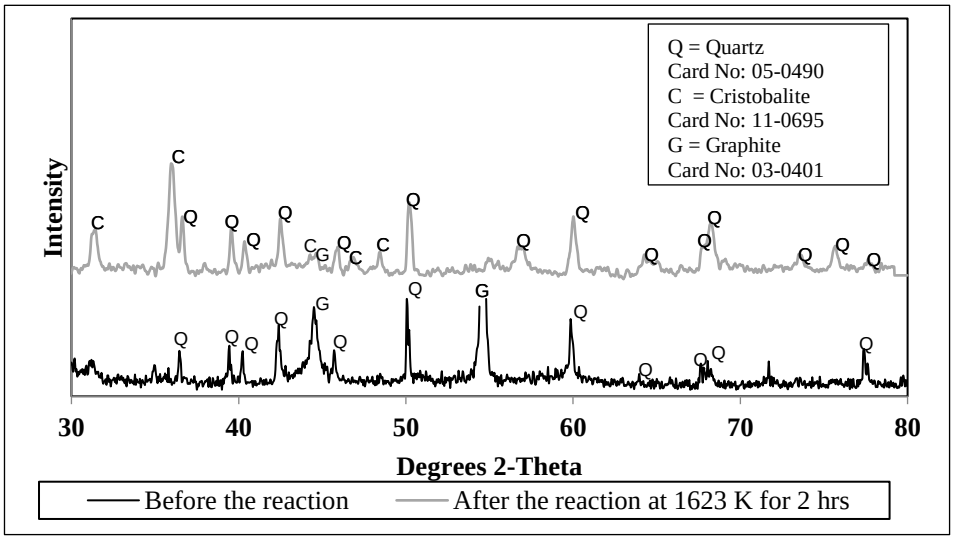

Figure 4.63: XRD patterns of the quartz doped coke analogue before and after the gasification reaction.

Table 4.25 shows the quantitative analysis of quartz doped coke analysis after the reaction.

Table 4.25: Quantitative analysis of the quartz doped coke analogue after the gasification reaction at 1623 K for 2 hours

	Quartz	Cristobalite	Sigma
Amount / %	52.5	47.5	1.95

Graphite peak of Ca-containing minerals added coke analogues

The full width at half maximum (FWHM) of graphite 002 peaks at 26.4° was measured for graphite, base coke analogue and some minerals (lime, CA6, CA and C3A) added coke analogues. This was carried out to check for the possibility of Ca intercalation. *Figure 4.64* shows a comparison of the graphite peaks of the coke analogues and graphite. Given in *Table 4.26* are the FWHM values obtained from Traces, an XRD data analysis software [160].

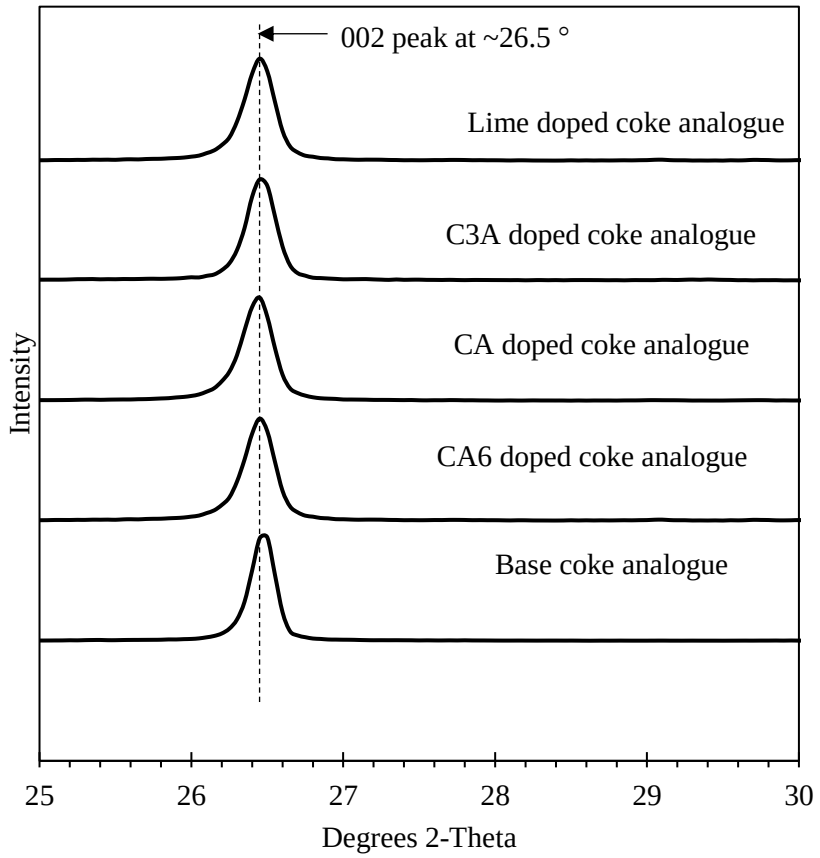

Figure 4.64: XRD patterns of base coke analogue and minerals (CA6, Ca, C3A and lime) doped coke analogues showing the graphite 002 peak at ~26.5 °.

Table 4.26: d spacing of graphite 002 peak

Sample	d spacing (nm)
Base coke analogue	0.345
CA6 doped coke analogue	0.345
CA doped coke analogue	0.346
C3A doped coke analogue	0.346
Lime doped coke analogue	0.346

4.3.Dispersion of lime in the coke analogue

The mineral dispersion of the lime doped analogue given in *Figures 4.35* to *4.38* was significantly different from the other coke analogues studied. Distinct particles of the original added size of 38 – 53 µm were not readily observed in the lime doped coke analogue. The lime was dispersed throughout the analogue carbon matrix < 1 µm sized particles and appeared like clusters (*Figure 4.65*).

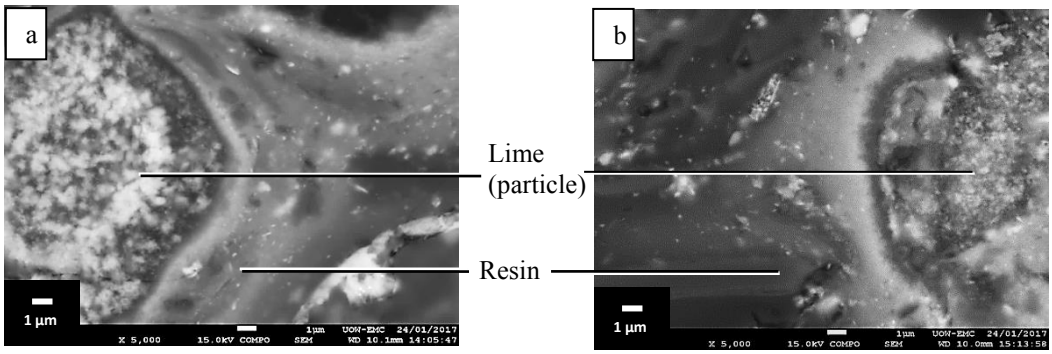

Figure 4.65: SEM backscattered images of selected lime (particles) of the lime doped coke analogue before the gasification reaction, at X5000 magnification.

Lime was suspected to be dissolved in/ reacted with liquid Novolac resin in propylene glycol. To test this possibility of this reaction lime was added to the Novolac in propylene glycol and assessed for the reaction using SEM-EDS. For comparison, this procedure was also carried out for alumina and calcium aluminates (CA6, CA and C3A). These mixtures were cured and fired under the same conditions provided for coke analogue preparation. As with the coke analogue, HTMA was added to the samples as a curing agent. Given in *Figures 4.66 – 4.70* are the SEM backscattered images and EDS maps for the samples. The original mineral particles of size 38 – 53 µm are also shown.

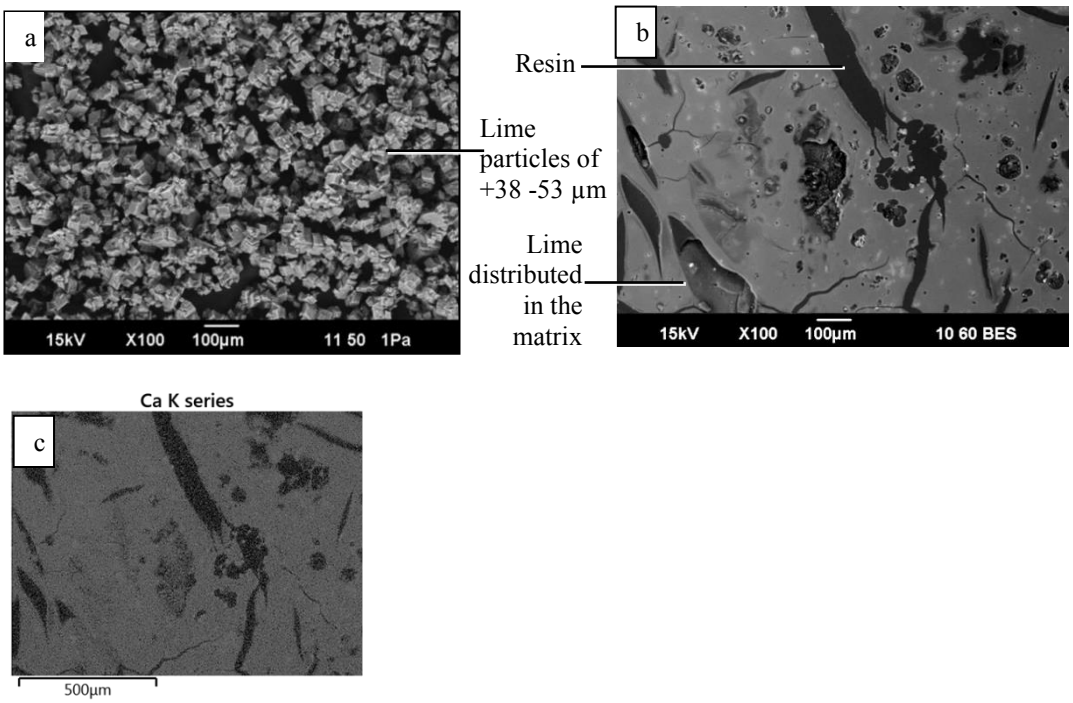

Figure 4.66: a) An SEM backscattered image of lime particles of the size 38 – 53 µm. b) An SEM backscattered image of the lime + Novolac mixture. c) The EDS map of the Ca K series in the lime + Novolac mixture.

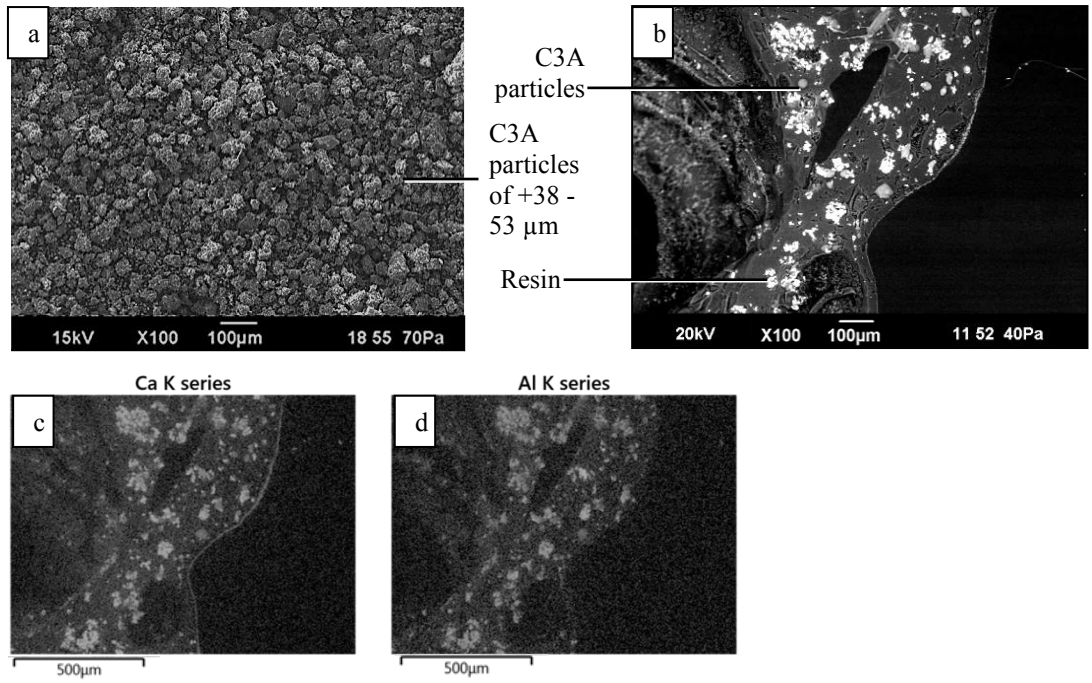

Figure 4.67: a) An SEM backscattered image C3A particles of the size 38 – 53 µm. b) An SEM backscattered image of the C3A + Novolac mixture. c) – d) EDS maps of the Ca K series and Al K series in the C3A + Novolac mixture.

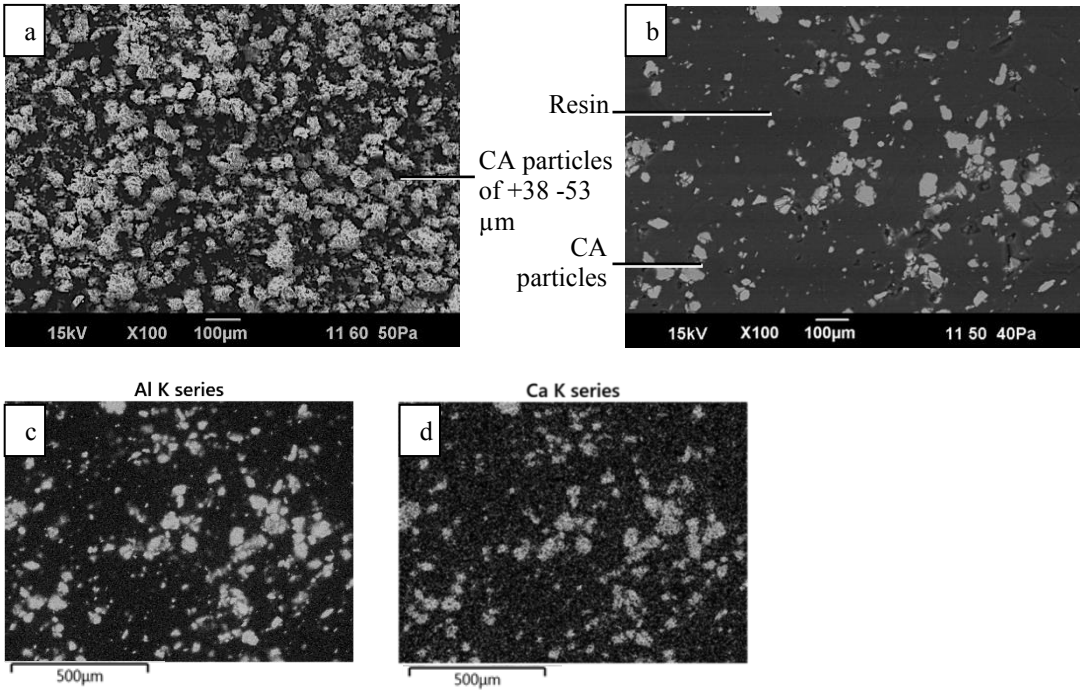

Figure 4.68: a) An SEM backscattered image CA particles of the size 38 – 53 µm. b) An SEM backscattered image of the CA + Novolac mixture. c) – d) EDS maps of the Ca K series and Al K series in the CA + Novolac mixture.

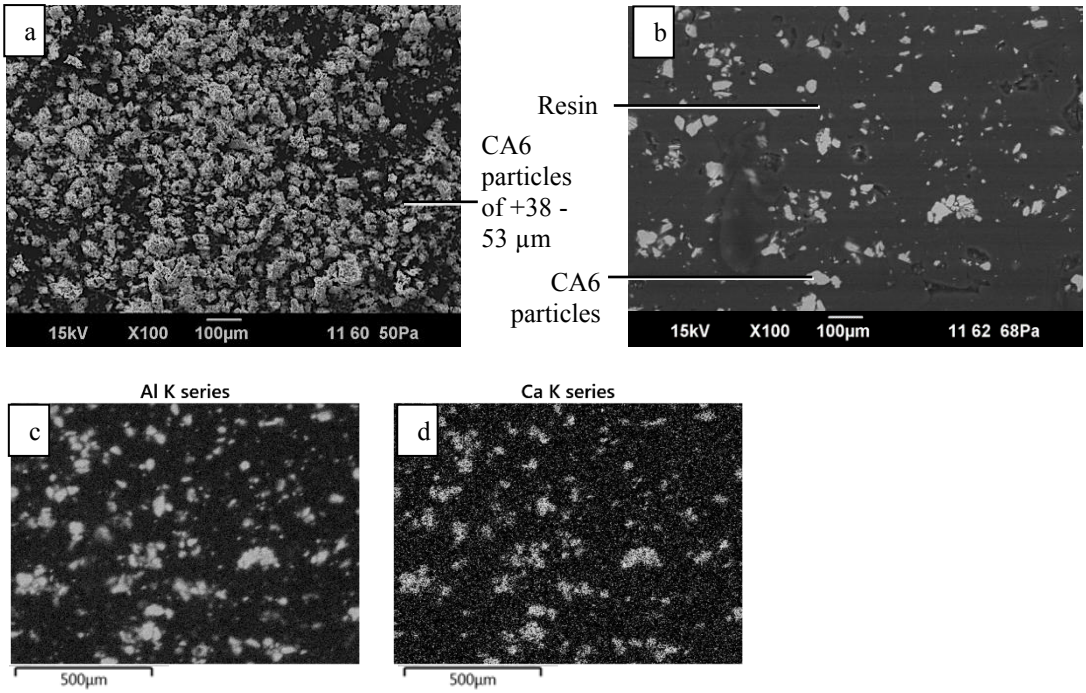

Figure 4.69: a) An SEM backscattered image CA6 particles of the size 38 – 53 µm. b) An SEM backscattered image of the CA6 + Novolac mixture. c) – d) EDS maps of the Ca K series and Al K series in the CA6 + Novolac mixture.

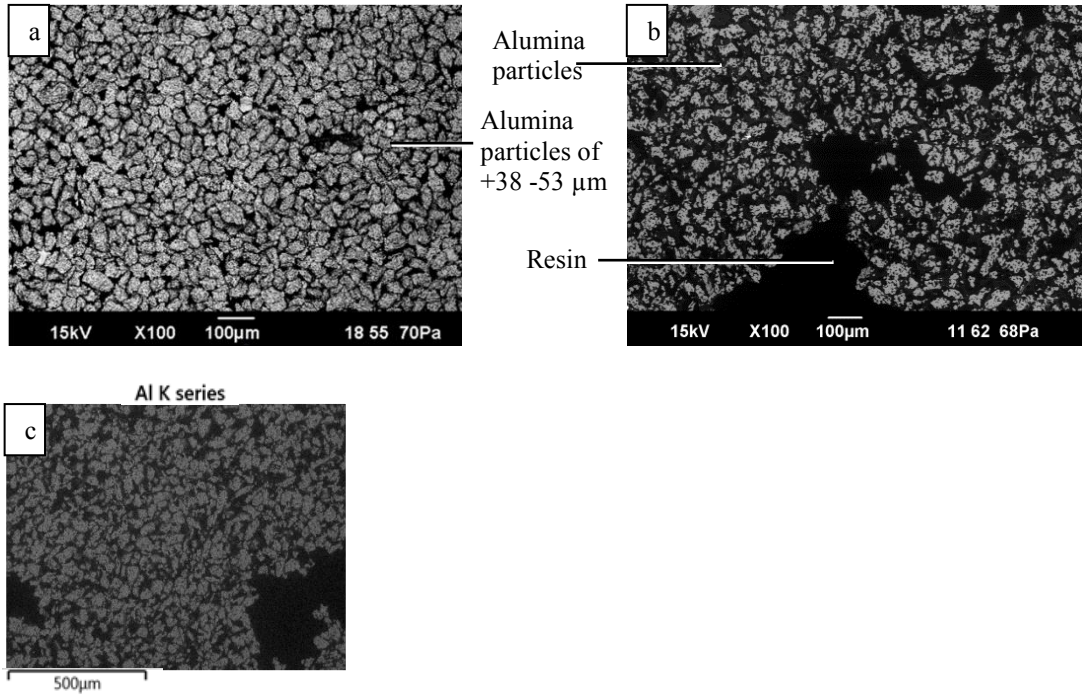

Figure 4.70: a) An SEM backscattered image Alumina particles of the size 38 – 53 µm. b) An SEM backscattered image of the Alumina + Novolac mixture. c) The EDS map of the Al K series in the alumina + Novolac mixture.

XRD pattern of Lime +Novolac mixture was compared to that of Lime.

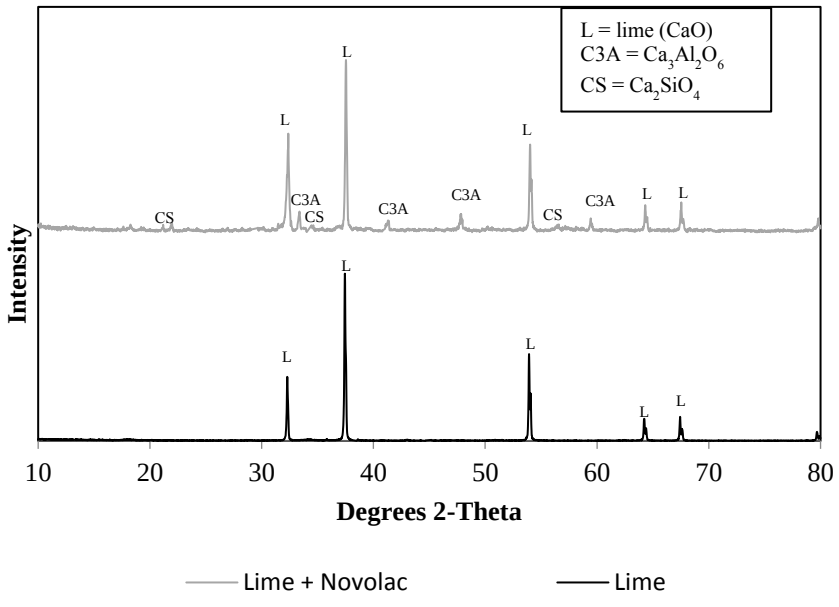

Figure 4.71: XRD patterns of Lime and Lime + Novolac mixture

4.4.Thermodynamics of the coke analogue samples/ minerals

4.4.1. Phase stability of the coke analogue samples

The mineral phases and the elemental compositions of the coke analogues were analysed using XRD and EDS respectively. The mineral phases were also predicted using MTDATA calculations. *Table 4.27* summarises the predicted phases vs observed phases from XRD, EDS analysis and MTDATA. The atomic % EDS analyses expected and observed (for a selected mineral particle) for the phase identification are given in Appendix VII.

The thermodynamic stability of the minerals doped coke analogue samples was evaluated using MTDATA [152]. The basis of the calculation was the phase stability in an excess of carbon-graphite.

Table 4.27: A summary of predicted and observed phases in minerals doped coke analogues.

Coke analogue	Added minerals	Observed phase(s)		
		XRD	EDS	MTDATA
Alumina doped coke analogue	Corundum (Al_2O_3)	Corundum (Al_2O_3)	Al_2O_3	Corundum (Al_2O_3)
CA6 doped coke analogue	CA6	CA6	CA6	CA6
CA doped coke analogue	CA	CA	CA	CA
C3Adoped coke analogue	C3A	C3A	C3A	C3A
Lime doped coke analogue	Lime (CaO)	Lime (minor amounts of C3A and Calcium silicate)	Not definable	*Halite (CaO)
CAS doped coke analogue	Mullite ($Al_6Si_2O_{13}$) Anorthite ($CaAl_2Si_2O_8$), Ghelenite ($Ca_2Al[AlSiO_7]$)	Mullite ($Al_6Si_2O_{13}$), Anorthite ($CaAl_2Si_2O_8$)	Not readily definable	Mullite ($Al_6Si_2O_{13}$), Andalusite (Al_2SiO_5), Ghelenite ($Ca_2Al[AlSiO_7]$), Plagioclase Feldspar (Anorthite [161] ($CaAl_2Si_2O_8$))
Quartz doped coke analogue	Quartz (SiO_2)	Quartz, Cristobalite (SiO_2)	SiO_2	Tridymite (SiO_2)

*Halite = lime (Note that in MTDATA, CaO is identified as Halite due to the halite like structure of lime)

4.4.2. CaO activities in calcium aluminates used in coke analogue preparation

Figure 4.78 is the plot of CaO activities vs number of moles of CaO in calcium aluminates at 1373 K. The activity increases with increasing number of moles of CaO in the calcium aluminates.

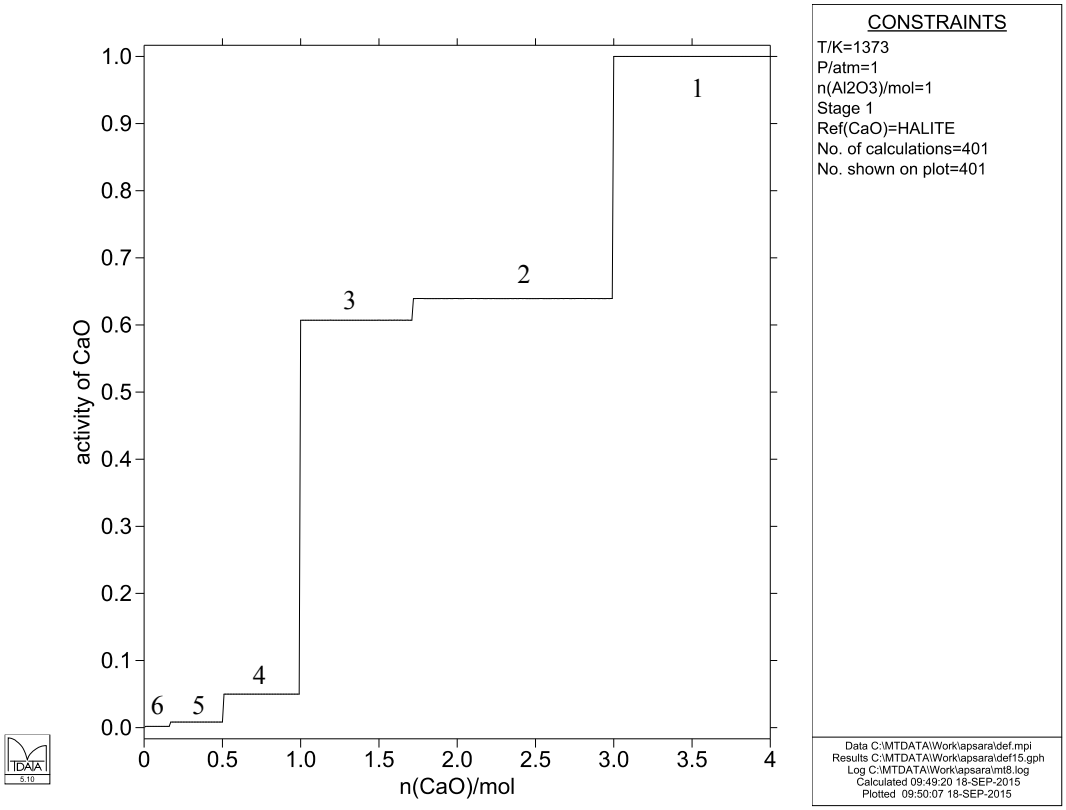

1 – C3A/ CaO
2 – C12A7/ C3A
3 – CA/ C12A7
4 – CA2/ CA
5 – CA6/ CA2
6 – Al_2O_3/ CA6

Figure 4.71: The plot of CaO activity vs the number of moles of CaO in calcium aluminates at 1373 K, where the reference state Halite represents the lime phase.

4.4.3. Mass fraction of calcium aluminates

Figure 4.79 is the plot of the mass fraction of all the calcium aluminate phases vs the number of moles of CaO. This diagram shows the available phases and the mass fraction at any number of moles of CaO.

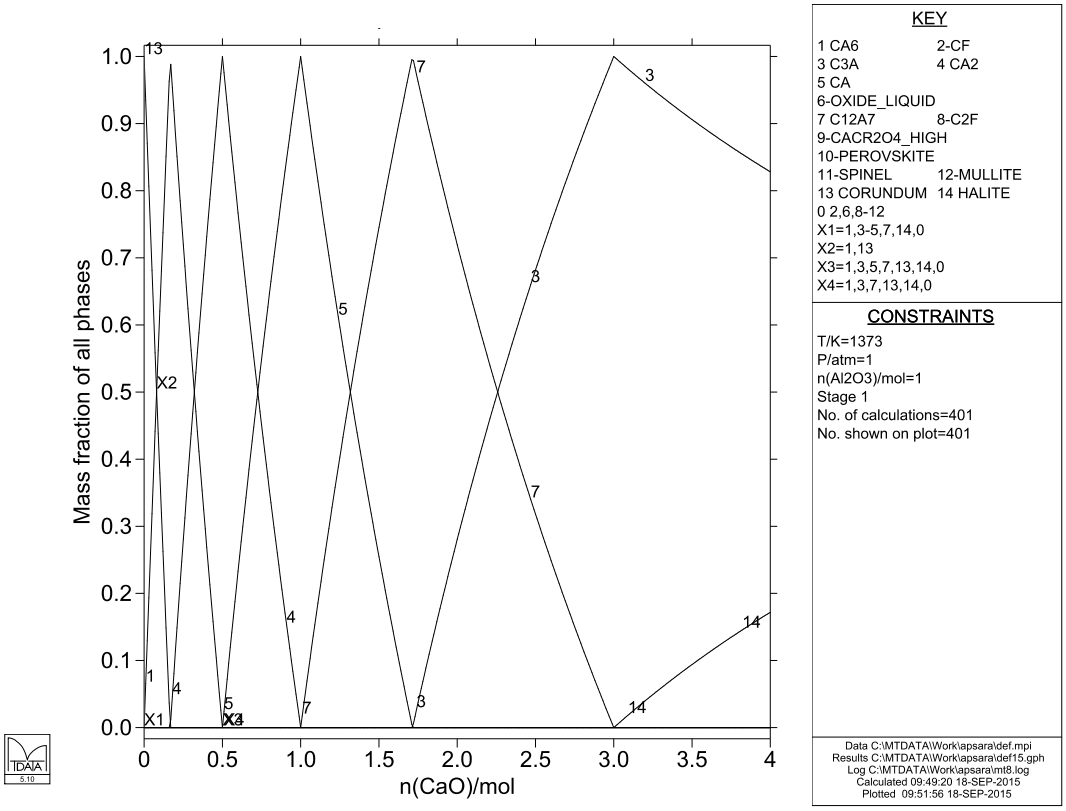

1 – CA6 3 – C3A 4 – CA2 5 – CA 7 – C12A7

Figure 4.72: The plot of mass fraction of calcium aluminates vs number of moles of CaO in calcium aluminates at 1373 K.

Chapter 5

Suitability of coke analogue for metallurgical coke studies

From the literature review, it was identified that the understanding and predicting of coke behaviour in the blast furnace is difficult. The different sources provide contradictory or widely variable information. For example, the most common method of assessing coke reactivity, CRI, shows values in a wide range, even for cokes derived from the same coal [17].

The reasons for the observed variations in results are often related to coke's;

1. complexity, and
2. heterogeneity.

Coke has a complex structure made up of different carbonaceous forms/textural components and minerals, and has a highly variable porous structure. These features are primarily based on the maceral groups and minerals of the parent coal, volatiles given off during coking, and the coking conditions. In addition to this complexity, coke often displays significant heterogeneity in any metric(s) used to characterise its carbonaceous forms, mineralogy, phase dispersion, morphology, porosity, and reactivity [18, 19].

When exposed to high temperatures and reactive atmospheres, the inherent complexity, as well as the heterogeneous compositional and structural features of coke, make it difficult to isolate the effects of specific components on coke behaviour and reaction kinetics [24, 34, 162]. This has to some degree limited the progress in coke studies in assessing and predicting the impact of minerals on reactivity and reaction kinetics [18, 19].

In this PhD project, the complexity and heterogeneity issues associated with coke kinetic studies were avoided by using a coke analogue. The coke analogue has been produced using laboratory grade materials (graphite, Bakelite, Novolac and minerals). This coke analogue was developed to have a simplified carbon structure and offers control in the selection and combination of minerals, mineral particle size and dispersion, and porosity.

The use of a coke analogue leads to two main questions, the addressing of which are the primary aims of this thesis,

1. How representative is the coke analogue of the metallurgical coke with respect to general characteristics?

2. Does the analogue have similar rate controlling kinetics to that of industrial coke?

This chapter will discuss these two questions, thereby fulfilling the first two aims of the thesis.

In subsequent chapters, the other aims are discussed as follows.

- Chapter 6: Aim 3, understanding the effect of Ca in added minerals on coke reactivity. The Ca-containing minerals were studied under two categories; minerals in the $CaO – Al_2O_3$ binary system and minerals in the $CaO – Al_2O_3 – SiO_2$ ternary mineral system.
- Chapter 7: Aim 3, understanding the mechanism of the gasification of coke analogue with Ca-containing binary and ternary mineral systems.
- Chapter 8: Aim 4, the applicability of the RPM to examine the coke analogue gasification.

5.1. How representative of metallurgical coke is the coke analogue?

For the coke analogue to represent the metallurgical coke, there should be similarities in the key characteristic properties of both materials. In this section, the following properties in the coke analogues will be discussed and compared with those of the metallurgical coke.

1. Porosity.
2. Microscopic analysis.
3. Carbon bonding.
4. General reactivity with CO_2 gas.
5. A general mechanism for the coke analogue reactivity with CO_2 gas.

For the coke analogue to be a suitable material in metallurgical coke studies, it is also necessary for the coke analogue to have good control and reproducibility in the aforementioned characteristic properties.

5.1.1. Porosity

The porosities of the coke analogues with and without mineral addition were measured using optical microscopy, followed by image analysis and mercury porosimetry.

Coke analogue porosity

Given in *Table 5.1* are the porosity values of the base coke analogue (analogue without added minerals) obtained from two methods; optical microscopy and mercury porosimetry. The two methods show different porosity values as the result of different pore diameter ranges being accessible to each technique.

Table 5.1: The porosity of coke analogue measured using optical microscopy and mercury porosimetry methods

Method	Accessible pore diameter range / µm	Porosity / %	Advantages	Disadvantages
Optical Microscopy followed by image analysis	10-500	29.3 ±2.3	• Simple method • Repeatable • Measurements can be carried out on-campus	• Cannot measure the pores with diameters < 10 µm
Mercury porosimetry	0.003-300	39.6±2.8	• A standard technique • Can measure pores with a lower diameter as 0.03 µm	• Not available on-campus • Samples damage during the measurements

The coke analogue has shown repeatability in porosity and pore size distribution. Given in *Figure 3.20* are the pore size distribution of different base coke analogues (the average result is reproduced below in *Figure 5.1(a)*). These results show the controllability in porosity values. The repeatability and the controllability were also confirmed for the coke analogues prepared by doping with different minerals. Given in *Figure 5.1 (a)* are the pore size distribution of different minerals-doped coke analogues (reproduced from *Table 4.1* and *Figure 4.12*). Porosity values of the coke analogues are in a narrow range of 29.3 – 33.3 % with a ± 2.3 % of scattering, showing the controllability in porosity and pore size distribution.

Comparison of coke analogue porosity with the metallurgical coke porosity

In *Figure 5.1*, the porosity distributions of the metallurgical coke measured in this study, and the metallurgical coke data reported in the literature, are given and compared to the coke analogue. *Figure 5.1 (b)* represents measurements of three separate pieces of coke from one batch, and *Figure 5.1 (c)* represents three measurements each on two different batches of the same coke. These data were originally reported in *Figures 2.6, 4.12* and *4.13*.

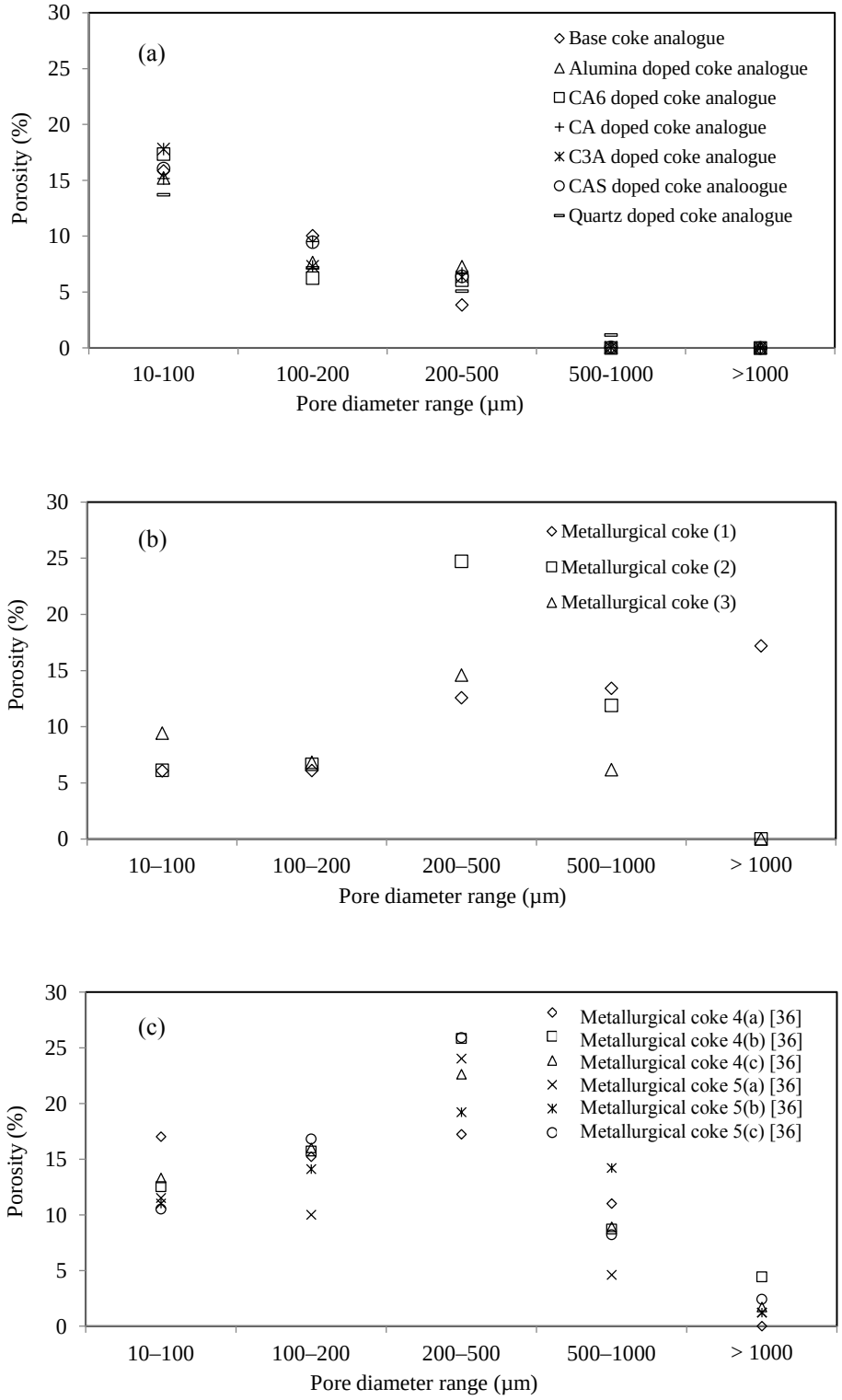

Figure 5.1: Figure 5.1: A plot of pore size distribution in (a) coke analogues, (b) metallurgical coke (this study) and (c) metallurgical coke from the literature [34]. The base coke analogue results are the average of that given in Figure 3.20. The metallurgical cokes (1) to (3) used in this study are from the same source. The metallurgical coke 4(a, b, c) are from the same batch, 5(a, b, c) from a different batch.

From *Figure 5.1* it can be seen that all the coke analogues have a similar porosity distribution. The porosity distribution of the metallurgical coke is highly variable, with a scatter much greater than the scatter of the coke analogue. These results confirm not only that the analogue's porosity is controllable / reproducible but also that it has much less inherent scatter than that of metallurgical coke porosity. The majority of the analogue porosity data are in the 10 – 200 µm range. This at least in part overlaps with pore sizes representative of metallurgical coke (see *Figures 5.1 (b) and (c)*).

Therefore, the porosity in the pore size range of 10-200 µm the coke analogue is representative of the metallurgical coke. It is also more reproducible and controllable with respect to porosity and pore size distribution than the metallurgical coke.

5.1.2. Microscopic analysis

The coke analogue microstructure was characterised using optical and electro-optical (SEM) microscopy. These methods are the widely used methods in coke analysis [2, 4, 6, 7, 17, 20-22, 25, 27, 34, 38, 46, 47, 49, 76].

Coke analogue microscopic analysis

Microscopic analyses of the analogues using plane polarised optical microscopy, cross polarised microscopy, and SEM are given in *Figures 5.2 (a)* to *(c)* respectively. In the coke analogue, the carbon matrix is made up of carbon from added graphite and fired phenolic resin (Bakelite and Novolac resin). In the plane polarised and the cross polarised optical microscopy the graphite grains were sensitive to reflection, *i.e*. they had an anisotropic character. The carbon derived from the fired phenolic resin is not sensitive to reflection, *i.e*. they are isotropic in character. Under the SEM, graphite had a grain-like structure with two different size ranges, similar in size to the graphite added to the coke analogue (<45 µm and <150 µm). The carbon derived from the fired phenolic resins had little or a less obvious grain structure.

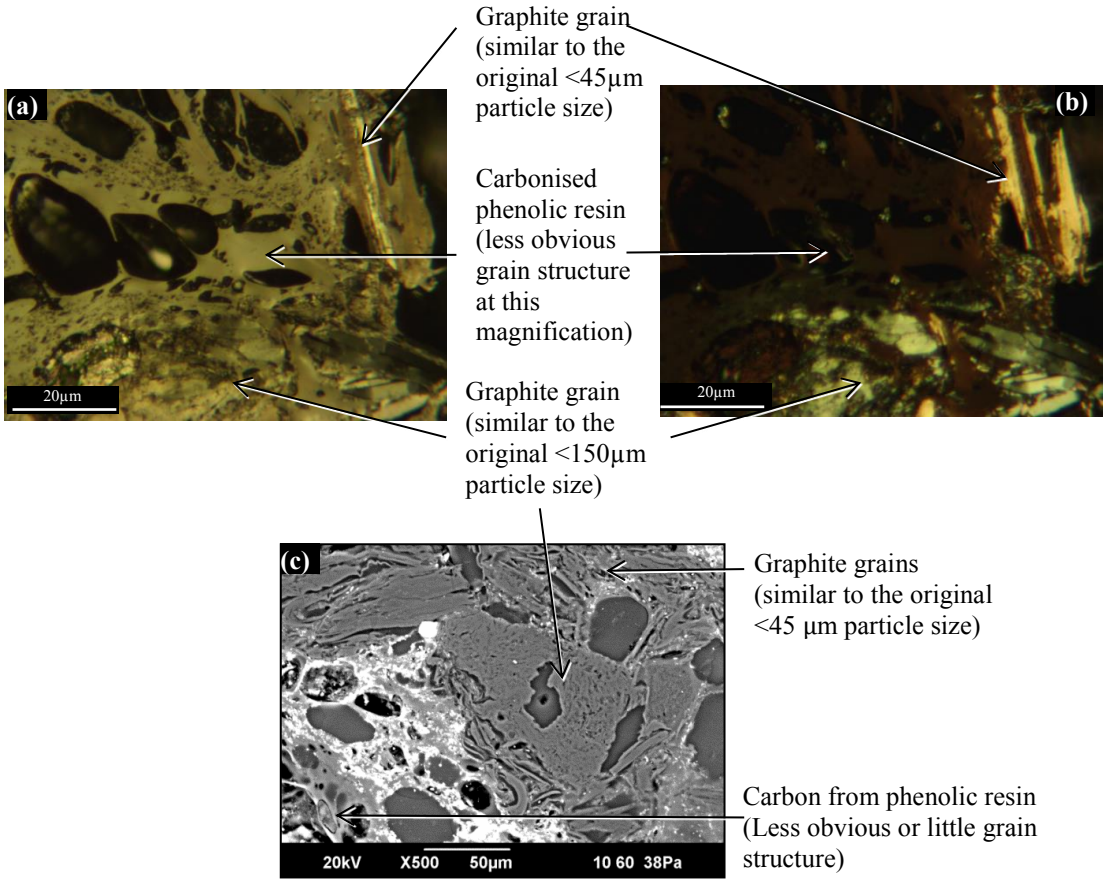

Figure 5.2: The micrographs of the fired base coke analogue. (a) Plane polarised optical microscopy (b) crossed polarised optical microscopy and (c) SEM backscattered image.

Comparison of coke analogue and coke microscopic analyses

Coke carbon microstructures are generally classified as IMDC and RMDC. Generally, it can be stated that IMDC and RMDC show isotropic and anisotropic characteristics respectively [49, 69, 163-165].

A comparison of the microscopic analyses of coke analogue and metallurgical coke using non-polarised optical microscopy and SEM are given in *Figure 5.3*. Inspection of this figure shows some common features with respect to the analogue and the metallurgical coke, in particular, the RMDC and IMDC-like structure in the analogue. These RMDC/IMDC-like features found in coke analogue are aligned with the RMDC/IMDC in cokes made from very low-rank coals with Ro max < 0.8 [34].

The coke analogue's microstructure is less complex than that of metallurgical coke. Furthermore, its microstructural features are more homogeneous with respect to size

and distribution.

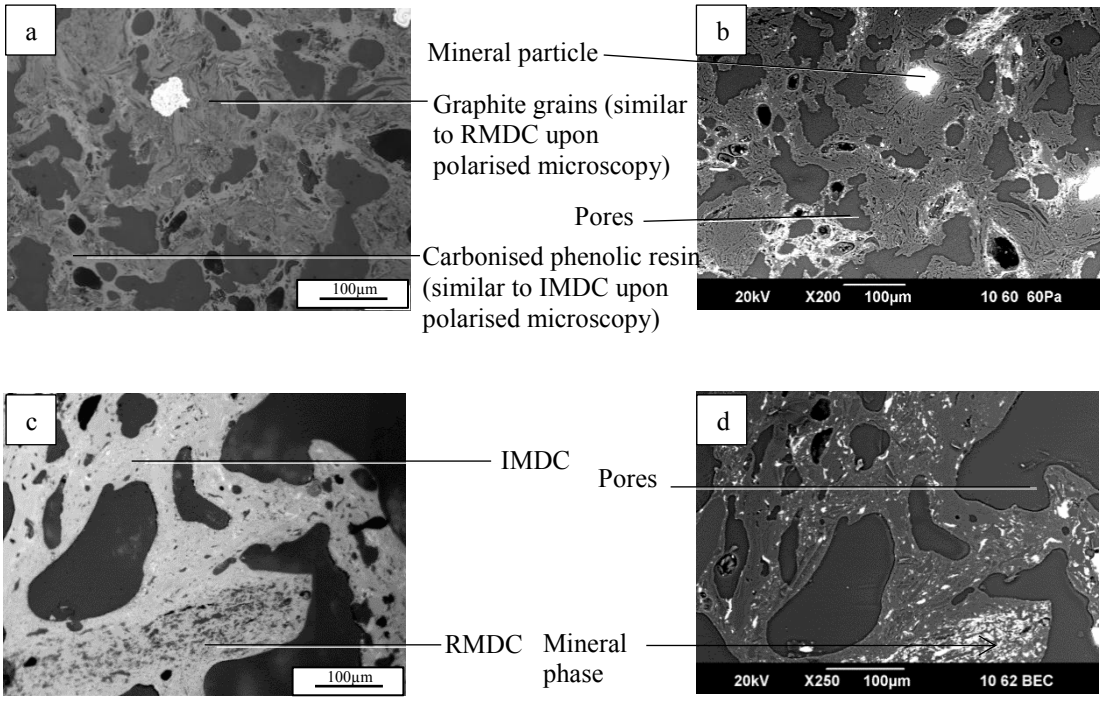

Figure 5.3: A comparison of the microscopic analysis of coke analogue and metallurgical coke (a) non-polarised optical micrograph of CA doped coke analogue (b) SEM backscattered image of CA doped coke analogue (c)) non-polarised optical micrograph of a metallurgical coke (d) SEM backscattered image of a metallurgical coke.

The similarity with respect to RMDC/IMDC, the simpler microstructure and the homogeneous nature of the analogue indicate that, from a microstructure perspective, the analogue may have application in the study of coke.

Comparison of mineral distribution in coke analogue and metallurgical coke

The coke analogue mineral distribution was assessed using SEM. In the coke analogue, the mineral particles were distributed evenly throughout the coke analogue (*Figures 4.19 - 4.50*). The mineral particles observed were within the added size range except for the lime-doped coke analogue. The change in lime particle size will be discussed in detail in Section 6.4. This even mineral distribution is different from that of metallurgical coke. Given in *Figure 5.4* are SEM backscattered images of CA-doped coke analogue (as an example) and two different randomly selected positions from a metallurgical coke lump. In the metallurgical coke, there was a significant difference

in the mineral distribution, carbon structure and pore distribution (heterogeneous) within the coke lump. In contrast, coke analogues had even mineral distribution, carbon forms and pores. The "even" homogeneous nature of the coke analogue with respect to these characteristics is advantageous with respect to its use as a laboratory material for studying the effect of mineralogy.

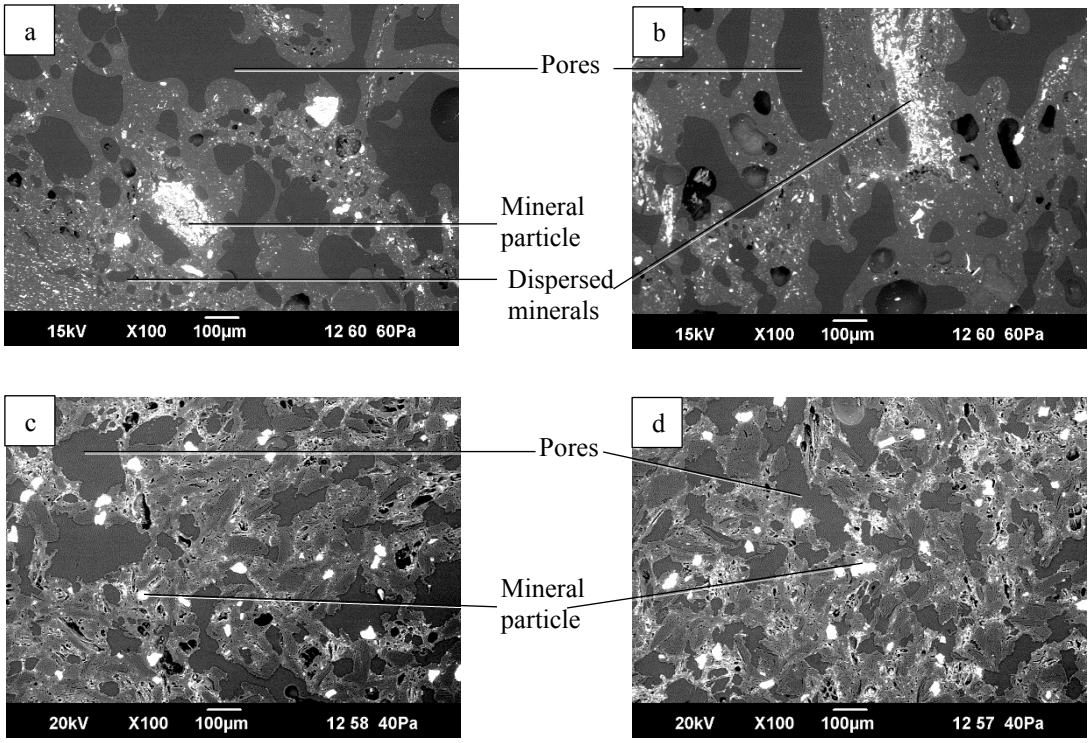

Figure 5.4: A comparison of mineral distribution in metallurgical coke and coke analogue (a) and (b) SEM backscattered images of two positions of a metallurgical coke lump at X100 magnification (c) SEM backscattered images of the centre of a CA doped coke analogue at X100 magnification (reproduced from Figure 4.24) (d) SEM backscattered images of the annulus of a CA doped coke analogue at X100 magnification.

In the coke analogue, the carbon from the phenolic resin was associated with Al-Si-Ca mineral impurities (Appendix III). This introduced ~1.1 % of mineral impurity to the coke analogue. These mineral impurities are homogeneously spread throughout the analogue. The impurities represent a baseline or a limit to the resolution with respect to mineral addition, to understand the effect of mineral on gasification in CO_2 gas. The 1.1 % of impurities, however, are significantly smaller than the ~6% of the mineral matter added to the coke analogue. Therefore, the effect of the added mineral will dominate over any effect from the impurities.

As summarised in *Table 4.27*, the minerals added to the analogue did not change on firing. The partial exception to this was the lime-doped analogue, which will be discussed later in Section 6.4. This indicates that the mineralogy of the coke analogue is, to a large degree, controlled and this should better facilitate the study of the mineral effect on the metallurgical coke.

5.1.3. Carbon bonding

Carbon bonding in carbonaceous materials was characterised using Raman spectroscopy.

Coke analogue carbon bonding

From Raman spectroscopy studies it was observed that the analogue had sp^2-sp^3 carbon bonding [88, 151]. Plots of $I_{(D)}/I_{(G)}$ *vs* $I_{(V)}/I_{(G)}$ (*Figure 2.27*) for the base coke analogue, show that the analogue exhibits a broad range of bonding types.

Comparison of coke analogue and metallurgical coke carbon bonding

Plots of $I_{(D)}/I_{(G)}$ *vs* $I_{(V)}/I_{(G)}$ for coke analogue and metallurgical coke were originally given in *Figure 2.27* and *Figure 2.12* respectively and are reproduced in *Figure 5.5* for a clear comparison.

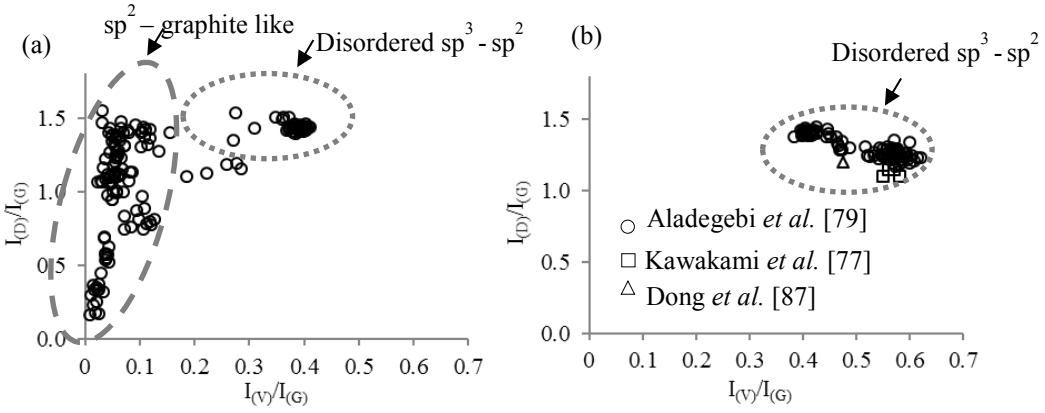

Figure 5.5: Plots of $I_{(D)}/I_{(G)}$ vs $I_{(V)}/I_{(G)}$ for (a) base coke analogue [88] (b) metallurgical cokes[88].

The Raman peak intensity ratios stated in Chapter 2 for metallurgical coke and coke analogue are also reproduced and given in *Table 5.2.*

Table 5.2: Raman peak intensity ratios for coke analogue and metallurgical cokes [88].

Material	$I_{(D)}/I_{(G)}$	$I_{(V)}/I_{(G)}$
Base coke analogue [79]	0.2 -1.5	0-0.4
Metallurgical coke [79]	1.1-1.5	0.4-0.6
Metallurgical coke [77]	0.1-1.7	0-0.6
Metallurgical coke [87]	1.3-1.4	0.1-0.6

A review of Figure 5.5 and Table 5.2 shows that the coke analogue and the metallurgical coke have a range of $sp^2 – sp^3$ type carbon bonding and that the range found in the analogue overlaps with that of the metallurgical coke. The analogue has a broader range of $sp^2 – sp^3$ bonding and is more graphitic than the metallurgical coke.

While the broader range indicates a difference, there is much similarities. The bonding type in the analogue is reproducible and well controlled [88]. It should prove a useful reference condition in this study on the effect of mineralogy on coke gasification.

5.1.4. General reactivity in CO_2

The coke analogue reactivity in CO_2 was studied using a TGA. The principle of the test is similar to the NSC reactivity test (CRI and CSR) that is used in metallurgical coke studies [9, 19, 24, 65, 66, 73, 121, 123, 137]. This was carried out to allow a comparison of the reactivity of coke analogue with metallurgical coke reactivity in other studies.

Coke analogue reactivity

Coke analogue reactivity was assessed using FWC vs time plots, in which more negative FWC indicates a higher reactivity.

Comparison of reactivities of coke analogue and coke

The comparison of the reactivities of coke analogue and metallurgical coke was carried out to assess:

- The reproducibility of coke analogue reactivity compared to the metallurgical coke.
- The similarity of the kinetics of the coke analogue and the kinetics of metallurgical coke gasification in CO_2 gas.

Reproducibility of coke analogue reactivity compared to the metallurgical coke

The reproducibility of coke analogue reactivity was assessed using FWC curves for the coke analogue gasification at 1373 K at 2 L/min CO_2 gas flow rate, i.e. the same experimental conditions as for industrial CRI test [121]. These FWC curves were compared with the FWC curves obtained for three different metallurgical cokes under the same experimental conditions [65]. Given in *Figure 5.6(a)* are the FWC curves for three base coke analogue samples. The curves are overlapping, representing the excellent reproducibility of coke analogue reactivity. For comparison, when considering FWC curves for Coke A in *Figure 5.6 (b)*, there are three curves that do not overlap and are easily distinguished from each other. A similar observation can also be made in the FWC curves for Coke B and Coke C. This indicates that there is lower reproducibility for metallurgical coke reactivity, compared to that of the coke analogue.

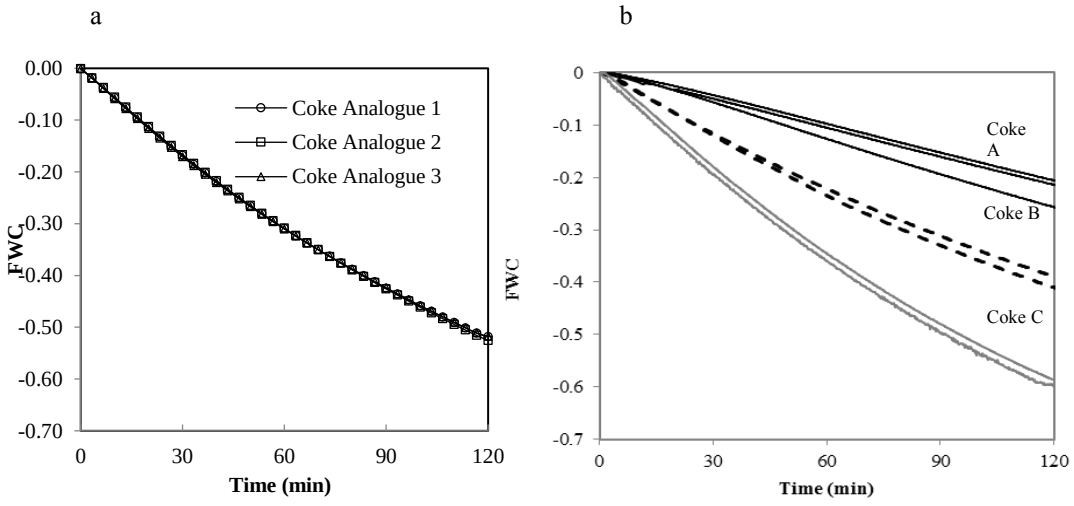

Figure 5.6: A comparison of FWC vs time plots of (a) coke analogue (b) metallurgical coke at 1373 K in CO_2 2 L/min. Note: Coke analogues 1 and 2 are from the same batch and 3 is from a different batch. Coke A, B and C are different metallurgical coke samples [65].

Furthermore, the FWC after 2 hours of the reaction of base coke analogue with CO_2, was −0.52. This value is between the FWC range measured for metallurgical coke (−0.15 to −0.80) under similar experimental conditions [17, 120, 141, 166]. The reproducibility of the analogue, and the similarity of the analogue reactivity to that of

metallurgical coke, indicate that the analogue may be a useful material to study, the metallurgical coke.

Kinetics of coke analogue and metallurgical coke gasification

The coke analogue kinetics were assessed over the temperature range of 1173–1623 K. In this thesis, for understanding of the coke analogue gasification reaction mechanism in CO_2, the experimental conditions used were slightly different from the conditions in the industrial CRI test. The flow rate employed was 4.5 L/min compared to the 2 L/min in the industrial CRI test. To ensure a direct comparison, a metallurgical coke (see Section 3.4 for details of the coke) was measured and assessed under identical conditions to those of the base coke analogue, *i.e*. the same temperature range and gas flow rate. Given in *Figure 5.7(a)* and *(b)* are the FWC curves for the gasification of the base coke analogue and the metallurgical coke respectively over the temperature range of 1173 – 1623 K.

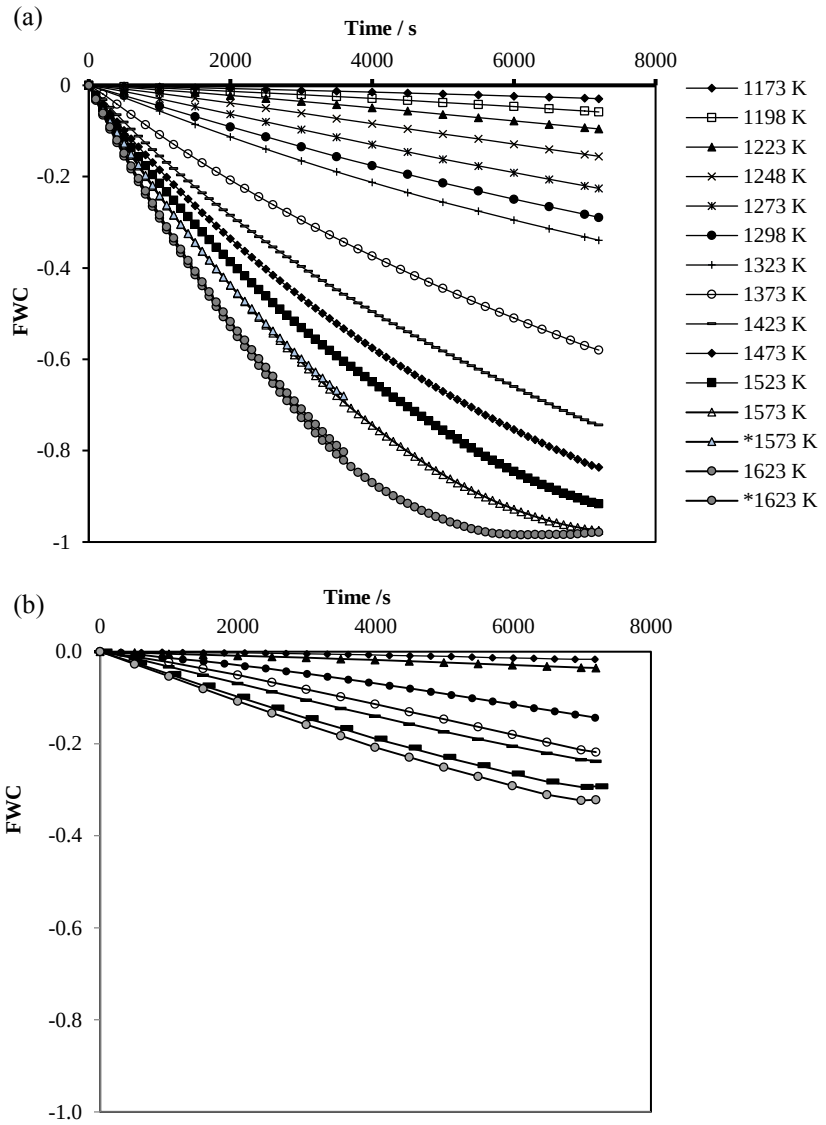

Figure 5.7: Comparison of FWC vs time plots of (a) base coke analogue (b) metallurgical coke in CO_2 of a gas flow rate of 4.5 L/min, over the temperature range of 1173 – 1623 K.

The trend of the FWC with respect to the temperature and time appear similar for both coke analogue and metallurgical coke. The selected metallurgical coke has lower reactivity than the coke analogue, which is most likely due to the difference in mineralogy, porosity and carbonaceous matter in these two materials.

5.1.5. Gasification reaction mechanism

To check whether the coke analogue has a similar rate controlling mechanism, the general approach used by Walker *et al.* [91] on carbonaceous materials is applied to the base coke analogue and compared with that of metallurgical coke. This is a standard approach used by

many researchers in coke/carbon kinetic studies [2, 38, 66, 104].

Mechanism of coke analogue gasification with CO_2

In the Walker *et al.* approach [91], the kinetics were evaluated using the Arrhenius equation (*Equation 2.22*),

$$R_C = k_o e^{-\frac{E_a}{RT}}$$

From a plot of *ln* R_C vs *1/T*, a Walker *et al.* plot [91], it is possible to define the reaction zones of the different rate controlling mechanisms. *Figure 5.8* is an ideal representation of a Walker *et al.* plot [91]. The three zones indicate different rate controlling mechanisms [90, 91].

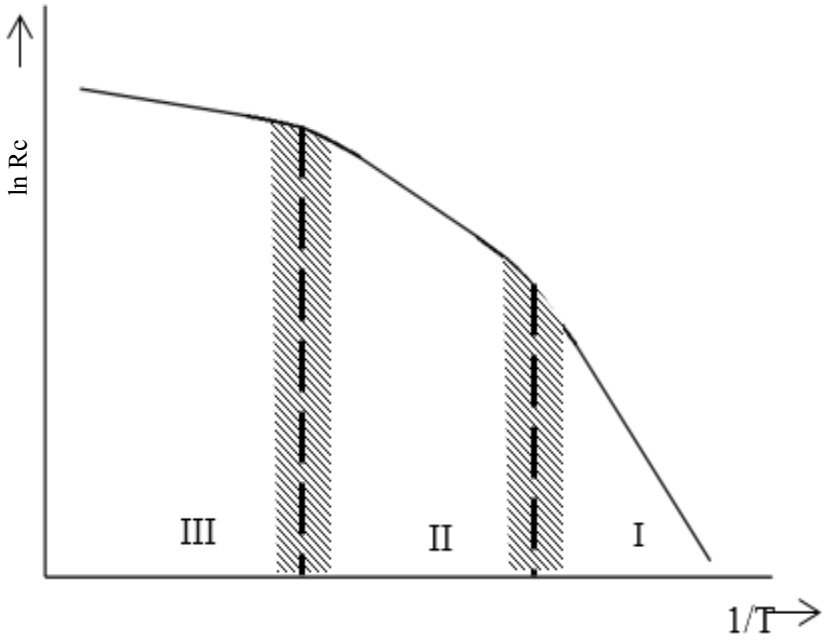

Figure 5.8: Ideal representation of three zones of gas- carbon reaction[91].

Zone I:

In this zone, the reaction rate is controlled by the chemical reaction at the coke – gas (CO_2) interface. At lower temperatures, the chemical reaction at the coke – gas interface is slower than the diffusion of the reactant gas from the surface to the reaction site. The probability that the gaseous reactants will diffuse into the solid is higher. Therefore, the gas concentration is uniform throughout the solid (see *Figure 5.9* for the concentration profile) and the reaction occurs evenly throughout the solid.

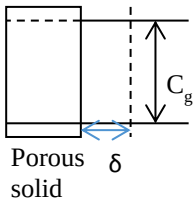

δ = the thickness of the surrounding gas film

Figure 5.9: An illustration of the reactant gas concentration profile for the Zone I kinetics.

Zone II: Chemical reaction and pore diffusion control

In this zone, the reaction rate is controlled by a combination of the chemical reaction and pore diffusion. When the temperature increases the rate of the chemical reaction becomes similar to that of the pore diffusion. Under such circumstances, there is a depth profile (from the outer surface) for gas penetration, and mostly the reaction is biased to the external surface (see *Figure 5.10* for the concentration profile).

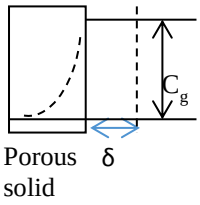

δ = the thickness of the surrounding gas film

Figure 5.10: An illustration of the reactant gas concentration profile for the Zone II kinetics.

Zone III: Gas phase mass transfer control

In this zone, the reaction rate is controlled by the mass transfer of the gas species to the external coke surface through the surrounding gas film. The reaction is completed soon after the gas reactant contacts the solid surface (see *Figure 5.11* for the concentration profile).

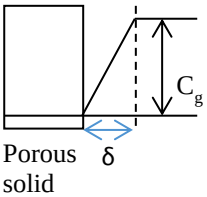

δ = the thickness of the surrounding gas film

Figure 5.11: An illustration of the reactant gas concentration profile for the Zone III kinetics.

In this thesis, *ln* R_C values for the base coke analogue were calculated using the FWC vs time

plot given in Figure 4.1 (also in *Figure 5.7 (a)*), and the values were plotted against 1/T. Given in Figure 5.12 is a Walker *et al.* plot [91], for the base coke analogue gasification in CO_2.

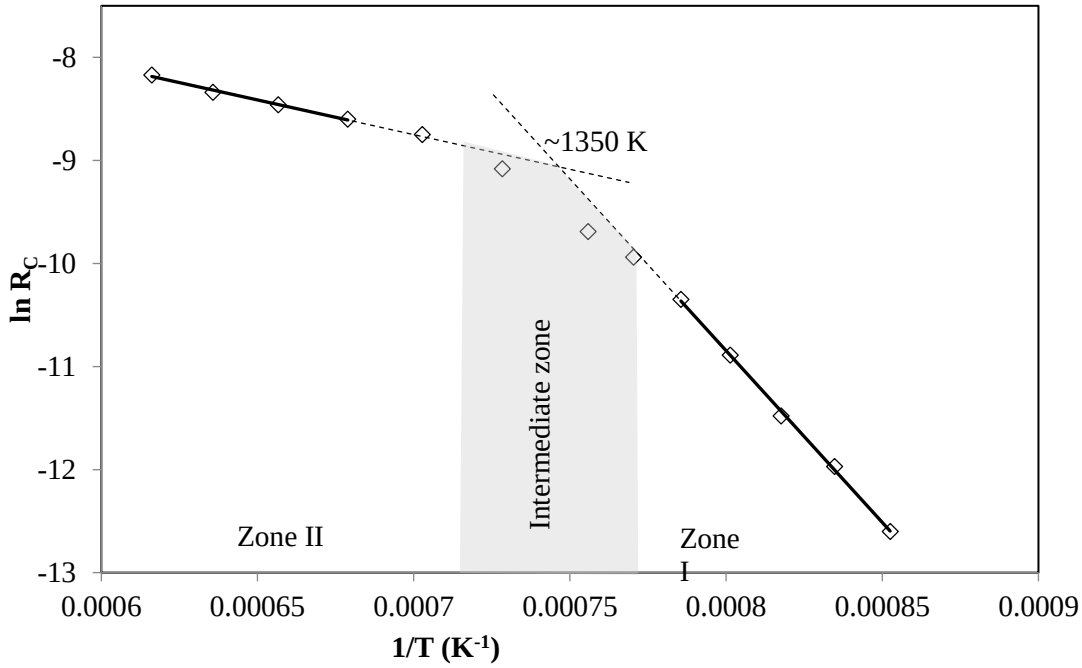

Figure 5.12: The Walker et al. plot [91] for the gasification of base coke analogue in CO_2 for the temperature range of 1173 – 1623 K.

From a comparison of *Figures 5.8* and *5.12*, it appears that the coke analogue shows similar reaction behaviour to that of metallurgical coke [91, 104]. *Figure 5.12* it can be seen that the base coke analogue has two zones. Under the experimental conditions employed in this study, only Zones I and II are expected to be seen as the gas boundary layer is expected to be eliminated, as discussed in Section 3.1.1. [167]. The transition from Zone I to Zone II is in the temperature range of 1298−1423 K.

The confirmation of the zone identification was carried out using:

1. Optical microscopy.
2. The physical appearance of the sample after the reaction.

Zone I

Expected results:

In this zone, if the chemical reaction is the rate determining step, the CO_2 concentration is expected to be uniform throughout the solid, and the reaction occurs uniformly throughout the analogue. Under such circumstance,

- the external geometry of the analogue should remain approximately constant until the final stages of the reaction and,
- the pores are expected to become enlarged inside the solid as a result of the even reaction throughout the solid.

Observed results:

- The analogue maintained its shape after the reaction, although there was some pitting on the external surface over the temperature range of 1173−1298 K (*Table 4.2*).
- Optical micrographs of cross sections of the coke analogue samples at the centre and annulus of the sample before and after the reaction (*Figure 5.13*) showed there was an increase in the pore sizes of the reacted samples, both at the centre and at the annulus of the sample after the reaction.

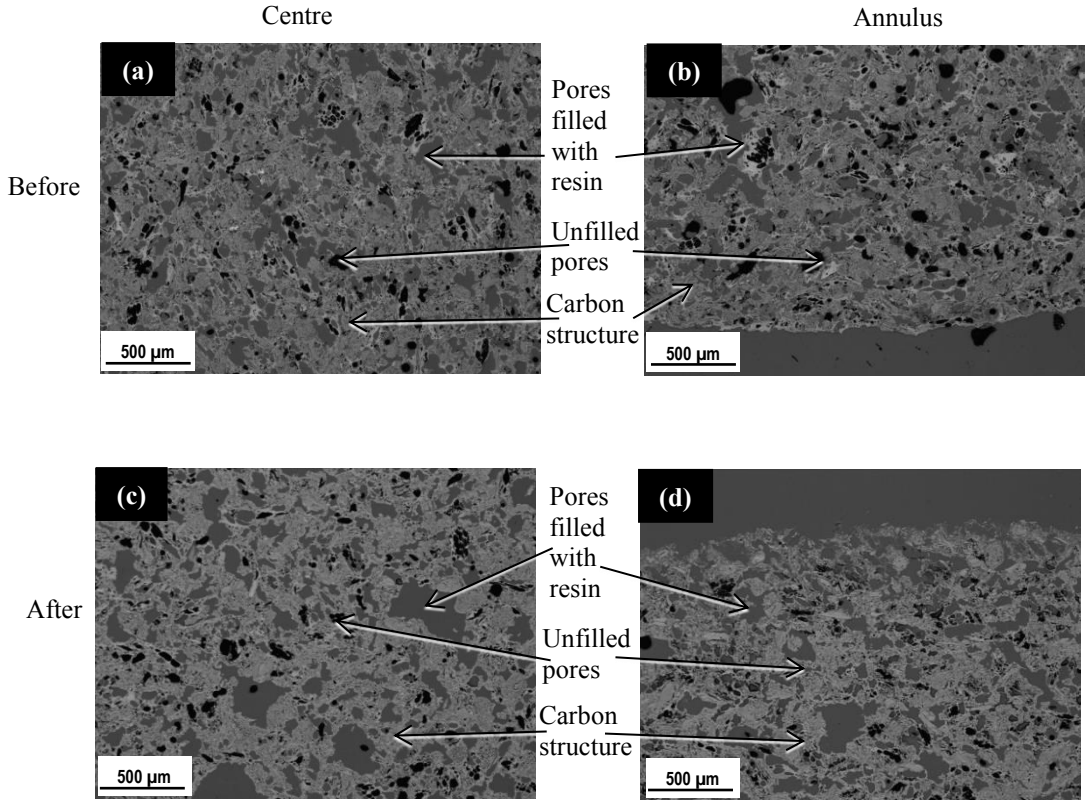

Figure 5.13: Optical micrographs of before the reaction at a) centre b) annulus of the sample c) centre, and d) annulus of the sample after the gasification reaction at 1223 K.

Conclusion:

The observed physical appearance and optical micrographs at the temperature range 1173 - 1298 K are consistent with the expected results for the Zone I rate controlling mechanism.

Zone II

Expected results:

Relative to Zone I there is a lower probability that CO_2 will diffuse deep into the solid. As in Zone I the reaction can still occur internally, but the reaction will be biased to the external surface. Therefore in this region,

- the centre of the solid will remain relatively unreacted early in the reaction process, or less reacted later in the reaction process. The overall rate of the reaction is greater than the rate in Zone I, resulting in significant mass loss and dimensional change in

the analogue and

- a greater reaction is expected at the annulus of the sample than at the centre of the sample.

Observed results:

- There was an increasing dimensional change of the coke analogue samples in the temperature range of 1323 – 1623 K (see *Table 4.2*).
- There was not enough or no analogue left at higher temperatures to assess the internal structure using optical microscopy. Therefore to address this, a further set of experiments was carried out at 1573 and 1623 K for 1 hour.
- Cross-sectional optical micrographs of the samples reacted for 1 hour are given in *Figure 5.14*, and they show increasing pore size in both the centre and the annulus of the sample, with greater pore size at the annulus relative to the centre.

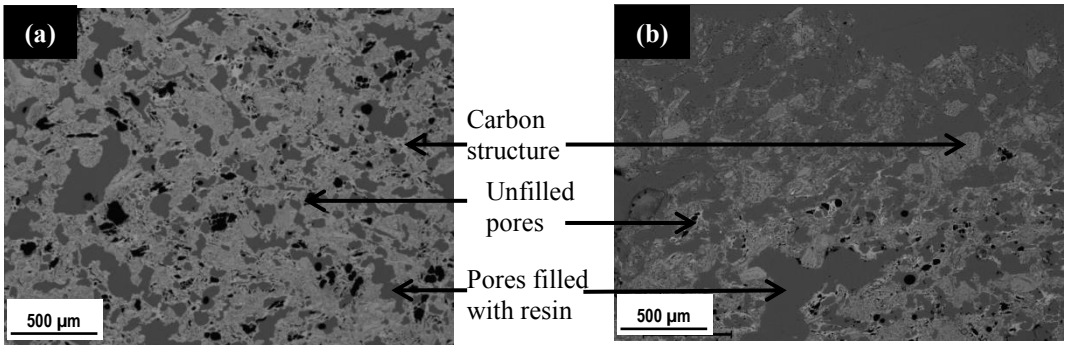

Figure 5.14: Optical micrographs of the base coke analogue sample after the gasification reaction at 1573 K at a) the centre of sample, and b) the annulus of the sample.

Conclusion:

The observed physical appearance and optical micrographs in the temperature range of 1323 – 1623 K are consistent with the expected results for the Zone II rate controlling system.

Comparison of the coke analogue gasification mechanism with a metallurgical coke

The reactivity of the metallurgical coke was studied under the same experimental conditions as employed for the coke analogues. *Figure 5.15* is the comparison of Walker *et al.* plots [91] for the metallurgical coke studied in this study, and for the base coke analogue (refer to

Figure 5.7 for the FWC vs time plot).

Similar to the coke analogue, two reaction zones were identified for the metallurgical coke based on the regions showing a linear relationship between *ln* R_C and *1/T*. These zones can be identified as Zones I and II, similar to the base coke analogue and the zones found in the literature [91, 104]. As discussed in the previous section, the metallurgical coke studied in this project had a lower reactivity than that of the base coke analogue. This is likely due to its mineralogy, porosity and/or carbon structure. Although the reactivity of the metallurgical coke and the base coke analogue was different, the relationship between the Walker *et al.* plots [91] was similar, with similar gradients and transition temperatures from Zone I to Zone II. This similarity in behaviour of the coke analogue to the metallurgical coke, to a large degree, validates the use of coke analogue in the study of the metallurgical coke.

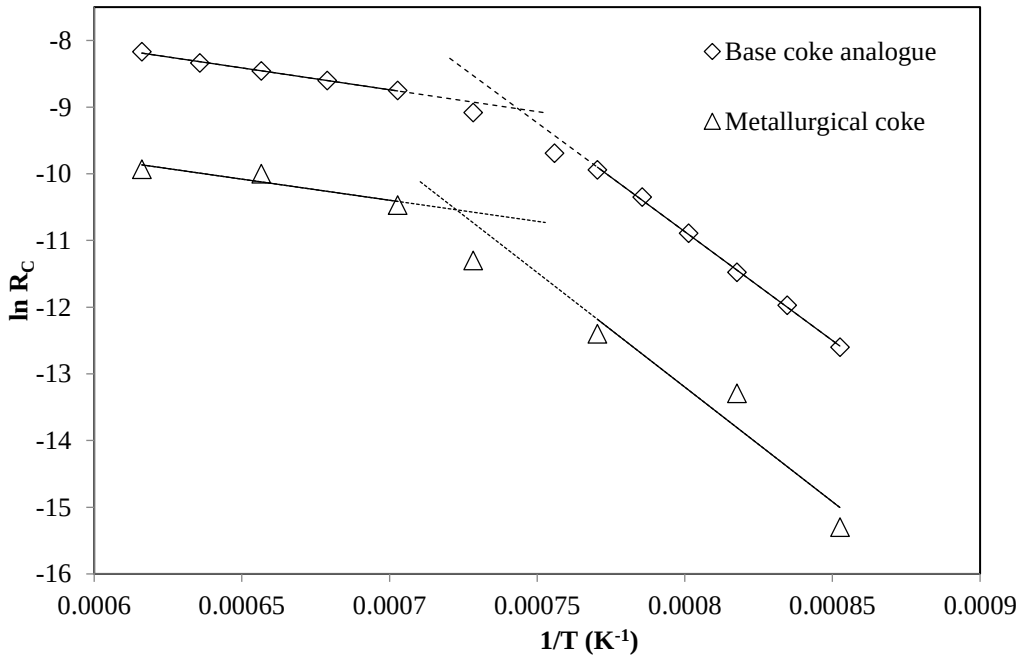

Figure 5.15: Combined Walker et al. plots [91] for the gasification of metallurgical coke and base coke analogue in CO_2 for the temperature range of 1173 – 1623 K.

Effect of temperature on reaction kinetics

The reaction between coke/carbon and CO_2 gas is a heterogeneous reaction which can be expressed in the form of *Equation 5.1*.

$$\frac{dX}{dt} = k\ A\ \Delta C^n \qquad 5.1$$

where k = rate constant, g s^{-1} m^{-2}

ΔC = gas concentration change, g m^{-3}

A = initially available surface area for the reactions, m^2

n = order of the reaction.

It can be seen from *Equation 5.1* that the rate of reaction is a function of k, A and ΔC. The specific or appropriate values for k, A and ΔC in *Equation 5.1* are dependent on the prevailing rate controlling mechanism, which varies with temperature.

The rate constant k, whether in Zone I (a chemical reaction control system) or Zone II (a mixed diffusion / mass transfer control system) will have an Arrhenius, and hence exponential, relationship with temperature [168]. All other things being equal, this increase in k due to an increase in temperature would result in an increased rate of reaction.

The term ΔC will be proportional to the Gibbs free energy for all the rate controlling zones (Zone I to III) [169]. The Gibbs free energy for the coke gasification reaction in CO_2 (*Equations 2.10* and *2.11*) is given in *Equation 5.2*.

$$\Delta G° = 165300 - 170.76T \qquad 5.2$$

From *Equation 5.2* it can be seen that increasing the temperature makes the Gibbs free energy more negative, *i.e.* the thermodynamic driving force for the reaction increases with increasing temperature. All other things being equal, this increase in driving force would increase the rate of reaction.

The area term, A, changes in the rate controlling mechanism. Therefore, A will change with changing temperature. For Zone I, at lower temperatures, A is greater than the A for Zone II, which in turn will be greater than the A for Zone III. In Zone I, a chemical reaction control system, all surfaces including pore surfaces, providing the gas can reach the pores, are available for reaction. In Zone II, a mixed control system, the penetration of the pores by the reaction gas by diffusion is at least in part a function of the pore size [168], which limits the

depth of penetration and therefore the area available for reaction. In Zone III, a mass transfer control system, the appropriate area of the solid is its external geometry. It can, therefore, be expected that with increasing temperature, moving from Zones I to II to III will result in a decrease in A. All other factors in *Equation 5.1* being equal, this decrease in A due to the change of rate controlling kinetics would result in a decreased rate of reaction.

From *Figure 5.9* it can be seen that the effect of temperature on reaction rate is consistent with what would be expected in terms of k and ΔC, but not A. Therefore, the effects of temperature on k and ΔC dominate effect on A.

Comparison of the activation energy of base coke analogue with metallurgical coke

Much of the published work on CO_2 reactivity with coke has been carried out in Zone I. A comparison of the gasification results of Zone I for the base coke analogue, the metallurgical coke in this study, and the metallurgical coke reported in the literature, using the Walker *et al.* approach [91], is given in *Figure 5.16* [38, 66, 119, 146].

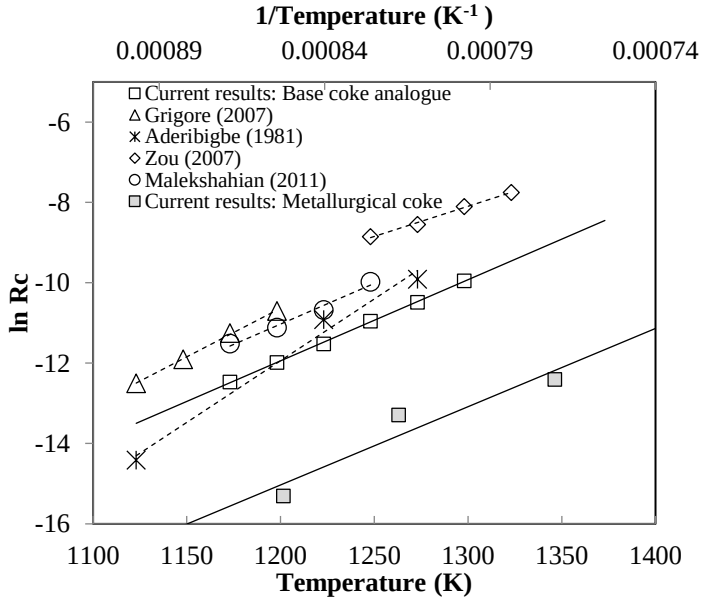

Figure 5.16: A plot of the comparison of the current results in Zone I with previous studies.

The published activation energies [38, 119, 170-173] of metallurgical cokes for Zone I, and the activation energy for the metallurgical coke studied in the current project, are close (equivalent or slightly lower) to the base coke analogue gasification activation energy (see *Table 5.3*). Many of the previous studies did not identify Zone II in their results

Table 5.3: Comparison of activation energies

Author	Type of Carbon	Apparent activation energies/kJ mol^{-1}	
		Zone I	Zone II
Current results	Base Coke analogue	271.5 ±1.8	54.5±0.3
Current results	Metallurgical coke	285.8 ± 1.9	52.6 ±0.5
Grigore (2007) [19]	Metallurgical coke	222-266	-
Aderibigbe (1981) [66]	Metallurgical coke	249 ± 47	
Zou [146]	Petroleum coke	198	
Malekshahian and Hill (2011) [29]	Petroleum coke char	260±24	

Activation energy values in Zone I, the chemical reaction controlled region, are associated with bond breaking and bond formation [106]. Therefore, the similarity of the activation energies obtained for coke analogue and metallurgical cokes suggests that the coke analogue follows the same gasification reaction mechanism for the reaction with CO_2, and that the carbon bonding present in the coke analogue is similar to that of metallurgical cokes.

Given that the starting mixture for the coke analogue contains approximately 50% by mass graphite (see *Table 3.2*) it might be expected that the activation energy for Zone I for the analogue would be similar. The activation energy for graphite is 305 kJ mol^{-1} [167]. This is significantly higher than that for the analogue. From these activation energies, it can be concluded that the coke analogue reactivity more closely replicates that of metallurgical coke than graphite.

5.2. Summary of the suitability of coke analogue to study the metallurgical coke

From a number of viewpoints, it can be seen that the coke analogue has similarities to the metallurgical coke. Use of the coke analogue allows control of the porosity, mineralogy, mineral particle size and distribution and the general reactivity with CO_2. This similarity and the control of those properties make the coke analogue a useful tool in coke studies. *Table 5.4* summarises the comparison of coke analogue and metallurgical coke characteristics.

Table 5.4: A comparison of coke analogue and metallurgical coke characteristics

Characteristic	Coke analogue	Metallurgical coke	Comments
Porosity / % and pore size distribution	29.3 ± 2.3 Majority of the pores in 10 -100 µm range.	24.7 – 70.0 [34, 69, 88] The highly variable pore size distribution.	Coke analogue porosity is within the range observed for metallurgical coke, but porosity and the pore size distribution is controlled and reproducible.
Microscopic analysis Carbon matrix Mineral distribution	Graphite grains with RMDC like the character Carbonised phenolic resin with IMDC similar character. Simple and homogeneous distribution.	RMDC and IMDC Complex and heterogeneous	Coke analogue carbon matrix is similar but less complex than metallurgical coke and reproducible. Controlled with simple and homogeneous mineral distribution (except CaO).
Carbon bonding $I_{(D)}/I_{(G)}$ $I_{(V)}/I_{(G)}$	0.16– 1.55 0– 0.41	1.16– 1.45 0.38 – 0.62	Coke analogue covers a broader range of carbon bonding types than metallurgical coke but overlaps the range of metallurgical coke.
Reactivity in CO_2	Reproducible	Highly variable	The reactivity of coke analogue has similar trends with time and temperature to that of metallurgical coke.

Chapter 6

Effect of Ca-bearing minerals on coke analogue gasification in CO_2

In this chapter, the reactivity of coke analogues doped with minerals in CO_2 is discussed. The minerals studied can basically be classified into two groups:

1. $CaO – Al_2O_3$ binary mineral system.
2. $CaO – Al_2O_3 – SiO_2$ ternary mineral system.

It is known that the following coke characteristics have an impact on reactivity:

1. Coke carbon structure.
2. Porosity.
3. Mineral matter: Type of minerals, mineral concentration, particle size and distribution.

To study the effect of mineral matter on the reactivity, other factors need to be kept constant. This was carried out by using the coke analogue, rather than using metallurgical coke. As discussed in Chapter 5, the coke analogue gives control over porosity, pore size distribution, carbon structure and mineral particle size and distribution.

The mineral concentration was kept at a constant value, at a total cation mole basis of 0.1 mol/100 g of coke analogue. The particle size of the minerals added to the analogues was in the range of +38 – 53 µm for each mineral added to the coke analogue. SEM backscattered images and corresponding EDS maps show minerals were distributed evenly through the analogue (See *Figures 4.19 – 4.50*). (In all the coke analogues except the lime-doped analogue, mineral particles were found to be in the added size range. The reasons why the different particle sizes were observed with lime-doped analogue is discussed in Section 6.4). The similar mineral concentration and distribution would eliminate any effects due to the variations in mineral concentration, mineral particle size and distribution. Therefore, in this study, the primary composition/phase variable is the mineral type.

To understand the gasification of the coke analogues containing minerals, the Walker *et al.* approach [91] was employed, which is similar to the approach used for the base

coke analogue. The coke analogues containing minerals were reacted with CO_2 gas at 4.5 L/min over the temperature range of 1173 – 1623 K. The comparisons of the reactivities of the coke analogues were carried out using FWC vs time plots and Walker *et al.* plots [91].

6.1. Reactivity of coke analogue containing minerals of $CaO – Al_2O_3$ binary system

The effect of $CaO – Al_2O_3$ binary minerals was studied by varying the CaO concentration in the minerals from 0 to 0.1 mol/ 100 g of the coke analogue. The minerals used were Al_2O_3, CA6, CA, C3A and CaO where the Ca concentrations were 0, 0.007, 0.031, 0.055 and 0.100 mol/ 100 g respectively. These minerals were chosen based on the $CaO – Al_2O_3$ phase diagram given in *Figure 3.15*. The use of the same total mineral concentration allows the total mineral concentration in each coke analogue to be constant while changing the chemical activity of CaO (a_{CaO}) and the number of moles of Ca (n_{Ca}).

It would be useful to compare the FWC curves at each temperature for the coke analogues doped with $CaO – Al_2O_3$ binary minerals, with the curves for the base coke analogue. Given in *Figure 6.1* is the FWC vs time plots for the $CaO – Al_2O_3$ minerals at 1173 and 1373 K (a complete set of FWC vs time plots for each coke analogue is given in Chapter 4).

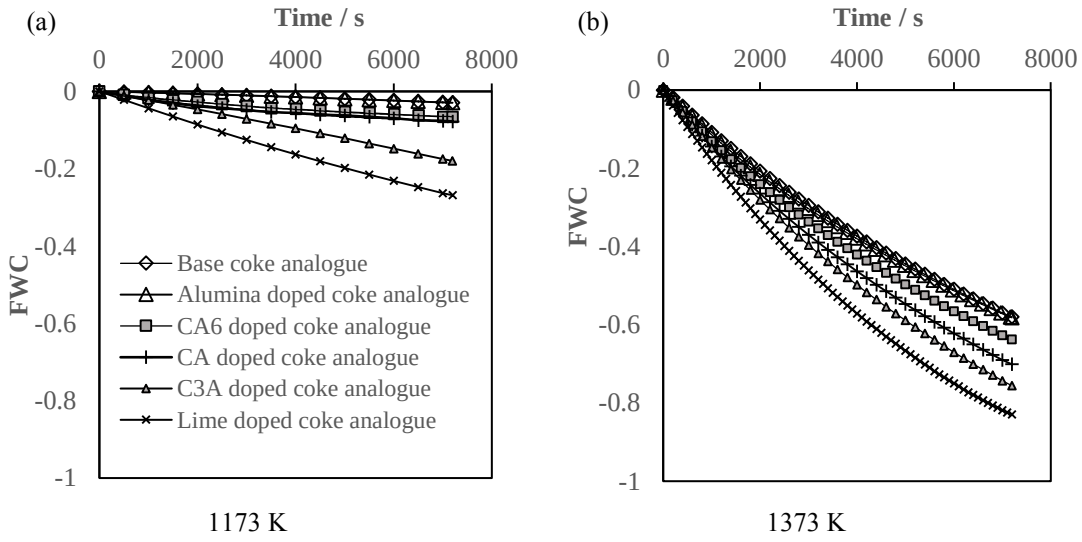

Figure 6.1: FWC vs time plots at (a) 1173 and (b) 1373 K for the coke analogues containing $CaO – Al_2O_3$ binary minerals compared to the base coke analogue.

From *Figure 6.1,* as expected, it can be seen that the reactivity at 1373 K is higher than the reactivities at 1173 K. The FWC curves for the base coke analogue and alumina-doped coke analogue overlap at both temperatures, suggesting a minimal effect of alumina on coke analogue gasification. Based on both temperatures, the reactivity of the analogues increased in the order of,

Base ≈ Alumina < CA6 < CA < C3A < Lime.

Regardless of the differences in the relative reactivities, all the coke analogues show similar reaction behaviours with temperature, consistent with reported studies for the gasification of metallurgical cokes and carbon [38, 64, 66, 119, 146, 147].

To evaluate the rate controlling mechanism, the Walker *et al.* approach[91] was employed. The Walker *et al.* plots [91] made for all the coke analogues doped with $CaO - Al_2O_3$ are given in *Figure 6.2.*

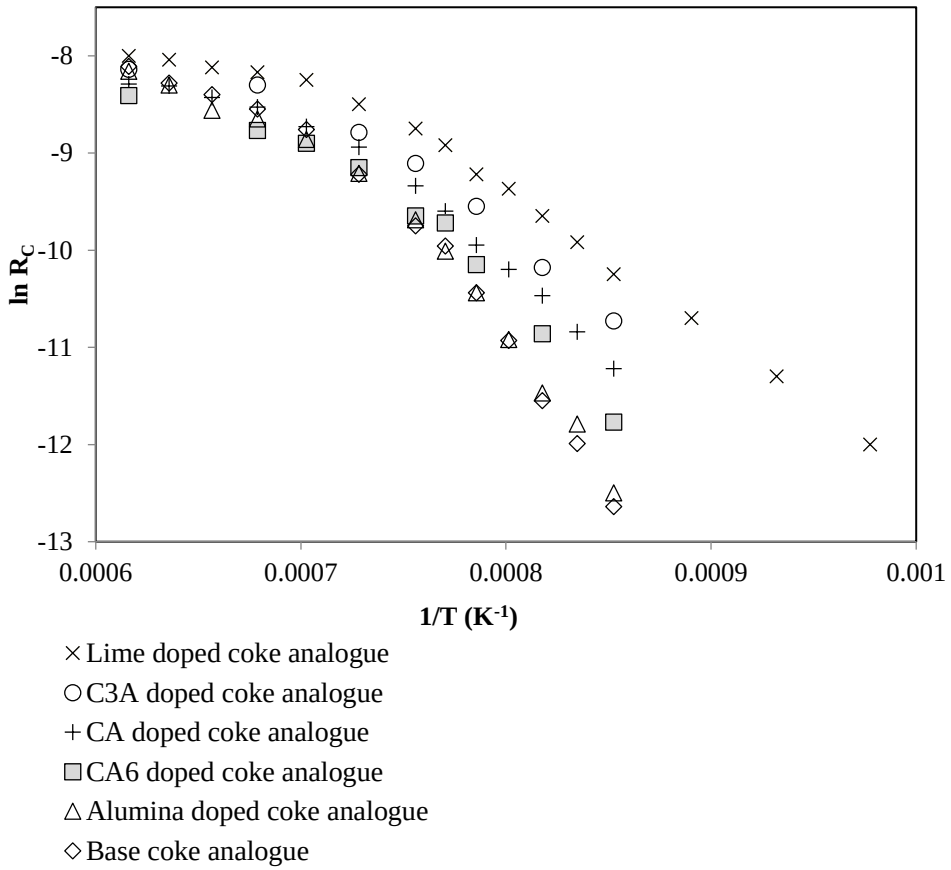

Figure 6.2: Walker et al. plots [91] for coke analogues doped with CaO - Al_2O_3 containing minerals for the temperature range 1173 – 1623 K for all the minerals except lime, where the temperature range is 1023 – 1623 K.

It was observed that the coke analogues containing Ca in the added minerals have higher reactivity compared to the base coke analogue. The observations made about the higher reaction rates for Ca-containing coke analogues are consistent with previous studies that have reported on the effects of Ca on coke [16, 33, 174], coke analogue [24] and char [29-32] reactivity. To improve the resolution/definition of the Walker *et al.* [91] plot of lime-doped coke analogue, a wider range of temperatures was assessed than for that of the other analogues. As expected for lime, an alkaline earth species, gasification reaction started at lower temperatures [15] than for the base coke analogue. In the temperature range of 1023 – 1123 K the base coke analogue could be considered to have reacted with CO_2 as shown by the negligibly small FWC (FWC<0.005). In comparison, the coke analogue-containing lime had FWCs in the range 0.04 – 0.2 for the same temperatures. This may indicate a catalytic effect of Ca/CaO on coke analogue gasification. Any possible catalytic effect will be discussed in more detail in Chapter 7.

As a result of the negligible effect from the alumina on the coke analogue gasification, in CaO – Al_2O_3 binary mineral combinations added-coke analogues, CaO can be considered as the primary component that caused the difference in the reactivity.

Similar to the base coke analogue as well as for metallurgical coke/carbon [91, 104] distinct reaction zones were identified in coke analogues doped with minerals (see *Figure 6.3*).The zones were identified as the areas exhibiting a linear relationship between $ln\ R_C$ and $1/T$, similar to the procedure with base coke analogue. The gradients at each zone were used to calculate the apparent activation energies for the coke analogue gasification in CO_2 gas.

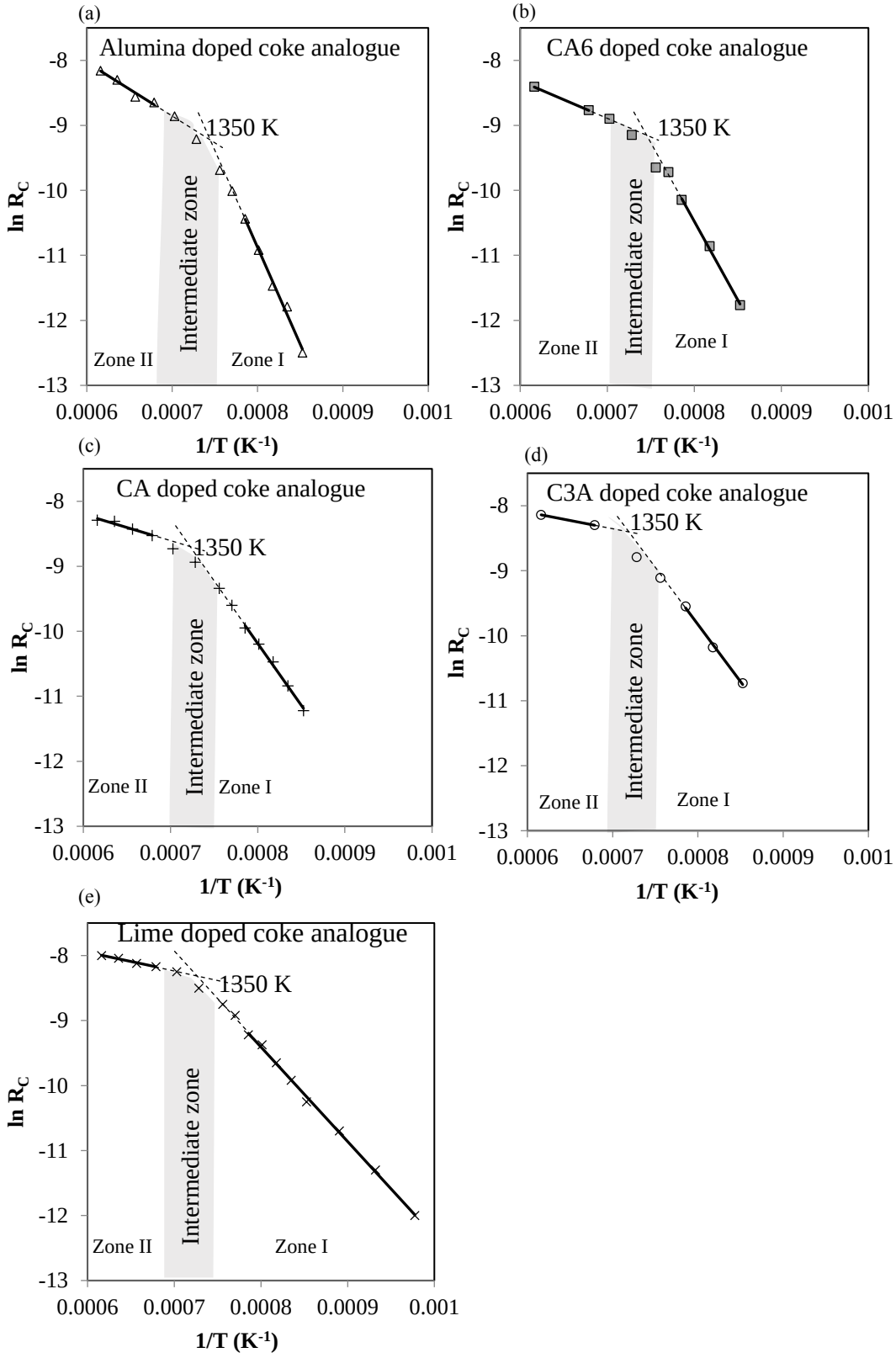

Figure 6.3: Walker et al. plots [91] for the coke analogues doped with (a) alumina (b) CA6 (c) CA (d) C3A and (e) lime.

The apparent activation energies for each of the mineral-doped coke analogues were calculated for both zones identified in *Figure 6.3* and are given in *Table 6.1*.

Table 6.1: Apparent activation energies of the coke analogues of minerals of CaO – Al_2O_3 binary system calculated from the gradients of the Walker et al. plots [91].

Coke analogue	Activation energy (kJ mol^{-1})	
	Zone I	Zone II
Base coke analogue	271.5 ±1.8	54.5±0.3
Alumina-doped coke analogue	251.3 ±1.8	47.2±0.3
CA6-doped coke analogue	204.4 ±1.5	39.5±0.4
CA-doped coke analogue	159.9 ±1.7	37.8±0.3
C3A-doped coke analogue	146.3 ±1.8	34.5±0.3
Lime-doped coke analogue	119.8 ±1.5	20.7±0.3

It can be seen that the activation energy decreased with increasing CaO content in the binary mineral combination. This relationship is clearly shown in *Figure 6.4*, a plot of activation energy for the Zone I vs the number of moles of Ca in each mineral added. This may indicate a catalytic effect of Ca / CaO in coke analogue gasification (which will be discussed in more detail in Chapter 7).

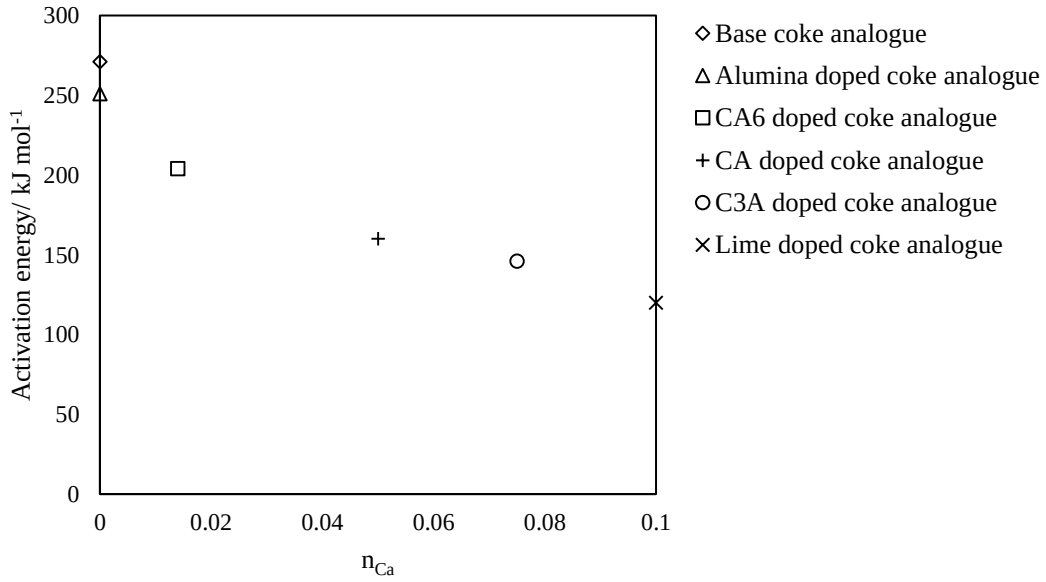

Figure 6.4: A plot of Activation energy for Zone I vs n_{Ca} in each mineral added.

6.2. Reactivity of coke analogue-containing minerals of CAS ternary system ($CaO – Al_2O_3 - SiO_2$)

In the previous section, it was found that Ca added to the coke analogue in the form of $CaO – Al_2O_3$ binary mineral combinations affected the coke analogue gasification and increased the gasification. Would the addition of a third component make any difference? To answer this question, the effect of a ternary mineral combination, CAS ($CaO – Al_2O_3 – SiO_2$), was evaluated. Further, to facilitate the analysis, the specific effect of the third component in CAS, SiO_2 (quartz), was studied. This section deals with the specific effects of the ternary and unary minerals added to the analogue on gasification. Whether the third component has a significant effect on the gasification is dealt with in Section 6.3.

Given in *Figure 6.5* are the FWC vs time plots of CAS-doped coke analogues compared to that of the base coke analogue. As mentioned in Chapter 4, two CAS batches, CAS1 and CAS2, with similar characteristics in terms of porosity, carbon forms mineralogy, mineral concentration, particle size and mineral distribution were used in this study. At both temperatures, the CAS-doped coke analogue had higher rates compared to the rates for the base coke analogue.

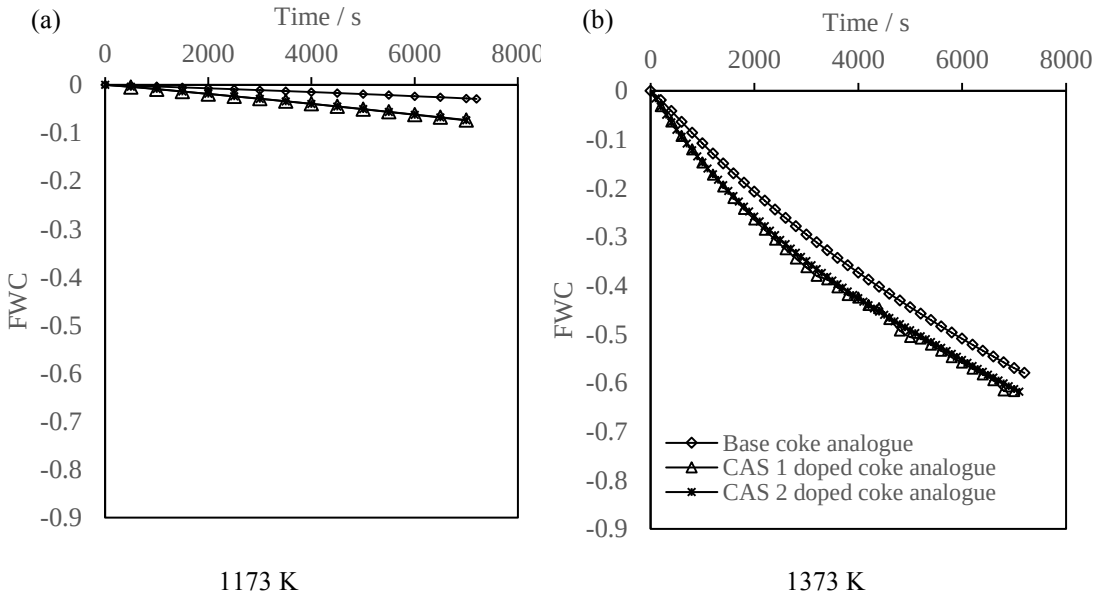

Figure 6.5: FWC vs time plots at (a) 1173 and (b) 1373 K for the coke analogues containing CAS ternary mineral combinations compared to the base coke analogue.

The reactivities of CAS-doped analogues were further analysed using the Walker *et al.* plots [91] where there were two temperature zones identified, similar to the metallurgical coke and base and CaO – Al_2O_3 minerals-doped coke analogues. The results are given in Figure 6.6. The R_C values used to represent CAS are the average of CAS 1 and CAS 2.

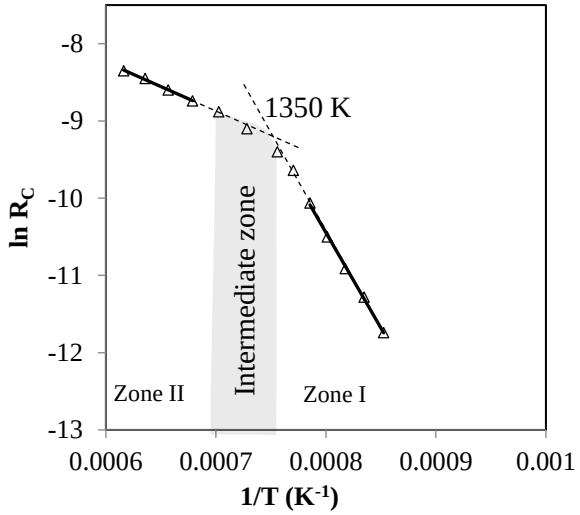

Figure 6.6: Walker et al. plots [91] of CAS-doped coke analogue.

The apparent activation energy was calculated using the gradients of the Walker *et al.* plots [91], in the same way to that of the previous coke analogues and are given in *Table 6.2*. The activation energy values were lower than the activation energy observed for base coke analogue gasification in CO_2.

Table 6.2: Apparent activation energies of the coke analogues with added CAS calculated from the gradients of the Walker et al. plots [91].

Coke analogue	Activation energy (kJ mol^{-1})	
	Zone I	Zone II
Base coke analogue	271.5 ±1.8	54.5±0.3
CAS-doped coke analogue	210.4 ±1.7	52.2±0.3

To evaluate the specific effect of the third component, SiO_2-doped coke analogue was studied over the same temperature range, 1173 – 1623 K. Given in *Figure 6.7* are the FWC vs time plots of quartz-doped coke analogue at 1173 and 1373 K compared to the base coke analogue (FWC vs time plots for all the temperatures was given in Section 4.1).

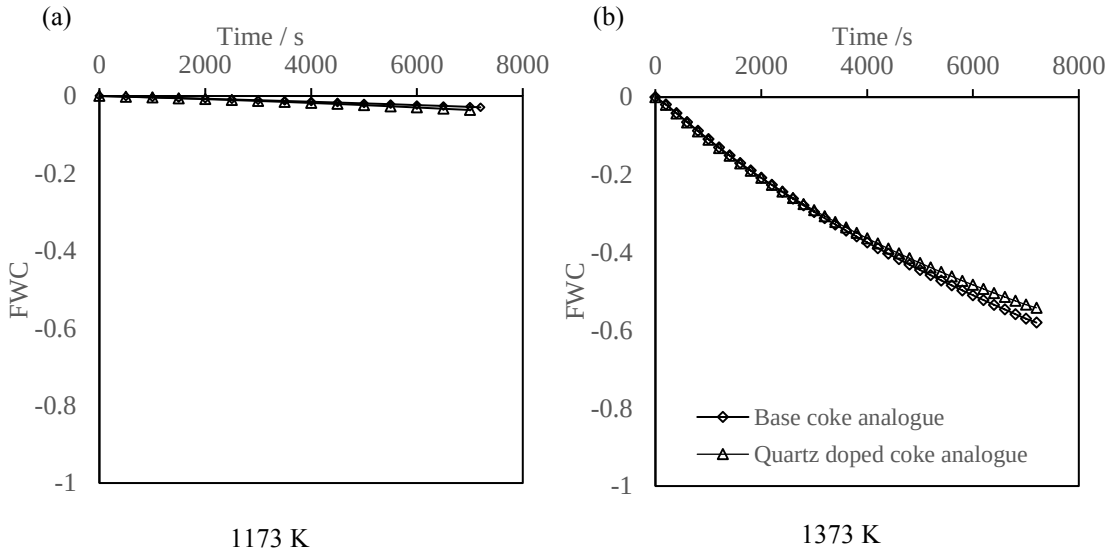

Figure 6.7: FWC vs time plots at (a) 1173 and (b) 1373 K for the quartz-doped coke analogue compared to the base coke analogue.

It can be seen that at both temperatures, there is no significant effect of quartz on the reactivity. At 1373 K, the final FWC was slightly lower than the FWC for the base coke analogue. Quartz is expected to lower the gasification [24, 65]. However, the difference is not significant in the temperature range used in this study. See the Walker *et al.* plot [91] in *Figure 6.8* for a comparison between the base and quartz-doped coke analogue reactivity.

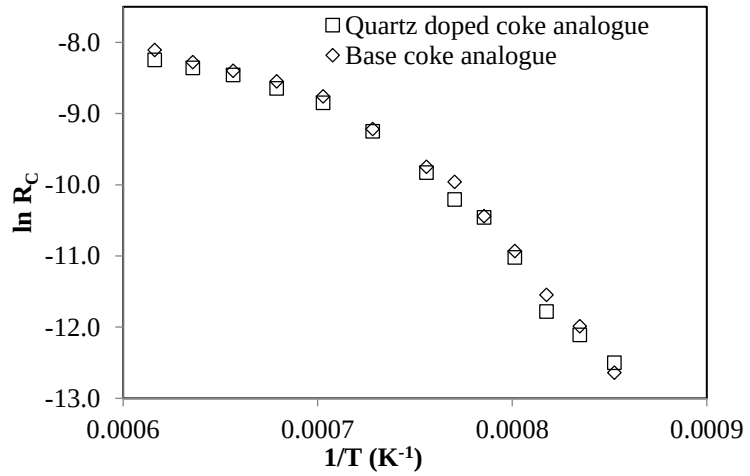

Figure 6.8: A comparison of the Walker et al. plots [91] of the base coke analogue and quartz doped coke analogue over the temperature range of 1173 – 1623 K.

Both Al_2O_3 and SiO_2 have similar reactivities to those of the base coke analogue. Therefore, similarly to the CaO – Al_2O_3 binary minerals-doped coke analogues, it can be suggested that CaO is the component that is primarily responsible for the observed higher reactivity of CAS-doped coke analogues.

6.3. Assessment of the effect of Ca in the added minerals on the coke analogue reactivity

To assess the effect of Ca in the added minerals on the reactivities of coke analogues prepared with CaO – Al_2O_3 binary and CaO – Al_2O_3 – SiO_2 ternary combinations of minerals, plots of the total number of moles of Ca (n_{Ca}) versus R_C (*Figure 6.9*) and the chemical activity of CaO (a_{CaO}) versus R_C (*Figure 6.10*) were made. MTDATA [152] was used to evaluate a_{CaO}. The reference state used for CaO was halite (lime). The n_{Ca} and the a_{CaO} for the respective minerals at different temperatures are given in *Table 6.3.* Temperatures representative of Zone I (1223 K) and Zone II (1623K) have been considered in this comparison. The solid line in the figures represents the best fit linear regression of the data.

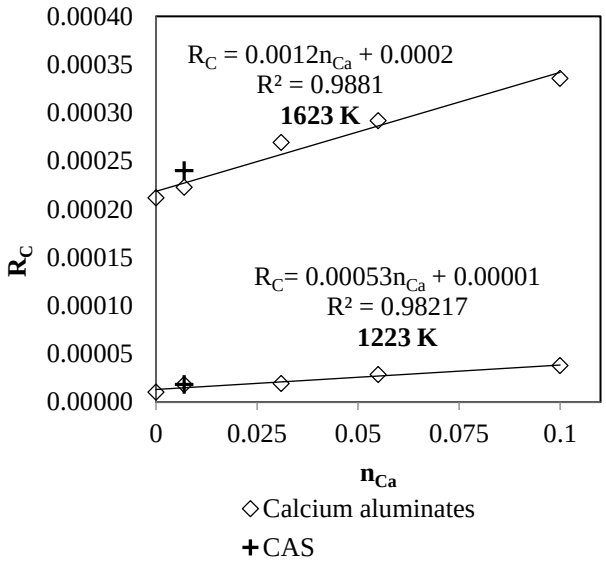

Figure 6.9: The plot of R_C vs n_{Ca}

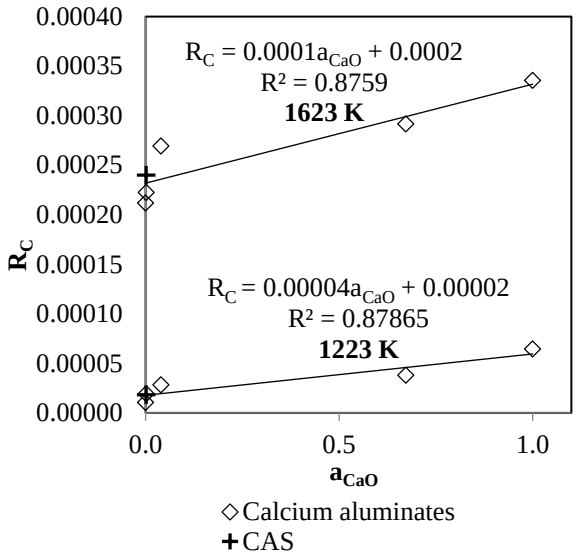

Figure 6.10: The plot of R_C vs a_{CaO}

Table 6.3: n_{Ca} and a_{CaO} values of the minerals studied at 1223 K and 1623 K

Mineral	n_{Ca} in 100 g of base coke analogue	a_{CaO} at 1223 K	a_{CaO} at 1623 K
Alumina	0.000	0.0000	0.0000
CASs	0.007	0.0014	0.0011
CA6	0.007	0.0015	0.0012
CA	0.031	0.0400	0.0800
C3A	0.055	0.6720	0.6000
Lime	0.100	1.0000	1.0000

From the *Figures 6.9* and *6.10,* it can be seen that there is no significant effect of the third component SiO_2, on the coke analogue gasification. The figures also show a stronger correlation of R_C with n_{Ca} than with a_{CaO} as indicated by the higher R^2. CAS is a phase mixture containing anorthite, gehlenite and mullite. The Ca concentration in anorthite and gehlenite is higher than that of CA6. However, the Ca concentration in total amount of the added mineral mixture (CAS) is similar to the Ca concentration in CA6. This would tend to indicate that the effect of Ca in the added minerals is simply a mass effect, rather than a chemistry effect associated with the bonding in the mineral phase.

Notwithstanding the distinction between n_{Ca} and a_{CaO} on R_C, the data shown in *Figures 6.9* and *6.10* are in general consistent with that data reported in the literature

concerning the effects of Ca in the ash on the rate of metallurgical coke gasification in CO_2.

The effect of Ca is greater at higher temperatures, as indicated by the increased slope of the regression lines at higher temperatures. This was further analysed by considering the activation energies for Zone I and Zone II for the gasification of the coke analogues (see *Tables 6.1 and 6.2*). The apparent activation energies for both zones decrease with increasing calcium content of the mineral in the analogue. This is indicative of a strong catalytic effect of Ca in the minerals on the gasification, and is consistent with the observations other researchers have reported for the effect of Ca-containing minerals on gasification for metallurgical coke [24, 29-33].

Table 6.3 shows that CA6 and CAS have the same n_{Ca} and very close a_{CaO} at 1223 and 1623 K. *Figures 6.9* and *6.10* show that the R_C of the coke analogues doped with those minerals are also similar. To see this relationship clearly, Walker *et al.* plots [91] of CA6 and CAS are compared in *Figure 6.11*. From the figure it can be seen that the plots are similar, almost overlapping for these coke analogues. This is expected, as the relative reactivities of alumina-doped and quartz-doped coke analogues are very close to those of the base coke analogue. The third component, SiO_2 in the added mineral did not have a significant effect on the coke analogue reactivity.

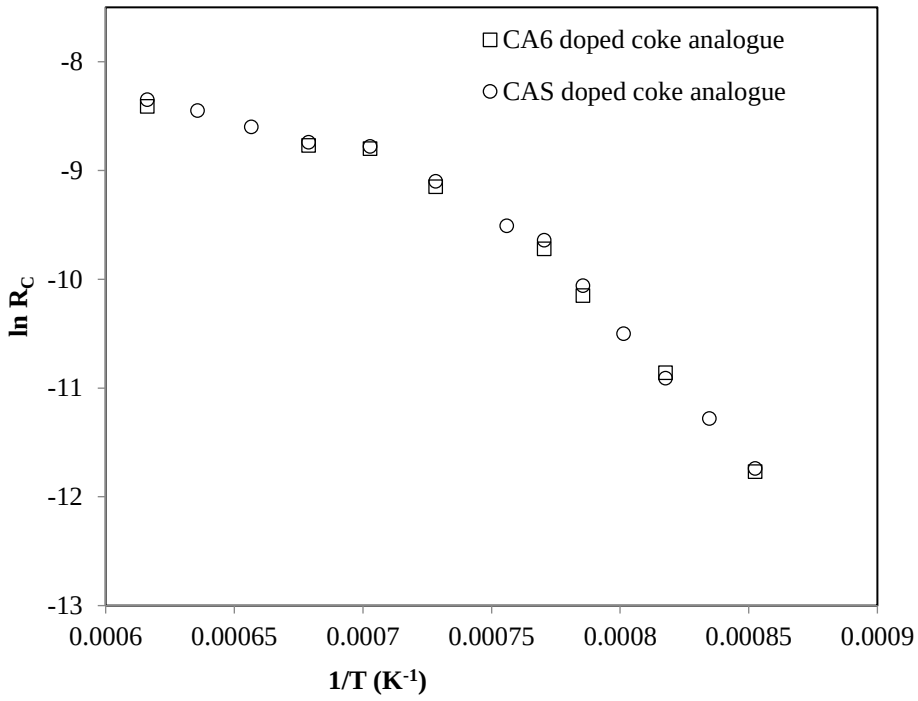

Figure 6.11: A comparison of the Walker et al. plots [91] of the CAS-doped coke analogues and CA6-doped coke analogues.

6.4. Dispersion of lime in the coke analogue

In the previous sections of this chapter, it was observed that the lime-doped coke analogue had the highest reaction rate compared to the other coke analogues, and that its rate was significantly higher compared to the rate for the base coke analogue. To understand the reasons for this behaviour, further analysis was carried out using SEM/EDS.

6.4.1. SEM/EDS analysis of lime-doped coke analogue

Given in *Figure 6.12a* is the SEM image of a cross-section of lime-doped coke analogue and a Ca EDS map (the complete set of elemental EDS maps were given in Section 4.4). Distinct lime particles of the original added size of 38 – 53 μm were not observed. The calcium (from lime) was dispersed throughout the analogue, probably in nanometer sized particles. If compared with micrographs and Ca EDS maps of analogues doped with C3A (*Figure 6.12 b*), CA (*Figure 6.12 c*) or CA6 (*Figure 6.12 d*), it can be seen that the mineral particles were angular, and of similar size to those which were originally added to the analogue (38 – 53 μm) (see

Figures 4.20, 4.24,4.28 and 4.32). The minerals were found within the carbon matrix formed from the graphite particles, Novalac and Bakelite resin. This was also found to be true for the majority of the other materials (quartz, CAS, hematite, iron, magnetite, pyrite, troilite, K/Na feldspar, gypsum and kaolinite) that have been investigated using the coke analogue [24].

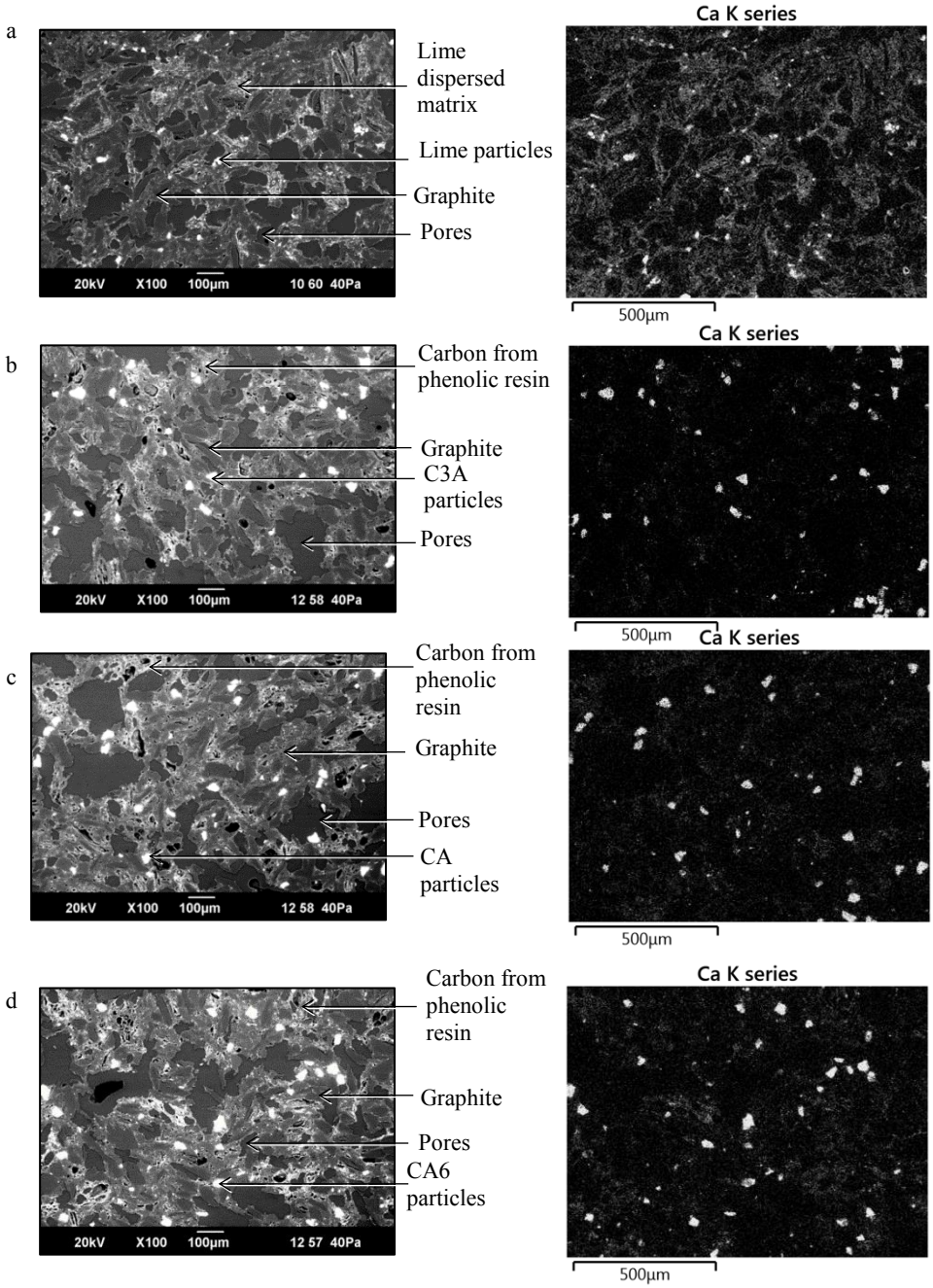

Figure 6.12: SEM backscattered images and Ca EDS maps of (a) lime (b) C3A (c) CA and (d) CA6.

The mineral particle size distribution of the lime-doped analogue given in *Figure 6.12* was significantly different from the distribution for the other analogues. Though the mass of the minerals was similar in each of the minerals-doped coke analogues, the reduced particle size in the lime-doped coke analogue resulted in a greater contact area. This increased surface area can, at least in part, be the cause of the increased measured reaction rate of the lime-doped coke analogue. Consider *Equation 5.1,* the general heterogeneous reaction rate equation [122, 142-144],

$$\frac{dX}{dt} = k\ A\ \Delta C^n$$

It can be seen from *Equation 5.1* that the reaction rate is proportional to k, ΔC and A. These terms were discussed previously in Section 5.1.5. However, the term A is discussed here in more detail relative to the mineral addition.

For the carbon gasification reaction given in *Equations 2.10* and *2.11*,

$$C_f + CO_{2(g)} \underset{j_2}{\overset{j_1}{\rightleftarrows}} C(O) + CO_{(g)}$$

$$C(O) \xrightarrow{j_3} CO_{(g)} + C_f$$

A is principally the contact area between C and CO_2. However, the presence of minerals introduces another contact area between the mineral and C. This additional contact area can be expected to increase the number of C_f s in the coke analogue. Therefore, it can be expected that the rate of reaction would be, at least in part, proportional to the contact area between C and the mineral.

It would appear that the lime has reacted with the carbon matrix, mainly with Bakelite and Novolac, and spread throughout the analogue. This reaction has resulted in lime particles of a smaller size in smaller particle sizes. The smaller size of the lime particles will result in an increase in the contact between the mineral and C. This, in turn, would increase C_f and the rate of gasification.

6.4.2. Dispersion behaviour of Ca in the coke analogue

While this dispersed mineral behaviour has not been observed for Ca in other mineral additions to the analogue, it is similar to that found in low ranked lignite coals [59-61] and coke produced from low ranked coals [33]. In lignites, Ca is dispersed throughout the coal as salts of carboxylic acids [59-61]. These salts are thought to be products of acid-based reactions. The liquid Novolac resin in propylene glycol used in coke analogue preparation is weakly acidic, containing phenolic –OH groups (*Figure 6.13 a* and *b*). These phenolic groups may be reacting with the lime in a manner similar to the known reaction between carboxylic acids and Ca in coals, possibly through a neutralisation reaction.

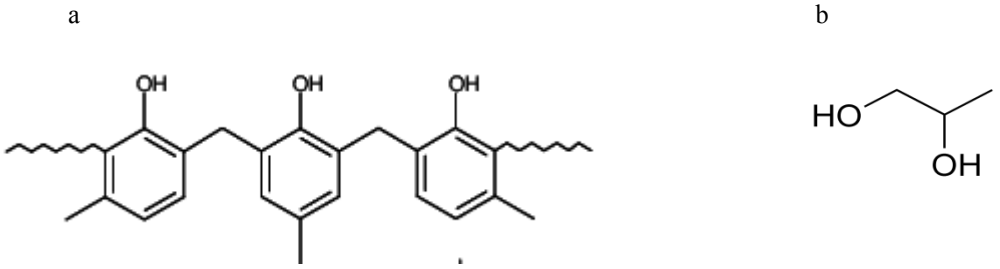

Figure 6.13: Chemical structures of (a) Novolac resin and (b) Propylene glycol [175].

The observed form of the calcium species in the coke analogue by XRD was principally CaO (> 80 %) (see *Figure 4.60* for the XRD pattern). This may be due to the formation of stable CaO due to the heat treatment during the coke analogue preparation procedure.

To test the possibility of lime reacting with coke analogue ingredients, lime was added to the liquid Novolac in propylene glycol resin. This mixture was cured and fired under the same conditions provided for the coke analogue preparation (see Section 3.2). As with the coke analogue, HTMA was added to the samples as a curing agent. For comparison, this procedure was also carried out for C3A, CA, CA6 and alumina. Similarly to the coke analogues, these samples were sectioned, mounted and polished to observe through SEM. *Figures 4.62 – 4.66* are SEM images of particles before addition to the coke analogue/ novalac mixture and after addition to the novalac mixture. They also show EDS elemental maps of the mixtures. Given in *Figure 6.14*

is a summary of the SEM images of the particles after being added to the Novolac resin.

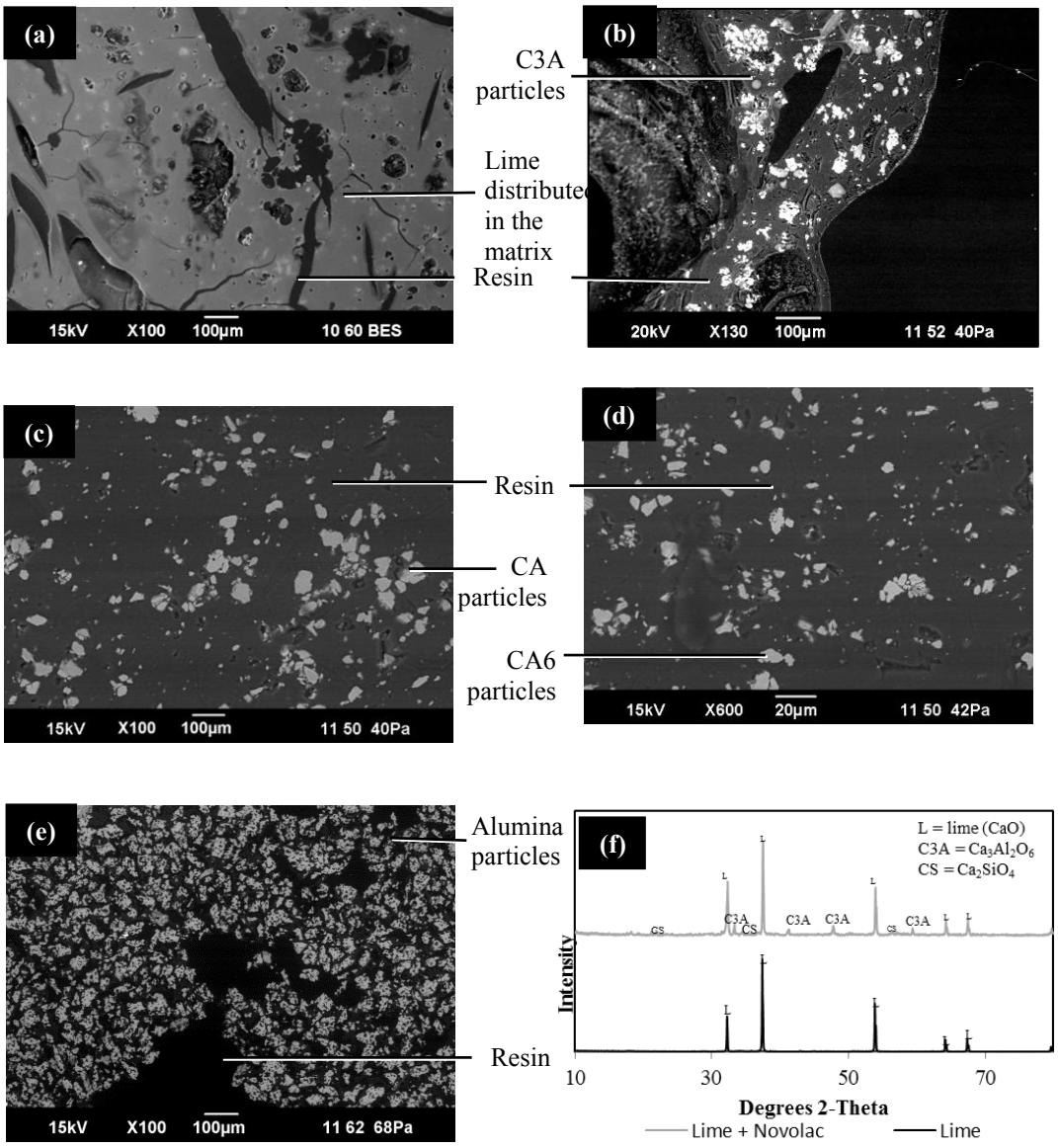

Figure 6.14: SEM backscattered images of minerals and novalc mixtures: (a) lime+Novalac (b) C3A + Novalac (c) CA + Novalac (d) CA6 +Novalac and (e) alumina + Novalac (f) XRD patterns of Lime and Lime +Novolac.

Figure 6.14 (a) shows that the lime has reacted with the Novolac resin. It was no longer in discrete particles but dispersed throughout the fired sample, similar to the results for the coke analogue. Contrast this with the other minerals in *Figures 6.14 (b) – (e)* where the minerals were still observable as discrete particles after firing. EDS analysis for the elemental Ca for mixtures prepared with lime, C3A, CA and CA6 shown in

Figure 6.15 indicate that the Ca in the-lime added mixture has reacted with Novolac, while in other mixtures (C3A, CA and CA6 added mixtures), Ca distribution shows that it is still present as discrete particles.

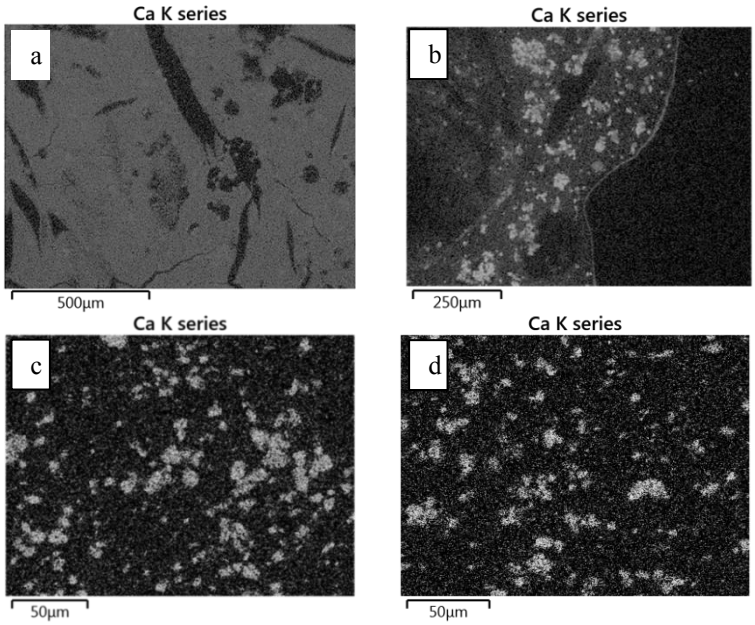

Figure 6.15: EDS maps for the elemental Ca in minerals and Novalc mixture (a) lime+Novalac (b) C3A + Novalac (c) CA + Novalac and (d) CA6 +Novalac.

The reaction of lime with the Novalac resin evidenced in *Figures 6.14* and *6.15* offers a plausible mechanism for the behaviour of lime in the coke analogue. Though Novalac resin does not exist in metallurgical coke, the parent coals and cokes have similar compounds such as carboxylic acid groups that could lead Ca to react and disperse throughout the coke.

High mobility of Ca has previously been observed in coke. Coke dissolution in iron studies that have been carried out using blast furnace coke observed a similar type of behaviour, producing a calcium enriched mineral layer [27, 176-180]. This Ca-enriched mineral layer is considered very important in the formation and subsequent densification of the mineral layer [27]. High mobility of Ca in coke [25-27] has been suggested as a possible reason for the observation of this Ca-enriched mineral layer in the form(s) of mobile calcia products [27]. The formation of such mobile calcia products is however not yet clearly understood. The present study indicates a possible pathway and may in part explain this phenomenon.

Chapter 7

A discussion on the catalysis mechanism of Ca-bearing minerals

From *Figures 6.9* and *6.10,* it can be seen that increasing the Ca content in the added minerals to the coke analogue increased the coke analogue gasification. It was also shown that the apparent activation energies, E_a, decreased with increasing Ca content in the added mineral (*Table 6.1* and *Figure 6.4*). This was found to be true in both the CaO – Al_2O_3 binary and CaO – Al_2O_3 – SiO_2 ternary systems. As discussed in Section 6.4, the reaction rate is a function of the contact area, A, where A can be the contact area between C and gas or C and mineral. With the exception of the lime-added (CaO) coke analogue, all the gasification results were conducted under specific conditions so that the starting contact areas between the minerals and C were approximately similar. In Table 7.1, the total surface contact area between C and the mineral (calculated based on the density values from [181-184]) are shown. Full details of how the contact area was calculated are given in Appendix VIII.

Table 7.1: The total contact surface area between the added mineral and C in the coke analogues.

Mineral added to the coke analogue	Total surface area / m^2 per analogue
CA6	0.19
CA	0.21
C3A	0.21
CAS	0.22

Note: The total surface area was calculated to show the similar surface area of the mineral particles.

This poses the question, why do the Ca-containing minerals increase the rate of coke analogue gasification?

The effect of Ca-containing minerals on the gasification reactivity is often explained as a catalytic effect.

If the mineral is behaving as a catalyst in the coke analogue gasification, then it may be affecting the rate by,

- increasing the amount of active carbon sites (C_f),
- increasing the CO_2 dissociation rate at the solid-gas interface, or
- increasing the rate of CO removal from the carbon surface.

These effects can be seen to increase the coke gasification reaction mechanism detailed in Section 2.5.1, using *Equations 2.10* and *2.11,*

$$C_f + CO_{2(g)} \underset{j_2}{\overset{j_1}{\rightleftarrows}} C(O) + CO_{(g)}$$

$$C(O) \overset{j_3}{\rightarrow} CO_{(g)} + C_f$$

The following mechanisms have been proposed to deal with the effects of Ca containing minerals on coke / coke analogue gasification (see Section 2.5.1):

1. Dissociation of carbon on to the mineral.
2. Dissociation of CO_2 on the mineral surface.
3. Formation of carbonates.
4. Increasing electron density of the neighbouring carbons.
5. Formation of intercalates in between the crystal structure of graphite.

These are discussed here in terms of the context of the experimental conditions used in this study.

7.1.Dissociation of carbon on to the mineral

If carbon is dissociated on to the mineral, Ca in the added minerals reacts with C to form CaC_2 (*Reaction 7.1*) [129-131, 185].

$$CaO_{(S)} + 3C_{(S)} \rightarrow CaC_{2(S)} + CO_{(S)} \qquad 7.1$$

Therefore, the C – C bonds at the C – Ca interface are weakened. These weakened C-C bonds can act like active sites, C_f s, in *Equations 2.10* and *2.11* that can ultimately increase the carbon gasification. The possibility of this reaction occurring under the experimental conditions of this study was assessed thermodynamically by calculating ΔG^o using the reaction module of FactSage 7.0 [155]. For FactSage 7.0 calculations,

the available CaO_2 was used and assumed to be equivalent to CaO.O. Given in *Figure 7.1* is a plot of ΔG^{o} vs Temperature for the *Reaction 7.1.*

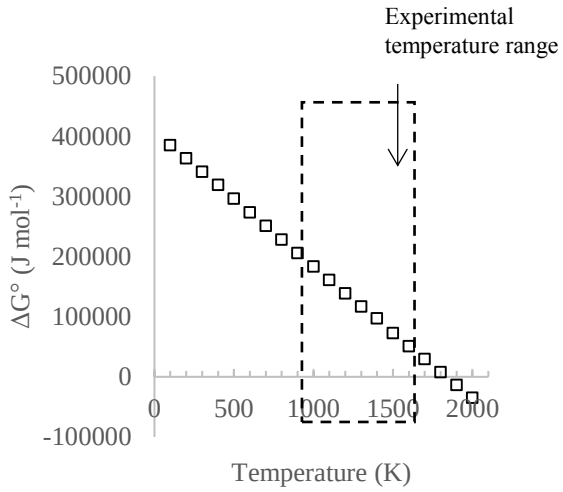

Figure 7.1: A plot of ΔG° vs temperature for the reactions 7.1.

It was found that the *Reaction 7.1* had a $\Delta G^{o} > 0$ for the temperature ranges evaluated in this study. It is therefore unlikely that a CaO - C reaction occurred during the gasification experiments.

Given in *Figure 7.1* is the reactivity of pure lime (CaO) as per the reaction given in *Equation 7.1.* Pure lime will have an $a_{CaO} = 1$ while the Ca in the other minerals will have a lower a_{CaO} value (see *Table 6.3*). These lower a_{CaO} values likely represent lower reactivities of other Ca-containing minerals and therefore higher ΔG^{o} values than for the values in *Figure 7.1, i.e.* the Ca in other minerals will be less reactive than CaO with C. This would make the mechanism of dissociation of C on to the mineral even less favourable, making the mechanism unlikely to be the one applicable to this study.

7.2.Dissociation of CO_2 on mineral surface

Dissociation of CO_2 on the mineral surface has been suggested for carbon gasification in the presence of CaO [129, 130, 132] (see Section 2.5.1). In this mechanism, CO_2 gas is dissociated on the CaO to form CO and surface oxygen complexes with CaO (CaO.O). Then the oxygen in the surface oxygen complex can spill over the carbon-creating surface oxygen complex with carbon. This mechanism is represented by reactions given in *Equations 7.2 – 7.4.*

$$CaO_{(s)} + CO_{2(g)} \leftrightarrow CaO.O_{(s)} + CO_{(g)} \quad 7.2$$

$$CaO.O_{(s)} + C_{(s)} \leftrightarrow CaO_{(s)} + C(O)_{(s)} \quad 7.3$$

$$C(O)_{(s)} \leftrightarrow CO_{(g)} \quad 7.4$$

The possibility of *Equation 7.2* occurring under the experimental conditions of this study was assessed thermodynamically by calculating ΔGº using the reaction module of FactSage 7.0 [155]. For FactSage 7.0 calculations, the available CaO_2 was used and assumed to be equivalent to CaO.O. *Figure 7.2* plots ΔGº vs Temperature for *Reaction 7.2.*

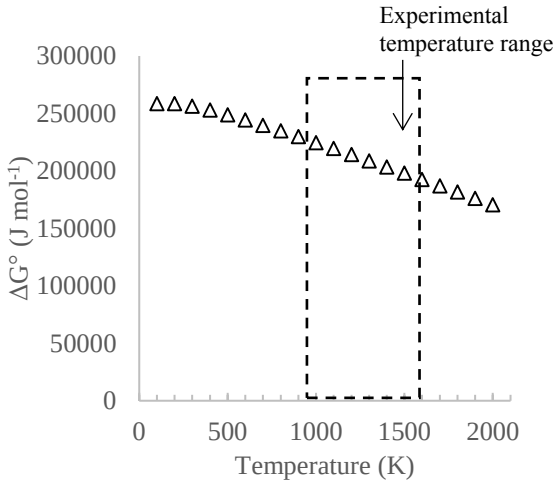

Figure 7.2: A plot of ΔG° vs temperature for Reaction 7.2.

It was found that *Equation 7.2* had a ΔGº >> 0 for the temperature ranges evaluated in this study. *Figure 7.2* represents a reaction with pure lime. The activities of other Ca-containing minerals will be lower and therefore have higher ΔGº values than for the reaction with lime. It is therefore unlikely that this reaction occurred during the gasification experiments, making the mechanism unlikely to be the one applicable to this study.

7.3.Formation of $CaCO_3$

If $CaCO_3$ formed during the gasification, CaO in the carbonaceous matrix might act as a medium for the transport of CO_2 to the carbon surface, as represented by the reactions given in *Equations 7.5 and 7.6* (detailed in Section 2.5.1).

$$CaO_{(s)} + CO_{2(g)} \leftrightarrow CaCO_{3(s)} \quad 7.5$$

$$CaCO_{3(s)} + C_{(s)} \leftrightarrow CaO_{(s)} + 2CO_{(g)} \quad 7.6$$

However, it was found that the reaction given in *Equation 7.5* had a $\Delta G^o > 0$ (from FactSage calculations) for the temperature ranges evaluated in this study (see *Figure 7.3).*

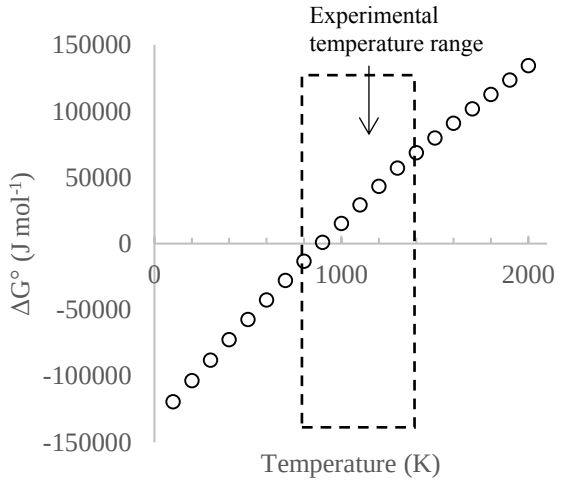

Figure 7.3: A plot of ΔG° vs temperature for Reaction 7.5.

The reactivity will be lower for other Ca-containing minerals, and therefore the reactions with other Ca-containing minerals will have higher ΔG^o compared to the ΔG^o for the reaction given in *Equation 7.5*. It is therefore unlikely that this reaction occurs during the gasification experiments, making the mechanism unlikely to be the one applicable to this study.

7.4.Formation of intercalates in between the crystal structure of graphite

Particular minerals can form intercalates in the crystal structure of graphite, as first discussed in Section 2.5.1. The formation of intercalates can cause an expansion of the

coke carbon lattice (to form cracks), increase stress, modify the coke surface area, weaken coke strength and weaken coke structure. All these effects have the potential to create active carbon sites, C_f s (*Equation 2.10* and *2.11),* and thereby increase the reaction rate. If this happens in the coke analogue-containing Ca in the added minerals, a change in d spacing as defined using Bragg's equation (Equation 7.7) is expected [106].

$$d = \frac{\lambda}{2 \sin \theta} \qquad 7.7$$

The formation of intercalates in coke analogue was assessed using the XRD patterns of the Ca-containing coke analogue. The d spacing was calculated for the observed graphite 002 peaks for coke analogues with Ca in the added minerals (*Figure 7.4*).

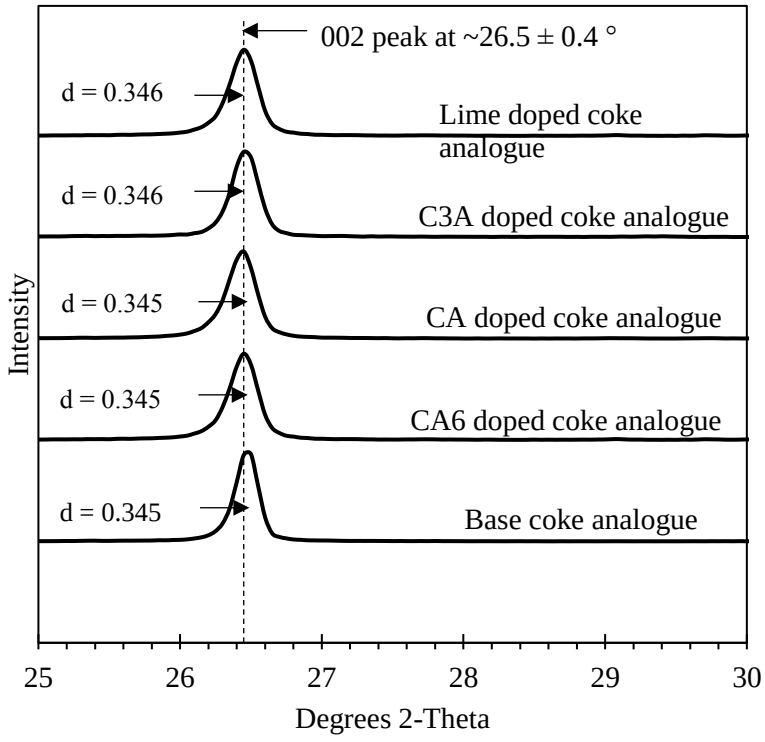

Figure 7.4: XRD patterns of base coke analogue and minerals-doped (CA6, Ca, C3A and lime) coke analogues showing the graphite 002 peak at ~26.5 °and its d spacing value.

The d spacing values do not show any significant trend with Ca in the mineral and are relatively constant; the values are less than 0.3 % different. It is, therefore, unlikely

that Ca in the added minerals will form an intercalation product with the graphite in the coke analogue carbon matrix, making the mechanism unlikely to be the one applicable to this study.

7.5.Increasing electron density of the neighbouring carbons

Increasing the electron density of the neighbouring carbons was suggested for the catalysis of carbon gasification in the presence of Ca species, as discussed in Section 2.5.1 [134]. In a previous study carried out by Gonzales *et al.* [134], density functional theory (DFT) was used to evaluate the interaction between Ca in the added mineral and the carbonaceous materials. It has been suggested that the interaction between Ca and C can affect the neighbouring C atoms where the reaction with oxygen coming from CO_2 dissociation could take place. *Figure 7.5* is an illustration summarising this mechanism.

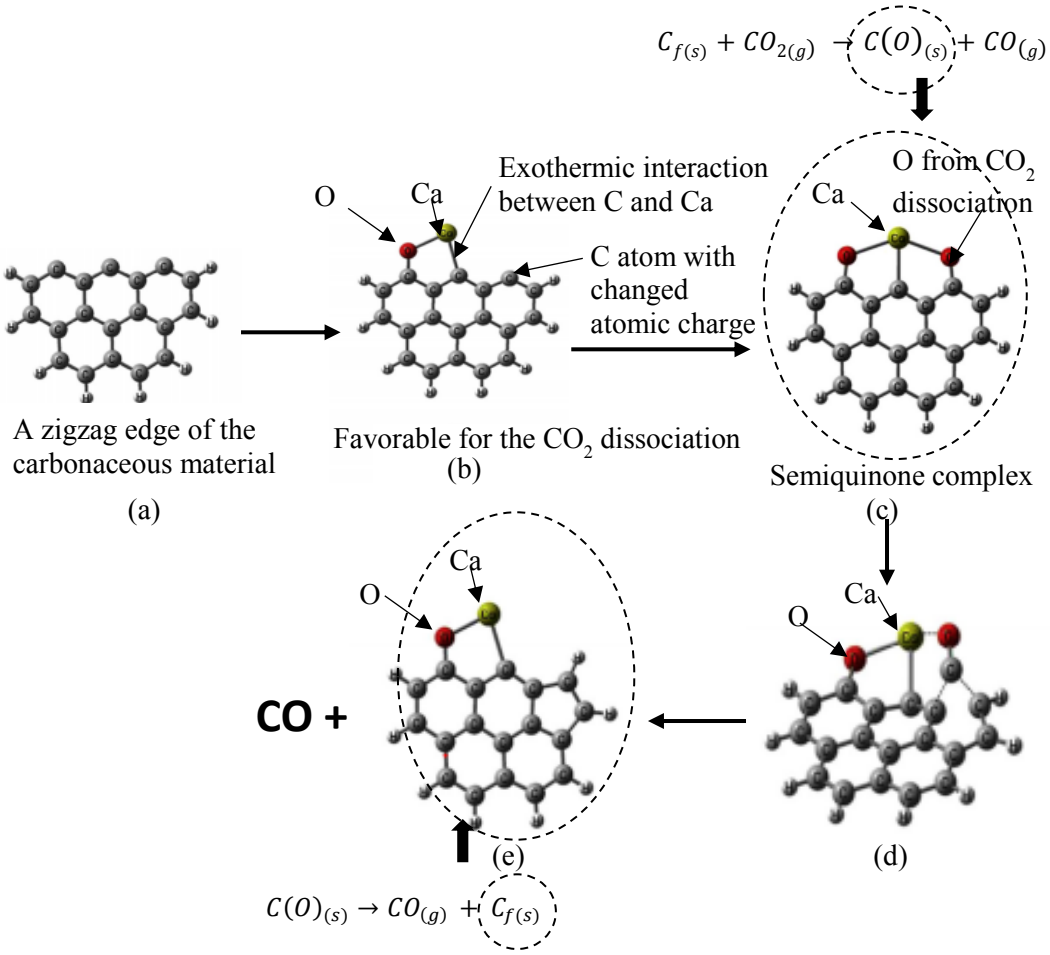

Figure 7.5: An illustration of a summary of the possible mechanism of carbonaceous material catalysis by CaO (modified from [134]).

Gonzales *et al.* [134] found that the interaction between C and Ca is exothermic. An increase in the electron density in the C close to the C - Ca interaction site was found. This increased electron density would make the edge carbon more reactive and suitable for chemisorption of oxygen coming from CO_2 dissociation, *i.e*. it would increase the rate of *Equation 2.10* (Section 2.3.2). The chemisorbed oxygen can form a semiquinone structure (*i.e*. surface oxygen complex) as shown in *Figure 7.5 (c).*

Therefore, these carbons with increased electron density act as active sites (C_f) that are stronger than the C_f s in an un-catalysed carbonaceous matter, which can increase the CO_2 dissociation [134]. It can then be expected to increase the rate of CO_2 dissociation. Gonzales *et al.* [134] also found that the removal of CO from the complex is thermodynamically more favourable, as per *Figures 7.5 (c)* and *(d),* after the catalysis by Ca/CaO.

This increased strength of C_fs offers a plausible explanation as to why Ca increases the reactivity of the coke analogues in this study. However, this mechanism does not suggest that it has any effect on the rate determining step (*Equation 2.11* as discussed in Section 2.3.2), and therefore, does not explain the decreasing trend in the apparent activation energy.

Among the mechanisms discussed in this chapter, only the mechanism that involves increasing electron density of the neighbouring C can be considered possible under the experimental conditions in this study.

A summary of the discussed catalytic mechanisms for the coke analogues with Ca-containing minerals is given in *Table 7.2.*

Table 7.2: A summary of the possible mechanisms and comments based on the experimental observations.

Mechanism	Comments
Dissociation of carbon on to the mineral $CaO_{(S)} + 3C_{(S)} \rightarrow CaC_{2(S)} + CO_{(S)}$	It was not possible for the reaction to occur thermodynamically under the experimental conditions used in this study.
Dissociation of CO_2 on mineral surface $CaO_{(s)} + CO_{2(g)} \leftrightarrow CaO.O_{(s)} + CO_{(g)}$	It was not possible for the reaction to occur thermodynamically under the experimental conditions used in this study.
Formation of $CaCO_3$ $CaO_{(s)} + CO_{2(g)} \leftrightarrow CaCO_{3(s)}$	It was not possible for the reaction to occur thermodynamically under the experimental conditions used in this study.
Formation of intercalates in between the crystal structure of graphite.	There was no broadening of the (002) carbon XRD peak indicating that interaction did not occur in the coke analogue.
Increasing electron density of the neighbouring carbons.	Offers a plausible explanation as to why Ca increases the reactivity of the coke analogues used in this study.

Chapter 8

Application of the random pore model (RPM) for Zone I of the coke analogue

In Chapters 4 -7 coke analogue reactivity in CO_2, and the effect of Ca-bearing minerals on coke analogue gasification, were analysed and discussed using the Walker *et al.* approach [91]. This approach does not require the contact surface area of the gas and C (in metallurgical coke or coke analogue) for the evaluation of the gasification reactivities. This can cause problems in the predictability of coke gasification and comparisons of the gasification reactivity between cokes, particularly of cokes with significantly different porosities and pore structures. The complex pore structure of metallurgical coke makes the contact area between the gas and the carbon difficult to evaluate, hence the common usage of the Walker *et al.* approach [91]. Details of the relative importance of the contact area in zones I to III are discussed in Section 5.1.4 and 6.4.1.

The RPM is a model that has been applied with some success to porous carbonaceous materials [113, 115, 186] (see Section 2.3.3). The RPM considers pore development during gasification. This pore development represents a change in the contact area for the gas and C (from the carbonaceous material). The RPM model will be applied to the coke analogue gasification results in this thesis to test its applicability to examine the effect of pore development.

In the RPM, in the absence of any diffusion control, *i.e.* for Zone I, the reaction rate is expressed as *Equation 2.23* [113, 116-118],

$$\left(\frac{dX}{dt}\right) = \frac{R_C S A_0 (1-X)\sqrt{1-\varphi \ln(1-X)}}{(1-\varepsilon_0)} = K_{RPM}(1-X)\sqrt{[1-\varphi \ln(1-X)]}$$

where φ was given by *Equation 2.24*,

$$\varphi = \frac{4\pi L_0 (1-\varepsilon_0)}{A_0^2}$$

8.1. Determination of the structural parameter, φ for coke analogues

To use the RPM for the coke analogue, it is necessary to determine the coke analogue structural parameter φ, which is normally established through either,

- BET measurements and image analysis, or
- Experimental gasification rate results and *Equation 2.27,*

$$\varphi = 2(1 - \varphi \ln(1 - X_m) = \frac{2}{(1 + 2ln(1 - X_m)}$$

where X_m is the carbon conversion at maximum reaction rate, R_C (see *Figure 8.1* for a typical plot of R_C vs X for a coke).

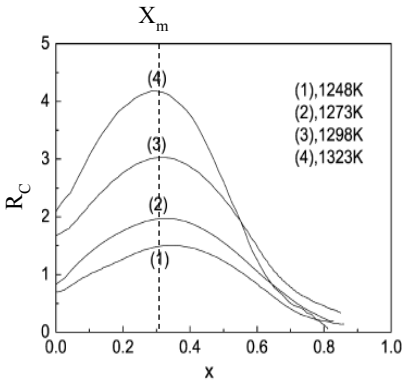

Figure 8.1: A typical plot of R_C vs X for a coke (after [146])

In this study, it was not possible to carry out BET measurements on the coke analogue (see Appendix V). Therefore, the possibility of using *Equation 2.27* to calculate φ was evaluated.

It was stated that *Equation 2.27* only has allowable values for X_m of,

$$0 < X_m < 0.393 \text{ [113].}$$

This was confirmed in the current study by evaluating φ from $X_m = 0$ to $X_m = 0.5$ and the results are given in *Figure 8.2*. From this figure, it can be seen that above 0.393, φ becomes negative. This is not a physically realisable value for gasification of metallurgical coke or coke analogue in CO_2 gas.

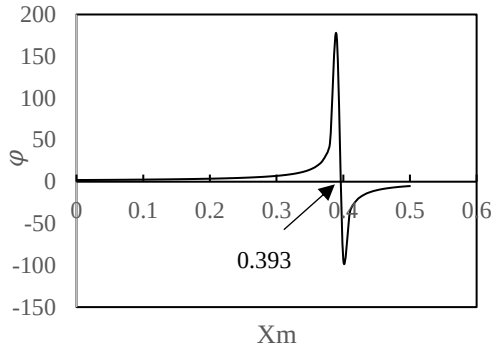

Figure 8.2: A theoretical plot of φ vs X_m.

The relationship between R_C and X (where $0 < X < 0.4$) of the base coke analogue was studied at 1273 and 1298 K to check the applicability of this equation for the coke analogue to determine φ. These two additional tests were carried out because not all the available data for coke analogue gasification reached X = 0.4. Given in *Figure 8.3* are the R_C vs X plots for the coke analogue gasification in CO_2 for $X < 0.4$. The shape of the curve given in *Figure 8.3* is similar to that of *Figure 8.1* indicating that the approach is suitable for determining φ in the analogue. The maximum of the curve occurs at approximately X = 0.12, therefore, X_m is approximately 0.12.

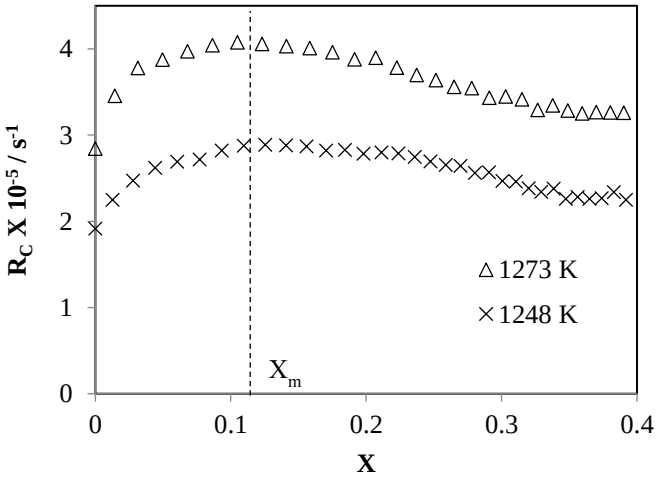

Figure 8.3: A plot of R_C vs X plots for the coke analogue gasification in CO_2 at 1273 and 1298 K.

Evaluation of an acceptable φ for base and minerals-doped coke analogues studied

By definition, the structural parameter, φ, given in *Equation 2.26*,

$$\varphi = \frac{4\pi L_0(1-\varepsilon_0)}{S_0^2}$$

is primarily affected by the initial values of porosity, surface area and total pore length. The coke analogues are controlled materials and were designed to have similar characteristics as much as possible, while varying only the mineral type. Therefore, it is expected that each of the coke analogues would have similar or close φ values. The φ value was evaluated by using the results obtained for the coke analogues gasification in CO_2 for the temperatures identified as in Zone I by Walker *et al.*'s approach [91] *i.e.* 1173 – 1298 K. However, at lower temperatures, (1173 – 1223 K) the reaction time of 2 hours, which was generally used in the experimental program, was not enough to establish a maximum reaction rate, *i.e.* X_m was not identified. Therefore only the data for 1248 – 1298 K were used in the assessment. *Table 8.1* shows the calculated φ values for the base and mineral-doped coke analogues. The R_C vs X plots that were used to obtain X_m are given in Appendix IX.

Table 8.1: Calculated φ values for the coke analogues at the temperatures where X_m was observed.

Temperature / K	φ							
	Base coke analogue	Alumina doped coke analogue	CA6 doped coke analogue	CA doped coke analogue	C3A doped coke analogue	Lime doped coke analogue	CAS doped coke analogue	Quartz doped coke analogue
1248	2.96	2.77	(-)	3.06	No maximum value observed	2.23	2.69	2.77
1273	2.77	2.96	2.20	3.19*		2.23	2.96	2.61
1298	2.69	3.46	(-)	2.19		2.19	3.46	2.86

(-) means experiments were not carried out at this temperature

* The X_m was observed for a range of X values and φ was calculated from the X value at the centre of the observed X_m range.

The φ values were plotted against temperature for all the available data (see

Figure8.4). From this figure, it can be seen that φ appears to be reasonably independent of temperature for these phases and is scattered around a mean value of 2.75. The calculated constant value of φ is consistent with what might be expected for a coke analogue of constant or fixed initial porosity and pore distribution. Therefore, this constant value, 2.75, was used as φ for the RPM.

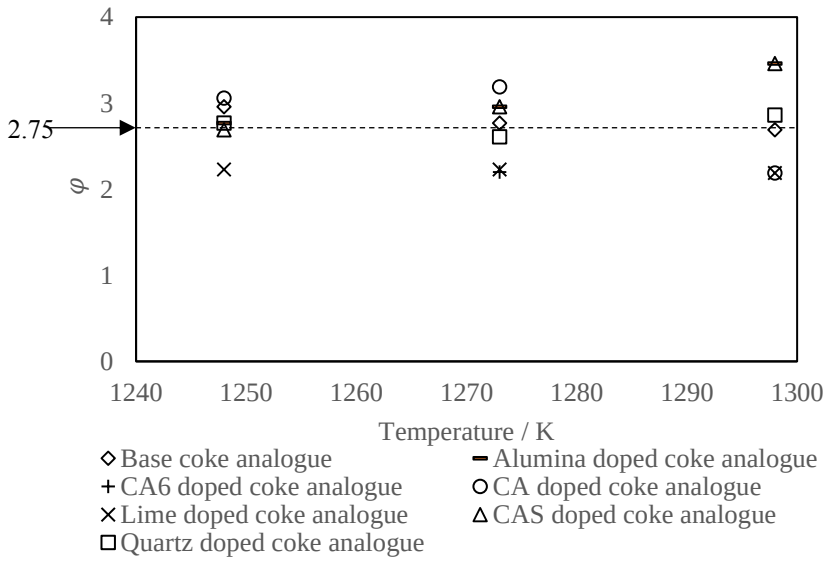

Figure 8.4: The calculated φ values for all the coke analogues for the temperature range 1248 – 1298 K

8.2. Application of RPM to the coke analogue

In this thesis, the RPM has been used to,

1. evaluate the K_{RPM}, the random pore model rate constant,
2. predict the FWC with time behaviour of the coke analogue,
3. obtain the activation energies for Zone I kinetics, where Zone I was defined by Walker *et al.* approach [91] and
4. assess the model's use in predicting the Zone I to II transition temperature.

8.2.1. Evaluation of K_{RPM}

The RPM as expressed in *Equation 2.23,*

$$\left(\frac{dX}{dt}\right) = \frac{R_C S_0 (1-X)\sqrt{1-\varphi \ln(1-X)}}{(1-\varepsilon_0)} = K_{RPM}(1-X)\sqrt{[1-\varphi \ln(1-X)]}$$

was written as an integral and evaluated from X = 0 to X = X and t = 0 to t = t, to obtain *Equation 8.1,*

$$\int_0^X \frac{dX}{(1-X)\sqrt{[1-\varphi ln(1-X)]}} = \int_0^t K_{RPM}\, dt \qquad 8.1$$

Solving and re-arranging *Equation 8.1* gives *Equation 8.2,*

$$\frac{2}{\varphi}\left[\sqrt{1-\varphi \ln(1-X)} - 1\right] = K_{RPM}.t \qquad 8.2$$

To obtain K_{RPM}, the term $\frac{2}{\varphi}\left[\sqrt{1-\varphi \ln(1-X)} - 1\right]$ was plotted against time for the temperature range of 1173 – 1273 K (see *Figure 8.5*). The temperature range used to establish K_{RPM} was that found to be representative of Zone I using the Walker *et al.* approach [91]. The K_{RPM}s obtained from the gradients of the curves are given in *Table 8.2.*

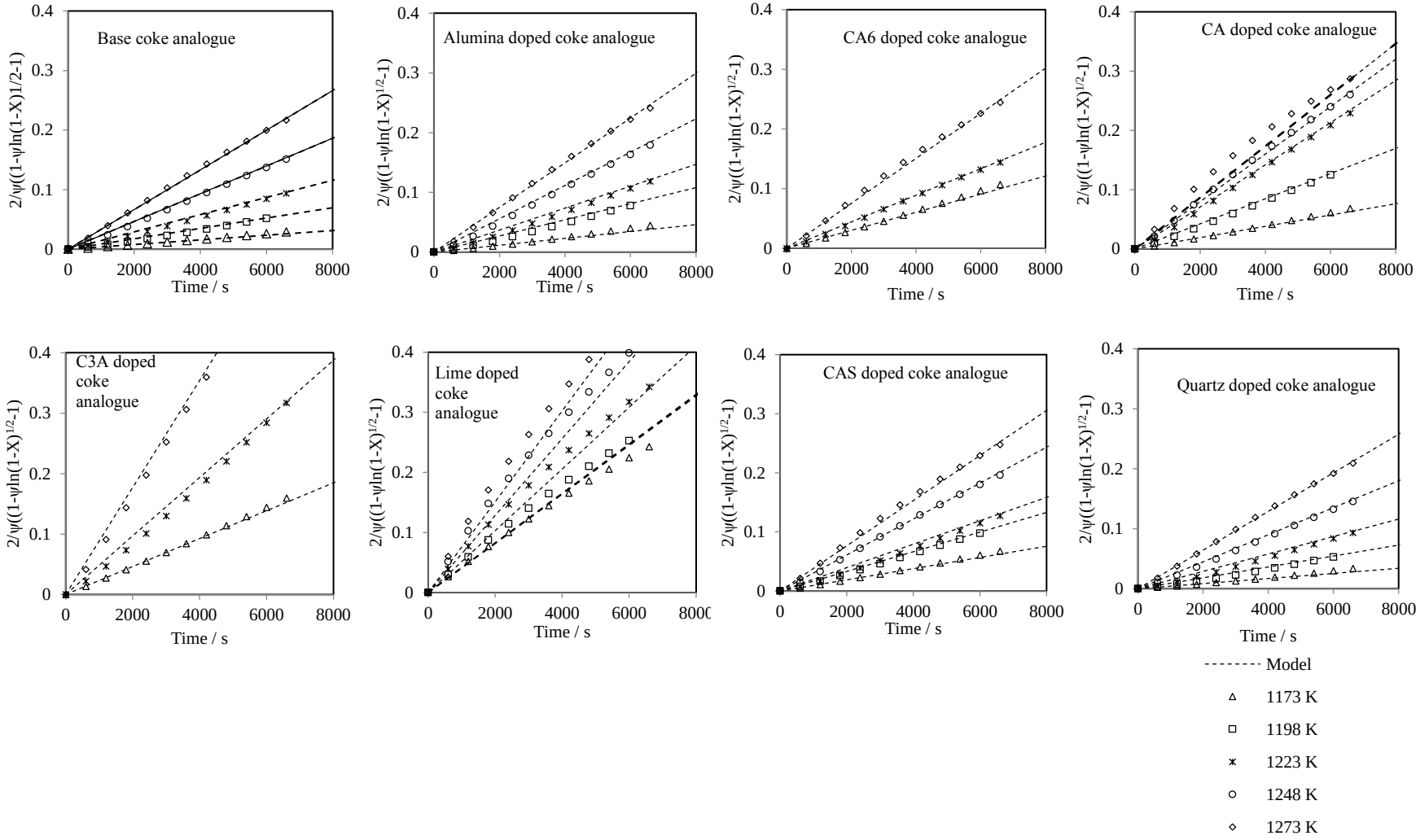

Figure 8.5: Plots of predicted and experimental $\frac{2}{\varphi}\left[\sqrt{1-\varphi\ln(1-X)}-1\right]$ *vs time for the coke analogues*

Table 8.2: Calculated K_{RPM} from the gradients of $\frac{2}{\varphi}\left[\sqrt{1-\varphi\, ln(1-X)}-1\right]$ vs time for the coke analogues.

Temperature / K	$K_{RPM} X\ 10^{-5}$							
	Base coke analogue	Alumina doped coke analogue	CA6 doped coke analogue	CA doped coke analogue	C3A doped coke analogue	Lime doped coke analogue	CAS doped coke analogue	Quartz doped coke analogue
1173	0.392	0.568	0.822	1.20	2.31	3.60	0.847	0.444
1198	0.871	1.35	-	2.12	-	4.13	1.66	0.913
1223	1.45	1.84	2.22	3.15	4.84	5.14	2.20	1.45
1248	2.33	2.79	-	4.00	-	6.41	3.04	2.25
1273	3.33	3.74	4.07	5.53	7.55	9.40	4.00	3.22

The calculated K_{RPM} increased with increasing temperature and the values increased with increasing Ca content of the mineral addition.

8.2.2. Prediction of FWC with time behaviour of the coke analogue

FWC is related to X and is defined in *Equation 2.29* which is reproduced below,

$$X = \frac{W_0 - W}{W_0} = -FWC$$

Substituting *Equation 2.29* into *Equation 8.2* and re-arranging to solve for FWC gives *Equation 8.3,*

$$FWC = e^{\left(\frac{\left(2+(t.\varphi.K_{RPM})^2\right)+1}{\varphi}\right)} - 1 \qquad 8.3$$

FWC values were calculated using K_{RPM} values in *Table 8.2,* and *Equation 8.3* values were plotted against time. The plots were compared with the measured FWC curves for the temperature zone identified as for Zone I from Walker *et al.*'s approach [91] (1173 – 1298 K). The plots are given in *Figure 8.6.*

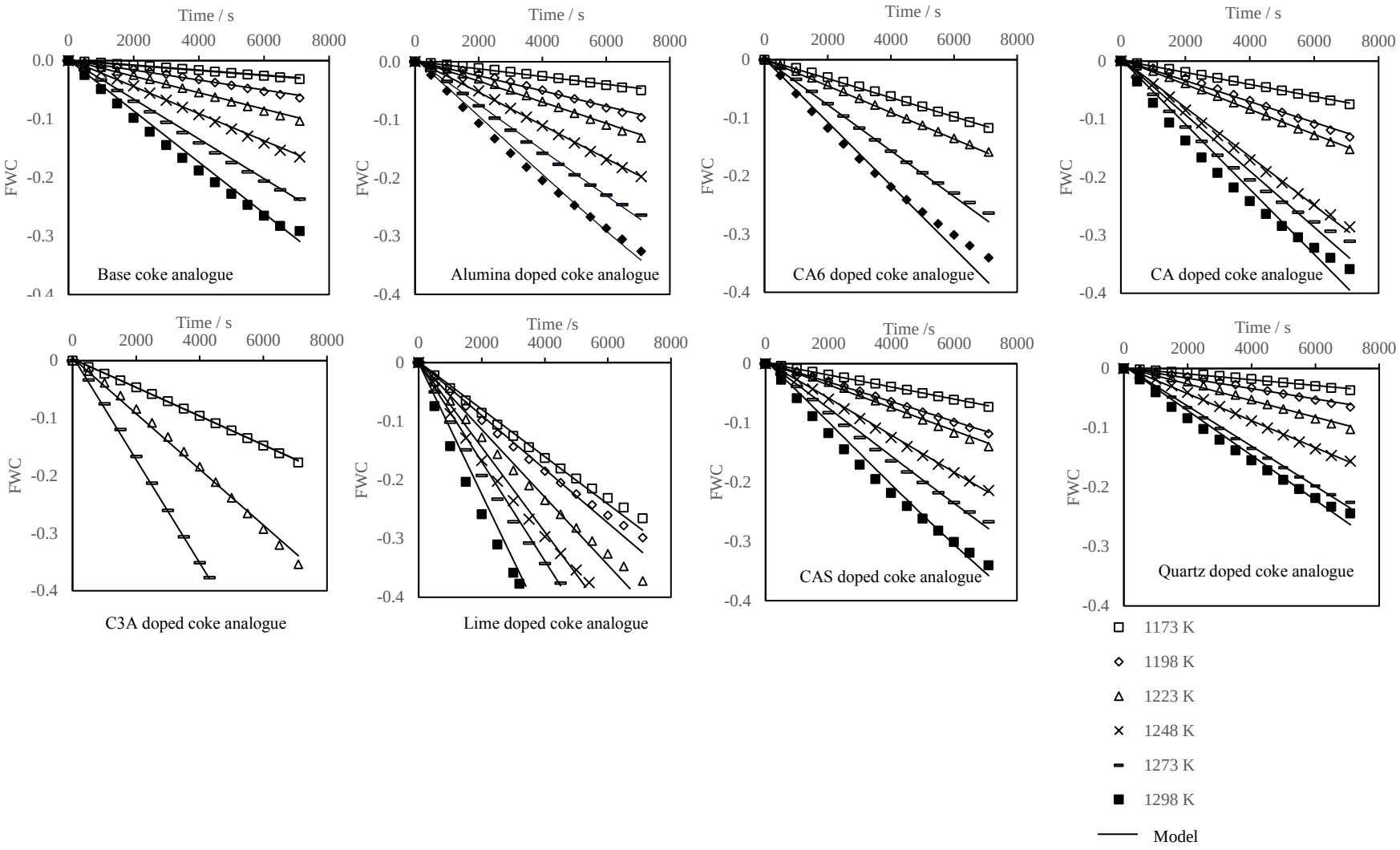

Figure 8.6: Plots of predicted and true FWC vs time for the coke analogues

Except for the lime-doped analogue, the predicted FWC from the RPM fits well with the FWC values obtained from Walker *et al.* approach [91] for the temperatures in the range of 1173 – 1273 K. At 1298 K, the highest temperature considered in this analysis, the fit is poor. For all the temperatures the RPM fit for the lime-doped coke analogue is poor. This poor fit for lime is most probably explained by the difference in the surface area available for the gasification. As discussed in Chapters 5 and 6, any gasification reaction is dependent on the surface / contact area available for the reaction to take place. Two different contact areas should be taken into account for mineral added coke analogues. These are the contact area between the carbon and the gas and the contact area between the minerals and the carbon. The contact area between the carbon and the gas is dependent on the porosity of the coke analogue. This is reasonably constant for all the minerals doped coke analogues (see Section 3.3.1). Moreover, the contact between the mineral and the carbon is different in lime-doped coke analogue as a result of the lime being dispersed with a fine particle size. This is the likely reason for the observed difference between FWCs obtained from Walker *et al.* approach [91] and RPM in the lime-doped coke analogue.

The fact that the RPM fits the coke analogue data well indicates that it could be successfully used in studying not only the mineral effects on reactivity for analogues, but also the porosity effect. This would be a relevant potential area of study for future research.

8.2.3. Activation energies for Zone I using RPM

It is expected that the K_{RPM} will have an Arrhenius (*Equation 2.20*, reproduced below) form of relationship with the temperature, similar to any rate constant,

$$k = k_o e^{-\frac{E_a}{RT}}$$

rewriting *Equation 2.20* for K_{RPM} gives *Equation 8.4*,

$$K_{RPM} = k_o e^{-\frac{E_{a,RPM}}{RT}} \qquad 8.4$$

and in the linearised form (*Equation 8.5*),

$$\ln K_{RPM} = -\frac{E_a}{R}\frac{1}{T} + \ln k_o \qquad 8.5$$

Activation energies were calculated from the gradients of plots of ln K_{RPM} vs 1/T (*Figure 8.7*) and reported in *Table 8.3*. Also given in *Table 8.3*, E_a is the activation energies calculated using the Walker *et al.* approach [91] and the E_{aRPM} values are from RPM.

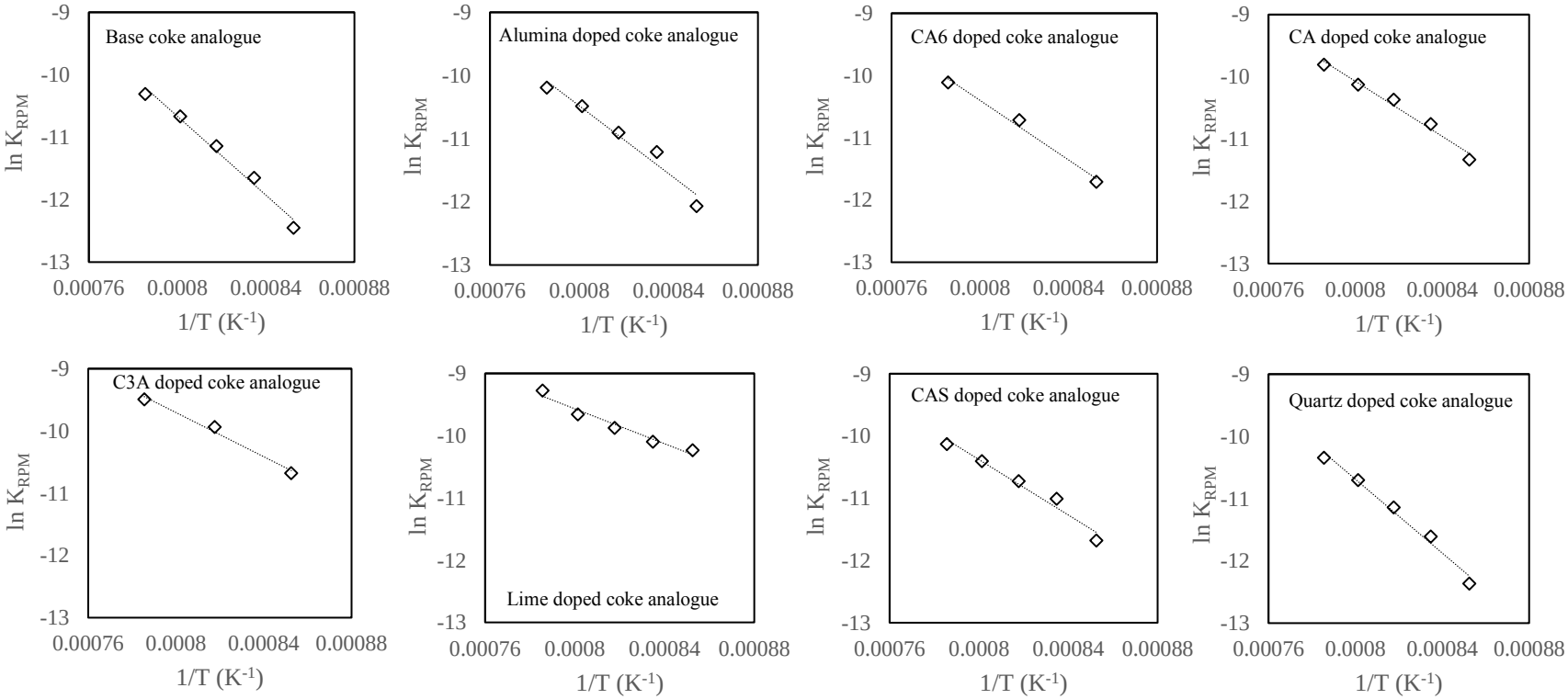

Figure 8.7: Plots of ln K_{RPM} vs 1/T for the coke analogues

Table 8.3: Calculated activation energies from the K_{RPM} (E_{aRPM}) and the Walker et al. approach [91] (E_a).

Coke analogue	Activation energy (kJ mol^{-1})		
	E_a	E_{aRPM}	*Error value**
Base coke analogue	271.5	262.5	±1.8
Alumina doped coke analogue	251.3	222.9	±1.8
CA6 doped coke analogue	204.4	198.8	±1.5
CA doped coke analogue	159.9	183.8	±1.7
C3A doped coke analogue	146.3	147.4	±1.7
Lime doped coke analogue	119.8	116.6	±1.5
CAS doped coke analogue	210.5	185.0	±1.7
Quartz doped coke analogue	248.0	246.6	±1.5

*error values based on Ea analysis.

From the comparison of E_{aRPM} and E_a it can be seen that the activation energies calculated by the Walker *et al.* approach [91] and RPM are in excellent agreement. Although the two approaches utilise two different factors, the consistency of the activation energies from both approaches validate their use in the coke analogue gasification study.

8.2.4. Use of the RPM in the prediction of Zone I

It has been shown from the previous sections that the RPM predicted FWC and activation energies were similar to the Walker *et al.* approach [91]. Therefore, perhaps it also can be used to define Zone I. The use of the RPM to evaluate the zone transition temperature from Zone I to Zone II was carried out using FWC vs time plots over the temperature range of 1173 -1623 K for the base coke analogue. As mentioned in Section 2.3.3, the RPM equation given in *Equation 2.23* was proposed for the Zone I kinetics. Therefore, any deviation of the actual FWC curves and predicted FWC curves using the RPM indicates a deviation from the Zone I mechanism.

Given in *Figure 8.8* are the true and predicted FWCs for the base coke analogue over the temperature range of 1173 – 1623 K. It can be seen that there is a clear discrepancy between the true and predicted data above approximately 1273 to 1298 K.

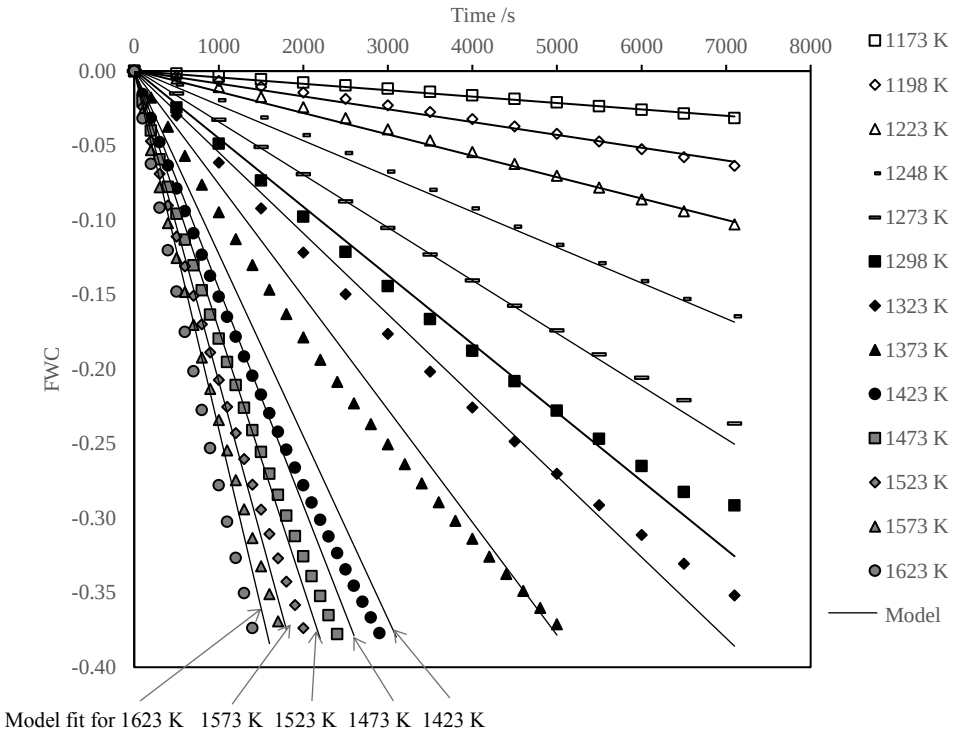

Figure 8.8: The FWC vs time plot for the predicted and true data for the base coke analogue over the temperature range of 1173 – 1623 K.

In an attempt to be quantitative in the deviation, the sum of the deviation of the Walker *et al.* [91] FWC and predicted FWC for each of the data points were calculated using *Equations 8.3* and *8.4*.

$$Deviation = Walker\ et\ al.\,[91]\ FWC - RPM\ Predicted\ FWC \tag{8.3}$$

$$Sum\ of\ Deviation = \sum\sqrt{(Deviation)^2} \tag{8.4}$$

Given in *Table 8.4* is the calculated sum of deviation of the base coke analogue. The data in *Table 8.4* were also plotted in *Figure 8.9.*

Table 8.4: Calculated deviation of the true and the RPM predicted data over the temperature range of 1173 – 1623 K

Temperature /K	Sum of Deviation
1173	0.03
1198	0.08
1223	0.12
1248	0.20
1273	0.26
1298	0.40
1323	0.42
1373	0.47
1423	0.50
1473	0.50
1523	0.52
1573	0.57
1623	0.64

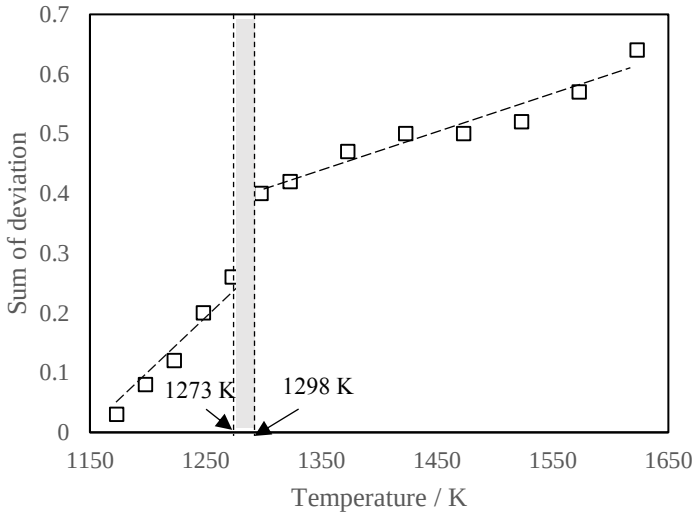

Figure 8.9: A plot of the sum of deviation vs temperature for the base coke analogue over the temperature range of 1173 – 1623 K.

From *Figure 8.9* it can be seen that the deviation increased suddenly after 1273 - 1298 K, introducing two regions in the plot. This may be considered evidence of the change in the rate controlling mechanism after ~1273 K, close to the zone transition identified in the Walker *et al.* [91] approach (~1298 K).

8.3. Summary of the application of the RPM to coke analogue gasification study

In this thesis, two approaches were used to study coke analogue gasification; the Walker *et al.* approach [91] and the RPM [113]. As discussed in previous sections of this chapter, both approaches were consistent with each other in terms of FWC with time, activation energies and zone transition temperature. With an exception with the lime-doped coke analogue, the true FWC fitted well with the RPM predicted FWC. *Table 8.5* summarises the comparison of the two approaches using the base coke analogue results.

Table 8.5: A comparison of base coke analogue results from the Walker et al. approach [91] and the RPM.

	Walker *et al.* approach [91]	RPM [113]
Zone I activation energy	271.5 kJ mol^{-1}	262.5 kJ mol^{-1}
Zone I transition temperature	1298 K	1273 – 1298 K

This consistency validates the use of both of these methods in coke analogue gasification study, and the RPM can be used to successfully predict the coke analogue gasification.

Chapter 9

Conclusions

Metallurgical coke is a complex material with respect to its carbonaceous materials, mineral components and a pore structure and also shows significant heterogeneity in its mineralogy, carbon forms and phase dispersion. This has limited the progress in the assessment of key fundamental issues relating to coke reactivity. The mineralogy of coke is one of the key factors controlling gasification in CO_2. Calcium-containing minerals are of particular interest as they are known to strongly increase the coke gasification rate. To overcome the problems associated with complexity and heterogeneity of metallurgical cokes, a coke analogue has been developed using laboratory grade materials (graphite, Bakelite, Novolac and minerals). This approach simplifies coke by doping with minerals required, while porosity, carbon type, mineral size, and mineral dispersion are controlled.

In this thesis, the first aim was to establish how representative of the metallurgical coke is the coke analogue. A few key aspects of the coke were characterised or measured and compared with the coke analogue. The assessments were carried out in terms of porosity, microstructure, carbon-bonding, general reaction mechanism in CO_2 and general reactivity behaviour, and confirmed that the analogue was representative of metallurgical coke. The key findings are addressed below in point 1 – 4.

1. Porosity measurements were carried out for the coke analogues and a metallurgical coke using two different but complementary techniques, optical microscopy and mercury porosimetry. It was found that the porosity and pore size distribution of the analogues are well controlled and more reproducible compared to the metallurgical coke. The majority of pores for the coke analogues were observed in the 10–100 μm pore diameter range which broadly represents the pores in metallurgical coke in the range of <200 μm.

2. Carbon structure and type in the coke analogue were characterised using microscopy and Raman spectroscopy. Optical and electro-optical microscopy (SEM) showed that the microstructure of the coke analogues is uniform and well-controlled compared to metallurgical coke. The microstructure of the

analogue was made up of graphite grains and carbonised phenolic resin, minerals and pores. Under optical microscopy, the graphite grains showed similar characteristics to those of RMDC while the carbonised phenolic resin of the fired analogue was similar to IMDC in metallurgical coke.

The Raman spectroscopy assessment of the coke analogue carbon bonding showed carbon bonding representative of the sp^2 and sp^2–sp^3 bonding found in fired raw materials. The $I_{(D)}/I_{(G)}$ and $I_{(V)}/I_{(G)}$ ratios for the coke analogue were 0.16–1.55 and 0–0.41. The values for metallurgical coke were found to be 1.16–1.45 and 0.38–0.62 respectively. Though the coke analogue showed a broader range of bonding from disordered to ordered, this range overlaps with that of metallurgical coke.

3. The mineralogy of the fires coke analogue was characterised by scanning electron microscopy and XRD. The mineral phase was generally found to be the same as that added to the analogue in the "given" state. In general, the size, composition and morphology of the minerals in the coke analogue was less complex, homogenously dispersed, and well controlled when compared to that of metallurgical coke.

4. The general reactivity of the coke analogue in CO_2 was assessed over the temperature range of 1173 – 1623 K using TGA. The reactivity trend with respect to time and the effects of temperature on the kinetics of the reactivity of the coke analogue were similar to that of metallurgical coke. The coke analogue showed a greater reproducibility than metallurgical coke. This reproducibility is a consequence of the controlled porosity, mineralogy, and simplified characteristics of the coke analogue.

   Applying the Walker *et al.* Arrhenius approach to the kinetics of analogue gasification in CO_2, two temperature zones corresponding to different kinetic control regimes were identified. These were the chemical reaction controlled regime (zone I) and the mixed controlled regime (zone II). The activation energy value obtained for the coke analogue (no minerals added) zone I was 271.6 ± 0.5 kJ mol^{-1}. This is within the range of activation energies reported for metallurgical coke in literature and this study, *i.e.* 222–285 $kJmol^{-1}$. This

similar activation energy is an indication of similar reaction mechanisms are active for the coke analogue and metallurgical coke gasification.

The second aim of the thesis was to understand the effects of Ca-containing minerals on coke gasification in CO_2. These effects were assessed by adding Ca-containing minerals to the coke analogue and reacting them with CO_2. The Ca-containing minerals added to the coke analogue fit into two categories.

- Minerals in the $CaO - Al_2O_3$ binary system: Al_2O_3, CA6, CA, C3A and lime (CaO)
- Minerals in the $CaO - Al_2O_3 - SiO_2$ (CAS) ternary system: A mixture of calcium aluminosilicates anorthite, gehlenite and mullite

The microstructure and the reactivity of the coke analogues doped with the above minerals were assessed. The effect of Ca-containing minerals on the coke analogue gasification was addressed in the points 5 – 7 below.

5. Increasing Ca content in the $CaO - Al_2O_3$ binary mineral systems increased the gasification reaction rate of the coke analogue. The reaction rate was found to be proportional to the total amount of Ca (n_{Ca}) in the analogue rather than a_{CaO}. The activation energies decreased with increasing Ca content in the added minerals. CAS and CA6 contained similar amounts of Ca and were found to have similar reactivities and activation energies. Alumina and quartz had no or negligible effect on the reactivity over the temperature range used in this thesis.

6. Ca in the lime doped coke analogue was dispersed throughout the coke analogue carbon matrix at significantly smaller sizes than the originally added particle size range. It was proposed that this dispersion be due to a reaction between acidic -OH groups in the phenolic resins and the basic CaO.

7. The mechanism of catalysis of the gasification reaction by Ca was suggested to be by interactions between Ca and the carbon matrix to increase the electron (e^-) density of the neighbouring carbon atoms. This has the effect of both increasing the number of active carbon sites (C_f) and by increasing the e^- density of these C_f, increase their ability to dissociate CO_2. Both of these factors increase the rate of gasification of coke in CO_2.

The effect of the changing gas – carbon contact area on coke analogue gasification was considered by evaluating the suitability of the RPM to replicate the results of coke analogue gasification. It was found that the RPM, developed for the chemical reaction control region (zone I) of a porous solid, does replicate the coke analogue gasification to a large degree, as summarised by point 8.

8. The coke analogue gasification was replicated using RPM for all the coke analogues studied, except for the lime doped coke analogue. The activation energies were obtained from the RPM and found to be similar to those obtained from the Walker *et al.* approach. The application of RPM for the base coke analogue over the temperature range of 1173 – 1623 K showed increasing deviation from the RPM above 1273. This is indicative of a changing rate controlling mechanism and also consistent with the transition temperature found from the Walker *et al.* approach.

   Gasification of lime doped coke analogue could not be replicated by the RPM likely due to its different mineral dispersion. This different mineral dispersion likely leads to mineral – carbon surface area playing a larger role in the gasification rate. The RPM only accounts for gas – carbon surface area and not the mineral – carbon contact area.

This study has shown that the coke analogue can be used to study metallurgical coke behaviour in the ironmaking blast furnace and potentially can be extended to study other coke related applications. This study broadens the knowledge of the effect of Ca-containing minerals on the fundamental coke gasification kinetics. The effect of different minerals identified using coke analogue may in the future be used to select and design a coke's reactivity in use. Furthermore, this study showed that coke analogue gasification could be explained and predicted using the gasification kinetic model, RPM.

Chapter 10

Recommendation for future studies

During the course of this study, areas in which further study is necessary were identified / highlighted.

1. Other than the minerals examined in this work, other important and commonly identified minerals in coke include spinel ($MgAl_2O_4$), iron sulphides (pyrrhotite ($Fe_{1-x}S$), troilite (FeS) and pyrite (FeS_2)) and iron oxides (magnetite (Fe_3O_4), hematite (Fe_2O_3) and Wüstite (FeO). It is recommended that the kinetics and characterisation of coke analogues containing those minerals should be carried out using the experimental techniques adopted in this study.

2. The maximum temperature employed in this study was 1623 K. It is generally known that SiO_2 in contact with carbon becomes unstable at temperatures >1673 K. This will likely have an effect on the coke/ coke analogue reactivity. It is recommended to examine the reactivity at higher temperatures. Similar effects may be seen for coke analogues containing other minerals as well.

3. It was suggested from the study with Ca containing coke analogues that there could be a different reaction mechanism for the Ca containing coke analogue gasification. It was thought that the number of active sites increases with the increasing Ca content in the coke analogue. This is related to the changing electron density of the carbon atoms adjacent to Ca. Advanced techniques such as DFT (Density Functional Theory) studies are recommended to study the electron density changes in coke analogue carbon structure due to the presence of Ca to provide evidence for the suggested mechanism.

4. It was identified that the coke analogue and metallurgical coke analogue carbon bonding types overlapped. It is recommended that future studies to be carried out to identify possible changes to the carbon bonding type in minerals

containing coke analogues, especially for the coke analogues containing Ca as they were identified to follow a different reaction mechanism during the gasification.

5. An attempt was made to use the BET to investigate the surface area of the coke analogue, but baseline values proved difficult due to degassing issues associated with the coke analogue. Therefore, other techniques such as micro computed tomography (micro-CT) should be explored to better characterise the coke-gas surface. This would help to understand gas–solid surface area and how it changes with reaction and possible changes to the rate controlling mechanism.

6. It was found that the RPM derived for the chemical reaction control region is valid for the coke analogue to some extent. The prediction of reactivity results deviated with increasing Ca content in the coke analogue. This could be related to a change to the structural parameter (φ) with increasing Ca content. It is recommended to modify the RPM for the coke analogue with Ca considering the possible changes to the structural parameter. It is further recommended to evaluate the meaning of change in φ in terms of changing surface area/ pore development etc.

7. It also recommended to examine the RPM for the coke analogues containing other minerals such as iron bearing minerals. It is also suggested to carry out more mathematical study to develop / modify the RPM for the temperature region identified as zone II including the diffusion effect in to the reactivity.

Reference

[1] Biswas AK, Principles of blast furnace iron making, Cootha publishing house, Brisbane, Australia, 1981.

[2] Grigore M, Sakurovs R, French D, Sahajwalla V, Influence of mineral matter on coke reactivity with carbon dioxide, ISIJ International, 46 (2006) 503-512.

[3] Kong D, Zhang J, Pang Q, Miao G, Wu X, Gao B, Coke mineral characteristics and its behavior in blast furnace, Metalurgia International, 17 (2012) 57-63.

[4] Gupta S, French D, Sakurovs R, Grigore M, Sun H, Cham T, Hilding T, Hailin M, Lindblom B, Sahajwalla V, Minerals and iron-making reactions in blast furnace, Progress in energy and combustion science, 34 (2008) 155-197.

[5] Coin CDA, Coke microtextural description: Comparison of nomenclature, classification and methods, Fuel, 66 (1987) 702-705.

[6] Quinn G, Faraj B, Callcott R, Callcott T, Elucidation of the Effects of Minerals on Coke Behaviour in the Blast Furnace, in: ACARP (Ed.) C10054, 2002.

[7] Chapman MW, Monaghan BJ, Nightingale SA, Mathieson JG, Nightingale RJ, Observations of the mineral matter material present at the coke/iron interface during coke disolution into iron, ISIJ International, 47 (2007) 973-981.

[8] Vassilev SV, Vasileva CG, A new approach for the combined chemical and mineral classification of the inorganic matter in coal. 1. Chemical and mineral classification systems, Fuel, 88 (2009) 235-245.

[9] Van der Velden B, Trouw J, Chaigneau R, Van den Berg J, Coke recativity under simulated blast furnace conditions, in: Ironmaking conference proceedings, 1999, pp. 275-285.

[10] Tran KN, Bhatia SK, Air reactivity of petroleum cokes: Role of inaccessible porosity, Industrial and engineering chemistry, 46 (2007) 3265-3274.

[11] Tomita A, Catalysis of carbon-gas reactions, Catalysis surveys from Japan, 5 (2001) 17-24.

[12] Sakawa M, Sakurai Y, Hara Y, Influence of coal characteristics on CO_2 gasification, Fuel, 61 (1982) 717-720.

[13] Tanaka S, U-emura T, Ishizaki K, Nagayoshi K, Ikenaga N, Ohme H, Suzuki T, Yamashita H, Ampo M, C02 Gasification of Iron-Loaded Carbons: Activation of the Iron Catalyst with CO, Energy and fuels, 89 (1995) 45-52.

[14] Turkdogan ET, Vinters JV, Catalytic oxidation of carbon, Cabon, 10 (1972) 97-111

[15] Hilding T, Kazuberns K, Guptha S, Sahajwalla V, Sakurovs R, Bjorkman B, Wikstrom JO, Effect of Temperature on Coke Properties and CO2 Reactivity Under Laboratory Conditions and in an Experimental Blast Furnace, in: AISTech, 2005.

[16] Gill WW, Brown NA, Coin CDA, Mahoney MR, The influence of ash on the weakening of coke, in: Ironmaking conference proceedings, 1985, pp. 233-238.

[17] Bennett P, Reifenstein A, O'Brien G, Jenkins B, Coke reactivity and characterization, in: ACARP C12057, ACIRL, CSIRO Exploration & Mining, Jenkins-Kwan Technology

[18] Monaghan BJ, Chapman MW, Nightingale SA, Carbon transfer in the lower zone of a blast furnace, Steel research international, 81 (2010) 829-833.

[19] Longbottom R, Monaghan BJ, Scholes O, Mahoney MR, Development of a metallurgical coke analogue to Investigate the effects of coke mineralogy on coke reactivity, in: Scanmet IV, 4th International Conference on Process Development in Iron and Steelmaking, Lulea, Sweden: Swerea MEFOS, 2012, pp. 147-156.

[20] French D, Sakurovs R, Grigore M, ACARP C14074, Mineral matter reactions in coke, in, 2009.

[21] Kim B, Gupta S, French D, Sakurovs R, Sahajwalla V, Effect of thermal treatment on coke reactivity and catalytic iron mineralogy., Enerfy and fuels, 23 (2009) 3694-3702.

[22] Sakurovs R, French D, Grigore M, Quantification of mineral matter in commercial cokes and their parent coals, International journal of coal geology, 72 (2007) 81-88.

[23] Van Niekerk WH, Dippenaar RJ, Kotze DA, The influence of potassium on the reactivity and strength of coke, with special reference to the role of coke ash, Journal of the south African institute of mining and metallurgy, 86 (1986) 25-29.

[24] Reid MH, Mahoney MR, Monaghan BJ, A coke analogue for the study of the effects of minerals on coke reactivity, ISIJ International, 54 (2014) 628-633.

[25] Gornostayev S, Kerkkonen O, Harkki J, Occurance and composition of some mineral phases in the tuyere coke, ISIJ International, 45 (2005) 1-7.

[26] Kerkkonen O, Influence of ash reactions on feed coke degradation in the blast furnace, Coke making international, 9 (1997) 34-41.
[27] Chapman MW, Insoluble Oxide Product Formation and its Effect on Coke Dissolution in Liquid Iron, in: Materials Engineering, University of Wollongong, 2009.
[28] Grigore M, Sakurovs R, French D, Sahajwalla V, Mineral ractions during coke gasification with carbon dioxide, International journal of coal geology, 75 (2008) 213-224.
[29] Hengal TD, Walker PL, Catalysis of lignite char gasification by exchangeable calcium and magnesium, Fuel, 63 (1984).
[30] Hippo E, Walker PL, Reactivity of heat-treated coals in carbon dioxide at 900 °C, Fuel, 54 (1975) 245-248.
[31] Radovic LR, Walker PL, Jenkins RG, Effect of lignite pyrolysis conditions on calcium oxide dispersion and subsequent char reactivity, Fuel, 62 (1983) 209-212.
[32] Linares-Solano A, Hippo EJ, Walker PL, Catalytic activity of calcium for lignite char gasification in various atmospheres, Fuel, 65 (1986) 776-779.
[33] Nomura S, Reaction behaviour of Ca-loaded highly reactive coke, ISIJ International, 54 (2014) 2533-2540.
[34] Loison P, Foch P, Boyer A, Coke quality and production, Butterworth & Co Press, London, 1989.
[35] Diez M, Alvarez R, Barrocanal C, Coal For Metallurgical Coke Production: Predictions of Coke Quality and Future Requirements For Coke Making, International Journal of Coal Geology, 50 (2002) 389-412.
[36] Hunty WP, Lee GK, Price JT, Fundamentals of coal combustion during injection into a blast furnace, Progress in energy and combustion science, 17 (1991) 373-395.
[37] Marsh H, Introduction to Carbon Science, Butterworth and Co., London, UK, 1989.
[38] Grigore M, Factors influencing coke gasification with Carbon dioxide, in: School of Material Science and Engineering, University of New South Wales, 2007, pp. 6-114.
[39] Smedowski L, Krzesinska M, Kwasny W, Kozanecki M, Development of Ordered Structures in the High-Temperature (HT) Cokes from Binary and Ternary Coal Blends

Studied by means of X-Ray Diffraction and Raman Spectroscopy, American Chemical Society, 25 (2011) 3142-3149.
[40] Turkdogan ET, Fundamentals of Steelmaking, Institute of Materials, London, UK, 1996.
[41] Bertling H, Coal and Coke for Blast Furnaces, ISIJ International, 38 (1999) 617-624.
[42] Kaczorowski J, The boudouard reaction in manganese production, in: Department of materials science and engineering, Norwegian University of Science and Technology, 2006.
[43] Rosenqvist T, Principles of extractive metallurgy, 2nd ed., McGraw-Hill book company.
[44] Gaskell DR, I ntroduction to the thermodynamics of materials, Fourth ed., Taylor and Francis.
[45] Gornostayev S, Harkki J, Kerkkonen O, Transformations of pyrite during formation of metallurgical coke, Fuel, 88 (2009) 2032-2036.
[46] Grigore M, Sakurovs R, French D, Sahajwalla V, Effect of carbonisation on mineral matter in coke, ISIJ International, 47 (2007) 62-66.
[47] Rodrigues S, Marques M, Ward CR, Suarez-Ruiz I, Flores D, Mineral Transformations During High Temperature Treatment of Antracite, International journal of coal geology, 94 (2012) 191-200.
[48] Cham ST, Investigating factors that influence carbon dissolution from coke into molten iron, in: Faculty of science, School of Material Science and Engineering, The University of New South Wales, 2007.
[49] Andriopoulos N, Loo CE, Dukino R, McGuire SJ, Micro-properties of Australian coking coals, ISIJ International, 43 (2003) 1528-1537.
[50] Omori Y, Blast furnace phenomena and modeling, Eleevier applied science, 1987.
[51] Chapman MW, Monaghan BJ, Nightingale SA, Mathieson JG, Nightingale RJ, Formation of a mineral layer during coke dissolution into liquid iron and its influence on the kinetics of coke dissolution rate, Metallurgical and Materials Transactions B, 39 (2008) 418-430.
[52] Li K, Zhang J, Liu Y, Barati M, Liu Z, Zhong J, Su B, Wei M, Wang G, Yang T, Graphitization of Coke and Its Interaction with Slag in the Hearth of a Blast Furnace, Metallurgical and Materials Transactions B, 47 (2016) 811-818.

[53] Gornostayev S, Harkki J, Mechanism of Physical Transformation of Mineral Matter in The Blast Furnace Coke with Reference to Its Reactivity and Strength, Energy and fuels, 20 (2006) 2632-2635.
[54] Hilding T, Gupta S, Sahajwallla V, Bjorkman B, Wikstrom J-O, Degradation behavior of a high CSR coke in an experimental blast furnace: Effect of carbon structure and alkali reaction, ISIJ International, 45 (2005) 1041-1050.
[55] Li K, Zhang J, Barati M, Khanna R, Liu Z, Zhong J, Ning X, Ren S, Yang T, sahajwalla V, Influence of alkaline (Na, K) vapors on carbon and mineral behavior in blast furnace cokes, Fuel, 145 (2015) 202-213.
[56] Gupta S, Dubikova M, French D, Sahajwalla V, Characterization of the origin and distribution of the minerals and phaes in metallurgical cokes, Enerfy and fuels, 21 (2007) 303-313.
[57] Gupta S, Dubikova M, French D, Sahajwalla V, Effect of CO_2 gasification on the transformations of coke minerals at high temperatures, Energy and fuels, 21 (2007) 1052-1061.
[58] Gornostayev S, Kerkkonen O, Harkki J, Behavior of coal associated minerals during coking and blast furnace processes- a review, Steel research international, 80 (2009) 390-395.
[59] Huffman GP, Huggins FE, Reactions and Transformations of Coal Mineral Matter at Elevated Temperatures, in: Mineral Matter and Ash in Coal: ACS Symposium Series, 1986, pp. 100-113.
[60] Huggins FE, Huffman GP, Lytle FW, Greegor RB, An EXAFS investigation of calcium in coal, in: International conference on coal science, Pittsburgh, PA, 1983, pp. 679-682.
[61] Morgan ME, Jenkins RG, Walker PL, Inorganic constituents in American lignites, Fuel, 60 (1981) 189-193.
[62] Vogt D, Weber JV, Rouzaud JN, Schneider M, Coke Proprieties and Their Microstructure: Part II Coke Carboxy Reactivity Relations to Their Texture, Fuel Processing Technology, 20 (1988) 155-162.
[63] Turkdogan ET, Olsson RG, Vinters JV, Pore characteristics of carbon, Carbon, 8 (1970) 545-561.

[64] Aderibigbe DA, Szekely J, Studies in coke reactivity:part2- mathematical model of reaction with allowance for pore diffusion and experimental verification, Ironmaking and Steelmaking, 1 (1982) 32-43.
[65] Longbottom RJ, Monaghan BJ, Chowdhury AA, Reid MH, Zhang G, Mahoney MR, Hockings K, Effect of mineral matter on the reactivity of coke and its replication in a coke analogue, ISIJ International, 56 (2016) 1553-1558.
[66] Aderibigbe DA, Szekely J, Studies in coke reactivity: part 1-Reaction of conventionally produced coke with CO-CO_2 mixtures over temperature range 850 ^oC-1000 ^oC, Ironmaking and Steelmaking, 1 (1981) 11-19.
[67] Pusz S, Krzesinska M, Smedowski L, Majewska J, Pilawa B, Kwiecinska B, Changes in a Coke Structure Due to Reaction with Carbon Dioxide, Journal of Coal Geology, 81 (2009) 287 -292.
[68] Patrick JW, Walker A, Macroporosity in cokes: its significance, measurement and control, Carbon, 27 (1989) 117-123.
[69] Xing X, Zhang G, Dell'amico M, Ciezki G, Meng Q, Ostrovski O, Effect of annealing on properties of carbonaceous materials. Part 2: porosity and pore geometry, Metallurgical and Materials Transactions B, 44B (2013) 862-869.
[70] Kerkkonen O, Mattila E, Heiniemi R, The correlation between reactivity and ash mineralogy of coke, in: Ironmaking conference proceedings, 1996, pp. 275-281.
[71] Ghosh B, Sahoo BK, Niyogi OS, Chakraborty B, Manjhi KK, Das TK, Das SK, Coke structure evaluation for BF coke making, Internationa journal of coal preparation and utilisation, (2017) 1-16.
[72] Marsh H, Metallurgical coke: formation, structure and properties, in: Ironmaking conference proceedings, 1982, pp. 2-10.
[73] Szekely J, Aderibigbe DA, Coke reactivity and its effect on blast furnace performance, 1981.
[74] Jenkins DR, Mahoney MR, Roest R, Lomas H, Pearce R, Li R, Mayo S, Wang D, Micro-CT analysis of coke and its relationship to coke quality indicators, in: AISTech 2015, Cleveland, OH, USA, 2015, pp. 77-86.
[75] Steel KM, Dawson RE, Jenkins DR, Pearce R, Mahoney MR, Use of rheometry and micro-CT analysis to understand pore structure development in coke, Fuel Processing Technology, 155 (2017) 106-113.

[76] Li K, Khanna R, Zhang J, Liu Z, Sahajwalla V, Yang T, Kong D, The evolution of structural order, microstructure and mineral matter of metallurgical coke in a blast furnace: A review, Fuel 133 (2014) 194-215.
[77] Kawakami M, karato T, Takenaka T, Yokoyama S, Structure Analysis of Coke, Wood Charcoal and Bamboo Charcoal by Raman Spectroscopy and Their Reaction Rate with CO_2, ISIJ International, 45 (2005) 1027 - 1034.
[78] Kawakami M, Kanba H, Sato K, Takenaka T, Gupta S, Chandratilleke R, Sahajwalla V, Characterization of Thermal Annealing Effects on the Evolution of Coke Carbon Structure Using Raman Spectroscopy and X-ray Diffraction, ISIJ International, 46 (2006) 1165-1170.
[79] Duval B, Guet JM, Richard JR, Rouzaud JN, Coke properties and their mictrotexture Part III: First results about relationship between microtexture and reactivity of some cokes Fuel Processing Technology, 20 (1988) 163-175.
[80] Dong S, Paterson N, Kazarian SG, Dugwell DR, Kandioti R, Characterization of Tuyere-Level Core-Drill Coke Samples from Blast Furnace Operation, Energy and fuels, 21 (2007) 3446-3454.
[81] Oberlin A, High-resolution TEM studies of carbonization and graphitization, Chemistry and physics of carbon, 22 (1989) 1-143.
[82] Rouzaud JN, Jehlicka J, Faugere AM, Pis JJ, Alvarez R, Influence of the oxidation of coals of different rank on coke microtexture and other relevant properties, Fuel, 73 (1994) 810-815.
[83] Gupta S, Sahajwalla V, Burgo J, Chaubal P, Youmans T, Carbon structure of coke at high temperatures and its influence on coke fines in blast furnace dust, Metallurgical and Materials Transactions B, 36B (2005) 385-394

[84] Franklin RE, The structure of graphitic carbons, Acta Crystallographica, 4 (1951) 253-261.
[85] Cullity BD, Elements of X-Ray Diffraction, in: Addison- Wesley Publishing Company INC (Ed.), 1978.
[86] Grigore M, Sakurovs R, French D, Sahajwalla V, Properties and CO_2 reactivity of the inert and reactive maceral-derived components in cokes, International journal of coal geology, 98 (2012) 1-9.

[87] Dong S, Alvarez P, Paterson N, Dugwell DR, Kandiyoti R, Study on the effect of heat treatment and gasification on the carbon structure of coal chars and metallurgical cokes using Fourier Transform Raman Spectroscopy, Enerfy and fuels, 23 (2009) 1651-1661.

[88] Aladejebi OA, Monaghan BJ, Reid MH, in het Panhuis M, Longbottom RJ, Metallic Iron Effects on Coke Analog Carbon Bonding and Reactivity, Steel research international, 88 (2017).

[89] Levenspiel O, Fluid particle reactions: Kinetics, in: Chemical Reaction Engineering, Third Edition, John Wiley and Sons, pp. 566-586.

[90] Szekely J, Evans JW, Sohn HY, Gas-solid reactions, Academic press, 1976.

[91] Walker PL, Rusinko F, Austin LG, Gas reactions of carbon, Advances in catalysis, 6 (1959) 134-217.

[92] Mochida I, Korai Y, Fujitsu H, Takeshita K, Komatsubara Y, Koba K, Marsh H, Aspects of gasification and structure in cokes from coals, Fuel, 63 (1984) 136-139.

[93] Reif AE, The mechanism of the carbon dioxide-carbon reaction, The journal of physical chemistry, 56 (1952) 785-788.

[94] Ergun S, Kinetics of the reaction of carbon dioxide with carbon, The journal of physical chemistry, 60 (1956) 480-485.

[95] Wu P, The kinetics of the reaction of carbon with carbon dioxide, in, Massachusetts institute of technology, 1949, pp. 1-222.

[96] Rao Y, Jalan B, A study of the rates of carbon-carbon dioxide reaction in the temperature range 839 to 1050 C, MMTB, 3 (1972) 2465-2477.

[97] Higman C, Vander Burgt M, Gasification, 2nd edition ed., Elsevier, 2008.

[98] Freund H, Gasification of carbon by CO_2 : A transient kinetic experiment, Fuel, 65 (1986) 63-66.

[99] Katta S, Keairns DL, Study of kinetics of carbon gasification reactions, Industrial and engineering chemistry fundamentals, 20 (1981) 6-13.

[100] Mentser M, Ergun S, Kinetics of oxygen exchange between CO_2 and CO on carbon, Carbon, 5 (1967) 331-337.

[101] Roberts D, Harris D, Char reactivity in gas mixtures: Towards an understanding of the C-CO-CO_2 reaction system, in, CSIRO Energy Technology, 2008.

[102] Austin LG, Walker PL, Effect of carbon monoxide in causing nonuniform gasification of graphite by carbon dioxide, AIChe Journal, 9 (1963) 303-306.

[103] Goerg KA, Cameron JH, A kinetic study of kraft char gasification with CO_2, IPL technical paper series, Number 197 (1986).
[104] Laurendeau NM, Heterogeneous kinetics of coal char gasification and combustion, Progress in energy and combustion science, 4 (1978) 221-270.
[105] Radovic LR, Walker PL, Jenkins RG, Importance of carbon active sites in the gasification of coal chars, Fuel, 62 (1983) 849-856.
[106] Atkins P, De Paula J, Atkins' Physical chemistry, Eighth edition ed.
[107] Laidler KJ, Theories of chemical reaction rates, McGraw-hill book company, 1969.
[108] Desai NJ, Yang RT, Kinetics of high temperature carbon gasification reaction, AIChe Journal, 28 (1982) 237-244.
[109] Tien RH, Turkdogan ET, Internal pore diffusion effect on internal burning of carbon, Carbon, 8 (1970) 607-621.
[110] Osafun K, Marsh H, Gasification kinetics of coal chars in carbon dioxide, Fuel, 67 (1988) 384-388.
[111] Tomaszewicz M, Labojko G, Tomaszewicz G, Moranska MK, The kinetics of CO_2 gasification of coal chars, Journal of Thermal Analysis and Calorimetry, 113 (2013) 1327-1335.
[112] Kasaoka S, Sakata Y, Tong C, Kinetic evaluation of the reactivity of various coal chars for gasification with carbon dioxide in comparison with steam, International Chemical Engineering, 25 (1985) 160-175.
[113] Bhatia SK, Perlmutter DD, A random pore model for fluid- solid reactions I : Isothermal, kinetic control, AIChe Journal, 26 (1980) 335-379.
[114] Bhatia SK, Vartak BJ, Reaction of microporous solids: the discrete random pore model, Carbon, 34 (1996) 1383-1391.
[115] Bhatia SK, Perlmutter DD, A random pore model for fluid-solid reactions: II Diffusion and transport effects, AIChe Journal, 27 (1981) 247-254.
[116] Everson RC, Neomagus HWJP, Kaitano R, Falcon R, Cann CM, Properties of high ash coal-char particles derived from inertinite-rich coal: II. Gasification kinetics with carbon dioxide, Fuel, 87 (2008) 3403-3408.
[117] Kabir KB, Tahmasebi A, Bhattacharya S, Yu J, Intrinsic kinetics of CO_2 gasification of a Victorian coal char, Journal of Thermal Analysis and Calorimetry, 123 (2016) 1685-1694.

[118] Fermoso J, Arias B, Pevida C, Plaza MG, Rubeira F, Pis JJ, Kinetic models comparison for steam gasification of different nature fuel chars, Journal of Thermal Analysis and Calorimetry, 91 (2008) 779-786.
[119] Malekshahian M, Hill JM, Kinetic analysis of CO_2 gasification of petroleum coke at high pressures, Energy and fuels, 25 (2011) 4043-4048.
[120] Menendez JA, Alvarez R, Pis JJ, Determination of Metallurgical coke reactivity at INCAR: NSC and ECE-INCAR reactivity tests, Ironmaking and Steelmaking, 26 (1999) 117-121.
[121] ASTM D5341 / D5341M-14, Standard Test Method for Measuring Coke Reactivity Index (CRI) and Coke Strength After Reaction (CSR), ASTM International, (2014).
[122] Mani T, Mahinpel N, Murugan P, Reaction kinetics and mass transfer studies of biomass char gasification with CO_2, Chemical engineering science, 66 (2011) 36-41.
[123] Zamalloa M, Utigard TA, Characterization of industrial coke structures, ISIJ International, 35 (1995) 449-457.
[124] McKee DW, Mechanisms of the alkali metal catalysed gasification of carbon, Fuel, 62 (1983) 170-175.
[125] Holstein WL, Boudart M, Transition Metal and Metal Oxide Catalysed Gasification of Carbon by Oxygen, Water and Carbon Dioxide, Fuel, 62 (1983) 162-165.
[126] Gulbransen EA, Andrew KF, Reaction of Carbon Dioxide with Pure Artificial Graphite at Temperatures of 500° to 900°C, Industrial and Engineering Chemistry, 44 (1952) 1048-1051.
[127] Smith RP, Equilibrium of Iron–Carbon Alloys with Mixtures of $CO–CO_2$ and $CH_4–H_2$, Journal of the American Chemical Society, 68 (1946) 1163-1175.
[128] Kyotani T, Zhang ZG, Hayashi S, Tomita A, TPD study on H2O-gasified and O2-chemisorbed coal chars, Energy & Fuels, 2 (1988) 136-141.
[129] Suzuki T, Ohme H, watanabe Y, Mechanisms of Alkaline-Earth Metals Catalyzed CO_2 Gasification of Carbon, Enerfy and fuels, 8 (1994) 649-658.
[130] Perez-Florindo A, Cazorla-Amoros D, Linares-Solano A, CO_2-Carbon gasification catalysed by alkaline earths:Comparative study of the metal-carbon interaction and of the specific activity, Carbon, 31 (1993) 493-500.

[131] Cazorla-Amoros D, Linares-Solano A, Salinas-Martines De Lecea C, Joly JP, Calcium-carbon intercalation study:It's importance in the carbon-gas reactions, Carbon, 29 (1991) 361-369.
[132] Cazorla-Amoros D, Linares-Solano A, Salinas-Martines De Lecea C, Kapteijn F, Assessment of the CO_2-carbon gasification catalyzed by calcium. A transient isotopic study, Carbon, 32 (1994) 423-430.
[133] Walker PL, Shelef M, Anderson RA, Catalysis of carbon gasification, Catalysis of carbon gasification, 4 (1968) 287-383.
[134] Gonzales JD, Mondragon F, Espinal JF, Effect of calcium on gasification of carbonaceous materials with CO2: A DFT study, Fuel, 114 (2013) 199-205.
[135] Wang Z, Longbottom RJ, Monaghan BJ, A coke analogue to examine the effect of mineralogy on coke reactivity ACARP C23049 Part II in, 2016.
[136] Adschiri T, Furusawa T, Relation between CO_2-reactivity of coal char and BET surface area, Fuel, 65 (1986) 927-931.
[137] Kawakami M, Taga H, Takenaka T, Yokoyama S, Micro pore structure and reaction rate of coke, wood charcoal and graphite with CO_2, ISIJ International, 44 (2004) 2018-2022.
[138] Causton P, McEnaney B, Determination of active surface areas of coal chars using a temperature programmed desorption technique, Fuel, 64 (1985) 1447-1452.
[139] Feng B, Bhatia SK, Variation of the pore structure of coal chars during gasification, Carbon, 41 (2003) 507-523.
[140] K. Koba, Ida, S.,, Gasification reactivities of metallurgical cokes with carbon dioxide, steam and their mixtures, Fuel, 59 (1980) 59-63.
[141] Sakurovs R, Burke L, Influence of Gas Composition on the Reactivity of Cokes, Fuel Processing Technology, 92 (2011) 1220-1224.
[142] Nyathi MS, Mastalerz M, Kruse R, Influence of coke particle size on pore structural determination by optical microscopy, International journal of coal geology, 118 (2013) 8-14.
[143] Kovacik G, Chambers A, Ozum B, CO_2 gasification kinetics of two alberta coal chars, Canadian Journal of Chemical Engineering, 69 (1991) 811-815.
[144] Kajitani S, Suzuki N, Ashizawa M, Hara S, CO_2 gasification rate analysis of coal char in entrained flow coal gasifier, Fuel, 85 (2006) 163-169.

[145] Hernandez JJ, Ballesteros R, Aranda G, Characterisation of tars from biomass gasification: effect of the operating conditions, Energy, 50 (2012) 333-342.

[146] Zou JH, Zhou ZJ, Wang FC, Zang W, Dai ZH, Liu HF, Yu ZH, Modeling reaction kinetics of petroleum coke gasification with CO_2, Chemical Engineering and Processing, 46 (2007) 630-636.

[147] Liu T, Fang Y, Wang Y, An experimental investigation into the gasification reactivity of chars prepared at high temperatures, Fuel, 87 (2008) 460-466.

[148] Liu H, Luo C, Kato S, Uemiya S, Kaneko M, Kojima T, Kinetics of CO_2/char gasification at elevated temperatures. Part 1: Experimental results, Fuel Processing Technology, 87 (2006) 775-781.

[149] Turkdogan ET, Vinters JV, Kinetics of oxidation of graphite and charcoal in carbon dioxide, Carbon, 7 (1969) 101-117.

[150] Longbottom RJ, Monaghan BJ, Chowdhury AA, Mahoney MR, Reid MH, Zhang G, Hockings K, The effect of combinations of iron-bearing minerals and quartz on coke reactivity, Ironmaking and steelmaking, (2017).

[151] Aladejebi OA, Monaghan BJ, Reid M, in het Panhuis M, Characterization of coke analogue, in: High temperature processing symposium, Melbourne, Australia, 2014.

[152] N.P. Laboratory, http://www.npl.co.uk/science-technology/mathematics-modelling-and-simulation/mtdata/, in.

[153] Eisenhuttenleute VD, in: Slag Atlas, Verlag Staheisen GmbH, 1981, pp. 95.

[154] http://maud.radiographema.com/, in, University of Trento, Italy.

[155] http://www.crct.polymtl.ca/factsage/fs_reaction.php - FactSage modules_ The Reaction module, in.

[156] www.struers.com, in, 2016.

[157] Wayne R, http://rsb.info.nih.gov/ij/ ImageJ version 1.48, in, National Institutes of Health, Bethesda, USA, 2008.

[158] Abell AB, Willis KL, Lange DA, Mercury intrusion porosimetry and image analysis of cement based materials, Journal of colloid and interface science, 211 (1999) 39-44.

[159] Taylor JC, Computer Programs for Standardless Quantitative Analysis of Minerals Using the Full Powder Diffraction Profile, Powder Diffraction, 6 (1991) 2-9.

[160] G.S. Equipment, http://www.gbcsci.com/products/xrd-products/xrd-software/, in.
[161] Deer WA, Howie RA, Zussman J, An introduction to the rock forming minerals, Second ed., Pearson Education Limited, 1992.
[162] Longbottom R, Monaghan BJ, Chapman MW, Nightingale SA, Mathieson JG, Nightingale RJ, Techniques in the study of carbon transfer in ironmaking, Steel research international, 82 (2011) 505-5011.
[163] Xing X, Effect of heat treatment on properties of carbonaceous materials, in: Faculty of Science, School of Materials Science and Engineering, The University of New South Wales, 2012.
[164] Chen YW, An application of coke microstructure and microtexture to Indonesian coal, China steel technical report, 28 (2015) 6-12.
[165] Xing X, Rogers H, Zhang G, Hockings K, Zulli P, Ostrovski O, Coke degradation under simulated blast furnace conditions, ISIJ International, 56 (2016) 786-793.
[166] Miroshnichenko DV, Preliminary estimation of coke's CRI and CSR values on the basis of the physical properties of coal ash, Coke and chemistry, 51 (2008) 447-450.
[167] Turkdogan ET, Koump V, Vinters JV, Perzak TF, Rate of oxidation of graphite in carbon dioxide, Carbon, 6 (1968) 467-484.
[168] Tien RH, Turkdogan ET, Incomplete pore diffusion effect on internal burning of carbon, Carbon, 8 (1970) 607-621.
[169] Turkdogan ET, Physical chemistry of high temperature technology, Academic press, INC. (London) LTD, 1980.
[170] Tyler RJ, Smith IW, Reactivity of petroleum coke to carbon dioxide between 1030 and 1180 K, Fuel, 54 (1975) 99-104.
[171] Jess A, Anderson AK, Influence of mass transfer on thermogravimetric analysis of combustion and gasification reactivity of coke, Fuel, 89 (2010) 1541-1548.
[172] Young BC, Smith IW, The kinetics of combustion of petroleum coke particles at 1000 to 1800 K: The reaction order, in: Eighteenth Symposium (International) on combustion, University of Waterloo Waterloo, Canada, 1981, pp. 1249-1255.

[173] Liu H, Kaneko M, Luo C, Kato S, Kojima T, Effect of pyrolysis time on the gasification reactivity of char with CO_2 at elevated temperatures, Fuel, 83 (2004) 1055-1061.

[174] Nomura S, Ayukawa H, Kitaguchi H, Tahara T, Matsuzaki S, Naito M, Koizumi S, Ogata Y, Nakayama T, Abe T, Improvement in blast furnace reaction efficiency through the use of highly reactive calcium rich coke, ISIJ International, 45 (2005) 316-324.

[175] Roy D, Basu PK, Raghunathan P, Eswaran SV, Designing of high-resolution photoresists: Use of modern NMR techniques for evaluating lithographic performance, Bulletin of Materials Science, 27 (2004) 303-316.

[176] McCarthy F, Interfacial phenomena and dissolution of carbon from chars into liquid iron during pulverized coal injection in a blast furnace, in: Materials science and Engineering, University of New South Wales, 2004.

[177] McCarthy F, Khanna R, Sahajwalla V, S. N, Interfacial phenomena occuring during iron/char interactions in a blast furnace, ISIJ International, 45 (2005) 1261-1268.

[178] McCarthy F, Sahajwalla V, Hart J, Saha-Chaudhury N, Influence of ash on interfacial reactions between coke and liquid iron, Metallurgical and Materials Transactions B, 34B (2003) 573-580.

[179] Wu C, Wiblen R, Sahajwalla V, Influence of ash on mass transfer and interfacial reaction between natural graphite and liquid iron, Metallurgical and Materials Transactions B, 31B (2000) 1099-1104.

[180] Khanna R, McCarthy F, Sun H, Simento N, S. V, Dissolution of carbon from coal chars into liquid iron at 1550 °C, Metallurgical and Materials Transactions B, 36B (2005) 719-729.

[181] Lide DR, CRC Handbook of Chemistry and Physics, CRC Press, Florida, USA, 2003.

[182] Li M, Kuribashi K, Phase selection in the containerless solidification of undercooled $CaO \cdot 6Al_2O_3$ melts, Acta Materialia, 52 (2004) 3639-3647.

[183] Jia D, Kriven WM, Sintering behavior of Gehlenite, Part II. Microstructure and mechanical propertis, Journal of American Chemical Society, 90 (2007) 2766-2770.

[184] Serra MF, Conconi MS, Gauna MR, Suarez G, Aglietti EF, Rendtorff NM, Mullite ($3Al_2O_3 \cdot 2SiO_2$) ceramics obtained by reaction sintering of rice husk ash and

alumina, phase evolution, sintering and microstructure, Journal of Asian Ceramic Societies, 4 (2016).
[185] Wang J, Morishita K, Takarada T, High-temperature interactions between coal char and mixtures of calcium oxide, quartz and kaolinite, Enerfy and fuels, 15 (2001) 1145-1152.
[186] Everson RC, Neomagus HWJP, Kaitano R, The random pore model with intraparticle diffusion for the description of combustion of char particles derived from mineral- and inertinite rich coal, Fuel, 90 (2011) 2347-2352.

List of Publications

Refereed Journal Papers

1. **Jayasekara AS**, Monaghan BJ, Longbottom RJ, The kinetics of reaction of a coke analogue in CO_2 gas, **Fuel**, 154 (2015) 45-51.
2. **Jayasekara AS**, Monaghan BJ, Longbottom RJ, Dispersion of lime in coke analogue and its effect on gasification in CO_2, **Fuel**, 182 (2016) 73-79.
3. **Jayasekara AS**, Monaghan BJ, Longbottom RJ, The effect of calcium aluminates on coke analogue gasification, **Fuel**, 225 (2018) 18 – 25.

Refereed Conference Papers

1. Monaghan BJ, Longbottom RJ, Reid M, Aladegebi OA, **Jayasekara AS**, in het Panhuis, A new approach to investigating coke reactivity, in: **Robertson symposium TMS**, San Diago, 2014
2. **Jayasekara AS**, Longbottom RJ, Monaghan BJ, Fundamental coke kinetic studies using a coke analogue, in**: AISTech 2015 & ICSTI**, Cleveland, Ohio, USA, 2015, pp. 56-63

Non-Refereed Conference Publications

1. **Jayasekara AS**, Monaghan BJ, Longbottom RJ, Kinetics of coke analogue reactivity, in**: High temperature processing symposium**, Melbourne, Australia, 2014

2. **Jayasekara AS,** Monaghan BJ, Longbottom RJ, Kinetics of coke analogue reactivity, in Second Australia – China joint symposium on Minerals and Metallurgy, Sydney, Australia 2014

3. Longbottom RJ**, Jayasekara AS,** Monaghan BJ, The kinetics of the reactivity of a coke analogue with carbon dioxide, The fifth Australia – China – Japan joint symposium on Iron and Steelmaking, 2014

4. Monaghan BJ**, Jayasekara AS**, Longbottom RJ, Coke analogue reactivity and effect of Ca in coke analogue reactivity, **SCANMET V** on process development in iron and steelmaking, Sweden 2016

5. **Jayasekara AS**, Monaghan BJ, Longbottom RJ, The Effects of Calcium Aluminates on the Reactivity of the Coke Analogue, in**: Engineering Materials Research Strength Workshop**, University of Wollongong, Australia, 2017

Appendix I– Calculation of CO_2, CO and O_2 Partial pressures for the coke/ coke analogue reaction with CO_2

Under the TGA experimental conditions, the reaction of coke or coke analogue in CO_2 was carried out under 100 % CO_2 atmosphere. The reaction in *Equation 3.1* is a possible side reaction that can introduce other gas species to the systems.

$$CO_{2(g)} \rightarrow CO_{(g)} + \frac{1}{2}O_{2(g)} \qquad \Delta G° = 279700 - 84.96\ T \qquad J\ mol^{-1}$$

The partial pressure of CO_2, CO and O_2 were determined as follows. The relationship between the partial pressures of CO_2, CO and O_2 and the equilibrium constant, K, in *Reaction 3.1* is,

$$K = \frac{p_{CO}\cdot\sqrt{p_{O_2}}}{p_{CO_2}} \qquad \text{I.1}$$

where p_{CO_2}, p_{CO} and p_{O_2} are the partial pressures of CO_2, CO and O_2 respectively.

If the total pressure in the reaction is 1 atmosphere, then

$$p_{CO_2} + p_{CO} + \sqrt{p_{O_2}} = 1 \qquad \text{I.2}$$

Based on the stoichiometry of the *Reaction 3.1*,

$$(1-X)CO_{2(g)} \rightarrow XCO_{(g)} + \frac{X}{2}O_{2(g)} \qquad \text{I.3}$$

Then the total number of moles I.3 is,

$$(1-X) + X + \frac{X}{2} = \frac{2+X}{2} \qquad \text{I.4}$$

where (1- X), X and (X/2) are number of moles of CO_2, CO and O_2 respectively,

then the partial pressures can be calculated from,

$$p_{CO_2} = \frac{1-X}{\frac{2+X}{2}} \qquad \text{I.5}$$

$$p_{CO} = \frac{X}{\frac{2+X}{2}} \qquad \text{I.6}$$

$$p_{O_2} = \frac{\frac{X}{2}}{\frac{2+X}{2}} \quad \text{I.7}$$

by substituting equations I.5 to I.7 into I.1,

$$K = \frac{\frac{X}{2+X}\cdot\sqrt{\frac{\frac{X}{2}}{\frac{2+X}{2}}}}{\frac{1-X}{\frac{2+X}{2}}} \quad \text{I.8}$$

The equation I.8 can be simplified as,

$$K^2(1-X)^2.(2+X) - X^3 = 0 \quad \text{I.9}$$

Equation I.9 can be solved graphically for values of $0 < n \leq 1$, to get p_{CO_2}, p_{CO} and p_{O_2}.

Given in Figure I.1 is a plot of p_{CO_2} or p_{CO} or p_{O_2} with temperature. It can be observed from the figure that under the experimental conditions of this study, the partial pressure of CO and O_2 are negligible, so that coke analogue TGA test is carried out in ~100% CO_2 atmosphere.

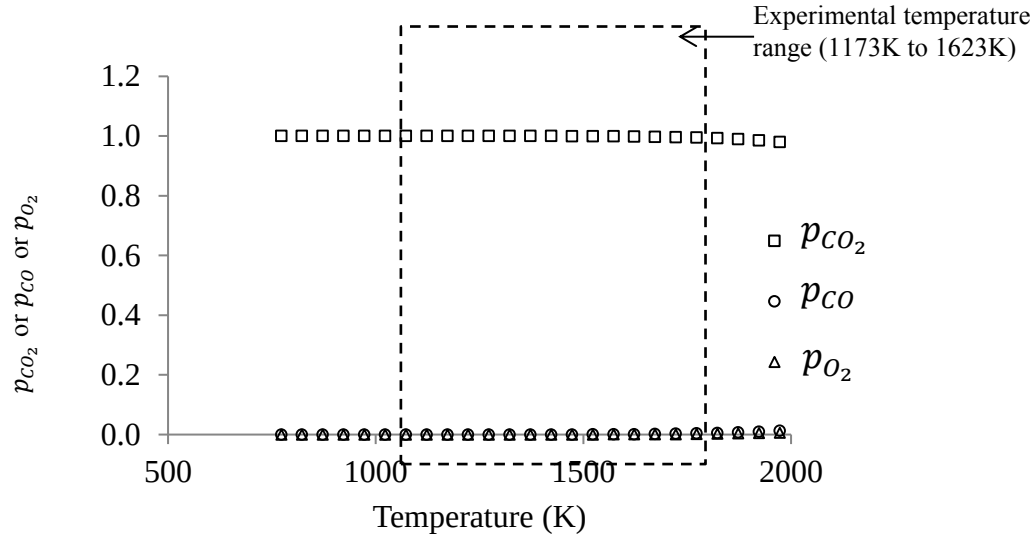

Figure I.1: A plot of partial pressures of CO_2, CO and O_2 with temperature.

Appendix II – propagation of errors of coke analogue reactivity results

The uncertainty in the TGA measurements is estimated using the partial derivatives approach [1] with respect to each variable used in the calculation.

In determining a quantity A, that is a function of variables b and c,

$$A = f(b, c) \qquad \text{II.1}$$

from the partial derivation,

$$dA = \left(\frac{\partial A}{\partial b}\right) db + \left(\frac{\partial A}{\partial c}\right) dc \qquad \text{II.2}$$

where db and dc are infinitesimal changes of the variables b and c that can be replaced by error/ uncertainty[1].

To estimate the maximum possible error, *Equation II.2* is squared (*Equation II.3*).

$$dA^2 = \left(\frac{\partial A}{\partial b}\right)^2 db^2 + \left(\frac{\partial A}{\partial c}\right)^2 dc^2 + \left(\frac{\partial A}{\partial b}\right)\left(\frac{\partial A}{\partial c}\right) dbdc \qquad \text{II.3}$$

The magnitude of $\left(\frac{\partial A}{\partial b}\right)\left(\frac{\partial A}{\partial c}\right) dbdc$ is assumed insignificant compared to the squared terms. This simplifies the *Equation II.3* to,

$$dA^2 = \left(\frac{\partial A}{\partial b}\right)^2 db^2 + \left(\frac{\partial A}{\partial c}\right)^2 dc^2 \qquad \text{II.4}$$

[1] Priyantha N., Propagation of errors of derived results, in: Measurements and errors in chemical analysis, University of Peradeniya, Sri Lanka, pp 43-50.

The square of the error/ uncertainty can also be considered as the square of the standard deviation, as the standard deviation is a measure of the uncertainty of a result[1]. Therefore II.4 can be written as II.5.

$$\sigma A^2 = \left(\frac{\partial A}{\partial b}\right)^2 \sigma b^2 + \left(\frac{\partial A}{\partial c}\right)^2 \sigma c^2 \qquad \text{II.5}$$

Equation II.5 is used as the basic equation to derive error/uncertainty values for coke analogue reaction rates.

II.1. Error of carbon conversion X

Carbon conversion X is defined in *Equation II.6.*

$$\mathrm{X} = \frac{(\mathrm{W_0} - \mathrm{W})}{\mathrm{W_0}} = \frac{\Delta W}{W_0} \qquad \text{II.6}$$

where, $$\Delta W = W_0 - W \qquad \text{II.7}$$

and X is a function of (ΔW) and W_0: $X = f(\Delta W, W_0)$.

ΔW is obtained from the TGA scale that has quantifiable uncertainty associated with the balance scale and buoyancy effect.

Then the error associated with the carbon conversion X (σX) can be estimated using,

$$\sigma X^2 = \left(\frac{-\Delta W}{W_0^2}\right)^2 \sigma W_0^2 + \left(\frac{1}{W_0}\right)^2 \sigma \Delta W^2 \qquad \text{II.8}$$

Rearranging *Equation II.8* and dividing by X^2 results in *Equation II.9,*

$$\sigma X = \left[X^2 \left(\left(\frac{\sigma W_0^2}{W_0^2}\right) + \frac{(\sigma \Delta W^2)}{(\Delta W^2)}\right)\right]^{\frac{1}{2}} \qquad \text{II.9}$$

II.2. Error of reaction rate (R_C)

The reaction rate R_C is given in *Equation II.10*

$$R_C = \left[\frac{1}{(1-X)}\right]\left(\frac{dX}{dt}\right) \quad \text{II.10}$$

By applying the same method as in II.1, the error of R_C can be determined using the *Equation II.11*.

$$\sigma R_C = \left[R_C^2\left(\frac{\sigma dX^2}{dX^2} + \frac{\sigma dt^2}{dt^2} + \frac{\sigma X^2}{X^2}\right)\right]^{1/2} \quad \text{II.11}$$

where, σdX is the error of conversion change and σX is the error of conversion. σdt is the resolution of the reading (± 1 s). dt, dX and σdX are obtained from the experimental FWC curves (see section 4.1) and the linear fit of FWC curves.

II.3. Error of ln R_C

The error of ln R_C is determined using *Equation II.12* which is derived using the basic equation (*Equation II.5*).

$$\sigma ln R_C = \frac{\sigma R_C}{R_C} \quad \text{II.12}$$

II.4. Estimated error values for coke analogues

Table II.1 shows the estimated percentage errors associated with the R_C and ln R_C.

Table II.1: Estimated error values for base coke analogue

Temperature	Coke analogue															
	Base		Lime doped		C3A doped		CA doped		CA6 doped		CAS doped		Alumina doped		Quartz doped*	
	%σ R_C	%σln R_C	%σ R_C	%σln R_C	%σ R_C	%σln R_C	%σ R_C	%σln R_C	%σ R_C	%σln R_C	%σ R_C	%σln R_C	%σ R_C	%σln R_C	%σ R_C	%σln R_C
1173	4.8	0.40	5.0	0.43	4.9	0.42	4.9	0.44	4.9	0.41	5.0	0.48	4.9	0.41	4.4	0.38
1198	4.2	0.35	4.1	0.35			3.8	0.35			3.7	0.38	4.0	0.33	3.8	0.34
1223	2.9	0.25	3.0	0.26	2.7	0.25	2.6	0.25	2.7	0.24	2.6	0.27	3.1	0.26	2.7	0.25
1248	1.7	0.16	2.2	0.21			2.0	0.19			2.1	0.22	2.2	0.20	2.1	0.20
1273	1.2	0.11	3.8	0.36	3.2	0.32	2.6	0.26	3.2	0.20	1.8	0.19	3.7	0.36	3.2	0.32
1298	1.0	0.10	5.2	0.52	3.9	0.40	3.8	0.39			2.1	0.24	7.0	0.39	4.4	0.46
1323	1.0	0.10	2.4	0.25			1.8	0.19	3.9	0.26	1.4	0.16	2.6	0.27	2.3	0.24
1373	1.0	0.11	0.9	0.10	0.9	0.09	0.8	0.09	0.9	0.09	0.8	0.09	0.9	0.09	0.8	0.09
1423	2.8	0.32	2.0	0.23	2.0	0.23	1.8	0.20			1.2	0.14	2.0	0.23	2.0	0.22
1473	0.8	0.10	3.3	0.38	3.6	0.41	2.7	0.32	3.6	0.30	2.1	0.25	3.3	0.38	3.5	0.40
1523	0.8	0.09	3.6	0.42			2.8	0.34			2.4	0.29	3.3	0.39	3.3	0.38
1573	0.7	0.08	0.9	0.10			0.8	0.09			0.7	0.09	0.9	0.11	1.0	0.12
1623	0.7	0.09	0.7	0.09	0.9	0.11	0.7	0.09	0.9	0.08	0.6	0.08	0.7	0.09	0.8	0.10

*Average of crystalline and non-crystalline CAS doped coke analogue

Appendix III – Analysis of Bakelite powder used in coke analogue preparation for impurity level analysis

To establish the mineral component of the Bakelite (impurities), 100 g of Bakelite was fired at 1000 °C in air. The firing was continued until there was no change in the measured weight of the fired Bakelite (ash). The % of impurity minerals were calculated as follows.

Initial mass of bakelite = 100.23 g

Final mass of bakelite (mass of impurity minerals) = 2.48 g

% of impurity minerals (ash) $= \frac{2.48}{100.23} \times 100\ \%$

$= \underline{\underline{2.47\ \%}}$

The remaining ash was analysed using X ray diffraction. The majority (~68 %) of the ash contains Anorthite ($CaAl_2Si_2O_8$) and the rest (32%) is identified as aluminum silicate ($Al_2(SiO_4)O$) (see *Figure III.1*)

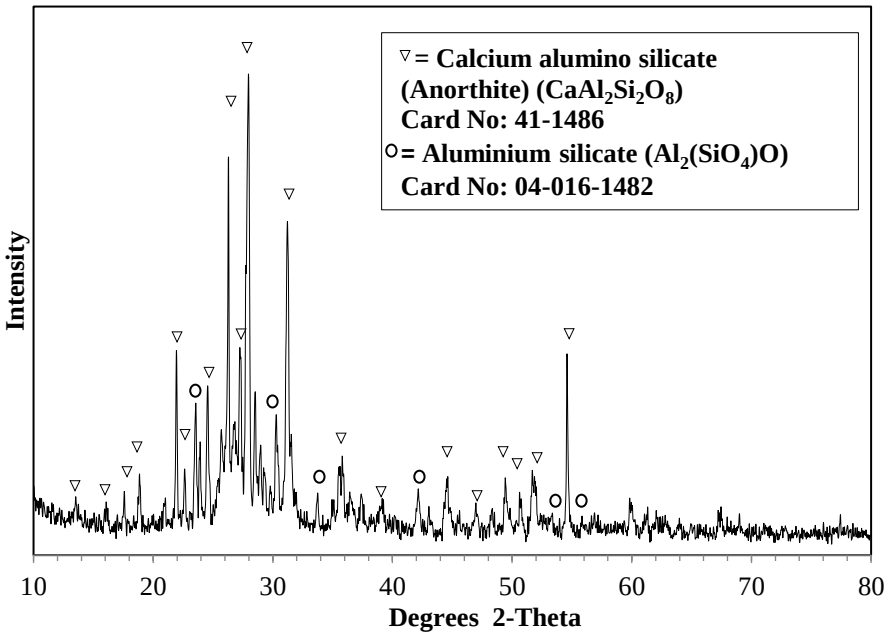

Figure III.1: The XRD pattern of the Bakelite.

The amount of these impurity minerals in a coke analogue batch was calculated as shown below.

Mass of bakelite use for one coke analogue batch = 39.522 g

Mass of impurity minerals in one coke analogue batch $= \frac{2.48}{100} \times 39.522$

$= \underline{0.980\ g}$

The percentage of impurity minerals in each coke analogue were calculated along with the percentage of mineral percentage added to each of them (see Table III.1).

Table III.1: Percentage of minerals added and impurity minerals present in each coke analogue

Coke analogue	Amount of minerals added/ g	Fired mass of coke analogue/ g	% of minerals in coke analogue	% of impurity minerals in coke analogue
Base coke analogue	0.000	80	0 %	1.22 %
Lime doped coke analogue	4.750	84.75	5.60 %	1.16 %
C3A doped coke analogue	4.926	84.926	5.80 %	1.16 %
CA doped coke analogue	4.822	84.822	5.68 %	1.16 %
CA6 doped coke analogue	4.409	84.409	5.22 %	1.15 %
CAS doped coke analogue	4.818	84.818	5.95 %	1.16 %`
Alumina doped coke analogue	9.070	89.07	10.18 %	1.10 %
Quartz doped coke analogue	5.110	85.11	6.00 %	1.15 %

Appendix IV – XRD characterization of minerals used in coke analogue preparation

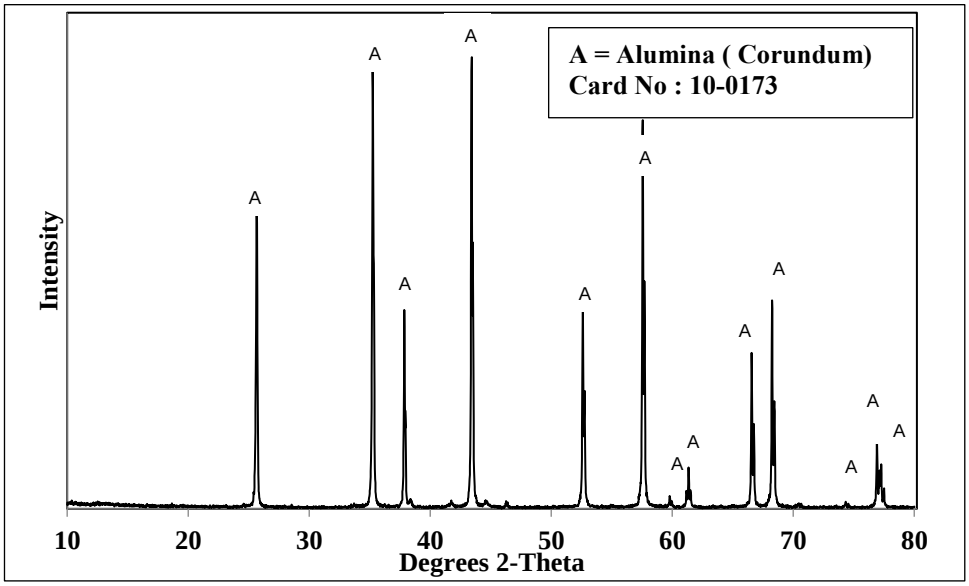

Figure IV.1: The XRD pattern of alumina powder.

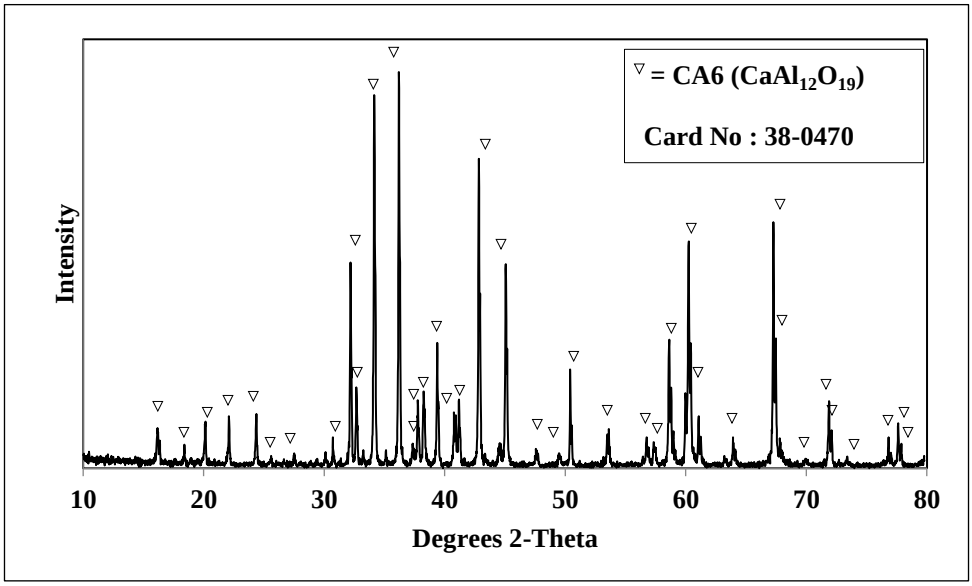

Figure IV.2: The XRD pattern of CA6 ($CaAl_{12}O_{19}$) powder.

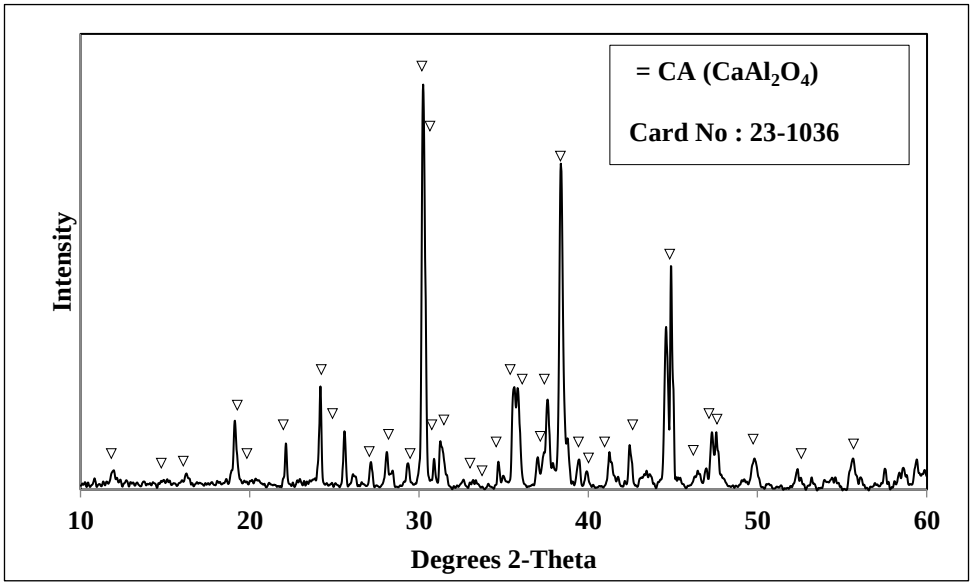

Figure IV.3: The XRD pattern of CA ($CaAl_2O_4$) powder.

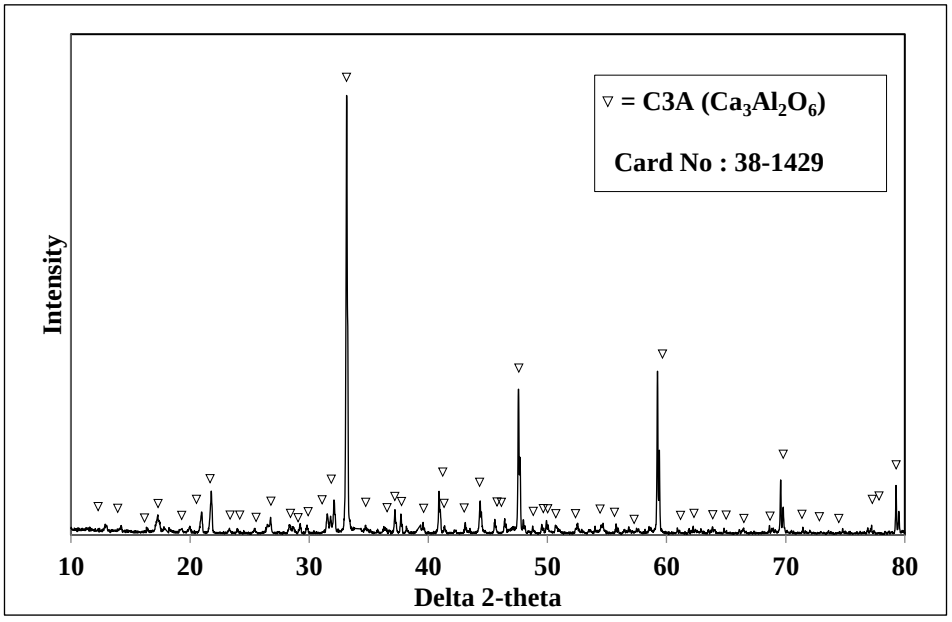

Figure IV.4: The XRD pattern of C3A ($Ca_3Al_2O_6$) powder.

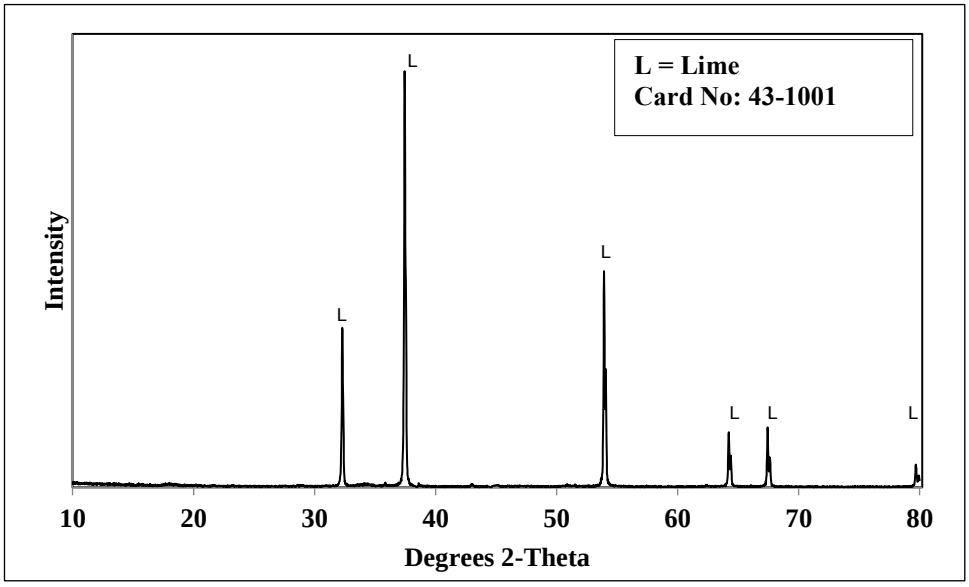

Figure IV.5: The XRD pattern of calcined lime powder.

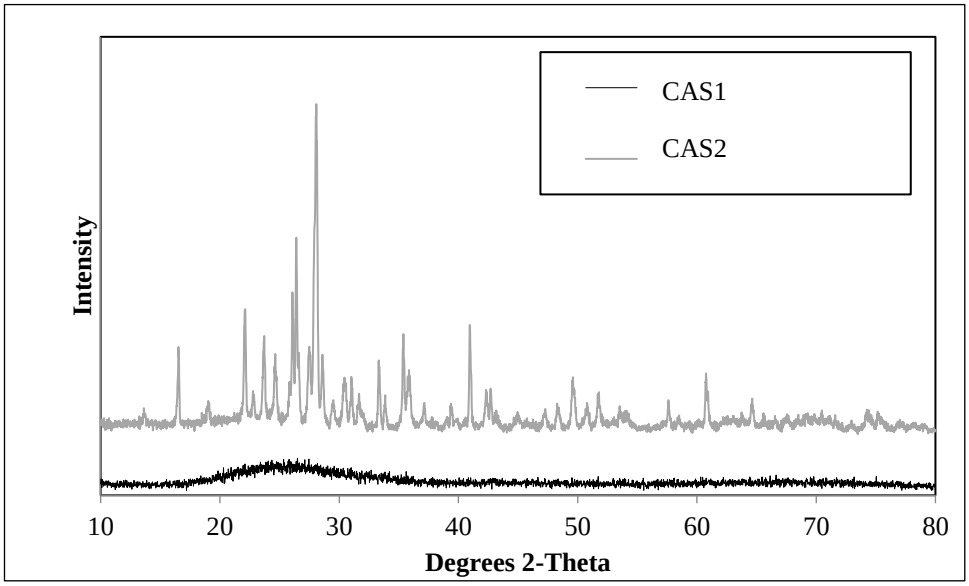

Figure IV.6: The XRD patterns crystalline and non-crystalline CASs. (Al_2O_3 – 40 %, SiO_2 – 50 %, CaO – 10 %)

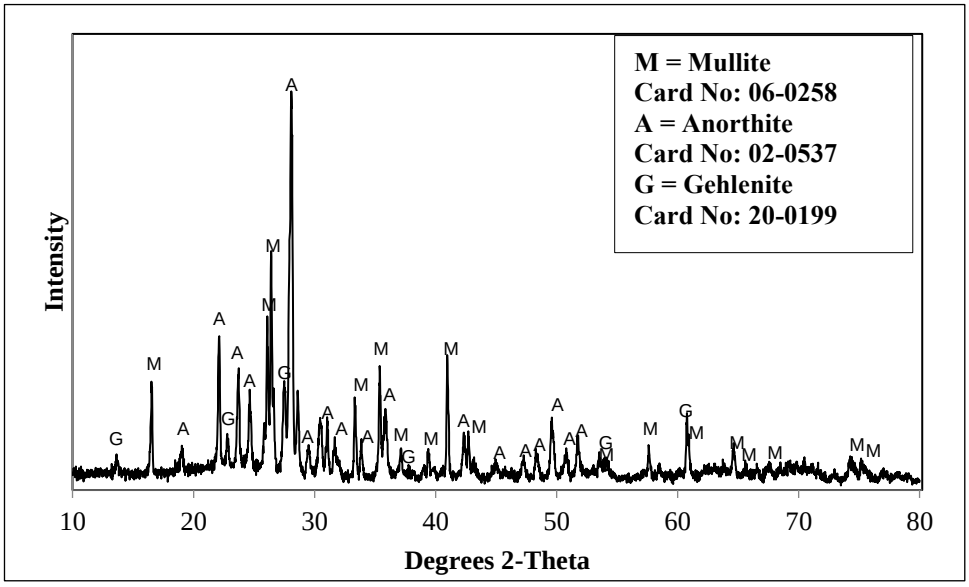

Figure IV.7: The XRD pattern of crystalline CAS mixture. (Al_2O_3 – 40 %, SiO_2 – 50 %, CaO – 10 %)

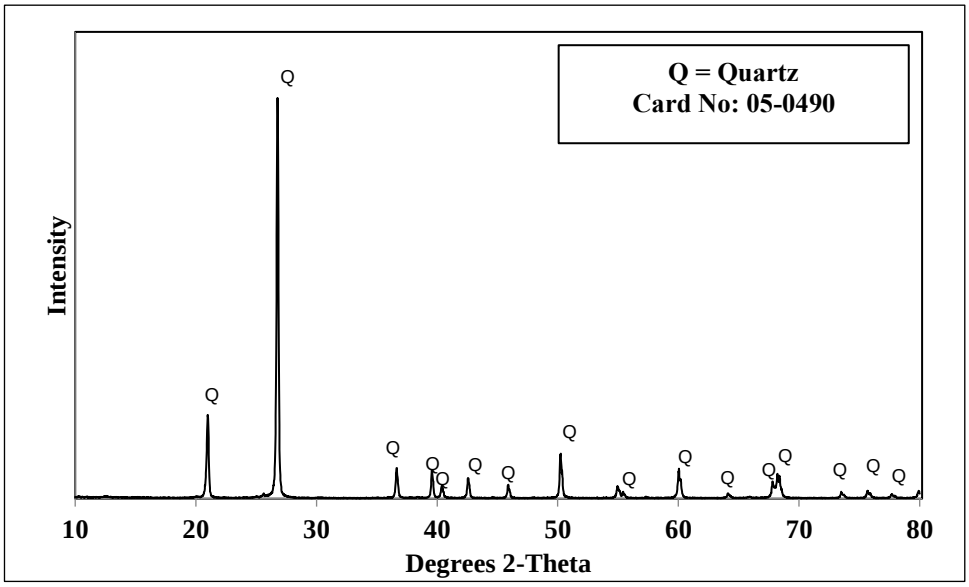

Figure IV.8: The XRD pattern of quartz powder.

Appendix V – An attempt to measure Brunauer, Emmett and Teller (BET) surface area of coke analogue

BET analysis allows for the BET surface area of a given sample to be determined from the nitrogen adsorption-desorption isotherms. During this study an attempt was taken to measure the coke analogue surface area using BET NOVA 1000 instrument.

The experiments were carried out using 200 mg of the coke analogue sample that was cut to about 2 mm size. The degassing temperature was chosen as 473 K in order to prevent any structural or compositional changes to the coke analogue.

Generally, the degassing time is chosen by conducting a series of experiments with different degassing time and the standard degassing time is (3 – 16 hours) [2]. If the degassing had taken place properly it is expected to the N_2 adsorption and desorption curves to be overlapped or lying very close to each other. However, with the coke analogue this was not able to achieve even after 48 hours of degassing and therefore discontinued. Given in Figure V.1 are the N_2 adsorption and desorption isotherms of the coke analogue samples after 6, 24 and 48 hours of degassing.

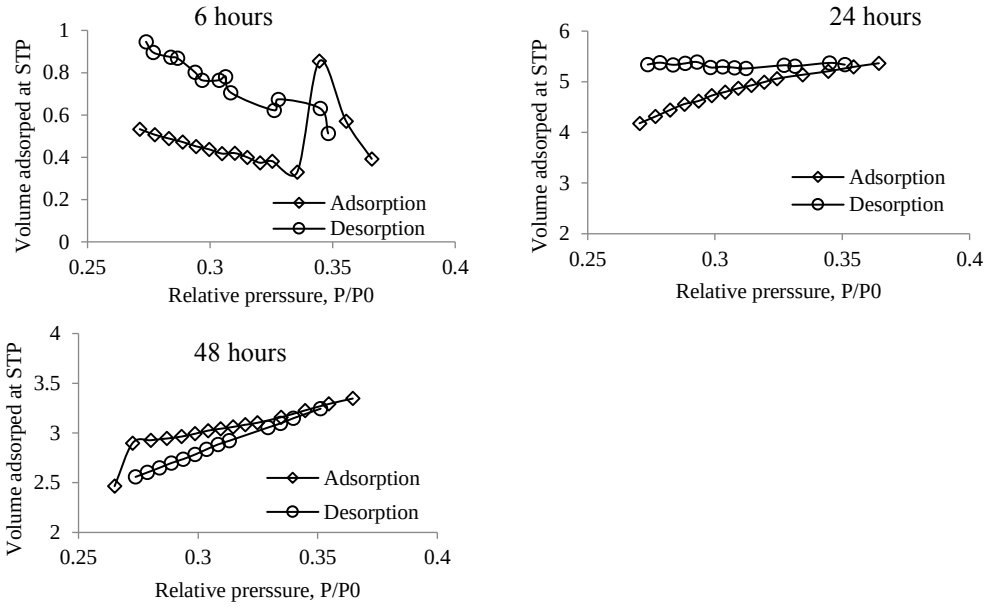

Figure V.1: Adsorption and desorption isotherms of coke analogue

[2] NOVA 1000 Gas sorption system operating manual

Appendix VI – Pore size distribution of coke analogue samples at each position

Table IV.1: Pore size distribution of the coke analogue (Refer Figure 3.18).

	10-100		100-200		200-300		300-400		400-500		>500	
	p1	pa	p1	pa	p1	pa	p1	pa	p1	pa	p1	pa
base	15.87	15.83	10.21	9.89	2.78	3.02	0.70	1.00	0.15	0.05	0.05	0.05
Alumina	15.32	15.08	7.55	7.75	3.80	4.60	1.90	2.10	0.34	0.56	0.10	0.00
CA6	17.45	17.25	7.30	5.20	3.40	3.70	1.76	1.74	1.50	0.60	0.00	0.00
CA	15.30	15.00	10.30	8.70	3.60	3.70	1.80	1.40	0.80	0.00	0.05	0.05
C3A	16.80	18.80	9.80	4.80	4.00	3.50	1.50	1.20	0.24	0.36	0.10	0.00
Lime	17.60	18.20	9.80	8.80	4.30	3.70	2.00	2.00	0.20	0.50	0.00	0.00
Quartz	13.40	14.00	8.50	5.80	4.20	4.10	2.00	3.30	0.50	0.46	0.90	1.41
CAS_n	15.80	16.30	9.10	9.80	3.50	3.80	1.90	0.80	0.10	0.00	0.05	0.05
CAS	15.30	15.00	12.00	11.00	3.80	1.10	1.00	1.20	0.08	0.02	0.00	0.00

Appendix VII – SEM point analyses of the annulus of coke analogue samples

Base coke analogue

Before the gasification reaction

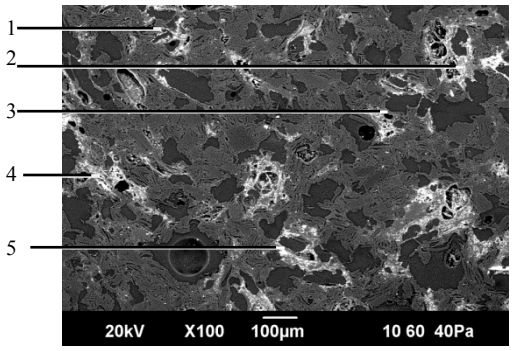

Figure VII.1: SEM backscattered image from the annulus of the base coke analogue

Table VII.1: Point analysis of the base coke analogue (mass %)

Label	1	2	3	4	5
O	35.9	36.7	28.8	31.7	41.9
Mg			1.8		
Al	15.7	27.6	21.7	15.7	21.6
Si	22.9	21.7	9.9	22.9	12.6
Ca	24.4	13.2	37.6	28.5	20.6
Fe	Trace			Trace	Trace
Total	100.0	100.0	100.0	100.0	100.0

After the gasification reaction

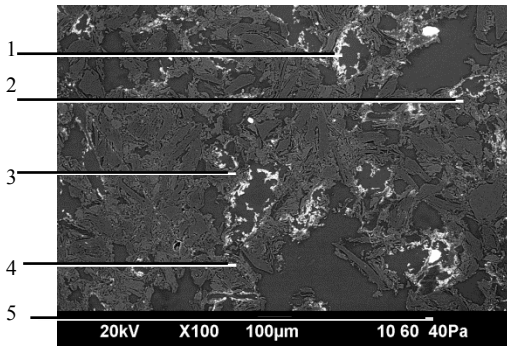

Figure VII.2: SEM backscattered image from the annulus of the base coke analogue

Table VII.2: Point analysis of the base coke analogue (mass %)

Label	1	2	3	4	5
O	48.7	47.6	38.9	42.6	45.1
Mg	Trace		Trace		
Al	12.8	21.5	12.8	24.6	18.9
Si	22.9	24.6	15.8	27.9	23.7
K		Trace		Trace	
Ca	12.5	4.5	26.8	1.4	7.6
Total	100.0	100.0	100.0	100.0	100.0

Alumina doped coke analogue

Before the gasification reaction

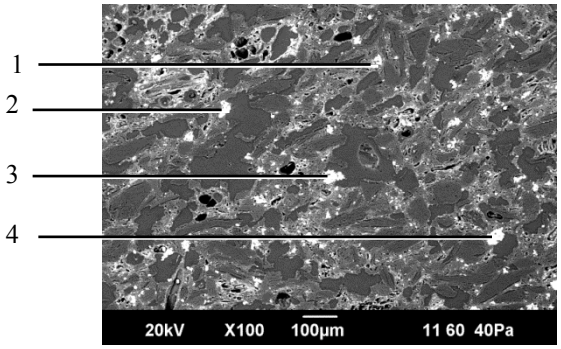

Figure VII.1: SEM backscattered image from the annulus of the alumina doped coke analogue

Table VII.1: Point analysis of the alumina doped coke analogue (mass %)

Label	1	2	3	4
O	44.7	48.7	46.9	47.9
Al	52.7	47.7	51.2	49.4
Si	Trace	2.5	Trace	Trace
Ca	Trace	Trace	Trace	Trace
K	Trace		Trace	
Total	100.0	100.0	100.0	100.0

After the gasification reaction

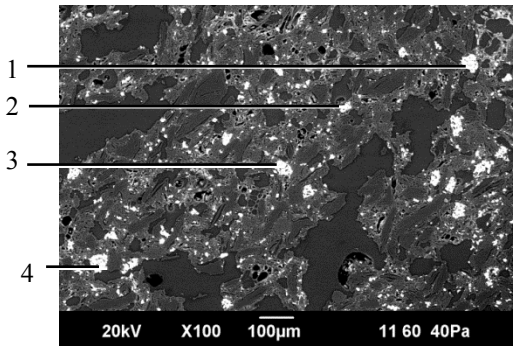

Figure VII.2: SEM backscattered image from the annulus of the alumina doped coke analogue

Table VII.2: Point analysis of the alumina doped coke analogue (mass %)

Label	1	2	3	4
O	48.9	46.8	46.9	48.8
Al	49.1	50.7	51.7	49.0
Si	1.7	1.1	Trace	1.1
Mg		Trace		
Ca	Trace	Trace	Trace	Trace
Total	100.0	100.0	100.0	100.0

CA6 doped coke analogue

Before the gasification reaction

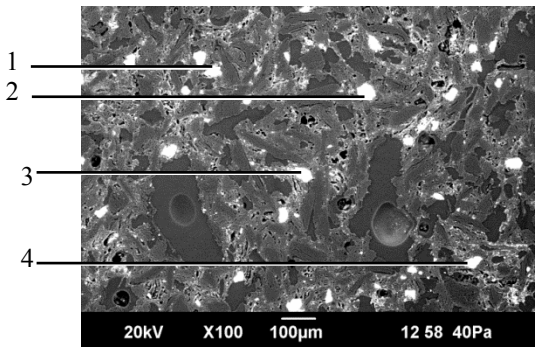

Figure VII.3: SEM backscattered image from the annulus of the CA6 doped coke analogue

Table VII.3: Point analysis of the CA6 doped coke analogue (mass %)

Label	1	2	3	4
O	43.4	42.5	41.9	45.0
Na	Trace		Trace	
Al	47.8	46.7	46.6	45.8
Si	Trace	Trace	Trace	
Ca	7.7	9.4	9.8	8.8
Total	100.0	100.0	100.0	100.0

After the gasification reaction

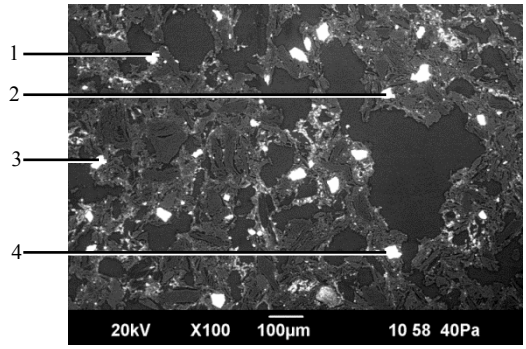

Figure VII.4: SEM backscattered image from the annulus of the CA6 doped coke analogue

Table VII.4: Point analysis of the CA6 doped coke analogue (mass %)

Label	1	2	3	4
O	46.4	47.5	48.5	46.3
Al	45.2	43.5	41.5	45.9
Si	Trace	Trace	Trace	Trace
Ca	7.2	7.9	8.9	6.8
Total	100.0	100.0	100.0	100.0

CA doped coke analogue

Before the gasification reaction

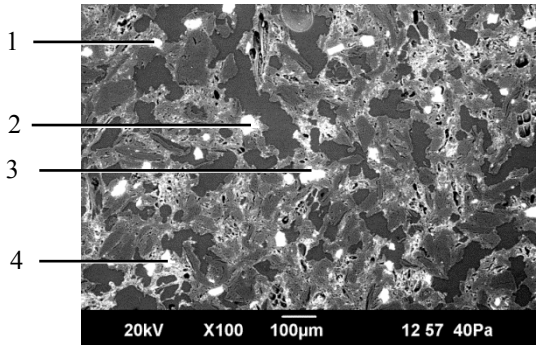

Figure VII.5: SEM backscattered image from the annulus of the CA doped coke analogue

Table VII.5: Point analysis of the CA doped coke analogue (mass %)

Label	1	2	3	4
O	39.8	40.8	39.7	40.2
Al	33.6	32.8	38.8	36.1
Si	Trace	Trace	Trace	Trace
Na	Trace			Trace
Ca	25.5	25.2	20.3	21.8
Total	100.0	100.0	100.0	100.0

After the gasification reaction

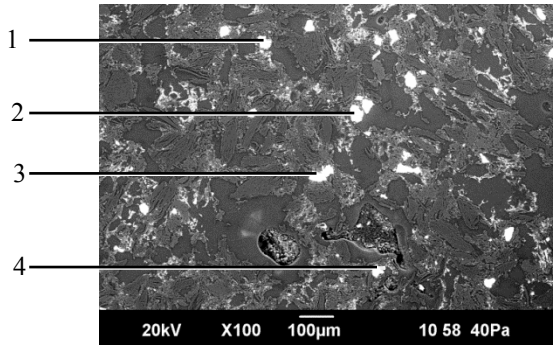

Figure VII.6: SEM backscattered image from the annulus of the CA doped coke analogue

Table VII.6: Point analysis of the CA doped coke analogue (mass %)

Label	1	2	3	4
O	38.7	40.0	41.6	40.1
Al	32.0	31.8	32.1	32.4
Si	Trace	Trace	Trace	Trace
Ca	28.2	25.5	24.7	26.9
Total	100.0	100.0	100.0	100.0

C3A doped coke analogue

Before the gasification reaction

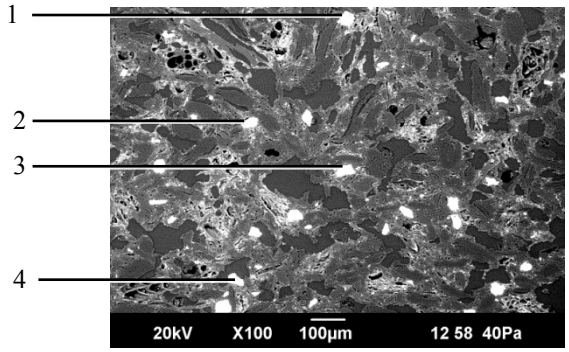

Figure VII.7: SEM backscattered image from the annulus of the C3A doped coke analogue

Table VII.7: Point analysis of the C3A doped coke analogue (mass %)

Label	1	2	3	4
O	37.7	36.8	35.6	39.1
Al	20.8	21.2	22.2	21.5
Si	Trace	Trace	Trace	Trace
Ca	40.1	41.4	41.8	39.2
Total	100.0	100.0	100.0	100.0

After the gasification reaction

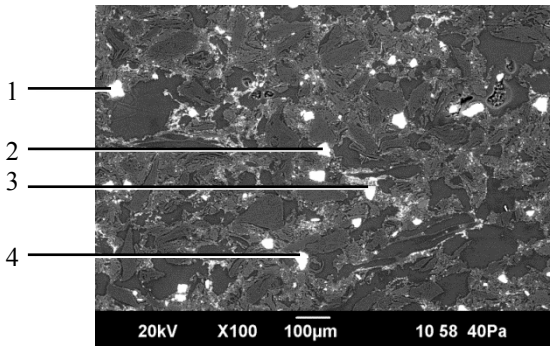

Figure VII.8: SEM backscattered image from the annulus of the C3A doped coke analogue

Table VII.8: Point analysis of the C3A doped coke analogue (mass %)

Label	1	2	3	4
O	35.4	35.7	35.4	34.8
Al	22.2	23.1	21.9	22.5
Si	Trace	Trace	Trace	Trace
Ca	41.7	40.7	41.9	42.2
Total	100.0	100.0	100.0	100.0

Lime doped coke analogue

Before the gasification reaction

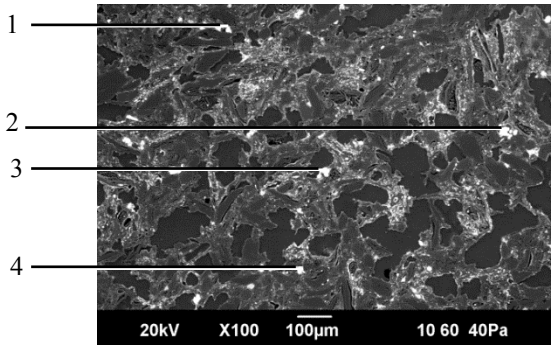

Figure VII.9: SEM backscattered image from the annulus of the lime doped coke analogue

Table VII.9: Point analysis of the lime doped coke analogue (mass %)

Label	1	2	3	4
O	28.7	29.7	29.2	29.5
Mg	Trace	Trace	Trace	Trace
Al	1.5	1.8	2.3	Trace
Si	2.5	Trace	2.6	3.0
Ca	63.5	64.9	63.9	63.1
Total	100.	100.0	100.0	100.0

After the gasification reaction

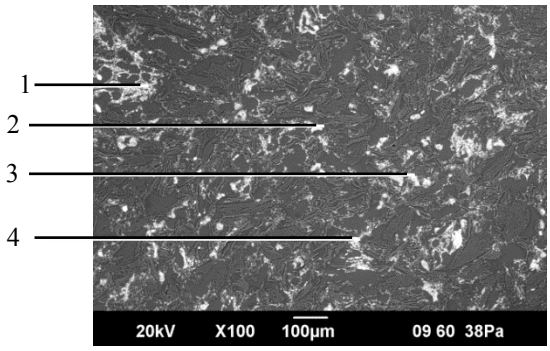

Figure VII.10: SEM backscattered image from the annulus of the lime doped coke analogue

Table VII.10: Point analysis of the lime doped coke analogue (mass %)

Label	1	2	3	4
O	29.7	30.4	29.0	29.2
Mg	Trace	Trace		Trace
Al	1.9	2.9	1.7	1.2
Si	2.3	3.4	2.1	1.5
Ca	61.7	58.7	62.8	64.8
Total	100.0	100.0	100.0	100.0

Non-crystalline CAS doped coke analogue

Before the gasification reaction

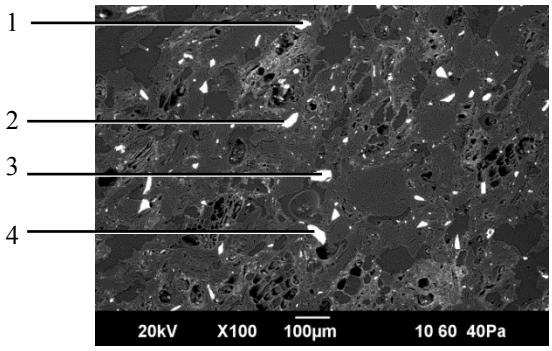

Figure VII.11: SEM backscattered image from the annulus of the non-crystalline CAS doped coke analogue

Table VII.11: Point analysis of the non-crystalline CAS doped coke analogue (mass %)

Label	1	2	3	4
O	46.7	47.1	44.9	47.2
Al	21.4	22.6	22.8	23.2
Si	22.1	22.3	22.9	21.9
Ca	8.1	7.6	8.2	7.6
Total	100.0	100.0	100.0	100.0

After the gasification reaction

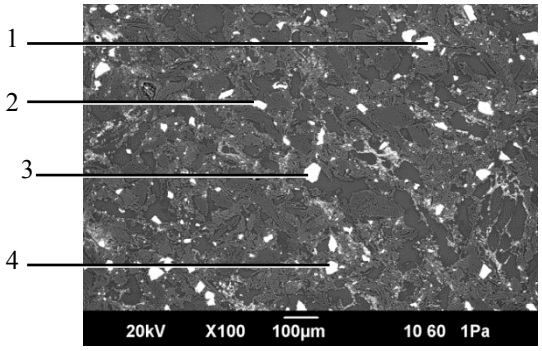

Figure VII.12: SEM backscattered image from the annulus of the non-crystalline CAS doped coke analogue

Table VII.12: Point analysis of the non-crystalline CAS doped coke analogue (mass %)

Label	1	2	3	4
O	47.1	47.2	46.8	47.0
Na	Trace			Trace
K	Trace	Trace		
Al	20.9	21.3	21.7	21.9
Si	22.5	22.3	22.8	22.1
Ca	8.3	6.6	7.5	8.1
Total	100.0	100.0	100.0	100.0

Crystalline CAS doped coke analogue

Before the gasification reaction

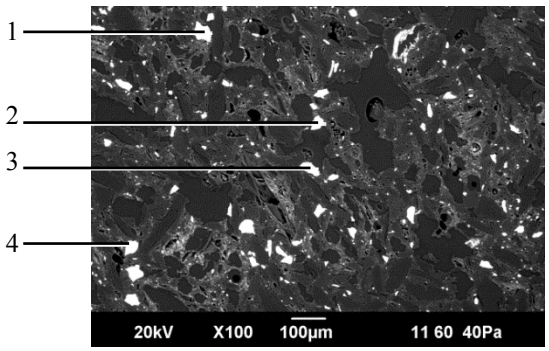

Figure VII.13: SEM backscattered image from the annulus of the crystalline CAS doped coke analogue

Table VII.13: Point analysis of the crystalline CAS doped coke analogue (mass %)

Label	1	2	3	4
O	46.7	47.2	47.0	47.1
Al	22.0	21.8	21.6	21.1
Si	22.3	21.8	21.8	22.5
K	Trace		Trace	
Ca	6.8	6.8	8.4	8.2
Total	100.0	100.0	100.0	100.0

After the gasification reaction

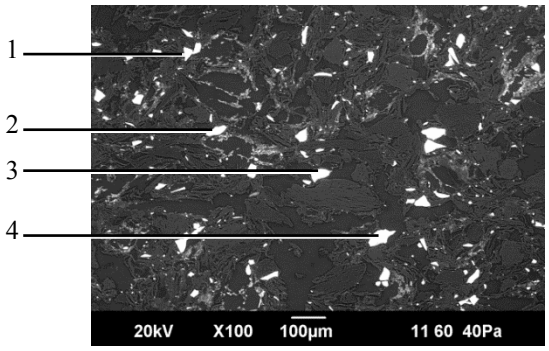

Figure VII.14: SEM backscattered image from the annulus of the crystalline CAS doped coke analogue

Table VII.14: Point analysis of the crystalline CAS doped coke analogue (mass %)

Label	1	2	3	4
O	47.3	46.8	46.6	46.6
Na	Trace			Trace
Mg		Trace		Trace
Al	20.3	20.1	20.3	20.3
Si	22.2	21.4	21.0	20.8
Ca	9.3	10.8	10.9	11.8
Fe		Trace	Trace	
Total	100.0	100.0	100.0	100.0

Quartz doped coke analogue

Before the gasification reaction

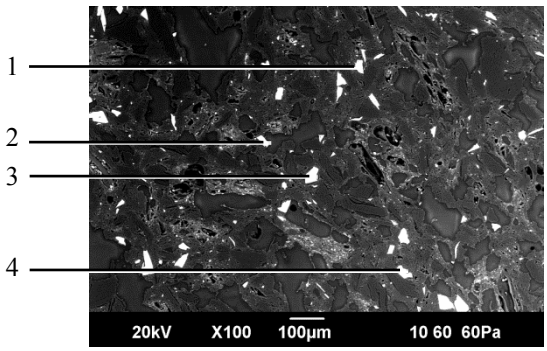

Figure VII.15: SEM backscattered image from the annulus of the quartz doped coke analogue

Table VII.15: Point analysis of the quartz doped coke analogue (mass %)

Label	1	2	3	4
O	51.9	52.0	52.7	52.6
Al	Trace	Trace	Trace	Trace
Si	45.3	44.9	45.8	45.4
Ca	Trace	Trace	Trace	Trace
Na	Trace	Trace	Trace	Trace
Total	100.0	100.0	100.0	100.0

After the gasification reaction

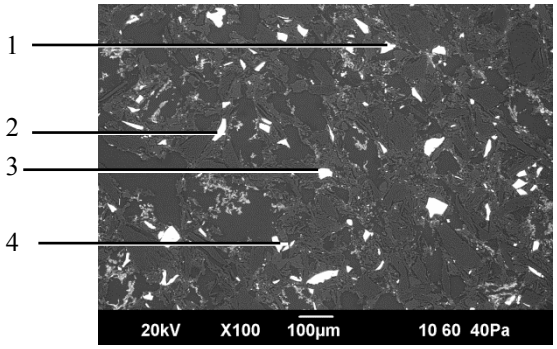

Figure VII.16: SEM backscattered image from the annulus of the quartz doped coke analogue

Table VII.16: Point analysis of the quartz doped coke analogue

Label	1	2	3	4
O	51.8	51.0	51.2	51.8
Al	Trace	Trace	Trace	Trace
Si	47.5	48.0	46.7	47.1
Ca	Trace	Trace	Trace	Trace
Fe		Trace		
Total	100.0	100.0	100.0	100.0

EDS point analysis (Atomic %) on selected particles.

Table VII.19: EDS point analysis (atomic %) for selected mineral particles in each coke analogue.

Coke analogue	Atomic %							
	O		Al		Si		Ca	
	Observed	Expected	Observed	Expected	Observed	Expected	Observed	Expected
Alumina doped coke analogue	60.6	60.0	39.4	40.0	Trace	0.0	Trace	0.0
CA6 doped coke analogue	58.0	59.4	37.8	37.5	Trace	0.0	7.7	6.0
CA doped coke analogue	57.4	57.2	28.2	28.5	Trace	0.0	14.3	14.3
C3A doped coke analogue	55.2	54.5	19.7	18.2	Trace	0.0	25.1	27.3
Lime doped coke analogue	51.3	50.0	2.7	0.0	1.7	0.0	44.3	50.0
Quartz doped coke analogue	66.9	66.7	Trace	0.0	33.1	33.3	Trace	0.0
CAS doped coke analogue	62.4	61.5	16.8	21.4	16.4	13.4	4.4	3.7

Appendix VIII – Calculation of the initial total contact area between minerals added to the coke analogue and C

To evaluate whether the total contact area between added mineral particles and C in the coke analogue, the total initial contact area were calculated. The calculations were carried out using the known mass and the density of the added minerals. Assuming the mean of the particle size range can be used to characterise the particle diameter and approximating the particles to a sphere, the surface area of the particles can be calculated. Details of the surface area calculation for the analogue are given in Table VIII.1

Table VIII.1: Initial total surface area between the added minerals and C in the coke analogue.

Mineral added	Particle size µm	Diameter, d µm	Conc. mol cation / 100g C	Mass, m g	Density, ρ $10^6 g/m^3$	Volume of a single particle, V_i $10^{-14} m^3$ $V_i = \frac{4}{3}\pi(d/2)^3$	Surface area of a single particle, A $10^{-9} m^2$ $A_i = 4\pi(d/2)^2$	Total volume of particle, V_T $10^{-6} m^3$ $V_T = \frac{m}{\rho}$	Total number of particles, N 10^7 $N = V_T / V_i$	Total surface area, A_T (m^2) $A_T = N \times A_i$
Alumina	38–53	45.5	0.1	9.07	[3]3.97	4.93	6.50	2.28	4.63	0.30
CA6	38–53	45.5	0.1	4.41	[4]3.13	4.93	6.50	1.41	2.86	0.19
CA	38–53	45.5	0.2	4.82	[3]2.96	4.93	6.50	1.63	3.30	0.21
C3A	38–53	45.5	0.1	4.93	[3]3.04	4.93	6.50	1.62	3.29	0.21
Lime	38–53	45.5	0.1	4.75	#[3]3.34	4.93	6.50	1.42	2.88	0.19
CAS	38–53	45.5	–	4.82	*2.90	4.93	6.50	1.66	3.37	0.22
Quartz	38–53	45.5	0.1	5.11	[3]2.65	4.93	6.50	1.93	3.91	0.25

*The density of CAS, a mixture of anorthite (63.5 %), gehlenite (5.1 %) and mullite (31.4 %) was calculated using the formula,

Density of CAS = (Density of anorthite X 0.635) + (Density of mullite X 0.314) + (Density of gehlenite X 0.051)

= (([3]2.76 X 0.635) + ([5]2.98 X 0.314) + ([6]3.17 X 0.051)) X 10^6 g/m^3 = 2.90 X 10^6 g/m^3

From microscopic assessment, it is known that the CaO particle size is significantly smaller and in greater numbers. Therefore, CaO contact area value is significantly underestimated.

[3] Lide DR, CRC Handbook of Chemistry and Physics, CRC Press, Florida, USA, 2003.
[4] Li M, Kuribashi K, Phase selection in the containerless solidification of undercooled $CaO \cdot 6Al_2O_3$ melts, Acta Materialia, 52 (2004) 3639-3647
[5] Jia D, Kriven WM, Sintering behavior of Gehlenite, Part II. Microstructure and mechanical propertis, Journal of American Chemical Society, 90 (2007) 2766-2770.
[6] Serra MF, Conconi MS, Gauna MR, Suarez G, Aglietti EF, Rendtorff NM, Mullite ($3Al_2O_3 \cdot 2SiO_2$) ceramics obtained by reaction sintering of rice husk ash and alumina, phase evolution, sintering and microstructure, Journal of Asian Ceramic Societies, 4 (2016)

Appendix IX – Plots for calculation of φ for RPM

Given in Figure IX.1 are the plots of R_C vs X that were used for all the coke analogues for the temperature range of 1248 – 1298 K (zone I) to determine the Xm value to be used in the RPM structural parameter determination. The C3A doped coke analogues were not presented here as there was no X_m was observed. Note that the R_C axis of lime doped coke analogues are extended than for the other coke analogues to resolve the higher reactivities.

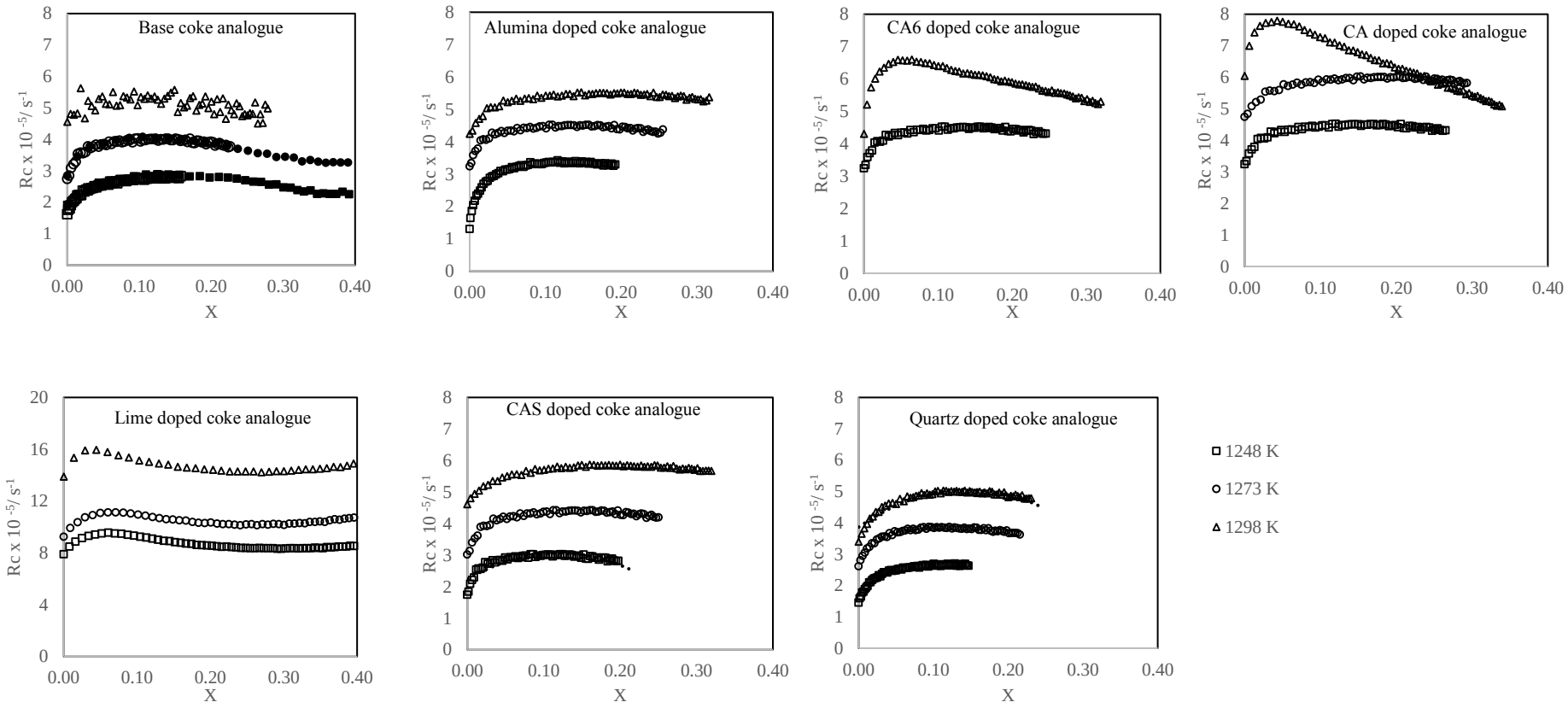

Figure IX.1: RC vs X plots for (a) base (b) lime doped (c) C3A doped (d) CA doped (e) CA6 doped (f) CAS doped (g) alumina doped (h) quartz doped coke analogues over the temperature range of 1173 – 1298 K